UNIVERSIDAD DE EXTREMADURA

TESIS DOCTORAL

DESARROLLO DE UN SISTEMA DE BIOIMPRESIÓN PARA POSICIONAR LÍNEAS CELULARES

Juan Carlos Gómez Blanco

Programa de Doctorado en
Modelización y Experimentación en Ciencia y Tecnología

2021

UNIVERSIDAD DE EXTREMADURA

TESIS DOCTORAL

DESARROLLO DE UN SISTEMA DE BIOIMPRESIÓN PARA POSICIONAR LÍNEAS CELULARES

Juan Carlos Gómez Blanco

Conformidad del director:

Fdo. Dr. D. José Blas Pagador Carrasco

Programa de Doctorado en
Modelización y Experimentación en Ciencia y Tecnología

2021

Agradecimientos

Esta tesis doctoral ha sido financiada a través de la ayuda PD16067 para la financiación de contratos predoctorales, el proyecto IB16200 "Optimización y mejora de técnicas de bioimpresión para regeneración de cartílago y prótesis vasculares" y la ayuda GR18199 a Grupos de Investigación Catalogados, todos de la Consejería de Economía, Ciencia y Agenda Digital de la Junta de Extremadura/FSE y FEDER. Así mismo, ha sido financiada por el proyecto 0633_BIOIMPACE_4_E "Impulso de la tecnología y las aplicaciones de Bioimpresión en Salud en la región EuroACE (BioimpACE)", cofinanciado por el Fondo Europeo de Desarrollo Regional (FEDER) a través del programa Interreg V-A España-Portugal (POCTEP).

Fondo Social Europeo
Fondo Europeo de Desarrollo Regional
Una manera de hacer Europa

La realización de esta tesis se ha llevado a cabo en la unidad U14-Cell Therapy de la ICTS distribuida NANBIOSIS y en el Laboratorio de Impresión Médica, localizados en el Centro de Cirugía de Mínima Invasión Jesús Usón.

Agradecimientos personales

Quiero agradecer a todas las personas que de una forma u otra han hecho posible que esta tesis se haya hecho realidad.

En primer lugar, quiero agradecer a mi director de tesis, José Blas Pagador. Él fue la primera persona en creer que una idea loca podría convertirse en una línea de investigación. No puedo tener nada más que buenas palabras para una persona que me ha dado todo su conocimiento y saber hacer. A pesar de los problemas y discusiones que hemos tenido, que no han sido pocas, hemos sido capaces de conseguir no sólo una línea de investigación funcional, sino varios proyectos e incluso un laboratorio. Me siento especialmente orgulloso de ser el primer doctorando que tienes, y aunque he pagado un poco el pato de ser el primero, tu dirección siempre ha tenido un claro fin, presentar el mejor trabajo de investigación posible. No podría haber tenido más suerte en tenerte como compañero de trabajo a pesar de ser el jefe. Aunque la verdad es que al final de este periodo siento que más que compañero o jefe tengo un amigo de los que son para siempre.

No puedo olvidarme de la gran mayoría de las personas que forman parte del Centro de Cirugía. De entre todas las personas me gustaría destacar un gran puñado de personas que me han ayudado y se han preocupado no sólo por este trabajo sino por mí. Sólo puedo agradecer todo lo que he aprendido de grandes investigadores, pero sobre todo de grandes personas. Hay muchos nombres, pero cuando pienso en el despacho de investigadores siempre se me viene a la cabeza Fede, Julia, Ferni, Claudia y Eva. Cada uno de vosotros me ha ayudado de una forma u otra, consejos, ideas, conocimientos, trabajo duro y lo más importante el escuchar mis problemas e intentar ayudarme con lo que estaba en vuestra mano, muchas gracias. También recordaré siempre los cafés después de las sesiones clínicas y de cómo esos cafés me ayudaron a conocer a grandes personas que estaban en mi misma situación. Algunos de ellos ya han conseguido terminar y al resto, ánimo que esto se termina seguro. Tampoco quiero olvidarme de agradecer toda la ayuda que Antequera siempre me ha brindado, no sólo al ayudarme a fabricar los mil chismes que he hecho, sino también con otros temas de índole más personal. José, tus consejos y vivencias me han hecho ser mejor persona, de eso estoy seguro. Por supuesto, tengo que nombrar y agradecer infinitamente a todas las chicas de Terapia Celular, cada una de vosotras me ha enseñado un poquito del vasto y complejo mundo que es la terapia celular y habéis hecho posible que tenga resultados finales en esta tesis. Vero, Esther y Federica, muchísimas gracias. También tengo que agradecer al jefe de Terapia Celular, Javi siempre has estado ahí para ayudarme con mis mil problemas y siempre te has dejado la piel para ayudar. Ahora es el turno de los bioinformáticos, he querido dejar a

los mejores para el final. Dentro de este grupo están las personas con las que he trabajado codo con codo y he podido compartir muchas horas de trabajo y muchos cafés, en definitiva, amigos más que compañeros. Tengo que nombrar a Juanmi, siempre me has ayudado y solucionado los mil y un problemas que surgen cuando intentas hacer algo importante y el ordenador se pone en huelga. María y Nuria, gracias a vuestras ilustraciones y maquetaciones hemos podido preparar congresos y publicaciones con una calidad que roza la perfección. Joaquín, de ti, al igual que del resto de los bioinformáticos, me llevo un amigo para siempre pero quiero agradecerte tus ánimos y el haber podido sacarme una sonrisa en los momentos más duros y estresantes de este camino. Por último, no tengo nada más que agradecimiento infinito a todas las personas, estén o no ya en el CCMI, con las que he tenido la inmensa suerte de encontrarme en mi unidad, Bioingeniería. Blas, ya he dicho mucho de ti y no voy a repetir, pero quiero recalcar y poner de manifiesto lo que muchos pensamos, eres el alma de la unidad y sin ti no se mantendría en pie. Paco, Juanfran, Chache y Marina, es cierto que vuestras líneas de investigación no tienen nada que ver con la mía, pero aun así, os ha faltado tiempo para echarme una mano cuando veíais que la necesitaba. Enrique, mi compañero de fatigas, fue una pena el no conocernos antes y mira que vivíamos enfrente. No podía pedir a nadie mejor con el que iniciar toda una línea de investigación. Desde casi el principio sabía que tú y yo no éramos compañeros, éramos amigos. He intentado aprender de ti todo lo que has podido enseñarme y gracias a esa mente inquieta que tienes la mía ha podido buscar más y mejorar. Sabes de sobra que esta tesis no es sólo mía, tú tienes la mitad. Así que ya sabes, te debo media tesis. También he tenido la suerte de conocer a las últimas incorporaciones en la unidad. Victor, María y David nos conocemos desde hace poco tiempo y me habéis pillado en los últimos momentos de este viaje, pero aun así siento que gracias a vosotros he podido avanzar a pasos agigantados. Aún queda una persona más en bioingeniería, pero esa persona tiene un espacio más importante reservado al final.

También quiero agradecer a todas las personas que han colaborado conmigo en este trabajo de la Escuela de Ingenierías Industriales de la Universidad de Extremadura. Muchas gracias a los dos Antonios, Macías y Parralejo, he aprendido mucho de vosotros sobre materiales cuando más perdido estaba. También quiero agradecer a Canito, a Alfonso y a Álvaro, siempre me habéis dado ánimos y ayudado con temas mecánicos y de simulaciones. Pero sobre todo quiero agradecer a Manuel, tu ayuda ha sido imprescindible para llegar a la meta. No sólo has montado los prototipos, sino que me has ayudado a tener claras muchas ideas clave.

A mis amigos de toda la vida, que me han apoyado desde el principio y se han preocupado por mi cuando estaba de bajón. De todos ellos, quiero agradecer a Angelica por su apoyo moral en infinidad de momentos y a Mikel por las charlas motivacionales que hemos tenido contándonos el estado de nuestras tesis. Pero sobre todo quiero agradecer a Lolo y a Corbacho, ellos me metieron en el mundo de la impresión 3D y sin ellos todo este trabajo ni siquiera habría empezado.

A mi familia, a todos ellos. Cada uno de ellos me ha apoyado en todo lo que podía en todo momento. Pero de forma especial a mis padres, a mi hermana y a mis abuelas, que han estado pendientes de mí y preocupándose por mí más que yo mismo.

Han sabido darme tanto el abrazo como el espacio que necesitaba justo en el mejor momento. Muchas gracias, sin vosotros no lo habría conseguido.

Este último párrafo es para una de las personas más importantes en mi vida, Luisa. Desde el primer momento como compañera de trabajo y amiga me has apoyado con todo lo que podías hacer. Ahora que nuestra relación ha evolucionado no tengo palabras suficientes para agradecerte todo lo que haces por mí. Me has aguantado en los malos momentos y me has aconsejado y cuidado como nadie puede hacer. A pesar de que estás inmersa en tu propia tesis dejas todo de lado cada vez que tengo el menor problema y te desvives por ayudarme a solucionarlo. He llegado hasta aquí sólo por tu ayuda y sólo puedo decirte GRACIAS desde el fondo más profundo de mi corazón. Ahora que estoy terminando sólo cuento las horas para poder ayudarte a ti y devolverte, aunque sólo sea una pequeña porción, todo lo que tú me has dado. Falafel.

Resumen

Actualmente, la bioimpresión por μ-extrusión es versátil y permite diferentes viscosidades de material, pero aún presenta problemas como su baja resolución y velocidad o el posible daño celular. Por este motivo, la presente tesis plantea el objetivo de mejorar la bioimpresión por μ-extrusión para posicionar líneas celulares. Para ello, se ha diseñado y desarrollado una bioimpresora con un sistema de pre-incubación y cabezal calefactado con cambio rápido de jeringa. Además, se ha estudiado el flujo de hidrogeles y la influencia de diferentes nozzles mediante simulación computacional. Los resultados muestran que el sistema de pre-incubación controla eficiente y rápidamente la temperatura y la humedad durante la bioimpresión. Tanto las simulaciones como un estudio experimental demuestran que es posible aumentar la velocidad de bioimpresión al usar un nozzle estándar de impresión 3D FDM sin aumentar las presiones internas, ni el estrés cortante durante la bioimpresión. En definitiva, estos scaffolds bioimpresos presentan una viabilidad celular tras ser cultivados superior al 80 %.

Abstract

Currently, μ-extrusion bioprinting is versatile and allows a wide range of viscosities for materials, but it still lacks of high printing resolution and speed further of possible cellular damage. For this reason, this thesis aims to improve current μ-extrusion bioprinting systems for positioning cell lines. Hence, a bioprinter consisted of a pre-incubation system and a piston-driven extrusion heated head with a quick syringe change system has been designed and developed. Furthermore, the hydrogel flow and the influence of several nozzles through computational simulation have been analysed. Results show that the pre-incubation system controls efficient and quickly both temperature and humidity during the bioprinting process. Additionally, several simulations and an experimental study demonstrate that is possible to speed up bioprinting using a standard FDM 3D printing nozzle without increasing the inner pressure or shear stress of this process. Finally, these bioprinted scaffolds show a cell viability after being cultured higher of 80 %.

Índice

Índice de figuras iii

Índice de tablas v

1 Justificación Unitaria de la Tesis 1

2 Introducción 3
2.1 Bioimpresión . . . 3
2.1.1 Fabricación aditiva . . . 3
2.1.2 Técnicas de bioimpresión . . . 4
2.1.2.1 μ-extrusión . . . 4
2.1.2.2 Inyección de tinta . . . 5
2.1.2.3 Asistida por láser . . . 6
2.1.2.4 Estereolitografía . . . 6
2.1.2.5 Electrospinning . . . 6
2.1.2.6 Comparación de técnicas . . . 6
2.2 Biomateriales . . . 8
2.2.1 Naturales vs. sintéticos . . . 9
2.2.2 Propiedades del hidrogel . . . 9
2.3 Dinámica de fluidos computacional . . . 10
2.3.1 Level Set . . . 10
2.3.2 Parámetros de salida . . . 10
2.4 Viabilidad celular . . . 11

3 Objetivos 13

4 Resumen de resultados y discusión 15
4.1 Revisión sistemática de hidrogeles para bioimpresión . . . 16
4.1.1 Generación del hidrogel . . . 16
4.1.2 Parámetros de bioimpresión por μ-extrusión . . . 16
4.1.3 Pruebas biológicas y mecánicas . . . 19
4.2 Revisión sistemática de simulaciones de cabezales . . . 20
4.3 Influencia de la temperatura del hidrogel en la presión, en la velocidad y en el esfuerzo cortante mediante simulación computacional . . . 21
4.4 Simulación computacional de nozzle FDM estándar vs. punta cónica . . . 23
4.5 Sistema de pre-incubación con control de temperatura y humedad . . . 25
4.6 Mejora de la velocidad de bioimpresión utilizando un nozzle estándar de impresión 3D FDM . . . 26

5 Conclusiones **31**

6 Bibliografía **33**

7 Resultados de la tesis **37**

7.1 Hydrogels for bioprinting: A systematic review of hydrogels synthesis, bioprinting parameters and bioprinted structures Behavior 41

7.2 Optimization of computational simulations on bioprinting nozzles: A combination of systematic review and design of experiments 71

7.3 Bioink temperature influence on shear stress, pressure and velocity using computational simulation 81

7.4 Computational simulation-based comparative analysis of standard 3D printing and conical nozzles for pneumatic and piston-driven bioprinting 101

7.5 Temperature and humidity PID controller for a bioprinter atmospheric enclosure system 117

7.6 Improving cell viability and velocity in μ-extrusion bioprinting with a novel pre-incubator bioprinter and a standard FDM 3D printing nozzle . 135

Índice de figuras

2.1 Tipos de bioimpresión más habituales. 5

4.1 Combinación de los diez materiales más utilizados en hidrogeles. . . . 17
4.2 Crosslinking utilizado en los tres materiales más comunes. 18
4.3 Líneas celulares más representativas en bioimpresión. 19
4.4 Datos reológicos de Cellink Bioink. 21
4.5 Fracción volumétrica de las simulaciones del estudio. 22
4.6 Volumen extruido (mm^3) de las simulaciones neumáticas. 24
4.7 Presión de impresión (kPa) de las simulaciones mecánicas. 24
4.8 Diseño tridimensional del sistema de pre-incubación. 25
4.9 Simulación teórica y experimental del sistema PID desacoplado. . . . 26
4.10 Cabezal de extrusión con cambio rápido de jeringas. 27
4.11 Viabilidad celular comparada de los nozzles agrupada por tiempo. . . 29

Índice de tablas

2.1 Ventajas y desventajas de las diferentes técnicas de bioimpresión. . . 7

4.1 Parámetros físicos más utilizados en las simulaciones de bioimpresión. 20

4.2 Parámetros de los cuatro grupos para las pruebas de viabilidad celular. 28

1. Justificación Unitaria de la Tesis

Las técnicas y los materiales para bioimpresión han evolucionado notablemente en los últimos años, aprovechando el conocimiento generado en impresión 3D y en ingeniería tisular y los avances en biomateriales. De esta forma, la bioimpresión ofrece nuevas posibilidades en diferentes aplicaciones del ámbito sanitario, como la generación de tejidos, y ya se utiliza con éxito en ensayos con medicamentos y en cierto tipo de prótesis. Esta confluencia de disciplinas científicas obliga a generar equipos de trabajo multidisciplinares con conocimientos tanto en el comportamiento biológico, ingenieril o químico, entre otros.

Sin embargo, la gran variedad de técnicas de bioimpresión y de biomateriales hace que aún existan muchos retos por resolver y que sea necesario un esfuerzo de consenso por definir criterios y métricas comunes que promuevan el avance de esta disciplina científica.

Por este motivo, y centrándose en una de las técnicas de bioimpresión más utilizadas en la actualidad, la μ-extrusión, este trabajo de tesis se ha planteado analizar en detalle algunos de los principales problemas asociados a esta técnica y proponer soluciones que mejoren la calidad de las estructuras bioimpresas.

En primer lugar, se ha revisado el estado del arte de los factores que pueden tener un mayor impacto en la calidad de la bioimpresión por μ-extrusión. Por un lado, los hidrogeles que forman parte de las biotintas: su fabricación, su uso y su curado, con especial interés en sus propiedades reológicas. Por otro lado, las simulaciones computacionales del cabezal de bioimpresión por donde fluyen dichos hidrogeles, atendiendo a su forma y a la definición de sus propiedades. Ambos factores pueden favorecer o comprometer tanto el proceso de bioimpresión como el resultado final del mismo. Esta información ha sido la base para el planteamiento de soluciones, el diseño conceptual de las aportaciones de la tesis y el desarrollo experimental de las pruebas para comprobar la validez de estas ideas.

Posteriormente, se ha diseñado y fabricado una bioimpresora basada en μ-extrusión donde varios de sus componentes tienen una importancia reseñable como resultados de la presente tesis. Para ello, se han estudiado mediante simulaciones computacionales, utilizando una biotinta concreta, la baja influencia de la temperatura en parámetros internos del proceso de μ-extrusión como la presión, la velocidad o el esfuerzo cortante;

o la relación entre el diámetro del nozzle y el flujo volumétrico obtenido. Por este motivo, antes de fabricar el nuevo cabezal de μ-extrusión con sistema de cambio rápido de jeringa, se ha comprobado también mediante simulación computacional que el uso de un nozzle estándar de impresión 3D FDM acelera el proceso de impresión sin aumentar excesivamente la presión y el esfuerzo cortante.

Además, para dotar a la bioimpresora de mejores condiciones ambientales que permitan asegurar la esterilidad y mantener unas condiciones de pre-incubación, se ha diseñado, desarrollado y validado una primera versión de este sistema específico que controla de forma eficiente y rápida la temperatura y la humedad dentro de la cabina de bioimpresión.

Finalmente, una vez integrados todos los desarrollos en la bioimpresora se ha realizado un estudio experimental generando un conjunto de scaffolds bioimpresos que ha confirmado los resultados de las simulaciones, ofreciendo tasas de supervivencia celular por encima del 80 % con la misma biotinta y el mismo nozzle usados en las simulaciones.

La ejecución del trabajo de investigación se ha realizado en el Centro de Cirugía de Mínima Invasión Jesús Usón (Cáceres, España), en estrecha colaboración con el resto de instituciones que han participado en los proyectos de investigación donde se enmarca la presente tesis. El Centro de Cirugía de Mínima Invasión Jesús Usón es un centro dedicado a la investigación y formación en técnicas quirúrgicas. La Unidad de Bioingeniería y Tecnologías Sanitarias y otras unidades del Centro de Cirugía de Mínima Invasión Jesús Usón trabajan actualmente en el desarrollo de la biompresión con diferentes aplicaciones en el sector sanitario.

2. Introducción

2.1 Bioimpresión

2.1.1 Fabricación aditiva

El proceso de fabricación en cadenas de producción semiautomatizadas para producir una gran cantidad de objetos iguales está siendo desplazado, en algunos sectores, por técnicas de fabricación orientadas a productos personalizados de tiradas cortas. Este nuevo proceso de fabricación ha sido impulsado en gran medida por la fabricación aditiva. Consiste en la creación de objetos mediante la superposición de capas y puede usarse con gran variedad de materiales. La primera idea de fabricación aditiva fue introducida por Hideo Kodama [1] en el año 1981 y consistía en un proceso sucesivo de endurecimiento de una capa delgada de un material fotosensible. Este proceso evolucionó a lo que actualmente se conoce como estereolitografía y fue patentado en 1984 por Alain Le Méhauté, Olivier de Witte y Jean Claude André [2]. Este proceso permaneció escondido hasta la liberación de la patente en 2014 y fue en ese momento cuando se comenzó a conocer y desarrollar este tipo de fabricación en la sociedad como impresión 3D.

La impresión 3D se puede clasificar en diferentes tipos de tecnologías atendiendo a la metodología utilizada para procesar el material base. Las más conocidas y utilizadas son las que se basan en depositar un polímero fundido (FDM), en fotopolimerizar una resina (SLA) o en fundir polvo (SLS, SLM, DMLS) [3–5]. Así mismo, cada tecnología utiliza el tipo de material más apropiado para su proceso. Algunos ejemplos son filamentos de polímeros con una temperatura de fusión entre 190 y 250 °C, como el ácido poliláctico y el acrilonitrilo butadieno estireno conocidos como PLA y ABS por sus siglas en inglés. Estos polímeros son habituales en FDM. Por otro lado, resinas con agentes iniciadores de fotopolimerización como ICSC: 1346 (Peróxido de bis(alfa,alfa-dimetilbencilo)) o el Irgacure 819 (Óxido de fenilbis(2,4,6-trimetilbenzoil)fosfina) se suelen usar con SLA. Mientras que los equipos de SLS usan polvos de poliamida-11 y 12 (Nilon) o de TPU. Las aplicaciones que tiene esta nueva forma de fabricación pueden extrapolarse a prácticamente todos los sectores de la industria. La posibilidad de crear objetos totalmente personalizados con un coste razonable hace que la impresión 3D se utilice tanto a nivel doméstico como a nivel profesional. La industria aeroespacial, del automóvil, alimentaria,

textil, de la construcción, mecánica, eléctrica y electrónica [4] son las que más se han beneficiado de este nuevo tipo de tecnología por el momento. Pero de todas estas posibles aplicaciones, la impresión 3D está empezando a ofrecer resultados muy prometedores en la industria médica y farmacéutica.

Dentro de las aplicaciones de la impresión 3D en medicina existen cuatro líneas de trabajo principales [4, 6–9]:

- Modelos preoperatorios
- Implantes permanentes no-bioactivos
- Fabricación de scaffolds bioactivos y biodegradables
- Fabricación de tejidos y órganos

Todas estas aplicaciones utilizan el concepto fundamental de personalización de la fabricación aditiva. No obstante, la fabricación de tejido con material biológico requiere de unas condiciones especiales que no se han tenido en cuenta en las técnicas industriales tradicionales. Esto se debe principalmente a que han sido ideadas para trabajar con materiales para cumplir una serie de características mecánicas o estéticas, pero no para trabajar con materiales biocompatibles ni con material biológico. Por esta razón, las técnicas de impresión 3D se han adaptado junto a la ingeniería tisular para evolucionar hacia la bioimpresión. Esta nueva disciplina se puede definir como la aplicación de técnicas de impresión 3D utilizando material biológico y biomateriales con el objetivo de generar estructuras biológicas funcionales [10, 11].

2.1.2 Técnicas de bioimpresión

Actualmente, en bioimpresión se investiga la generación de toda clase tejidos. Entre ellos se pueden destacar tejido vascular, tejido neuronal, cartílago, tejido óseo, tejido cardíaco, piel o músculo [12, 13]. Cada tipo de tejido tiene unas propiedades muy distintivas acorde con la función que desempeña en el cuerpo. Esto hace necesario la utilización de materiales compatibles con cada línea celular para poder fabricar dicho tejido. Además de la correcta elección de los materiales y de las células es imprescindible seleccionar adecuadamente el tipo de técnica de bioimpresión. Cada técnica aporta ventajas e inconvenientes que pueden influir en la correcta fabricación del tejido o, por el contrario, ser un factor limitante para obtener un buen resultado.

Existen una cantidad considerable de técnicas de bioimpresión y no hay un consenso acerca de una clasificación formal. No obstante, la mayoría de los autores coinciden en que las técnicas de μ-extrusión, inyección de tinta (*inkjet-assisted*), asistida por láser (*laser-assisted*), estereolitografía y electrospinning son los métodos de bioimpresión más extendidos [7, 11, 13, 14]. La figura 2.1 contiene un esquema de las partes principales y el funcionamiento de los diferentes tipos de bioimpresión más utilizados.

2.1.2.1 μ-extrusión

La bioimpresión por μ-extrusión se basa en *empujar* el material para que pase a través de un cabezal. El sistema está formado por un recipiente contenedor del material, un sistema de empuje de dicho material y un cabezal extrusor con un

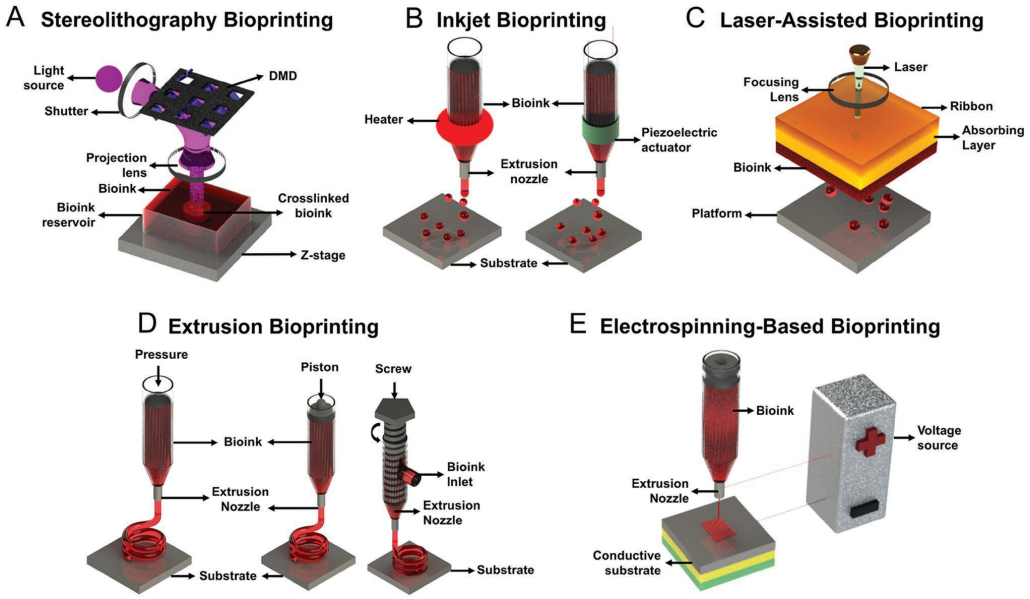

Figura 2.1: Tipos de bioimpresión más habituales. Figura reproducida con la autorización del editor de [13]

diámetro de salida variable según la aplicación. El sistema de extrusión se clasifica en: neumático, mecánico y tornillo sin fin, en función de la utilización de aire, un pistón o un tornillo sin fin, respectivamente (figura 2.1).

Este sistema de bioimpresión tiene una serie de ventajas como la posibilidad de imprimir materiales muy viscosos y con una alta concentración de células e imprimir varios materiales en el mismo proceso. También cuenta con una serie de limitaciones, como son una baja resolución de impresión (> 200 μm), una baja velocidad de impresión y la posibilidad de provocar cambios morfológicos e incluso la lisis celular debido a la presión ejercida sobre las células [11, 13, 15].

A pesar de todo es uno de los procesos de bioimpresión más simples, tanto en maquinaria como en protocolos, y más asequibles, por lo que es el proceso de bioimpresión más utilizado.

2.1.2.2 Inyección de tinta

El principio de funcionamiento de la bioimpresión por inyección de tinta consiste en crear una gota en la punta del cabezal de extrusión y lanzarla a un sustrato donde se deposita. Este sistema está compuesto por un recipiente contenedor del material, un cabezal extrusor y un sistema de generación de gotas. En función de si se utiliza calor u ondas ultrasónicas para generar las gotas, esta técnica de bioimpresión se puede dividir en inyección térmica e inyección piezoeléctrica.

La ventaja más relevante de este sistema de bioimpresión es la capacidad de obtener altas resoluciones (aproximadamente 50 μm) con altas viabilidades celulares. Además, es un sistema de bioimpresión rápido y bastante asequible. No obstante, el sistema no permite materiales muy viscosos y no es capaz de funcionar con materiales con altas densidades celulares, lo que limita sus posibles aplicaciones [11, 13, 15].

2.1.2.3 Asistida por láser

La bioimpresión asistida por láser consiste en la generación de una gota, al incidir un rayo láser en un sustrato de origen formado por el material y las células, que luego se lanza a un sustrato receptor. El sistema está compuesto por tres partes: un sustrato de origen, un pulso láser y un sustrato receptor. El sustrato de origen está formado por una lámina de vidrio y una lámina de metal al que se le adhiere una capa fina del material con las células (figura 2.1).

Esta técnica cuenta con las mayores resoluciones (10-50 μm) siendo incluso capaz de depositar una sola célula [16]. También cuenta con una tasa de viabilidad celular muy elevada (>95 %). La desventaja principal es la reducida estabilidad del sistema que junto con su coste elevado y la baja escalabilidad que posee hace que no sea tan utilizada como la extrusión o la inyección de tinta [11, 13, 15].

2.1.2.4 Estereolitografía

La bioimpresión por estereolitografía funciona exactamente igual que la técnica SLA de la impresión 3D tradicional. Los objetos se forman al fotopolimerizar mediante luz UV capas sucesivas de un material fotosensible. El sistema está formado por un recipiente donde se encuentra el material fotosensible, una superficie de impresión donde se crea la pieza y un láser UV (figura 2.1).

Esta técnica tiene una velocidad de impresión muy alta y además cuenta con una resolución ajustable (5-300 μm) al poder colimar el haz láser. Los mayores inconvenientes son que la reacción de fotopolimerización necesita un material poco viscoso y con una baja densidad celular. Además, los materiales más comunes de estereolitografía utilizan luz UV junto con fotoiniciadores que normalmente influyen negativamente en la viabilidad celular. En este sentido, las investigaciones actuales en este campo se centran en obtener materiales que fotopolimericen con luz visible y utilizando fotoiniciadores que no sean tan dañinos para las células [17, 18].

2.1.2.5 Electrospinning

La bioimpresión por electrospinning consiste en producir una microfibra utilizando una diferencia de potencial eléctrico. El sistema consta de un robot cartesiano junto con un sistema de electrospinning (bomba de jeringa o un regulador neumático y una fuente de alimentación de alto voltaje) (figura 2.1).

Este tipo de sistemas cuenta con una resolución muy alta (< 1 μm) y está muy optimizada para generar scaffolds. No obstante, es un sistema muy caro y complejo que no es capaz de imprimir directamente células [13, 19].

2.1.2.6 Comparación de técnicas

Con toda la información de cada una de las tecnologías de bioimpresión se presenta en la tabla 2.1 un resumen de sus ventajas e inconvenientes.

Tabla 2.1: Ventajas y desventajas de las diferentes técnicas de bioimpresión. Las resoluciones indicadas son nominales y pueden variar bajo condiciones concretas de bioimpresión. Traducido y reproducido con autorización del editor de [13]

Tecnologías de impresión 3D	Ventajas	Desventajas
Estereolitografía	Crosslinking simultáneo de la capa 2D completa evita la necesidad del movimiento X-Y	Crosslinking requiere biotinta transparente y fotosensible, limitando la elección de aditivos y densidad celular (10^8 células/mL)
	Viabilidad celular alta (>85 %)	Sistema comparativamente complejo
	Gran variedad de biotintas imprimibles	
	Gran resolución de bioimpresión ($\approx 1\mu m$)	
Inyección de tinta	Método de bioimpresión simple	Limitado a densidad celular baja (<10^6 células/mL)
	Bajo coste	Limitado a biotintas con viscosidad de entre 3.5 y 12 mPa·s
	Aplicabilidad de bioimpresión multimaterial	
	Alta resolución	
	Viabilidad celular alta	
Asistida por láser	Viabilidad celular alta	Limitado a densidad celular baja (<10^6 células/mL)
	Variedad de biotintas imprimibles con viscosidad de entre 1 y 300 mPa·s	Sistema complejo
		Coste comparativamente alto
Por extrusión	Capacidad para imprimir biotintas altamente viscosas (30 - 6 × 10^7 mPa·s)	Velocidad de impresión relativamente baja
	Capacidad para imprimir densidades celulares altas (incluyendo esferoides celulares)	Resolución baja-media altamente dependiente de la configuración
	Aplicabilidad de bioimpresión multimaterial	Viabilidad celular moderada (40-80 %) dependiente de la configuración
	Proceso de bioimpresión comparativamente simple	
Electrospinning	Alta resolución	No es posible imprimir células directamente
	Óptima para la fabricación de scaffolds	Sistema complejo
		Coste elevado

Se puede comprobar en la bibliografía que, pese a tener una menor resolución, menores velocidades de impresión y una viabilidad celular algo inferior a la de las otras técnicas, la bioimpresión por μ-extrusión es la más utilizada. La posibilidad de poder utilizar varios materiales con una amplia gama de viscosidades y densidades celulares hace que sea una técnica muy versátil y atractiva para investigadores y empresas.

2.2 Biomateriales

El proceso de bioimpresión no solo depende de la técnica utilizada. Hacer una correcta elección del material a imprimir es igual de importante. Como prueba se pueden encontrar numerosos trabajos científicos que intentan optimizar materiales para bioimpresión [15, 20–22]. La gran cantidad de estudios sobre materiales para bioimpresión, se debe a la necesidad de obtener materiales adecuados para las células (biocompatibles), pero que además proporcionen ciertas propiedades mecánicas. En este sentido, Groll et al.[20] definen dos conceptos básicos a tener en cuenta en los procesos de bioimpresión. El primero de ellos es el concepto de biotinta (bioink). La definición propuesta de biotinta es: "*una formulación de células apta para su elaboración mediante una tecnología de biofabricación automatizada que también puede contener componentes biológicamente activos y biomateriales*" [20, 22]. Esta definición indica que cualquier biotinta es un conjunto de células y materiales que deberían tener buenas propiedades biocompatibles y mecánicas además de poder utilizarse en uno de los procesos de bioimpresión [15]. Como ejemplo, el material a utilizar para bioimprimir un defecto óseo es totalmente diferente al utilizado para un parche liberador de fármacos. El primero necesita trabajar con osteocitos y tener una rigidez estructural elevada mientras que el segundo material requiere degradarse con el tiempo y ser lo más flexible posible. Esta lista de requisitos hace que las posibilidades de elección de materiales para biotintas se reduzcan.

La segunda definición propuesta por Groll *et al.* [20] se refiere a la tinta de biomaterial (biomaterial ink). En este caso, la definición es: "*cualquier formulación de materiales aptas para su elaboración mediante una tecnología de fabricación automatizada que puede contener componentes biológicamente activos y biomateriales*". Esta definición es muy similar a la propuesta para biotinta pero con una clara diferencia, dentro de una tinta de biomaterial no existen células. Por lo tanto, una biotinta es una tinta de biomaterial que contiene células. Estas definiciones se basan en un principio funcional de bioimpresión. Dentro de las tintas de biomaterial se englobarán los materiales que no pueden contener células en su interior, mientras que las biotintas serán generalmente compuestos similares a hidrogeles. Por lo tanto, se suele distinguir entre aquellos materiales que a temperatura ambiente se presentan en forma sólida (filamentos, pellet o polvo) y que necesitan ser fundidos, a temperaturas mayores a las que las células pueden sobrevivir, para ser extruidos. Por el contrario, los hidrogeles están formados por más de un 90 % de agua y, por lo tanto, tienen una consistencia parecida a la de una pasta o gel a temperatura ambiente [15]. En el caso de los hidrogeles, la solidificación de la estructura impresa o crosslinking se puede realizar mediante acciones térmicas, físicas, o químicas.

No obstante, la mayor distinción entre materiales se realiza en función de su naturaleza y las propiedades derivadas de esta naturaleza. La primera distinción de los materiales para bioimpresión se resume en materiales naturales y sintéticos [15, 22].

2.2.1 Naturales vs. sintéticos

Esta clasificación se basa en la naturaleza de los componentes que forman parte del material. Los materiales naturales se definen como aquellos derivados de materiales presentes en la naturaleza independientemente de que su extracción se realice por métodos físicos o químicos [23]. Como ejemplos se pueden nombrar el alginato, la gelatina, la celulosa o el colágeno. Por el contrario, los materiales sintéticos son aquellos sintetizados por los humanos [23] como pueden ser el ácido poliláctico (PLA) o la policaprolactona (PCL).

En término general, los materiales naturales se han utilizado más que los sintéticos debido su mejor comportamiento biológico [23]. No obstante, actualmente se observa una tendencia ascendente en la utilización de los materiales sintéticos, ya que aunque tienen peor biocompatibilidad, mejoran las propiedades mecánicas y reológicas de los materiales naturales [22, 24]. Buscar un equilibrio entre ambas propiedades es el principal reto de los materiales para bioimpresión.

2.2.2 Propiedades del hidrogel

El estudio del comportamiento de un hidrogel cuando se imprime es un proceso complejo debido a su naturaleza no newtoniana. En este tipo de materiales, la viscosidad varía en función de los esfuerzos a los que esté sometido el hidrogel [25]. Por lo que es necesario considerar una gran cantidad de variables al realizar estudios con hidrogeles. El estudio de los materiales en bioimpresión se puede realizar mediante pruebas experimentales, pero también con simulaciones computacionales. En cualquier caso, los parámetros mínimos necesarios para el estudio de los materiales se pueden resumir en la concentración de los componentes que forman parte del hidrogel y en la densidad, viscosidad y tensión superficial de la mezcla resultante.

La caracterización de estos parámetros es de suma importancia, ya que controlan determinados factores del proceso de bioimpresión. En concreto, tener los datos de concentración de los componentes del hidrogel es necesario para poder asegurar la reproducibilidad del proceso y poder sintetizar un hidrogel con las mismas propiedades reológicas ya estudiadas. De la misma forma, la facilidad con la que un material se puede imprimir (printability) viene dada por su densidad y viscosidad. Además, conseguir que el material depositado tenga una determinada forma (shape fidelity) está íntimamente relacionado tanto con la viscosidad como con la tensión superficial, junto con el proceso posterior de curado (crosslinking). Todos estos factores tienen que integrarse consiguiendo un equilibrio, junto con los parámetros internos del proceso que controlan la viabilidad celular, ya que mejorar una propiedad de la bioimpresión puede afectar negativamente a otra (p. ej. printability vs. shape fidelity). Parámetros como la presión interna o el esfuerzo cortante, producidas dentro del cabezal extrusor, dependen en gran medida de la geometría interna del cabezal y de la viscosidad del hidrogel. Por lo tanto, la viscosidad del hidrogel además de controlar la printabilidad o la fidelidad de forma, también puede influir de forma indirecta en la viabilidad celular del proceso de bioimpresión.

2.3 Dinámica de fluidos computacional

La simulación computacional es una herramienta muy utilizada en ingeniería para predecir el comportamiento de cuerpos, estructuras o fluidos. Estas simulaciones se basan en el concepto de elementos finitos que consiste en dividir el sistema a estudiar en porciones muy pequeñas y analizar cada una de ellas de manera secuencial. La dinámica de fluidos computacional (CFD de sus siglas en inglés) es la aplicación de esta metodología de cálculo a los fluidos con el fin de predecir su comportamiento. Con el avance de la tecnología y los métodos matemáticos, cada vez se pueden estudiar fluidos más complejos. La simulación CFD se utiliza en muchos aspectos de la ingeniería, pero en los últimos años se está utilizando cada vez más en el ámbito biomédico. La simulación del flujo de sangre [26] o del aire de los pulmones [27] son las aplicaciones más comunes del CFD en la medicina. En bioimpresión, esta herramienta puede ser de gran ayuda para entender cómo funcionan ciertos aspectos, a veces difíciles de medir de forma empírica. Existen trabajos que estudian cómo evolucionan los esfuerzos internos de diferentes biotintas, además de la relevancia de la geometría de la boquilla o nozzle [28–31].

Dependiendo del estudio a realizar se utilizan unos modelos matemáticos u otros. Por ejemplo, para estudiar el comportamiento de un solo fluido dentro de una tubería se suelen utilizar las ecuaciones matemáticas correspondientes al CFD estándar. No obstante, para estudiar cómo se extruye o se deposita una biotinta es necesario utilizar otros modelos más complejos como el Level Set o el Phase Field.

2.3.1 Level Set

Tanto el Level Set como el Phase Field son métodos numéricos para simular cómo evoluciona la interfaz entre dos fluidos. Existen ciertas diferencias que hacen que uno sea más adecuado que el otro para ciertas aplicaciones. Algunas de estas diferencias son el número de fluidos presentes o la escala de la geometría. En general, el Level Set tiene las limitaciones de poder estudiar dos fluidos como máximo y necesita que las geometrías sean lo suficientemente grandes para que el resultado tenga errores aceptables. El Phase Field, por otra parte, es más complejo que el Level Set permitiendo hasta tres fluidos con interacción fluido estructura y en geometrías de microfluídica [32]. En termino general, cuanto más compleja es la simulación mayor coste computacional es necesario y las simulaciones tienen más posibilidades de no converger, y por lo tanto, de no generar un resultado. Esto hace que muchos autores hagan simulaciones utilizando CDF, aunque cada vez hay más estudios que utilizan Level Set para analizar biotintas [33, 34].

2.3.2 Parámetros de salida

La cantidad de datos que se pueden extraer de los resultados de las simulaciones permiten conocer el proceso de bioimpresión en mayor profundidad. De entre todos ellos, para bioimpresión los más relevantes son las presiones, tanto internas como de impresión o entrada y salida, las velocidades de salida y sobre todo los esfuerzos cortantes. Valores elevados de estos parámetros pueden provocar una disminución en la supervivencia celular. En concreto, según Blaeser et al. tener esfuerzos cortantes mayores de 10 kPa puede provocar que la viabilidad celular sea menor al 75 % [35].

2.4 Viabilidad celular

La viabilidad celular es el método más utilizado para estudiar el resultado biológico de un proceso de bioimpresión. Se puede entender viabilidad celular como la cuantificación del número de células vivas una vez terminado el proceso de bioimpresión, expresado como un porcentaje de un control. Hay dos tipos diferentes de procedimientos utilizados para medir la viabilidad. El más común es un conteo directo de células vivas y muertas en función de algún compuesto químico utilizado para teñir y resaltar dichas células. Entre los diferentes compuestos para contabilizar células, la Calceina AM Green que mide células vivas, y el kit Live/Dead que tiñe de verde y rojo las células vivas y muertas son los más utilizados [21]. Sin embargo, existen otros compuestos como el Yoduro de Propidio, el Azul Alamar, el Azul Trypan o el Azul Hechst 33342 que también cumplen la misma finalidad. El otro método consiste en medir la actividad metabólica de las células. Para ello, se utilizan químicos como el CCK8, el MTT o el PET. Sin embargo, esta segunda manera de medir la viabilidad es mucho menos utilizada, ya que el resultado es una medida indirecta de la viabilidad basada en su respiración celular.

Los resultados de viabilidad celular pueden variar mucho en función del momento de la medición, el tipo de biotinta utilizado y la línea celular. Respecto al momento de realizar las mediciones, no existe un consenso que estandarice los tiempos en los que se debe controlar la viabilidad celular. No obstante, existe alguna recomendación de realizar la medición de la viabilidad justo después de la bioimpresión y pasados 1, 3, 7 y 21 días de incubación [21]. Esta heterogeneidad dificulta la comparación de resultados entre diferentes estudios y, por tanto, comprobar las mejoras propuestas en los protocolos existentes.

3. Objetivos

El objetivo principal del presente trabajo de tesis es diseñar, desarrollar y validar una bioimpresora funcional que permita posicionar con precisión líneas celulares utilizando técnicas de μ-extrusión, mejorando las tasas de viabilidad celular. Este objetivo general está divido en los siguientes objetivos específicos:

1. Análisis detallado y profundo de los diferentes retos de la bioimpresión, centrándonos en las características de los hidrogeles y los cabezales de μ-extrusión.
2. Obtención de un sistema de μ-extrusión para bioimpresoras que reduzca la presión interna en el depósito de material, mejorando la viabilidad celular del sistema final.
3. Desarrollo de un sistema de esterilidad y pre-incubación para la bioimpresora que permita su utilización fuera de la cabina de flujo laminar.
4. Obtención de un grado de supervivencia de las líneas celulares bioimpresas superior al 80 %.

4. Resumen de resultados y discusión

Esta tesis es un compendio de las siguientes publicaciones aceptadas:

[1] Mancha-Sánchez, E.; **Gómez-Blanco, J.C**; López Nieto, E.; Casado, J.G., Macías-García, A.; Díaz Díez, M.A.; Carrasco-Amador, J.P.; Torrejón Martín, D.; Sánchez-Margallo, F.M.; Pagador, J.B. Hydrogels for Bioprinting: A Systematic Review of Hydrogels Synthesis, Bioprinting Parameters, and Bioprinted Structures Behavior. Frontiers in Bioengineering and Biotechnology 2020, 8, 776.
DOI: https://doi.org/10.3389/fbioe.2020.00776

[2] **Gómez-Blanco, J.C.**; Mancha-Sánchez, E.; Marcos, A.C.; Matamoros, M.; Díaz-Parralejo, A.; Pagador, J.B. Bioink Temperature Influence on Shear Stress, Pressure and Velocity Using Computational Simulation. Processes 2020, 8, 865.
DOI: https://doi.org/10.3390/pr8070865

[3] Matamoros, M.; **Gómez-Blanco, J.C.**; Sánchez, Á.J.; Mancha, E.; Marcos, A.C.; Carrasco-Amador, J.P.; Pagador, J.B. Temperature and Humidity PID Controller for a Bioprinter Atmospheric Enclosure System. Micromachines 2020, 11, 999.
DOI: https://doi.org/10.3390/mi11110999

Además, se incluyen los siguientes artículos que a fecha de cierre del presente documento se encuentran en proceso de revisión por pares:

[1] **Gómez-Blanco, J.C.**; López-Espino, M.; Macías-García, A.; Díaz-Parralejo, A.; Macías-Blanco, P.; Pagador, J.B.; Sánchez-Margallo, F.M. Optimization of Computational Simulations on Bioprinting Nozzles: A Combination of Systematic Review and Design of Experiments. Applied Sciences *(En Revisión)*

[2] **Gómez-Blanco, J.C.**; Pagador, J.B.; Galván-Chacón, V.; Sánchez-Peralta, L.F.; Matamoros, M.; Marcos, A.C.; Sánchez-Margallo, F.M. Computational simulation-based comparative analysis of standard FDM 3D printing and conical nozzles for pneumatic and piston-driven bioprinting. Additive Manufacturing *(En Revisión)*

[3] **Gómez-Blanco, J.C.**; Galván-Chacón, V.; Patrocinio, D.; Matamoros, M.; Ojeda, A.; Marcos, A.C.; Duarte, M.; Marinaro, F.; Pagador, J.B.; Sánchez-Margallo, F.M. Improving cell viability and velocity in μ-extrusion bioprinting with a novel pre-incubator bioprinter and a standard FDM 3D printing nozzle. Materials *(En Revisión)*

4.1 Revisión sistemática de hidrogeles para bioimpresión

En este trabajo se realiza una revisión sistemática sobre los materiales biocompatibles más utilizados en bioimpresión, los hidrogeles. Se utiliza la metodología PRISMA y la cadena de búsqueda "Bioprinting AND Hydrogel" en PUBMED, WOS y SCOPUS, obteniendo un total de 1774 trabajos a analizar. Una vez analizados los abstracts y eliminados las duplicidades y los trabajos que no estaban dentro del rango de criterios, se analizan en detalle 118 artículos.

Los resultados se encuadran en tres secciones correspondientes al proceso de bioimpresión:

1. Generación del hidrogel (pre-printing)
2. Parámetros de la bioimpresión por μ-extrusión (printing)
3. Pruebas biológicas y mecánicas (post-printing)

4.1.1 Generación del hidrogel

En esta subsección se analizan los compuestos más habituales para crear hidrogeles. En este sentido, se comprueba una evolución de los materiales utilizados desde los naturales hacia los sintéticos desde 2009 hasta la actualidad. En este cambio de tendencia se observa que los investigadores están poniendo más énfasis en la posibilidad de ajustar las propiedades reológicas del hidrogel. Esto implica que actualmente los estudios de biomateriales se centran en sintetizar materiales con buenas propiedades biológicas pero que permitan ajustar sus propiedades estructurales antes y después de la impresión. Los materiales más utilizados se recogen en la Figura 4.1.

Junto con los materiales más utilizados y sus combinaciones, los estudios informan sobre las concentraciones usadas en el 81 % de los casos y sólo el 12 % de ellos muestra datos de la viscosidad del hidrogel. La falta de información sobre la síntesis de los hidrogeles, sobre todo relacionada con la viscosidad, hace muy difícil poder replicar los resultados obtenidos por los autores en la mayoría de los casos. Centrándonos en los tres materiales más usados, la mayoría de los estudios obtienen buenos resultados con concentraciones entre el 1 y el 20 % para el alginato, la gelatina y el GelMA. Con esas concentraciones, los hidrogeles tienen una buena printabilidad junto con una buena biocompatibilidad del material independientemente de si se trata de un compuesto natural o sintético.

4.1.2 Parámetros de bioimpresión por μ-extrusión

Un buen resultado en bioimpresión es muy dependiente de la configuración de los parámetros del proceso. En esta sección se estudian los parámetros más influyentes en el proceso, divididos en dos apartados. En el primero se estudian los parámetros que se pueden configurar en la bioimpresora como la temperatura de impresión del extrusor y de la cama o la presión y la velocidad de impresión. En el segundo se estudian los diferentes métodos de crosslinking para endurecer el hidrogel extruido y conseguir la estructura final bioimpresa.

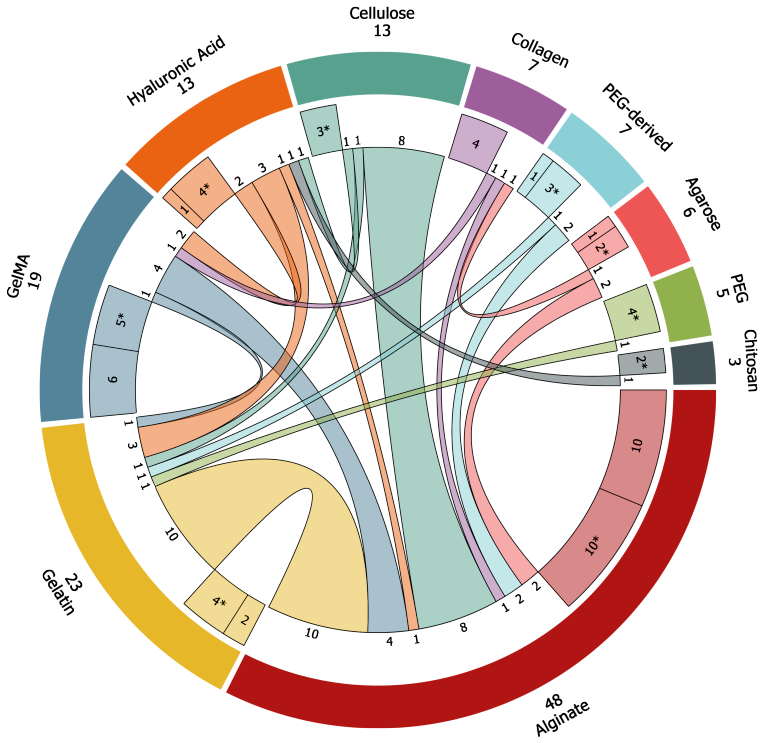

Figura 4.1: Combinación de los diez materiales más utilizados en hidrogeles. Los materiales se muestran en el anillo exterior (total de artículos y nombre). Los segmentos del anillo central representan hidrogeles compuestos por un solo material e hidrogeles, marcados con (*), que son una combinación de este material con materiales no seleccionados (artículos que utilizan ese material mezclado con otros materiales no seleccionados). Las líneas interiores representan hidrogeles con dos de los materiales seleccionados, pero en algún caso se pueden incluir otros materiales no seleccionados (número de artículos junto a cada línea interior).

Respecto al primer apartado, existe una gran disparidad de datos en función de si los hidrogeles llevan o no células en su interior (cell-laden vs. seeding) y del tipo de material del que está compuesto el hidrogel. En primer lugar, la temperatura de impresión suele estar cercana a la temperatura fisiológica (37 °C) y todos los hidrogeles cell-laden imprimen a 37 °C independientemente de los componentes del hidrogel. En segundo lugar, la temperatura de la cama de impresión es un dato que la mayoría de los trabajos no facilita, pero aquellos que lo indican suelen trabajar a 37 °C. En tercer lugar, la presión de impresión debe adaptarse a las propiedades reológicas del hidrogel. El rango de presiones es muy amplio, aunque la mayoría de ellas están entre 400 y 1000 kPa. Es importante señalar que este parámetro es crítico, ya que la viabilidad celular tiene un comportamiento inversamente proporcional a la presión. Por último, la velocidad de impresión varía en un rango de 1-30 mm/s y es uno de los parámetros a controlar para ajustar la precisión del resultado final y el tiempo total del proceso.

El segundo apartado de esta sección estudia el crosslinking. Existen tres tipos de crosslinking: químico, físico y térmico, que se utilizan dependiendo del material extruido y cuyos valores más relevantes se exponen en la Figura 4.2.

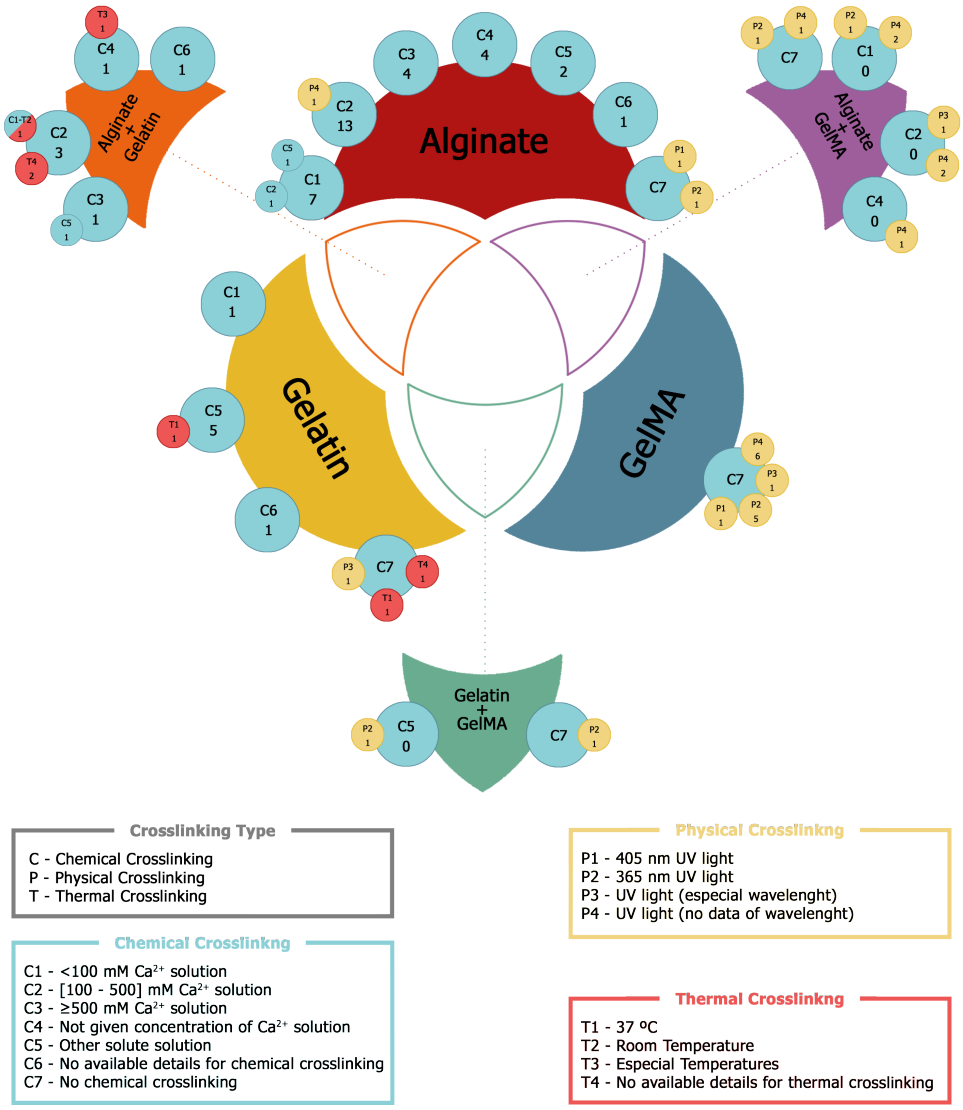

Figura 4.2: Crosslinking utilizado en los tres materiales más comunes. Los círculos azules, amarillos y rojos representan el crosslinking químico, físico y térmico, respectivamente. Los círculos superpuestos indican que se han combinado dos clasificaciones de crosslinking. Cada círculo contiene una codificación de la clasificación (código superior) y el número de artículos para la combinación de códigos correspondiente (número inferior). Se ha elegido el crosslinking químico como clasificación principal, por lo que los trabajos que no la utilizan se han codificado en C7 a efectos de representación gráfica y no se han asignado trabajos a este código solo. Por ejemplo, alginato C2/13 - P4/1 (círculos superpuestos azul y amarillo) indica que 13 trabajos utilizaron C2 (solución de Ca^{2+} [100-500] mM) para hacer el crosslinking del alginato y otro trabajo utilizó C2 y P4 (luz UV-sin datos de longitud de onda) para realizar el crosslinking.

En general, existe más información acerca del crosslinking químico, como la concentración de la disolución utilizada o el tiempo de curado. En este tipo, los cationes Ca^{2+} con concentraciones entre 100 y 500 mM son los más utilizados. Sin embargo, sobre el crosslinking físico sólo se suele indicar la longitud de onda (365 y 405 nm), pero no la potencia o el tiempo de exposición. En cuanto al crosslinking térmico hay todavía menos información, y sólo unos pocos autores especifican la temperatura mientras el resto indican que el proceso se realiza a temperatura ambiente.

4.1.3 Pruebas biológicas y mecánicas

En este apartado se analiza el comportamiento biológico y mecánico de las estructuras bioimpresas. Por una parte, se estudian las líneas celulares más utilizadas además de los test celulares, generalmente de viabilidad, y por otra parte test mecánicos, la mayoría de ellos de resistencia y elasticidad.

Existe una amplia variabilidad en el uso de líneas celulares (Figura 4.3), aunque las más utilizadas son las células mesenquimales. Estas células pueden diferenciarse a otros tipos de células en función de ciertas condiciones ambientales o compuestos químicos. Respecto a los test celulares, se suelen realizar test para medir los valores de viabilidad celular como resultado de la bioimpresión. De entre todos, destacan los de Calceina AM Verde y los kits Live/Dead, pero no existe aún un consenso sobre el momento de la medición. Por este motivo, las mediciones varían entre el día 0 (justo tras la impresión) y el día 21 (tras varios días de cultivo), haciendo muy difícil la comparación de resultados con esta heterogeneidad. Con esta limitación en cuenta a la hora de interpretar los análisis, la viabilidad celular varía en los estudios entre el 80 y el 95 %. El GelMA destaca como material más viable seguido de una mezcla de alginato y gelatina.

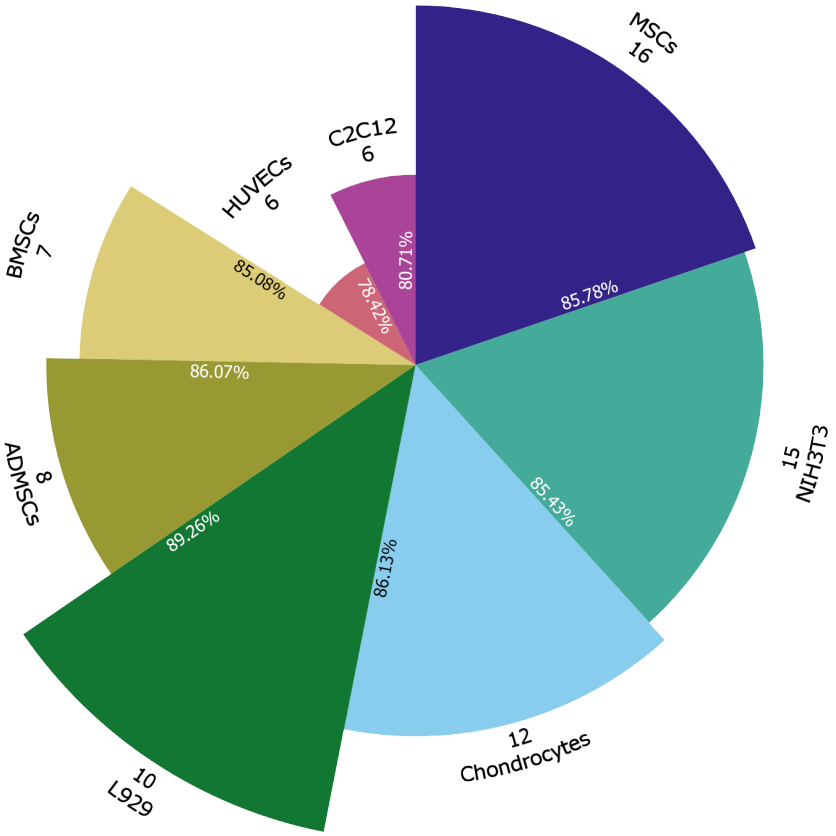

Figura 4.3: Líneas celulares más representativas en bioimpresión. El ángulo representa el número de artículos que utilizan cada línea celular (#) y el radio indica la viabilidad celular media de todos los artículos relacionados (%). Todas las secciones del círculo están escaladas proporcionalmente con la viabilidad para facilitar la comparación.

En referencia a los ensayos mecánicos también existe una gran variedad de pruebas: tensión de compresión, módulo elástico o de Young, módulo de compresión, límite

elástico y resistencia última a tracción (UTS). Pero en general, los ensayos mecánicos se centran en obtener los límites de rotura por compresión (resistencia) y el módulo de Young (elasticidad). Los valores obtenidos tienen una gran variabilidad y se pone de manifiesto que dependen tanto de la composición del hidrogel como del proceso de crosslinking.

4.2 Revisión sistemática de simulaciones de cabezales

En este trabajo se ha realizado una revisión sistemática acerca de los estudios sobre los cabezales de bioimpresión por μ-extrusión. Se utiliza la metodología PRISMA y las cadenas de búsqueda "bioprinting AND extrusion AND nozzle", "bioprinting AND nozzle AND computational", "bioprinting AND nozzle AND fluid", "bioprinting AND nozzle AND printhead" en PUBMED, WOS y SCOPUS, obteniendo un total de 74 trabajos a analizar. Una vez analizados los abstracts y eliminados las duplicidades y los trabajos que no estaban dentro del rango de criterios, se analizan en detalle 18 artículos.

En los resultados analizados hay una gran discrepancia entre las diferentes simulaciones de procesos de bioimpresión. Las geometrías más utilizadas son agujas concéntricas, jeringas con puntas cónicas y nozzles de microfluídica. Este conjunto de geometrías lleva además asociado una variedad de dimensiones de la punta del cabezal extrusor, variando su diámetro de salida entre 0,2 y 1,2 mm o la altura de la punta entre 8,9 y 10 mm. Así mismo, en los trabajos se recomienda que el cabezal tenga ángulos internos entre 20 y 30°para minimizar el esfuerzo cortante.

Otros parámetros importantes a estudiar son los referentes a los parámetros que controlan el proceso de bioimpresión. En la tabla 4.1 se muestra un resumen de los valores más utilizados para establecer las condiciones de contorno de las simulaciones.

Parámetro	Valores
Temperatura	20 - 37 °C
Flujos volumétricos	0,1 - 266 μL/s
Flujo másico	90 - 100 mg/min
Presión	14 - 40 kPa
Viscosidad (hidrogeles)	1 - 9,8 mPa·s
Viscosidad	30×10^5 - 30×10^8 mPa·s

Tabla 4.1: Parámetros físicos más utilizados en las simulaciones de bioimpresión.

Respecto a los resultados de la simulación, los diferentes autores suelen estudiar las presiones, velocidades o el esfuerzo cortante que se produce en el interior del cabezal extrusor. Los valores obtenidos varían las presiones entre 1 y 300 kPa y 1,6 y 266 mm/s para presiones y velocidades de salida. En cuanto al esfuerzo cortante, existen indicios acerca del valor límite de 5 kPa a partir del cual la viabilidad celular empieza a verse comprometida.

Como se ha visto, las diferencias entre los modelos a simular provocan una gran variabilidad en sus parámetros de entrada y también en los resultados de sus simulaciones. Esta variabilidad dificulta la posible comparación de los datos para

comprobar si un tipo de simulación tiene o no mejoras sobre otro. No obstante, se han obtenido unos rangos de valores sobre los que trabajar para poder realizar simulaciones posteriores.

4.3 Influencia de la temperatura del hidrogel en la presión, en la velocidad y en el esfuerzo cortante mediante simulación computacional

En este trabajo se estudia la influencia del cambio de viscosidad del material cuando varía la temperatura del extrusor en la presión, la velocidad y el esfuerzo cortante durante el proceso de bioimpresión. Para ello, se utilizan tres puntas cónicas comerciales de 20, 22 y 25G cuyas medidas se tomaron experimentalmente, junto con un hidrogel comercial. Las simulaciones se realizaron en COMSOL Multiphysics 5.4 utilizando una aproximación eje-simétrica, con una presión de entrada de 15 kPa y un modelo matemático de seguimiento de interfaz *Two-Phase Flow Level-set*.

El material simulado es un hidrogel comercial muy utilizado que está compuesto por una mezcla de alginato con fibras de nanocelulosa. Los datos reológicos del comportamiento del material fueron cedidos por la propia empresa y se ajustaron a una Ley Potencial de viscosidad para 15, 25 y 37 °C (Figura 4.4).

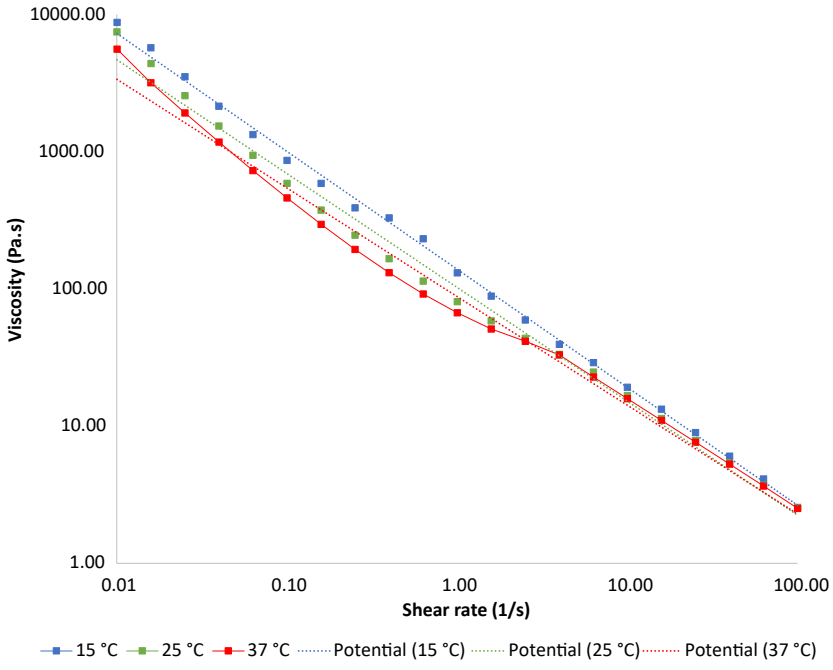

Figura 4.4: Datos reológicos de Cellink Bioink. Reproducido con permiso de Cellink®.

Se realizaron un total de nueve simulaciones, una por cada geometría y temperatura. Para comprobar que las simplificaciones y consideraciones realizadas eran correctas se calculó el número de Reynolds y el rango de valores de la tasa de cizallamiento. Ambos valores estaban en rangos aceptables para asegurar que la consideración de flujo laminar es correcta y que el ajuste de la Ley potencial de viscosidad es adecuado.

Como resultado de las simulaciones se comprobó que las diferentes geometrías y temperaturas provocan flujos volumétricos mayores cuando aumentan el diámetro del nozzle y la temperatura del extrusor. En algunas simulaciones se forman gotas que terminan desprendiéndose y cayendo (Figura 4.5), provocando picos en las gráficas de presiones, velocidades y esfuerzo cortante.

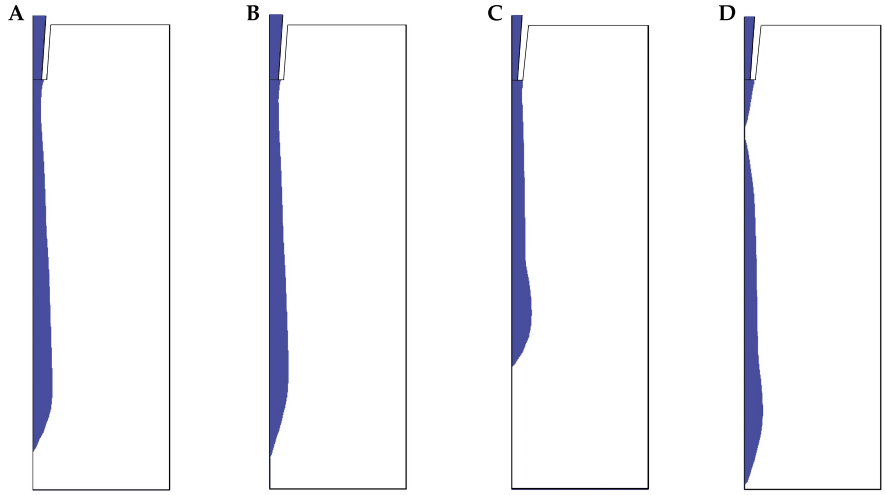

Figura 4.5: Fracción de volumen de Cellink Bioink. (A) 20G a 25 °C en t = 3,14 s; (B) 20G a 37 °C en t = 2,31 s; (C) 22G a 25 °C en t = 10,00 s y (D) 22G a 37 °C en t = 6,86 s. El color azul representa la biotinta Cellink y el blanco el aire.

La presión de entrada se fija en las simulaciones para estudiar la presión de salida que, según la bibliografía, tiene una gran influencia en la supervivencia celular. Los resultados de presión muestran que cuanto mayor es el diámetro del nozzle menor es la presión de salida. Además, también se comprueba que la temperatura no tiene un efecto muy marcado en dicha presión. Por otro lado, se observa que se provoca una abrupta disminución de presión cuando se forma una gota y esta cae.

Las velocidades muestran un comportamiento parecido, cuanto mayor es el flujo volumétrico mayor es la velocidad de salida. Al igual que con las presiones, existen picos en los momentos donde empieza a caer una gota.

El estudio del esfuerzo cortante es quizá el más relevante, ya que según la bibliografía su aumento tiene un efecto predominante en la disminución de la viabilidad celular. En el caso de las simulaciones realizadas, los valores de esfuerzo cortante máximo obtenidos varían entre 202 y 264 Pa, por lo que las diferencias entre ellos se pueden considerar despreciables. Estudios previos demuestran que valores menores de 5 kPa en el esfuerzo cortante, no tienen una influencia significativa en la viabilidad celular. Por lo tanto, nuestros resultados con los nozzles estudiados no deberían causar daños en las células durante el proceso de bioimpresión.

Con las simulaciones realizadas se ha podido comprobar que los valores de presión, velocidad y esfuerzo cortante son prácticamente despreciables al variar el diámetro de las puntas cónicas entre 22 y 25G. Además, la temperatura tampoco tiene un efecto muy marcado en los valores obtenidos. La conclusión principal es que, con este hidrogel, el flujo volumétrico se puede variar en función de su temperatura

y del diámetro de la punta cónica sin generar valores extremos de los parámetros estudiados. Los procesos de bioimpresión se caracterizan por ser lentos y se ha comprobado que cuanto mayor es el tiempo que las células pasan en el proceso, menor es la viabilidad. Por lo tanto, con el fin de maximizar la viabilidad se recomienda imprimir Cellink bioink a 37 °C (temperatura fisiológica) y con una punta cónica 22G para aumentar el flujo volumétrico y disminuir así el tiempo de bioimpresión.

4.4 Simulación computacional de nozzle FDM estándar vs. punta cónica

En este trabajo se estudia la viabilidad de un nozzle estándar de impresión 3D, en concreto un E3D V6, comparándolo con una punta cónica estándar para un proceso de bioimpresión por μ-extrusión. La hipótesis de partida es que estos nozzles, al estar diseñados para mover materiales muy viscosos con la menor fuerza posible, serían capaces de disminuir la presión de entrada necesaria para el proceso de bioimpresión. Para ello, se realizaron una serie de simulaciones utilizando COMSOL Multiphysics 5.4 junto con una aproximación eje-simétrica y un modelo matemático de seguimiento de interfaz *Two-Phase Flow Level-set*. Además, se simularon los dos tipos de bioimpresión por μ-extrusión más utilizados estableciendo una presión de entrada de 15 kPa y un flujo volumétrico de 10 mm^3/s para μ-extrusión neumática y mecánica respectivamente. En total se realizaron cuatro simulaciones, una por cada tipo de bioimpresión y cabezal, extruyendo el hidrogel comercial Cellink Bioink a 37 °C. Los datos reológicos de este material se han obtenido de la propia empresa y se han ajustado en trabajos previos.

Los resultados muestran dos comportamientos diferenciados según se analicen las simulaciones de μ-extrusión neumática o mecánica:

1. El nozzle propuesto genera un flujo volumétrico aproximadamente 15 veces superior que la punta cónica utilizando la misma presión de impresión (Figura 4.6).
2. El nozzle propuesto necesita una presión de impresión casi 2 veces menor que la punta cónica utilizando el mismo flujo volumétrico de entrada (Figura 4.7)

A estos resultados hay que añadir que el esfuerzo cortante que se genera en todas las simulaciones varía entre 242,16 y 455,43 Pa. En la bibliografía, se establece un valor de 5 kPa como límite de esfuerzo cortante a partir del cual la viabilidad celular empieza a verse comprometida. Los resultados obtenidos muestran valores aceptables y lejanos al límite establecido para el esfuerzo cortante en todas las configuraciones simuladas.

Además, las simulaciones se han validado mediante una serie de pruebas experimentales. En estas pruebas se ha comparado la forma geométrica de las gotas generadas, obteniendo un error que oscila entre un 4,70 y un 15,52 %. Estos errores son similares a los obtenidos por otros autores en la bibliografía.

Por lo tanto, este estudio nos permite hacer dos lecturas interesantes. La primera es que el nozzle propuesto es capaz de generar impresiones más rápidas con una misma presión de entrada. Y la segunda, que este nozzle es capaz de reducir las presiones

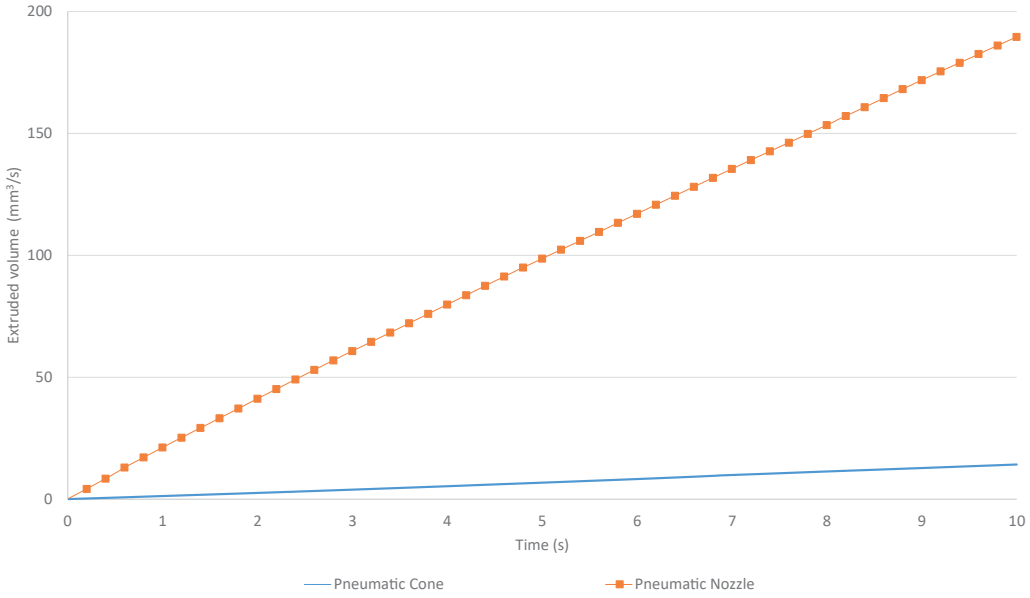

Figura 4.6: Volumen extruido (mm^3/s) de las simulaciones neumáticas. El volumen extruido de las simulaciones mecánicas no se muestra en la figura porque el flujo volumétrico se establece como entrada de la simulación ($10mm^3/s$, por lo que el volumen extruido en 10 s es de 100 mm^3.)

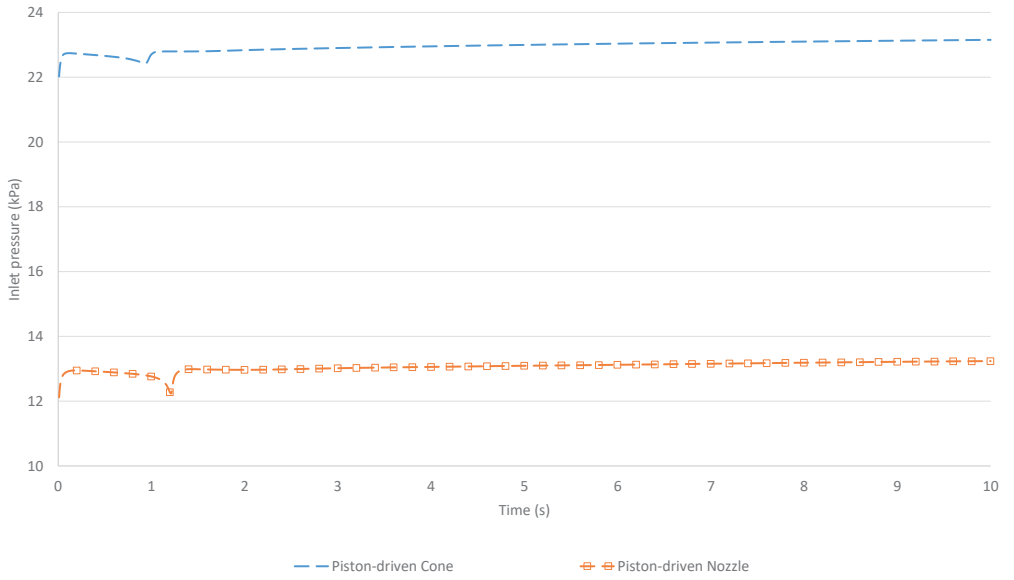

Figura 4.7: Presión de impresión (kPa) de las simulaciones mecánicas. Las presiones de impresión de las simulaciones neumáticas no se muestran en la figura porque se fijan en 15 kPa para las simulaciones.

de entrada hasta la mitad cuando se extruye una cantidad fija de material. Estos resultados indican que la utilización de nozzles estándares de impresión 3D pueden solucionar parcialmente uno de los mayores inconvenientes de la bioimpresión por μ-extrusión, la baja velocidad de impresión. Además, de acuerdo a los resultados, es posible acelerar impresiones utilizando menores presiones de entrada.

4.5 Sistema de pre-incubación con control de temperatura y humedad

Una parte del desarrollo de este trabajo de tesis es crear una bioimpresora que cuente con mejoras respecto a las que se encuentran en el mercado. En este sentido, la bioimpresora creada cuenta con un sistema de pre-incubación. Este sistema mejora las cabinas estancas que tienen las impresoras comerciales dotándolas de un sistema capaz de controlar la temperatura y humedad. Por lo tanto, en este trabajo se presenta una bioimpresora capaz de controlar la atmósfera durante el proceso de bioimpresión y de incubar durante un determinado tiempo las muestras biológicas resultado del proceso de bioimpresión.

En este capítulo se ha desarrollado, construido y probado el controlador de la cabina atmosférica. En el diseño de la cabina se han creado tres espacios concretos que se complementan entre sí asegurando el correcto funcionamiento de la cabina mientras que se mantiene la esterilización (Figura 4.8).

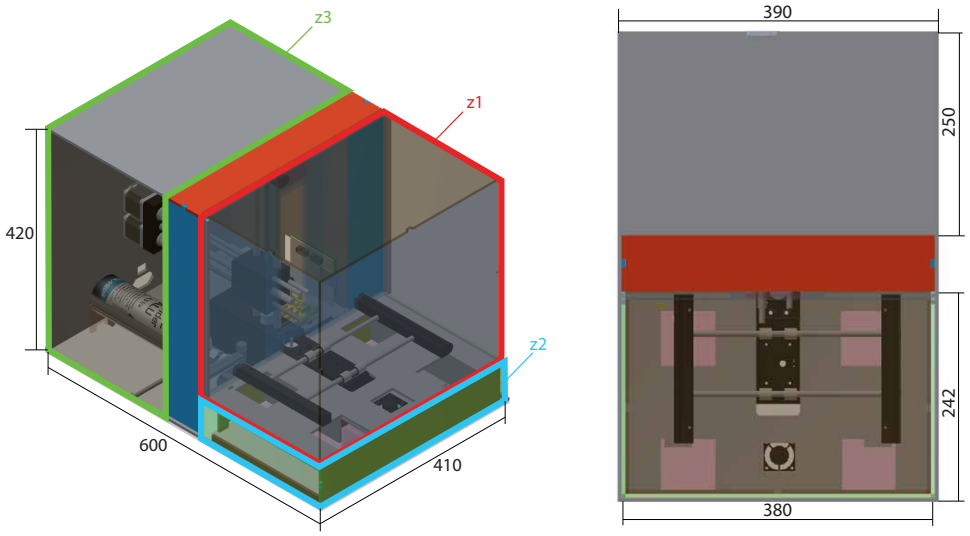

(a) Perspectiva. **(b)** Vista superior.

Figura 4.8: Diseño tridimensional del sistema de pre-incubación, donde se encuentran la subcámara de bioimpresión (z1), la subcámara de generación de condiciones climáticas (z2) y la subcámara de componentes electrónicos y mecánicos (z3).

El sistema está compuesto por dos sensores PT 100 PRO para la temperatura y dos sensores DHT22 para la humedad. El funcionamiento de la cabina se basa en tener una presión positiva dentro de la cabina con entrada de aire exterior que pasa por un filtro HEPA.

El controlador PID ofrece resultados precisos y robustos una vez calibrado correctamente. Para ello, el sistema se ajusta mediante las funciones de transferencia para la temperatura y la humedad de forma independiente, al que después se acopla el controlador PID en un sistema con realimentación negativa. Los controladores PID se ajustaron siguiendo el método de Ziegler-Nicholds mediante una serie de experimentos SISO (Single Input Single Output) y MIMO (Multiple Inputs Multiple Outputs). Dichos experimentos sirven de comprobación de la simplificación realizada al controlar los parámetros de forma independiente.

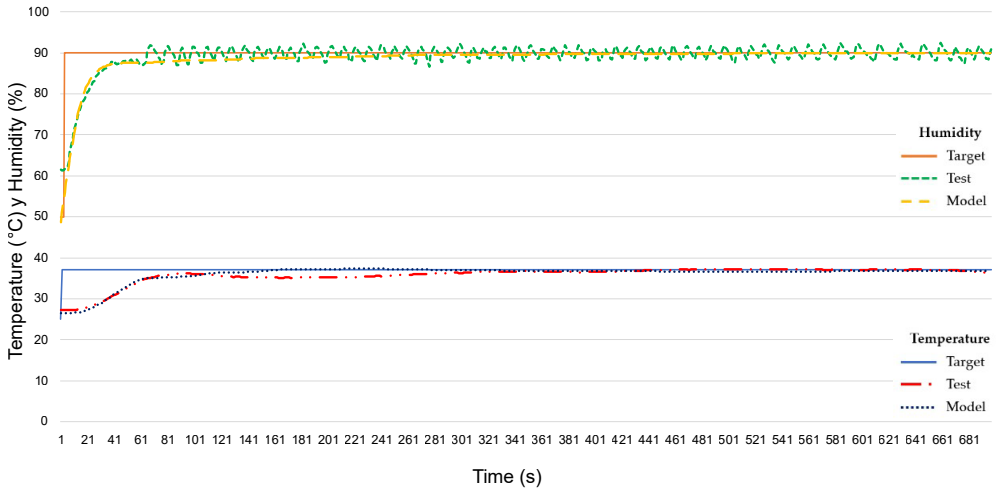

Figura 4.9: Simulación teórica y experimental del sistema PID desacoplado.

Los resultados obtenidos determinan que el controlador propuesto estabiliza tanto la temperatura como la humedad con errores menores al 1,89 % y al 1,30 %, respectivamente (Figura 4.9). A la vista de los resultados, también se puede asegurar que se puede conseguir una estabilización de la temperatura y de la humedad de forma independiente a pesar de tratarse de parámetros correlacionados. Además, el controlador PID es capaz de estabilizar tanto la temperatura como la humedad en el valor consigna en 311 s.

4.6 Mejora de la velocidad de bioimpresión utilizando un nozzle estándar de impresión 3D FDM

En el presente trabajo se describe el diseño y se valida experimentalmente una bioimpresora por μ-extrusión accionada por un sistema mecánico de pistón. Además, se realiza un estudio de viabilidad celular con el objetivo de comprobar la influencia que tiene la utilización de un nozzle estándar de impresión 3D FDM en la viabilidad celular, al aumentar el flujo volumétrico de la impresión. Este aumento de flujo volumétrico supone un incremento en la velocidad de impresión.

La nueva bioimpresora presenta principalmente dos mejoras sobre las que se encuentran en la bibliografía. La primera es una cabina atmosférica para controlar la temperatura y la humedad ambiental durante y después del proceso de bioimpresión. Esta cabina ha sido descrita y probada en el capítulo anterior. La segunda es un nuevo cabezal extrusor diseñado para una impresora 3D Atom Proton por la forma que tiene de transmitir el movimiento del motor de extrusión. Al eliminar el motor del cabezal de extrusión existen menos movimientos por inercia en los ejes y, además, se eliminan posibles focos de contaminación de las muestras. El cabezal está compuesto por dos bloques principales: el bloque de empuje (piezas grises y blancas de la Figura 4.10) y el contenedor del material (piezas negras de la Figura 4.10). El primero de ellos está formado por un sistema de cremallera y pistón que consigue el empuje del

material por el movimiento de la cremallera al mover el motor el piñón. El segundo se basa en un sistema de cambio rápido de herramienta y está formado por un bloque calentador de aluminio junto con dos resistencias calefactoras y un termistor para controlar la temperatura interna.

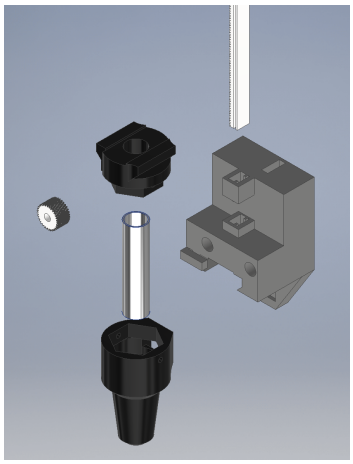

(a) Vista explotada de los componentes del sistema

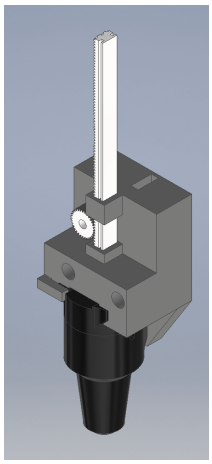

(b) Sistema completamente ensamblado

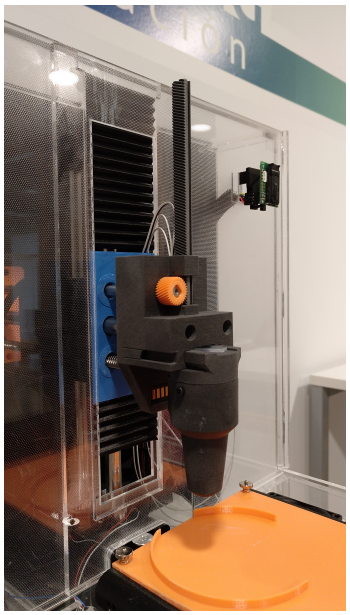

(c) Imagen del prototipo del sistema de cabezal de extrusión

Figura 4.10: Cabezal de extrusión con cambio rápido de jeringas.

Toda la impresora está controlada mediante una Raspberry Pi 3 modelo B con un firmware y software específico.

Los resultados de las pruebas arrojan valores de exactitud menores de 17 μm y valores de precisión menores de 12 μm para el movimiento de los ejes X, Y y Z. Para el movimiento lineal de la cremallera del extrusor los valores de exactitud y precisión son menores de 5 y 7 μm. Estos resultados están en línea con las precisiones obtenidas en otras bioimpresoras de bajo coste, aunque hay margen de mejora para aumentar la exactitud y la precisión en los ejes principales de movimiento.

Para comprobar experimentalmente la viabilidad celular con los dos tipos de nozzle, se bioimprimieron una serie de scaffolds utilizando un hidrogel formado por alginato y nanocelulosa con una concentración de 7,5x10^5 células/mL a través de una punta cónica y de un nozzle estándar de impresión 3D FDM. Los diferentes parámetros de las pruebas se resumen en la Tabla 4.2.

Test	Nozzle	Flujo volumétrico	Velocidad de impresión
T1	22G conical tip	10 mm^3/s	8,55 mm/s
T2	E3D v6 standard nozzle	10 mm^3/s	8,55 mm/s
T3	E3D v6 standard nozzle	15 mm^3/s	12,83 mm/s
T4	E3D v6 standard nozzle	20 mm^3/s	17,11 mm/s

Tabla 4.2: Parámetros de los cuatro grupos para las pruebas de viabilidad celular.

Estos scaffolds se imprimieron variando el flujo volumétrico para comprobar la influencia de diferentes velocidades de impresión en la viabilidad celular. Se realizaron medidas de viabilidad celular justo después de imprimir y pasados 1, 3 y 7 días. Los valores de viabilidad se muestran en la Figura 4.11 y ponen de manifiesto que la utilización de un nozzle estándar de impresión 3D FDM no tiene un efecto marcado en las viabilidades obtenidas al compararlo con una punta cónica. Solamente se encuentran diferencias significativas en los resultados cuando se analizan las viabilidades de cada prueba entre los diferentes días. En el caso de T1 y T4, las diferencias se producen por la regeneración de las células dañadas y la proliferación celular.

Por lo tanto, la nueva bioimpresora presentada con sus componentes mejorados demuestra que el cabezal extrusor propuesto es capaz de aumentar la velocidad de impresión sin afectar negativamente a las células, obteniendo en las mediciones del día 7 una viabilidad celular mayor al 80 %.

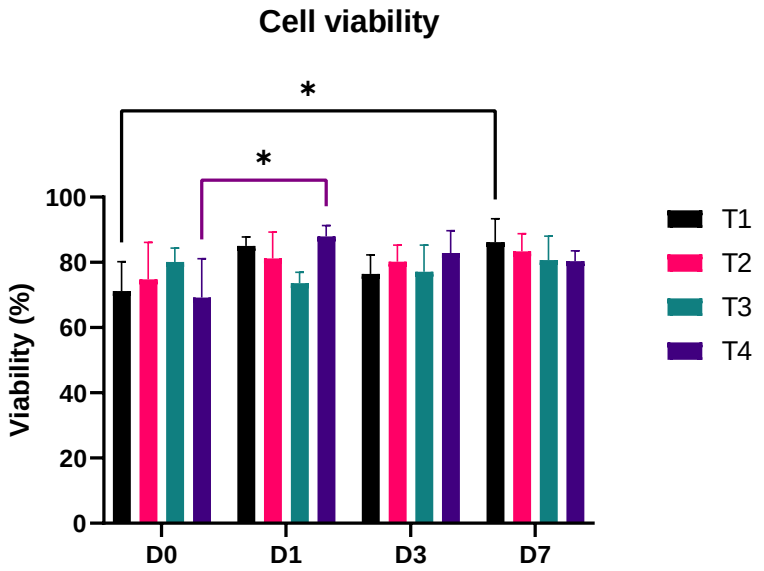

Figura 4.11: Viabilidad celular comparada de los nozzles agrupada por tiempo. El símbolo * representa una diferencia significativa ($p<0.05$).

5. Conclusiones

En el presente trabajo de tesis, se ha estudiado el funcionamiento de la bioimpresión por μ-extrusión para proponer mejoras aplicables a los sistemas actuales mediante el diseño y desarrollo de una bioimpresora con sistema de pre-incubación y un cabezal calefactado con cambio rápido de jeringa.

1. El estado del arte de la bioimpresión por μ-extrusión refleja que:
   - El alginato es el material más utilizado por sus buenas propiedades biológicas, aunque suele mezclarse con otros compuestos para aumentar sus propiedades estructurales.
   - Las células mesenquimales son el material biológico más utilizado en las biotintas.
   - La viabilidad celular de los modelos bioimpresos oscila entre el 80-95 %, con gran heterogeneidad en el tipo celular y en los criterios de medición utilizados.
   - Aunque no existe consenso en la geometría interna de los cabezales, se recomienda utilizar ángulos de pared internos entre 20 y 30°.
   - Valores de estrés cortante por encima de 5 kPa tienden a disminuir la viabilidad celular.
2. En simulaciones con un hidrogel de alginato y nanocelulosa que fluye a través de puntas cónicas estándar en bioimpresión por μ-extrusión se concluye que:
   - El aumento de temperatura del material acelera el proceso de bioimpresión al aumentar el flujo volumétrico modificando levemente la presión y el estrés cortante.
   - La sustitución de las puntas cónicas por un nozzle estándar de impresión 3D FDM del mismo diámetro reduce la presión de impresión a la vez que aumenta el flujo volumétrico.
3. El sistema de pre-incubación desarrollado controla la temperatura y la humedad definidas en menos de 300 s con un error menor al 1,89 %. Al mismo tiempo, esta pre-incubadora asegura la esterilidad utilizando un sistema de radiación UV y filtros HEPA.
4. Mediante el uso experimental del cabezal con cambio rápido de jeringa desarrollado y un nozzle de impresión 3D FDM se demuestra que se puede duplicar la velocidad de bioimpresión con respecto al uso de puntas cónicas, obteniendo valores de viabilidad celular mayores al 80 %.

6. Bibliografía

[1] H. Kodama, "Automatic method for fabricating a three-dimensional plastic model with photo-hardening polymer," *Review of Scientific Instruments*, vol. 52, no. 11, pp. 1770–1773, 1981. doi:10.1063/1.1136492

[2] J.-C. Andre, A. Le Mehaute, y O. De Witte, "Dispositif pour réaliser un modèle de pièce industrielle," Patente FR 2 567 668 A1, 1984.

[3] S. K. Parupelli y S. Desai, "A Comprehensive review of additive manufacturing (3D printing): processes, applications and future potential," *American Journal of Applied Sciences*, vol. 16, no. 8, pp. 244–272, 2019. doi:10.3844/ajassp.2019.244.272

[4] N. Shahrubudin, T. C. Lee, y R. Ramlan, "An overview on 3D printing technology: technological, materials, and applications," in *Procedia Manufacturing*, vol. 35. Elsevier B.V., 2019. doi:10.1016/j.promfg.2019.06.089. ISSN 23519789 pp. 1286–1296.

[5] H. D. Vora y S. Sanyal, *A comprehensive review: metrology in additive manufacturing and 3D printing technology.* Springer International Publishing, 2020, vol. 5, no. 4. ISBN 0123456789

[6] Q. Yan, H. Dong, J. Su, J. Han, B. Song, Q. Wei, y Y. Shi, "A review of 3D printing technology for medical applications," *Engineering*, vol. 4, no. 5, pp. 729–742, 2018. doi:10.1016/j.eng.2018.07.021

[7] J. Li, C. Wu, P. K. Chu, y M. Gelinsky, "3D printing of hydrogels: rational design strategies and emerging biomedical applications," *Materials Science and Engineering: R: Reports*, vol. 140, no. November 2019, p. 100543, 2020. doi:10.1016/j.mser.2020.100543

[8] S. V. Murphy, P. De Coppi, y A. Atala, "Opportunities and challenges of translational 3D bioprinting," *Nature Biomedical Engineering*, vol. 4, no. 4, pp. 370–380, 2020. doi:10.1038/s41551-019-0471-7

[9] A. Tejo-Otero, I. Buj-Corral, y F. Fenollosa-Artés, "3D Printing in medicine for preoperative surgical planning: a review," *Annals of Biomedical Engineering*, vol. 48, no. 2, pp. 536–555, 2020. doi:10.1007/s10439-019-02411-0

[10] Cambridge Dictionary, "Cambridge dictionary - Bioprinting." [Online]. Disponible en: https://dictionary.cambridge.org/es/diccionario/ingles/bioprinting

[11] Ž. Kačarević, P. Rider, S. Alkildani, S. Retnasingh, R. Smeets, O. Jung, Z. Ivanišević, y M. Barbeck, "An introduction to 3D bioprinting: possibilities, challenges and future aspects," *Materials*, vol. 11, no. 11, p. 2199, 2018. doi:10.3390/ma11112199

[12] I. T. Ozbolat, W. Peng, y V. Ozbolat, "Application areas of 3D bioprinting," *Drug Discovery Today*, vol. 21, no. 8, pp. 1257–1271, 2016. doi:10.1016/j.drudis.2016.04.006

[13] M. A. Heinrich, W. Liu, A. Jimenez, J. Yang, A. Akpek, X. Liu, Q. Pi, X. Mu, N. Hu, R. M. Schiffelers, J. Prakash, J. Xie, y Y. S. Zhang, "3D Bioprinting: from benches to translational applications," *Small*, vol. 15, no. 23, p. 1805510, 2019. doi:10.1002/smll.201805510

[14] A. N. Leberfinger, S. Dinda, Y. Wu, S. V. Koduru, V. Ozbolat, D. J. Ravnic, y I. T. Ozbolat, "Bioprinting functional tissues," *Acta Biomaterialia*, vol. 95, pp. 32–49, 2019. doi:10.1016/j.actbio.2019.01.009

[15] M. Mobaraki, M. Ghaffari, A. Yazdanpanah, Y. Luo, y D. K. Mills, "Bioinks and bioprinting: a focused review," *Bioprinting*, vol. 18, no. August 2019, p. e00080, 2020. doi:10.1016/j.bprint.2020.e00080

[16] F. Kawecki, W. P. Clafshenkel, F. A. Auger, J.-M. Bourget, J. Fradette, y R. Devillard, "Self-assembled human osseous cell sheets as living biopapers for the laser-assisted bioprinting of human endothelial cells," *Biofabrication*, vol. 10, no. 3, p. 035006, 2018. doi:10.1088/1758-5090/aabd5b

[17] R. J. Mondschein, A. Kanitkar, C. B. Williams, S. S. Verbridge, y T. E. Long, "Polymer structure-property requirements for stereolithographic 3D printing of soft tissue engineering scaffolds," *Biomaterials*, vol. 140, pp. 170–188, 2017. doi:10.1016/j.biomaterials.2017.06.005

[18] Z. Wang, Z. Tian, X. Jin, J. F. Holzman, F. Menard, y K. Kim, "Visible light-based stereolithography bioprinting of cell-adhesive gelatin hydrogels," in *2017 39th Annual International Conference of the IEEE Engineering in Medicine and Biology Society (EMBC)*, vol. 2017. IEEE, 2017. doi:10.1109/EMBC.2017.8037144. ISBN 978-1-5090-2809-2 pp. 1599–1602.

[19] N. Hong, G.-H. Yang, J. Lee, y G. Kim, "3D bioprinting and its in vivo applications," *Journal of Biomedical Materials Research Part B: Applied Biomaterials*, vol. 106, no. 1, pp. 444–459, 2018. doi:10.1002/jbm.b.33826

[20] J. Groll, J. A. Burdick, D.-W. Cho, B. Derby, M. Gelinsky, S. C. Heilshorn, T. Jüngst, J. Malda, V. A. Mironov, K. Nakayama, A. Ovsianikov, W. Sun, S. Takeuchi, J. J. Yoo, y T. B. F. Woodfield, "A definition of bioinks and their distinction from biomaterial inks," *Biofabrication*, vol. 11, no. 1, p. 013001, 2018. doi:10.1088/1758-5090/aaec52

[21] E. Mancha Sánchez, J. C. Gómez-Blanco, E. López Nieto, J. G. Casado, A. Macías-García, M. A. Díaz Díez, J. P. Carrasco-Amador, D. Torrejón Martín, F. M. Sánchez-Margallo, y J. B. Pagador, "Hydrogels for bioprinting: a systematic review of hydrogels synthesis, bioprinting parameters, and bioprinted structures behavior," *Frontiers in Bioengineering and Biotechnology*, vol. 8, no. August, 2020. doi:10.3389/fbioe.2020.00776

[22] F. L. C. Morgan, L. Moroni, y M. B. Baker, "Dynamic bioinks to advance bioprinting," *Advanced Healthcare Materials*, vol. 9, no. 15, p. 1901798, 2020. doi:10.1002/adhm.201901798

[23] L. P. Silva, "Current trends and challenges in biofabrication using biomaterials and nanomaterials: future perspectives for 3D/4D bioprinting," in *3D and 4D Printing in Biomedical Applications*. Wiley-VCH Verlag GmbH & Co. KGaA, 2018, pp. 373–421.

[24] E. Abelardo, "Synthetic material bioinks," in *3D Bioprinting for Reconstructive Surgery*. Elsevier, 2018, pp. 137–144. ISBN 9780081012161

[25] D. Chimene, R. Kaunas, y A. K. Gaharwar, "Hydrogel bioink reinforcement for additive manufacturing: a focused review of emerging strategies," *Advanced Materials*, vol. 32, no. 1, p. 1902026, 2020. doi:10.1002/adma.201902026

[26] D. Lopes, H. Puga, J. Teixeira, y R. Lima, "Blood flow simulations in patient-specific geometries of the carotid artery: a systematic review," *Journal of Biomechanics*, vol. 111, p. 110019, 2020. doi:10.1016/j.jbiomech.2020.110019

[27] W. Faizal, N. Ghazali, C. Khor, I. A. Badruddin, M. Zainon, A. A. Yazid, N. B. Ibrahim, y R. M. Razi, "Computational fluid dynamics modelling of human upper airway: a review," *Computer Methods and Programs in Biomedicine*, vol. 196, p. 105627, 2020. doi:10.1016/j.cmpb.2020.105627

[28] J. A. Reid, P. A. Mollica, G. D. Johnson, R. C. Ogle, R. D. Bruno, y P. C. Sachs, "Accessible bioprinting: adaptation of a low-cost 3D-printer for precise cell placement and stem cell differentiation," *Biofabrication*, vol. 8, no. 2, p. 025017, 2016. doi:10.1088/1758-5090/8/2/025017

[29] J. Leppiniemi, P. Lahtinen, A. Paajanen, R. Mahlberg, S. Metsä-Kortelainen, T. Pinomaa, H. Pajari, I. Vikholm-Lundin, P. Pursula, y V. P. Hytönen, "3D-printable bioactivated nanocellulose–alginate hydrogels," *ACS Applied Materials & Interfaces*, vol. 9, no. 26, pp. 21 959–21 970, 2017. doi:10.1021/acsami.7b02756

[30] J. Göhl, K. Markstedt, A. Mark, K. Håkansson, P. Gatenholm, y F. Edelvik, "Simulations of 3D bioprinting: predicting bioprintability of nanofibrillar inks," *Biofabrication*, vol. 10, no. 3, p. 034105, 2018. doi:10.1088/1758-5090/aac872

[31] I. P. Magalhães, P. M. de Oliveira, J. Dernowsek, E. B. L. Casas, y M. S. L. Casas, "Investigation of the effect of nozzle design on rheological bioprinting properties using computational fluid dynamics," *Matéria (Rio de Janeiro)*, vol. 24, no. 3, 2019. doi:10.1590/s1517-707620190003.0714

[32] COMSOL®, *CFD Module user's guide*, 2016. ISBN 1781273332

[33] R. Samanipour, Z. Wang, A. Ahmadi, y K. Kim, "Experimental and computational study of microfluidic flow-focusing generation of gelatin methacrylate hydrogel droplets," *Journal of Applied Polymer Science*, vol. 133, no. 29, pp. 24–26, 2016. doi:10.1002/app.43701

[34] F. Liravi, R. Darleux, y E. Toyserkani, "Additive manufacturing of 3D structures with non-Newtonian highly viscous fluids: finite element modeling and experimental validation," *Additive Manufacturing*, vol. 13, pp. 113–123, 2017. doi:10.1016/j.addma.2016.10.008

[35] A. Blaeser, D. F. Duarte Campos, U. Puster, W. Richtering, M. M. Stevens, y H. Fischer, "Controlling shear stress in 3D bioprinting is a key factor to balance printing resolution and stem cell integrity," *Advanced Healthcare Materials*, vol. 5, no. 3, pp. 326–333, 2016. doi:10.1002/adhm.201500677

7. Resultados de la tesis

Artículos aceptados

[1] Mancha Sánchez, E.; **Gómez-Blanco, J.C**; López Nieto, E.; Casado, J.G., Macías-García, A.; Díaz Díez, M.A.; Carrasco-Amador, J.P.; Torrejón Martín, D.; Sánchez-Margallo, F.M.; Pagador, J.B. Hydrogels for bioprinting: A systematic review of hydrogels synthesis, bioprinting parameters, and bioprinted structures behavior. Frontiers in Bioengineering and Biotechnology 2020, 8, 776. DOI: https://doi.org/10.3389/fbioe.2020.00776

[2] **Gómez-Blanco, J.C.**; Mancha-Sánchez, E.; Marcos, A.C.; Matamoros, M.; Díaz-Parralejo, A.; Pagador, J.B. Bioink temperature influence on shear stress, pressure and velocity using computational simulation. Processes 2020, 8, 865. DOI: https://doi.org/10.3390/pr8070865

[3] Matamoros, M.; **Gómez-Blanco, J.C.**; Sánchez, Á.J.; Mancha, E.; Marcos, A.C.; Carrasco-Amador, J.P.; Pagador, J.B. Temperature and humidity PID controller for a bioprinter atmospheric enclosure system. Micromachines 2020, 11, 999. DOI: https://doi.org/10.3390/mi11110999

Artículos enviados

[1] **Gómez-Blanco, J.C.**; López-Espino, M.; Macías-García, A.; Díaz-Parralejo, A.; Macías-Blanco, P.; Pagador, J.B.; Sánchez-Margallo, F.M. Optimization of computational simulations on bioprinting nozzles: A combination of systematic Review and design of experiments. Applied Sciences *(En Revisión)*

[2] **Gómez-Blanco, J.C.**; Pagador, J.B.; Galván-Chacón, V.; Sánchez-Peralta, L.F.; Matamoros, M.; Marcos, A.C.; Sánchez-Margallo, F.M. Computational simulation-based comparative analysis of standard FDM 3D printing and conical nozzles for pneumatic and piston-driven bioprinting. Additive Manufacturing *(En Revisión)*

[3] **Gómez-Blanco, J.C.**; Galván-Chacón, V.; Patrocinio, D.; Matamoros, M.; Ojeda, A.; Marcos, A.C.; Duarte, M.; Marinaro, F.; Pagador, J.B.; Sánchez-Margallo, F.M. Improving cell viability and velocity in μ-extrusion bioprinting with a novel pre-incubator bioprinter and a standard FDM 3D printing nozzle. Materials *(En Revisión)*

Proceedings en Revistas

[1] Mancha Sánchez, E.; **Gómez Blanco, J.C**; López Nieto, E.; Marinaro, F.; Macías García, A.; Carrasco Amador, J.P.; Sánchez Margallo, F.M.; Pagador Carrasco, J.B. (2020) Assessment of cellular viability in bioprinted scaffold with alginate-gelatin hydrogel. British Journal of Surgery, 107, 6-7

[2] Mancha Sánchez, E.; **Gómez Blanco, J.C**; López Nieto, E.; Marinaro, F.; Macías García, A.; Carrasco Amador, J.P.; Sánchez Margallo, F.M.; Pagador Carrasco, J.B. (2020) Comparison between a homemade and a commercial bioprinter. British Journal of Surgery, 107, 7-7

[3] Mancha Sánchez, E.; Sánchez Margallo, F.M.; **Gómez Blanco, J.C**; Pagador Carrasco, J.B. (2018) Influence of hidrogel in bioprinters' standarization. British Journal of Surgery, 105, 10-11

[4] **Gómez Blanco, J.C**; Sánchez Margallo, F.M.; Álvarez Pérez, V.; Casado, J.G; Pagador Carrasco, J.B. (2017) Preliminary accuracy study of 3D bioprinted scaffolds for regenerative cartilage therapies. Proceedings of the 31st International Congress and Exhibition Computer Assisted Radiology and Surgery, 12 (S1), S71

Comunicaciones a Congresos

[1] Mancha Sánchez, E; **Gómez Blanco, J.C**; Marcos, A.C.; Matamoros Pacheco, M.; Sánchez-Margallo, F.M.; Pagador Carrasco, J.B. (2020) Estudio de la influencia del diámetro y temperatura del nozzle en el grosor del filamento para bioimpresión. XXXVIII Congreso Anual de la Sociedad Española de Ingeniería Biomédica. 25-27 noviembre 2020. Valladolid (España)

[2] **Gómez Blanco, J.C**; Matamoros Pacheco, M.; Mancha Sánchez, E; Marcos, A.C.; Sánchez-Margallo, F.M.; Pagador Carrasco, J.B. (2020) Construcción de una cámara climática para bioimpresoras: Control de la temperatura y la humedad. XXXVIII Congreso Anual de la Sociedad Española de Ingeniería Biomédica. 25-27 noviembre 2020. Valladolid (España)

[3] Marcos, A.C.; Mancha Sánchez, E; Matamoros Pacheco, M.; Agujetas, R.; **Gómez Blanco, J.C**; Sánchez-Margallo, F.M.; Pagador Carrasco, J.B. (2020) Estudio numérico del flujo de temperatura en cámara climática de bioimpresión. XXXVIII Congreso Anual de la Sociedad Española de Ingeniería Biomédica. 25-27 noviembre 2020. Valladolid (España)

[4] **Gómez Blanco, J.C**; Mancha Sánchez, E; Matamoros Pacheco, M.; Marcos, A.C.; Sánchez-Margallo, F.M.; Pagador Carrasco, J.B. (2020) Estudio del estrés cortante en bioimpresión por extrusión mediante simulación computacional. XXXVIII Congreso Anual de la Sociedad Española de Ingeniería Biomédica. 25-27 noviembre 2020. Valladolid (España)

[5] Matamoros Pacheco, M., **Gómez Blanco, J.C**, Marcos, A.C, Carrasco Amador, J.P., Pagador Carrasco, J.B. (2020) Control PID de temperatura-humedad-CO2 en una cámara para técnicas de bioimpresión. 24th International Congress on Project Management and Engineering. 7-9 julio 2020. Alcoy (España)

[6] Mancha Sánchez, E.; **Gómez Blanco, J.C**; López Nieto, E.; Marinaro, F.; Macías García, A.; Carrasco Amador, J.P.; Sánchez Margallo, F.M.; Pagador

Carrasco, J.B. (2019) Assessment of cellular viability in bioprinted scaffold with alginate-gelatin hydrogel. XXV Congreso de la Sociedad Española de Investigaciones Quirúrgicas. 12-13 diciembre 2019. Barcelona (España)

[7] Mancha Sánchez, E.; **Gómez Blanco, J.C**; López Nieto, E.; Marinaro, F.; Macías García, A.; Carrasco Amador, J.P.; Sánchez Margallo, F.M.; Pagador Carrasco, J.B. (2020) Comparison between a homemade and a commercial bioprinter. XXV Congreso de la Sociedad Española de Investigaciones Quirúrgicas. 12-13 diciembre 2019. Barcelona (España)

[8] **Gómez Blanco, J.C**; Mancha Sánchez, E.; López Espino, M.; Díaz Parralejo, A.; Sánchez Margallo, F.M.; Pagador Carrasco, J.B. (2019) Conical tip gauge influence in extrusion bioprinting: computational simulation study. XXXVII Congreso Anual de la Sociedad Española de Ingeniería Biomédica. 27-29 noviembre 2019. Santander (España)

[9] Mancha Sánchez, E.; **Gómez Blanco, J.C**; López Espino, M.; Díaz Parralejo, A.; Sánchez Margallo, F.M.; Pagador Carrasco, J.B. (2019) Extrusion bioprinting of a commercial bioink: a computational simulation of the temperature / pressure relation. XXXVII Congreso Anual de la Sociedad Española de Ingeniería Biomédica. 27-29 noviembre 2019. Santander (España)

[10] **Gómez Blanco, J.C**; Mancha Sánchez, E.; Ortega Morán J.F.; Díaz Parralejo, A.; Sánchez Margallo, F.M.; Pagador Carrasco, J.B. (2019) Computational fluid dynamics study of inlet velocity on extrusion-based bioprinting. 15^{th} mediterranean conference on medical and biological engineering and computing. 26 septiembre 2019. Coimbra (Portugal)

[11] López Espino, M.; Díaz Parralejo, A.; **Gómez Blanco, J.C**; Mancha Sánchez, E. (2019) Study of micro-extrusion systems for 3D bioprinting. International Conference on Sustainable Materials Science and Technology. 17-19 julio 2019. París (Francia)

[12] **Gómez Blanco, J.C**; Mancha Sánchez, E.; Sánchez Margallo, F.M.; Pagador Carrasco, J.B. (2018) A comparative study of bioprinting extrusion nozzles geometries. XXXVI Congreso Anual de la Sociedad Española de Ingeniería Biomédica. 21-23 noviembre 2018. Ciudad Real (España)

[13] Matamoros Pacheco, M.; Sánchez Ortega, Á.; Canito Lobo, J.L.; Marcos Romero, A.C.; Carrasco Amador, J.P.; **Gómez Blanco, J.C.**; Mancha Sánchez, E.; Sánchez Margallo, F.M.; Pagador Carrasco, J.B (2018) Fabricación y evaluoación de una cámara climática para el desarrollo de técnicas de bioimpresión 3D. XXXIX Jornadas de Automática. 5-7 septiembre 2018. Badajoz (España)

[14] **Gómez Blanco, J.C.**; Mancha Sánchez, E.; Torrejón Martín, D.; Carrasco Amador, J.P.; Sánchez Margallo, F.M.; Pagador Carrasco, J.B (2018) Fabricación y evaluación de una cámara climática para el desarrollo de técnicas de bioimpresión 3D. XXXIX Jornadas de Automática. 5-7 septiembre 2018. Badajoz (España)

[15] Mancha Sánchez, E.; Sánchez Margallo, F.M.; **Gómez Blanco, J.C**; Pagador Carrasco, J.B. (2017) Influencia del hidrogel en la estandarización de bioimpresoras. XXIII Congreso de la Sociedad Española de de Investigaciones Quirúrgicas. 17 noviembre 2017. Madrid (España)

[16] **Gómez Blanco, J.C.**; Sánchez Margallo, F.M.; Álvarez Pérez, V.; Macías García, A.; Pagador Carrasco, J.B. (2017) Accuracy analysis of micro-extruded scaffolds

using 3D bioprinting: a preliminary study. 2nd International Conference on Sustainable Materials Science and Technology (SMST2). 19-21 julio 2017. Las Palmas de Gran Canarias (España)

[17] Mancha Sánchez, E.; Sánchez Margallo, F.M.; **Gómez Blanco, J.C.**; Álvarez Pérez, V.; Macías García, A.; Pagador Carrasco, J.B. (2017) Experimental 3D printable hydrogel protocol: preliminary study. 2nd International Conference on Sustainable Materials Science and Technology (SMST2). 19-21 julio 2017. Las Palmas de Gran Canarias (España)

[18] **Gómez Blanco, J.C.**; Sánchez Margallo, F.M.; Álvarez Pérez, V.; García, J.; Macías García, A.; Pagador Carrasco, J.B. (2017) Preliminary accuracy study of 3D bioprinted scaffolds for regenerative cartilage therapies. Conference of the International Foundation for Computer Assisted Radiology and Surgery. 20-24 junio 2017. Barcelona (España)

7.1 Hydrogels for bioprinting: A systematic review of hydrogels synthesis, bioprinting parameters and bioprinted structures Behavior

Dr. José Blas Pagador Carrasco, como director de la tesis titulada "Desarrollo de un sistema de bioimpresión para posicionar líneas celulares", certifico el factor de impacto y la categorizacion de la siguiente publicación, incluida en la tesis doctoral. Del mismo modo, se especifica la aportación del doctorando.

Autores: Enrique Mancha Sánchez, **J. Carlos Gómez-Blanco**, Esther López Nieto, Javier G. Casado, Antonio Macías-García, María A. Díaz Díez, Juan Pablo Carrasco-Amador, Diego Torrejón Martín, Francisco Miguel Sánchez-Margallo and J. Blas Pagador

Título: Hydrogels for Bioprinting: A Systematic Review of Hydrogels Synthesis, Bioprinting Parameters, and Bioprinted Structures Behavior

Revista: Frontiers in Bioengineering and Biotechnology

Otros datos: vol 8, pág. 776, año 2020

DOI: 10.3389/fbioe.2020.00776

Factor de impacto: 3.644 (Q2 – Multidisciplinary Sciences)

Abstract: Nowadays, bioprinting is rapidly evolving and hydrogels are a key component for its success. In this sense, synthesis of hydrogels, as well as bioprinting process, and cross-linking of bioinks represent different challenges for the scientific community. A set of unified criteria and a common framework are missing, so multidisciplinary research teams might not efficiently share the advances and limitations of bioprinting. Although multiple combinations of materials and proportions have been used for several applications, it is still unclear the relationship between good printability of hydrogels and better medical/clinical behavior of bioprinted structures. For this reason, a PRISMA methodology was conducted in this review. Thus, 1,774 papers were retrieved from PUBMED, WOS, and SCOPUS databases. After selection, 118 papers were analyzed to extract information about materials, hydrogel synthesis, bioprinting process, and tests performed on bioprinted structures. The aim of this systematic review is to analyze materials used and their influence on the bioprinting parameters that ultimately generate tridimensional structures. Furthermore, a comparison of mechanical and cellular behavior of those bioprinted structures is presented. Finally, some conclusions and recommendations are exposed to improve reproducibility and facilitate a fair comparison of results.

Contribución del doctorando: screening, data extraction, preparation of graphics, tables, and manuscript

Contribuciones de los coautores: EM performed literature search, screening, data extraction, preparation of graphics, tables, and manuscript. JG-B contributed to screening, data extraction, preparation of graphics, tables, and manuscript. JP contributed to screening, data extraction, and preparation of manuscript. EL, JC, AM-G, MD, JC-A, and DT contributed to screening, data extraction, and revision work to the manuscript. FS-M performed revision work to the manuscript. All authors contributed to the article and approved the submitted version.

frontiers in Bioengineering and Biotechnology

SYSTEMATIC REVIEW
published: 06 August 2020
doi: 10.3389/fbioe.2020.00776

Hydrogels for Bioprinting: A Systematic Review of Hydrogels Synthesis, Bioprinting Parameters, and Bioprinted Structures Behavior

Enrique Mancha Sánchez[1], J. Carlos Gómez-Blanco[1], Esther López Nieto[2], Javier G. Casado[2], Antonio Macías-García[3], María A. Díaz Díez[3], Juan Pablo Carrasco-Amador[3], Diego Torrejón Martín[3], Francisco Miguel Sánchez-Margallo[4] and J. Blas Pagador[1]*

[1] Bioengineering and Health Technologies Unit, Minimally Invasive Surgery Centre Jesús Usón, Cáceres, Spain, [2] Stem Cells Unit, Minimally Invasive Surgery Centre Jesús Usón, Cáceres, Spain, [3] School of Industrial Engineering, University of Extremadura, Badajoz, Spain, [4] Scientific Direction, Minimally Invasive Surgery Centre Jesús Usón, Cáceres, Spain

OPEN ACCESS

Edited by:
Jöns Gunnar Hilborn,
Uppsala University, Sweden

Reviewed by:
Ngan F. Huang,
Stanford University, United States
Marina Rubert,
ETH Zürich, Switzerland

***Correspondence:**
Enrique Mancha Sánchez
emancha@ccmijesususon.com

Specialty section:
This article was submitted to Tissue Engineering and Regenerative Medicine, a section of the journal Frontiers in Bioengineering and Biotechnology

Received: 09 March 2020
Accepted: 18 June 2020
Published: 06 August 2020

Citation:
Mancha Sánchez E, Gómez-Blanco JC, López Nieto E, Casado JG, Macías-García A, Díaz Díez MA, Carrasco-Amador JP, Torrejón Martín D, Sánchez-Margallo FM and Pagador JB (2020) Hydrogels for Bioprinting: A Systematic Review of Hydrogels Synthesis, Bioprinting Parameters, and Bioprinted Structures Behavior. Front. Bioeng. Biotechnol. 8:776. doi: 10.3389/fbioe.2020.00776

Nowadays, bioprinting is rapidly evolving and hydrogels are a key component for its success. In this sense, synthesis of hydrogels, as well as bioprinting process, and cross-linking of bioinks represent different challenges for the scientific community. A set of unified criteria and a common framework are missing, so multidisciplinary research teams might not efficiently share the advances and limitations of bioprinting. Although multiple combinations of materials and proportions have been used for several applications, it is still unclear the relationship between good printability of hydrogels and better medical/clinical behavior of bioprinted structures. For this reason, a PRISMA methodology was conducted in this review. Thus, 1,774 papers were retrieved from PUBMED, WOS, and SCOPUS databases. After selection, 118 papers were analyzed to extract information about materials, hydrogel synthesis, bioprinting process, and tests performed on bioprinted structures. The aim of this systematic review is to analyze materials used and their influence on the bioprinting parameters that ultimately generate tridimensional structures. Furthermore, a comparison of mechanical and cellular behavior of those bioprinted structures is presented. Finally, some conclusions and recommendations are exposed to improve reproducibility and facilitate a fair comparison of results.

Keywords: bioprinting, hydrogel, systematic review, biomaterial, bioink

INTRODUCTION

Biofabrication can be defined as a multidisciplinary research field with a combination of principles, protocols, and fabrication techniques from engineering, electronics, material science, cell biology, and biomedicine (Silva, 2018). Bioprinting is a biofabrication technique that can control deposition of cells, extracellular matrix components, and biochemical factors layer by layer to create defined structures with several kinds of materials, bioactive molecules, and cells (Moroni et al., 2018; Eswaramoorthy et al., 2019). In this sense, bioprinting allows the generation of complex structures mimicking biological cues, which increases the possibilities of tissue creation by supporting

and improving other traditional techniques of tissue engineering (Moldovan, 2019). Besides, all bioprinting techniques are also constantly and rapidly evolving thanks to the advances in technical processes and bioink (hydrogel with cells in culture medium) properties (Silva, 2018).

Synthesis, bioprinting, and cross-linking of bioinks have a great impact on the generation of biological structures and especially on its mechanical and cellular behavior. Therefore, bioink is one of the most critical components of 3D bioprinting and it is intimately related to the bioprinting technique and the selected cells (Kyle et al., 2017).

Although there are many bioprinting techniques, such as laser, inkjet, droplet, stereolithography, and electrospinning (Leberfinger et al., 2019), we have focused this review on extrusion-based bioprinting. This technique is widely used by researchers, mainly due to its low cost and versatility that allow mechanical modifications and a wide range of materials, but above all high cell densities (Kyle et al., 2017; Jovic et al., 2019; Leberfinger et al., 2019). It uses the widest range of biomaterials including hydrogels, biocompatible copolymers, and cell spheroids that have many different printability properties, such as viscosity, density, or shear thinning properties, among others.

Each bioprinting procedure needs a specific set of rheological and mechanical properties of the bioink to achieve a successful bioprinted structure. On the one hand, extrusion-based process must control the properties referred to shear thinning, like viscosity and shear stress, to mitigate cell damage. On the other hand, inkjet (droplet-based) process must control surface tension and viscosity of bioinks to get a proper droplet ejection (Leberfinger et al., 2019).

In this review, natural and synthetic materials used to produce hydrogels with different features and behaviors have been analyzed. According to the bioprinting process, those important parameters involved in the bioprinter setting have been exposed (He et al., 2016; Sodupe-Ortega et al., 2018). Finally, tests for validation of bioprinted structures have been included and grouped into two blocks: cell and mechanical properties.

Hence, the main goal of this systematic review is to analyze the impact of pre-printing stage (materials selection, hydrogel synthesis, and bioink generation) and extrusion-based bioprinting process (both bioprinting parameters and cross-linking methods) on post-printing results of the bioprinted structures (cell tests and mechanical properties) (**Figure 1**).

MATERIALS AND METHODS

Identification of Peer-Reviewed Manuscripts for Analysis Literature

A systematic review was conducted in accordance with PRISMA (P) guidelines. This review included original peer-reviewed studies based on the following criteria: (1) publication in an English-language journal; (2) papers related to extrusion-based bioprinting; (3) only original peer-reviewed papers were included, so editorials, proceedings, communications, letters, and reviews were excluded; (4) all papers based on complex tissue generation, organ generation or drug testing were excluded.

The search engines used to identify studies were PUBMED, WOS, and SCOPUS. The following search items were used for the literature search: (Bioprinting AND Hydrogel). Search was performed on April 15th, 2019. No restriction was set on publication date. No meta-analyses were performed due to the heterogeneity of studies.

Data Extraction and Analysis

Before reviewing papers, several categories for data extraction were defined. A form was created and divided into different categories: (1) ***general data*** compiles authors, title, publication year, and journal; (2) ***material*** categorizes different materials by

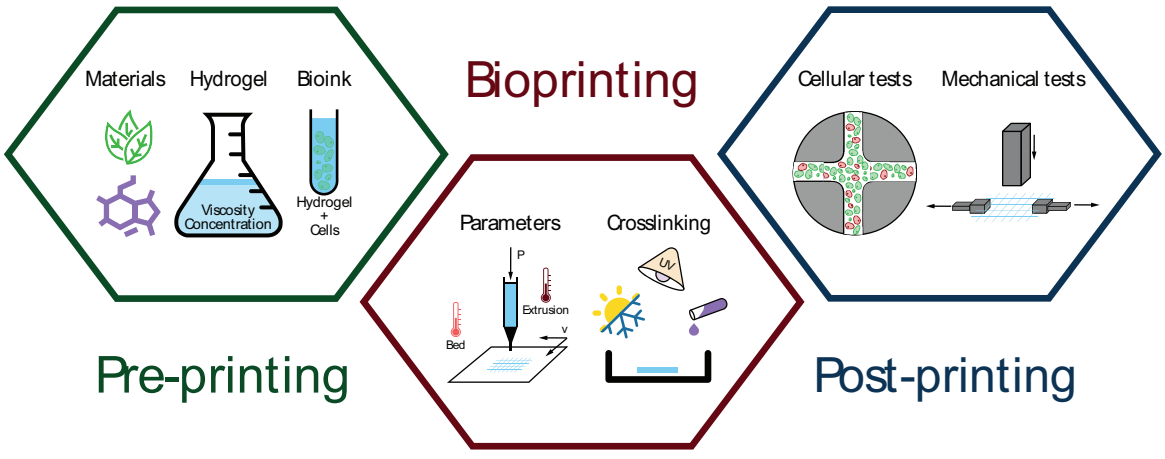

FIGURE 1 | Schematic representation of three bioprinting stages: pre-printing (material selection, hydrogel synthesis, and bioink generation), extrusion-based bioprinting (parameters and cross-linking methods), and post-printing analysis (cellular and mechanical tests).

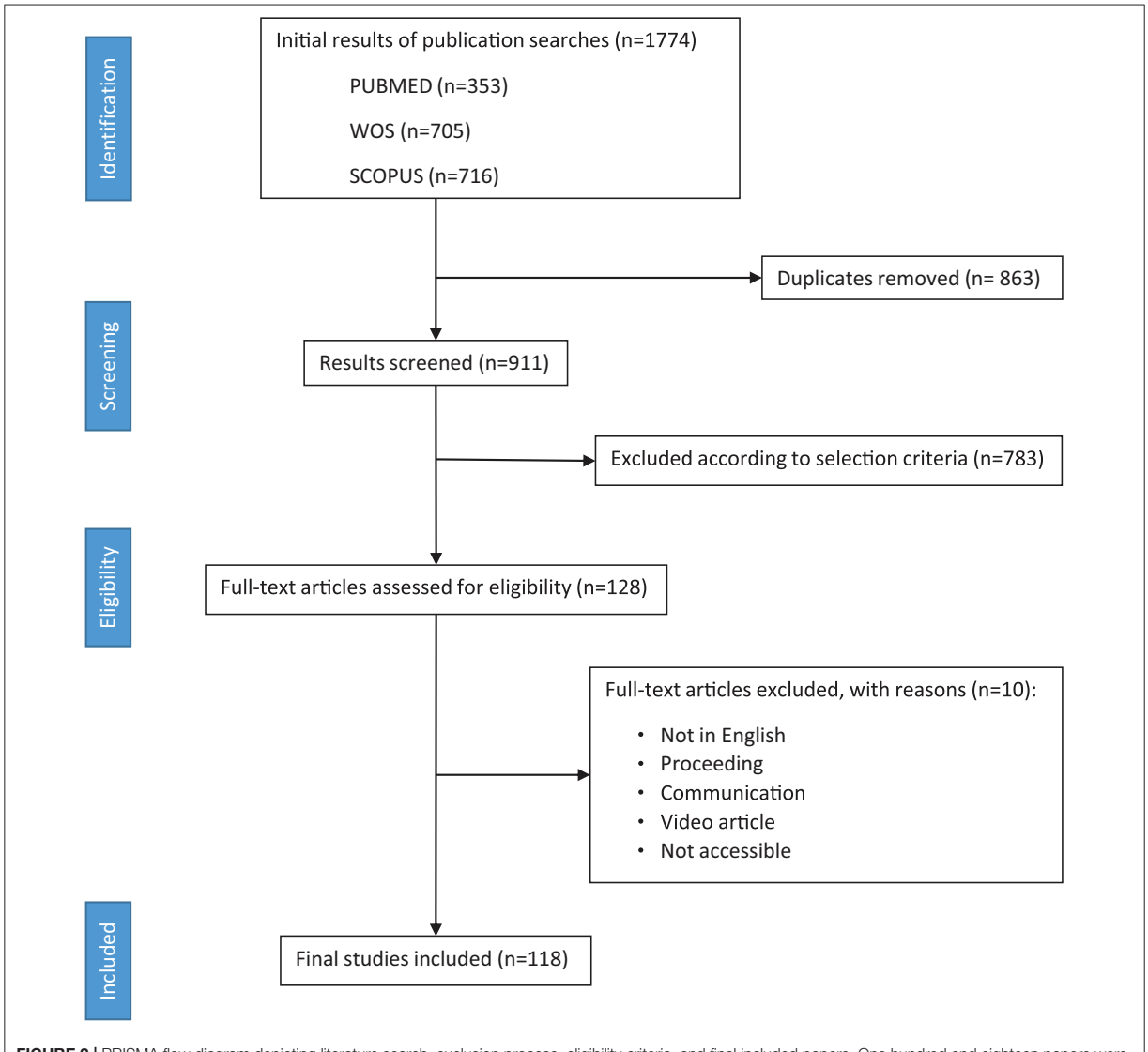

FIGURE 2 | PRISMA flow diagram depicting literature search, exclusion process, eligibility criteria, and final included papers. One hundred and eighteen papers were included without publication date restriction (search performed on April 15th, 2019).

their importance and/or functionalities, including concentration and viscosity; (3) ***printing settings*** gathers cartridge temperature, bed temperature, printing pressure, and printing speed; (4) ***cross-linking methods*** summarizes cross-linking process depending on its type and characteristics, and finally (5) ***validation tests*** registers types of cellular viability and mechanical tests. Specifically, *main materials* were classified as synthetic or natural, material name, cell-laden or post-printing cell addition, and according to its type of cross-linking (thermal, chemical, or physical). Furthermore, *structural material* was subdivided on material name and cross-linking type. Finally, *sacrificial material* was defined by material name, cross-linking type, and removal process. Papers were individually assigned to eight independent reviewers to be read in detail to extract available data.

RESULTS AND DISCUSSION

Overall Findings

In all, 1,774 abstracts were found using the search string (Bioprinting AND Hydrogel) in three databases (PUBMED, WOS, and SCOPUS). Nine hundred and eleven papers were screened after removing duplicated, 783 of them excluded according to selection criteria, and 128 revised in full text. From those, 118 were finally considered for the review analysis (**Figure 2**).

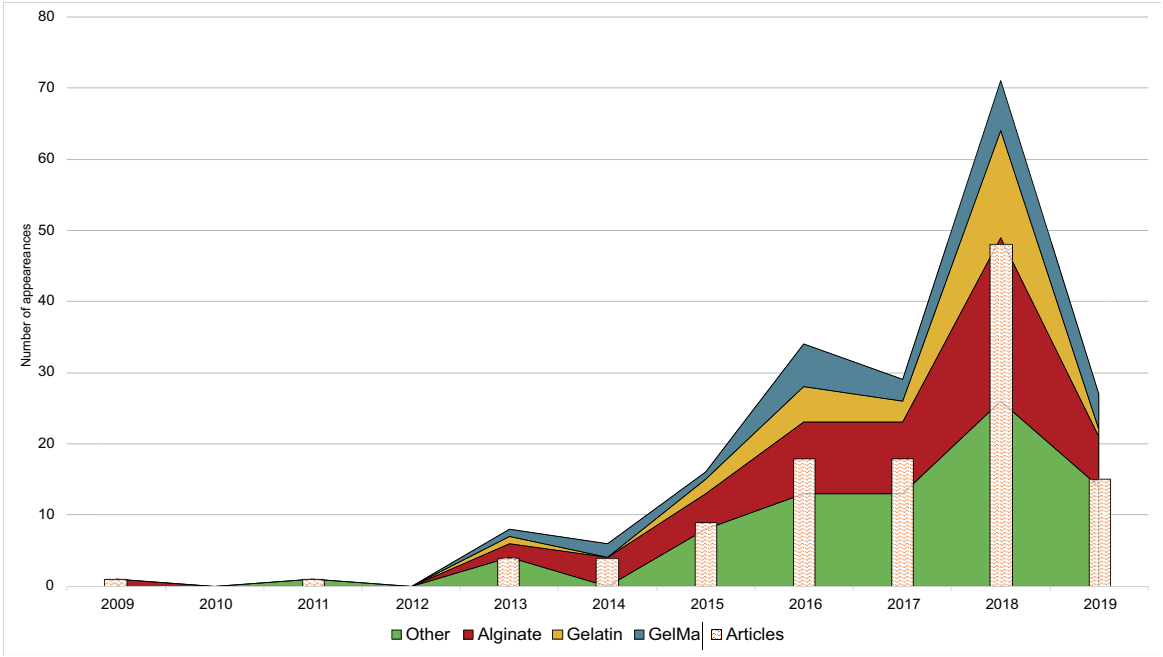

FIGURE 3 | Research trend in hydrogels for bioprinting using a bar chart (*papers per year*) combined with a stacked area chart (*total uses of a material per year*). The three most used materials (alginate, gelatin, and GelMA) are shown individually while the rest of materials are grouped in the category "other." It is important to note that some materials are used in more than one paper, so some stacked areas overtake its corresponding bar chart.

Figure 3 shows an upward trend in the number of published papers during the last decade. There were no papers prior to 2009, only one published in this year, and an increase from 2015 onwards. However, 2017 meant a year of stagnation that could be due to an increase of research studies focused on the creation of more complex tissues, organoids, drug testing, and lab-on-a chip (Ma J. et al., 2018; Ma X. et al., 2018; Reid et al., 2019), subjects that are out of the scope of this review. In 2018, the research community came back to the creation of new materials and structures. These studies could provide better results in terms of cellular viability, histo-differentiation of complex tissues and the formation of complex structures. On the other hand, a crucial point could rely on a higher accessibility to low-cost or home-made bioprinters (Ozbolat et al., 2017).

Additionally, **Figure 3** shows annual papers regarding the three most used materials as main component (alginate, gelatin, and GelMA) whereas Furthermore, the rest of materials was grouped in the category "other." Material trend is similar to year trend, with a few differences. In 2014 and 2017, total number of used materials is lower in comparison to previous years, which means that fewer papers used more than one material. On the other hand, papers published in the first trimester of 2019 showed a rising forecast for this year. It is difficult to make an approach to what kind of papers will be published in upcoming years, but everything indicates that new synthetic materials and mixtures of other complex materials could grow up (Ashammakhi et al., 2019).

Journals Analysis

In this section, a classification of journals has been made to analyze what type of publications deal with our topics. Four main categories and other four subcategories from JCR or SJR were used to group journals. The main categories are: (1) ***material***, journals of chemical/material-centered issues; (2) ***cellular***, journals focused on the cellular/histological/biochemical topic; (3) ***engineering***, journals focused on the technical and/or mechanical issues, and (4) ***multidisciplinary***, journals that allow multiple topics. Additionally, the four combined subcategories are: (1) **engineering/material**, (2) **cellular/material**, (3) **engineering/cellular**, and (4) **engineering/material/cellular**.

Figure 4 shows distribution of all 50 journals. **Material** contains the highest number of journals with 17 (29 papers). "Applied Materials & Interfaces" and "Biomaterials Science & Engineering" are the two most common journals in this category with 6 and 4 papers, respectively. All combinations of the **material** category reach 33 journals (86 papers). The remaining categories contain fewer journals. **Cellular** and **engineering** categories includ only four and seven journals (5 and 8 papers), respectively. "Scientific Reports" and "Plos One" are two journals associated to **multidisciplinary** category

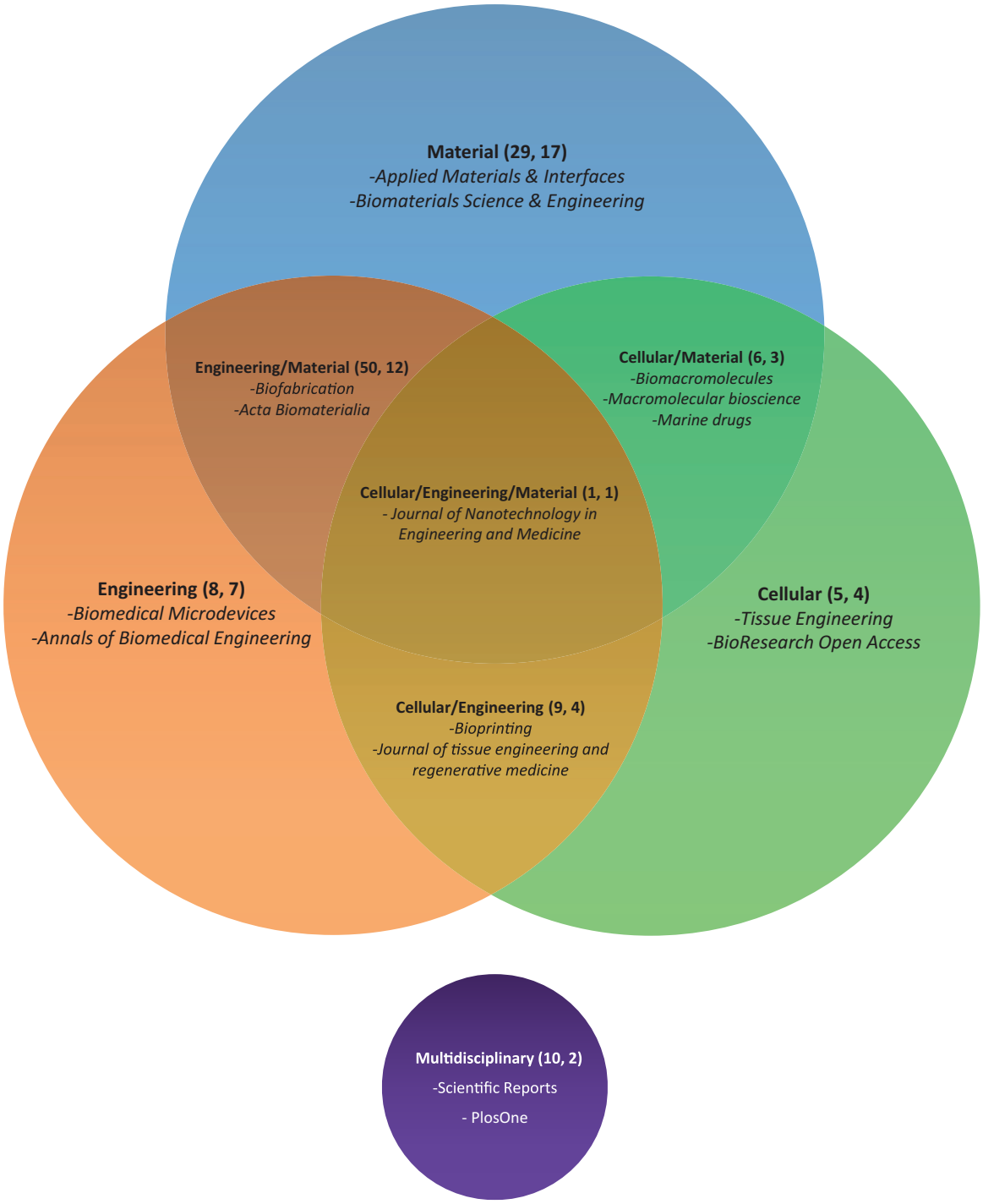

FIGURE 4 | Venn diagram of journals' categories selected in this review according to JCR/SJR categories. Diagram information is organized as follows: Topic of the journal (number of papers, number of journals) and some of the most represented journals are listed. We noted that intersection areas are exclusive, and sizes are not proportional.

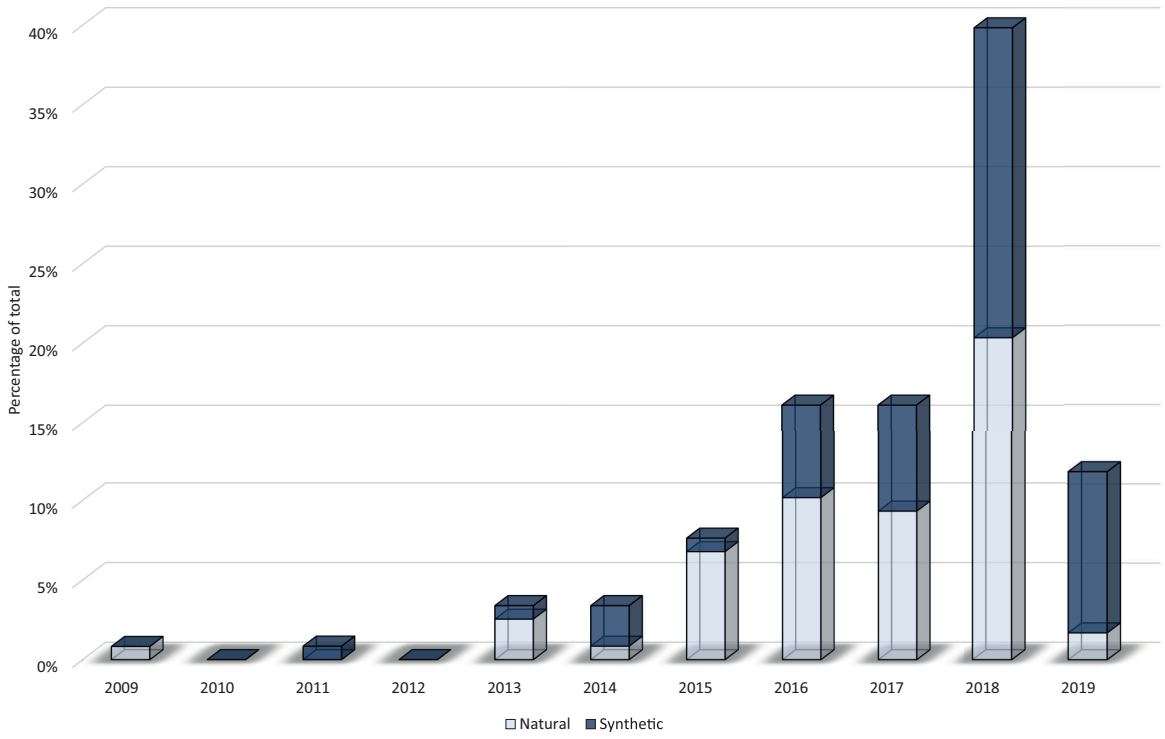

FIGURE 5 | Stacked columns graph that shows evolution per year of natural (white) and synthetic (blue) materials on the percentage of total.

with 8 and 3 papers, respectively. "Journal of nanotechnology in Engineering and Medicine" is the only journal associated to the **engineering/material/cellular** category with one paper. Finally, the **material/engineering** subcategory is by far the most common with 12 journals (50 papers). In this subcategory, most papers are published by "Biofabrication" (23 papers) and "Acta Biomateralia" (8 papers).

Hydrogel Generation (Pre-printing)

Natural vs. Synthetic

Natural and synthetic polymers can be considered as a broad cataloging of materials to synthesize hydrogels. In this sense, natural polymers are defined as bio-derived materials present in nature that can be extracted using physical or chemical methods (e.g., gelatin, alginate, or chitosan). On the other hand, those human-made polymers are named synthetic and are usually classified into plastics, elastomers, and synthetic fibers (Ouellette and Rawn, 2015).

In general, authors use natural materials more than synthetic (**Figure 5**) due to their better biological properties (Silva, 2018) at the expense of the best mechanical properties of synthetic materials (Abelardo, 2018). A chronological classification of papers show few studies between 2009 and 2014 (10 out of 118) followed by a huge increment in the use of natural materials in 2015 (89% of all papers in this year). After that, natural materials clearly have a downward trend in favor of synthetic materials that reached 36, 42, 48, and 85% throughout 2016, 2017, 2018, and 2019, respectively. Maybe this trend is due to high biocompatibility and affordable price of natural materials during the first years of bioprinting. However, rheological properties of natural materials are not the best for printability, and mechanical properties of the bioprinted structures are only appropriate for some applications. For this reason, once these natural materials reached their technical and biological limitations, the use of synthetic materials began to rise in order to solve these former problems.

Materials

The selection of materials is one of the most important decisions for the hydrogel generation. They have a great impact on biocompatibility and cellular viability as well as the mechanical behavior of the bioprinted structures, what is mandatory for a good bioprinting result. In this sense, all 118 papers used 34 different materials, although some chemical modifications were performed in some of them (e.g., alginate with norbornene) that are not considered as different material in this review. Specifically, the most common materials was alginate appearing in 58 papers followed by gelatin (26), GelMA (25), hyaluronic acid (16), and polyethylene glycol (PEG) with its chemical modifications (16).

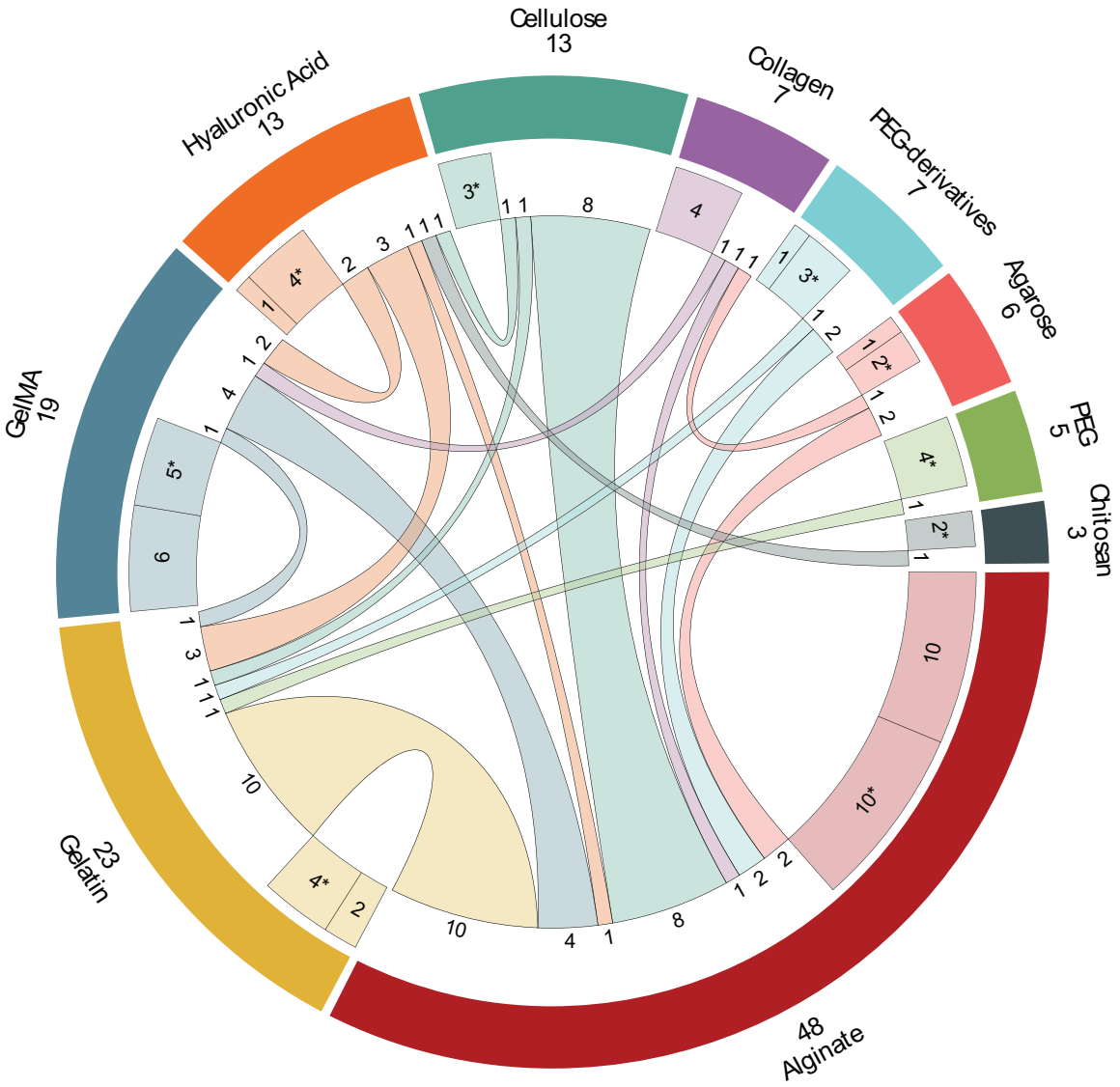

FIGURE 6 | Combination of the 10 most used materials in hydrogels among them. The materials are shown in the external ring (total of papers and name). The middle ring segments represent one-material hydrogels and hydrogels, marked with (*), that are a combination of this material with non-selected materials (one-material papers mixed with non-selected materials papers). Inner lines represent hydrogels with two of the selected materials, but in some case other non-selected materials can be included (number of papers next to each inner line).

Although complex tissues and organs generation are out of the scope of this review, we consider interesting to include some information about those papers that define its biological purpose (61 out of 118). Most of them have a low frequency or a generic soft tissue use, but cartilage (22 papers) and vascular (9) usually use alginate (12 and 6 papers) and GelMA (9 and 2 papers), respectively.

In this review, the 10 most used materials were selected for a detailed analysis. **Figure 6** shows the combination of these 10 materials in different hydrogels (103 papers). However, in order to make clear this figure, those papers that use hydrogels with more than two of these selected materials (12) and papers that use materials different of these ten (3) were excluded from this figure and analyzed later in this section.

Alginate is the most used material in bioprinting appearing in a total of 58 papers. It is used with the other selected materials in pairs in 28 papers, with more than two selected materials in 10 papers, alone in 10 papers and with other chemical modifications

in other 10 papers. Some of these interesting chemical modifications that improve its characteristics are: oxidized alginate (ox-alg) (Hafeez et al., 2018) which gives alginate a faster degradation and more reactive groups (Boontheekul et al., 2005), methacrylated alginate (MeAlg/AlgMA) which allows photo-polymerization thanks to its methacryloyl groups (García-Lizarribar et al., 2018; Ji et al., 2019), both oxidized and methacrylated together (ox-MeAlg) (Jeon et al., 2019), and alginate with norbornene (alg-norb) (Ooi et al., 2018) which provides alginate an ultrafast light-triggered cross-linking. Firstly, gelatin is the hydrogel which appears more times with alginate in just two materials combinations (Chung et al., 2013; He et al., 2016; Wang et al., 2016; Ding et al., 2017, 2018; Giuseppe et al., 2017; Aljohani et al., 2018; Berg et al., 2018; Gao et al., 2018; Li et al., 2018c). It is important to note that alginate/gelatin combination allows hydrogel to have good rheological properties (alginate) with proper thermoresponsive behavior (gelatin). Secondly, different types of cellulose have been used in combination with alginate: cellulose nanocrystals (CNC) (Habib et al., 2018; Wu Y. et al., 2018), methylcellulose (Li et al., 2017; Schütz et al., 2017; Ahlfeld et al., 2018; Gonzalez-Fernandez et al., 2019), and nanofibrillated cellulose (NFC) (Markstedt et al., 2015; Apelgren et al., 2017). Gelatin and cellulose are followed by GelMA (Liu et al., 2018; Zhang X. et al., 2018; Kosik-Kozioł et al., 2019; Krishnamoorthy et al., 2019), PEG-derived (Maiullari et al., 2018; Yu et al., 2018), agarose (Blaeser et al., 2013; López-Marcial et al., 2018), hyaluronic acid (Ji et al., 2019), and collagen (Campbell et al., 2015) to produce hydrogels of two materials. The rest of studies uses three and four-materials hydrogels with 7 and 3 papers, respectively. It is particularly interesting that 5 out of these 10 papers utilized alginate and GelMA with other different components: hyaluronic acid methacrylated (Costantini et al., 2016), PEG (Daly et al., 2016b), PEGDA (Kang et al., 2017), PEDGA/cellulose (García-Lizarribar et al., 2018), and PEGMA/agarose (Daly et al., 2016a). In the same way, four hydrogels are composed by alginate and collagen with different components: gelatin (Bandyopadhyay et al., 2018), chitosan (Aydogdu et al., 2019), agarose (Yang et al., 2017), and gelatin/chitosan (Akkineni et al., 2016). Finally, other hydrogel is composed by alginate, hyaluronic acid, and cellulose (Nguyen et al., 2017). Despite the lack of good rheological properties of natural materials, alginate is one of the best natural polymer in rheology. Additionally, good biocompatibility and its facility to form reticular structures using Ca^{2+} ions have popularized its use in bioprinting (Lee and Mooney, 2012).

Gelatin is the second most used material with 26 papers. It is a component of hydrogels with other selected materials (17 papers) and with other combinations (7) mainly due to its poor rheological properties. Maybe for this reason, it is used alone in just two papers (Choi et al., 2018; Tijore et al., 2018b). In other studies, several modifications have been performed to enhance its properties. So, furfuryl-gelatin (f-gelatin) allows cross-linking with visible light (AnilKumar et al., 2019), but other studies combined with hyaluronic acid (Zhang K. et al., 2016; Shin et al., 2018; AnilKumar et al., 2019), GelMA (McBeth et al., 2017), cellulose (Xu X. et al., 2018), PEGDA (Aied et al., 2018), and PEG (Irvine et al., 2015). Additionally, it is also used in three-materials (Bandyopadhyay et al., 2018; Haring et al., 2019) and four-materials (Akkineni et al., 2016) hydrogels. Specifically, two important features of gelatin can be remarked: cellular adhesion, mainly due to presence of RGD (arginine-glycine-aspartate) sequences, and thermoresponsive behavior that sustains the use of gelatin as supporting material.

GelMA is the third material and the first synthetic one, compose by gelatin with methacrylated groups (Billiet et al., 2014). In general, GelMA has excellent rheological properties that improve printability, shape fidelity, and stability of the hydrogel due to UV photopolymerization of its methacrylated groups (Pepelanova et al., 2018). For this reason, modifications of this material are unusual and only Haring et al. (2019) modifieds GelMA with a dopamine molecule. Hence, it appears in 25 papers, it is combined with other selected material in 8 papers, used alone in othersix (Bertassoni et al., 2014; Billiet et al., 2014; Ersumo et al., 2016; Gu et al., 2018; Pepelanova et al., 2018; Zhou et al., 2019), with more than two of the selected materials, and used with other different materials in 5 papers. Alginate is the most common combination of GelMA appearing in 4, 3, and 2 papers for two-, three-, and four-material hydrogels, respectively (further details in the alginate section). Other common materials used with GelMA are hyaluronic acid (Schuurman et al., 2013; Noh et al., 2019), gelatin (McBeth et al., 2017), and collagen (Du et al., 2015). The rest of papers combines GelMA with pluronic (Levato et al., 2017; Suntornnond et al., 2017), carrageenan (Li et al., 2018b,c), gellan gum (Mouser et al., 2016), and polyisocyanide (PIC) (Celikkin et al., 2018).

Hyaluronic acid (HA) and its derived materials are quite used being the fourth material in the list with 16 papers. It is an anionic, non-sulfated glycosaminoglycan that is present in connective and neural tissues as well as it is one of the major components of the skin. For this reason, HA is mostly used in skin tissue engineering. It appears alone in five papers (Mouser et al., 2017; Stichler et al., 2017; Lee et al., 2018; Wang et al., 2018; Kiyotake et al., 2019). Furthermore, there are three studies that use HA combined with gelatin (Zhang K. et al., 2016; Shin et al., 2018; AnilKumar et al., 2019) but other authors use GelMA (Schuurman et al., 2013; Noh et al., 2019), alginate/cellulose (Law et al., 2018), and chitosan (Kim et al., 2019). This material is modified in half of the papers, obtaining: hyaluronic acid methacrylated (HAMA) (Costantini et al., 2016; Mouser et al., 2017), acrylated-HA and tyramine-conjugated HA (Lee et al., 2018), dopamine-conjugated HA (Haring et al., 2019), and thiol functionalized HA (Stichler et al., 2017). Concretely, HAMA provides great tunability for specific uses at different methacrylation degrees (Xia et al., 2017).

Cellulose is the following material with 15 papers. Cellulose fibers are obtained from natural resources and are widely used in bioprinting to improve mechanical properties of hydrogels. Depending on the polymerization degree, the length of its polymeric chain, hydrogels with cellulose can have from high tensile strength (long chains) to solubility properties (short chains). It is usually modified replacing some hydroxyl groups with methoxy groups forming methylcellulose. Specifically, cellulose is used alone in three papers (Béduer et al., 2018;

Cochis et al., 2018; Contessi Negrini et al., 2018). Additionally, it is combined with alginate (detailed above), gelatin (Xu X. et al., 2018), or hyaluronic acid (Law et al., 2018), being the two remaining papers combinations of alginate/cellulose with hyaluronic acid (Nguyen et al., 2017) and GelMA/PEGDA (García-Lizarribar et al., 2018).

Collagen is other popular material in bioprinting appearing in 12 papers that is the main component of the extracellular matrix, e.g., connective tissues as cartilage. In this review, collagen is used alone in four papers (Hartwell et al., 2016; Kim et al., 2016; Ren et al., 2016; Ahn et al., 2017)and appears in combination with alginate (Campbell et al., 2015), GelMA (Du et al., 2015), and agarose (Köpf et al., 2016). The rest of combinations with more material was described in previous sections.

Polyethylene glycol (PEG) and its derivatives PEG diacrylated (PEGDA) and PEG methacrylated (PEGMA) are used in the included studies in 6, 8, and 2 papers, respectively. PEG is a synthetic material formed by polymerization of ethylene oxide, highly valuable for its hydrophilicity that facilitates exchange of cell's nutrients and waste. Despite the fact that PEG is used alone in one paper with norbornene groups (Xin et al., 2019) and combined with gelatin (Irvine et al., 2015), and alginate/GelMA (Daly et al., 2016b) in other studies, It also appears with silk fibroin (Zheng et al., 2018), poly(N -(2-hydroxypropyl) methacrylamide lactate) methacrylated (pHPMA-lactate) (Censi et al., 2011), and polycaprolactone-diacrylated (PCL-DA) (Xu C. et al., 2018). It is important to note that PEG-derived materials allow hydrogel to be photo-crosslinked, which provides better mechanical stability after bioprinting. Specifically, PEGDA presents high hydrophilicity, a bioinert structure, and lack of toxic or immunogenic responses (Zalipsky and Harris, 1997). PEGDA is used alone (Schmieg et al., 2018) and combined with alginate (Yu et al., 2018) and gelatin (Aied et al., 2018). It also appears with alginate/GelMA (Kang et al., 2017) and with alginate/GelMA/cellulose (García-Lizarribar et al., 2018). Additionally, it is combined with gellan gum (Wu D. et al., 2018), carbomer hydrogel (Chen et al., 2019), and laponite (Peak et al., 2018). Finally, PEGMA is used in two papers, one of them with alginate and a modification of PEGMA that includes a fibrinogen molecule (Maiullari et al., 2018) and the other one with alginate/GelMA/agarose (Daly et al., 2016a).

Agarose is used in nine papers. According to its thermal behavior, it can be compared to gelatin. In this review, it is used alone (Duarte Campos et al., 2013), combined with alginate (Blaeser et al., 2013; López-Marcial et al., 2018), collagen (Köpf et al., 2016), alginate/collagen (Yang et al., 2017), collagen/chitosan (Campos et al., 2015), and alginate/GelMA/PEGMA (Daly et al., 2016a). Additionally, it also appears combined with Matrigel (Tijore et al., 2018a) and Poly(N-isopropylacrylamide) (PNIPAAM) (Bakirci et al., 2017).

Chitosan is the last material included in this detailed analysis with six papers. It is a natural-obtained and biodegradable polymer very similar to other extracellular matrix components that provides great cellular viability. However, its low mechanical properties and its slow gelation make chitosan a material rarely used alone. For this reason, to solve these poor mechanical properties it is usually combined with other materials as hyaluronic acid (Kim et al., 2019), alginate/collagen (Aydogdu et al., 2019), collagen/agarose (Campos et al., 2015), and alginate/gelatin/collagen (Akkineni et al., 2016). Chitosan also appears combined with silk (Zhang J. et al., 2018) and modified with hydroxybutil groups to improve its water solubility or with oxidized chondroitin sulfate to improve its mechanical properties (Li et al., 2019).

Finally, the last three papers use polycaprolactone (PCL) (Lin et al., 2016), a blend of polyurethane (PU), PCL, poly(L-lactic acid) (PLLA) and poly[D,L-lactic acid] (PDLLA) (Hsiao and Hsu, 2018), and Thixotropic Magnesium Phosphate-based gel (TMP-BG) (Chen et al., 2018). This last hydrogel is prepared mildly (gelling method) with inorganic compound and thixotropic features that obtains promising results.

Hydrogel Properties

Concentration

Maybe, concentration is the most important parameter of hydrogels for to reasons: to assure reproducibility of the experiment, and to increase printability of the hydrogel. The importance of this parameter is clear when 89.3% of all papers define the amount of each material present in the hydrogel mixture accurately. Most papers reveal researchers are trying to develop new materials/mixtures or modifying former hydrogels to get new specific properties.

In the material section, three mains polymers stand out over the rest: alginate, gelatin and GelMA (**Table 1**). Alginate is the most used component in hydrogel mixtures with 122 different concentrations in 52 different papers. In general, the most used concentration range is 2–4% w/v (35 papers). Specifically, the frequency of use for 2, 3, and 4% w/v of alginate is 15, 14, and 12 papers, respectively. The rest of concentration varies between 1% w/v (10 papers) and 5% w/v (7 papers). Although standard concentrations of alginate are up to 5% w/v, Markstedt et al. (2015) and Nguyen et al. (2017) use 10, 20, 30 and 40% w/v of alginate mixed with NFC and Aljohani et al. (2018) uses 18% w/v of alginate mixed with 4% w/v of gelatin and 12% w/v of agar. In summary, the range of concentration 2–4% gives alginate its better viscosity for bioprinting as it will be seen in the next section (He et al., 2016; Wu Y. et al., 2018).

Gelatin is the second material with 45 concentrations in 22 papers, but with heterogeneity of values. Concentrations are distributed in a range of 1–20%, being 5% w/v the most common value (5 papers) and 10% w/v (4 papers), or 15% w/v (2 papers) other common values. It is noted that gelatin provides good thermoresponsive properties to hydrogel, but its concentration is highly dependent on the bioink application.

Finally, there are a total of 43 concentrations of GelMA in 21 papers distributed from 1% up to 20% w/v, being the most usual 10% w/v (12 papers). This concentration is followed by 5% w/v (5 papers) and 1, 6, and 20% w/v (3 papers each). Overal, the most used concentrations are 2–4, 5, and 10% w/v for alginate, gelatin, and GelMA, respectively.

Viscosity

This parameter can be considered an important factor for hydrogel printability. As it is known, viscosity indicates fluidity

TABLE 1 | Concentrations of most used materials (alginate, GelMA, and gelatin).

Concentration (% w/v)										
Alginate			GelMA			Gelatin				
<2	2–4	>4	<6	6–10	>10	<10	10–15	>15	References
	•								Blaeser et al., 2013; Bakarich et al., 2014; Narayanan et al., 2016; Freeman and Kelly, 2017; Gao et al., 2017; Li et al., 2017; Schütz et al., 2017; Yang et al., 2017; Ahlfeld et al., 2018; Habib et al., 2018; Hafeez et al., 2018; He et al., 2018; López-Marcial et al., 2018; Maiullari et al., 2018; Naghieh et al., 2018; Gonzalez-Fernandez et al., 2019; Kosik-Kozioł et al., 2019
		•							Jia et al., 2014; Markstedt et al., 2015; Nguyen et al., 2017; Aljohani et al., 2018; Datta et al., 2018; Ooi et al., 2018; Yu et al., 2018; Ji et al., 2019; Yoon et al., 2019
						•			Zhang K. et al., 2016; Aied et al., 2018; Choi et al., 2018; Li et al., 2018a,c; Shin et al., 2018; Tijore et al., 2018a,b; Yan et al., 2018
				•					Schuurman et al., 2013; Bertassoni et al., 2014; Billiet et al., 2014; Costantini et al., 2016; Levato et al., 2017
	•			•					Daly et al., 2016a,b; Kosik-Kozioł et al., 2019; Zhou et al., 2019
	•	•							Gao et al., 2015; Kundu et al., 2015; Izadifar et al., 2016; Wu Y. et al., 2018
	•					•			Akkineni et al., 2016; He et al., 2016; Berg et al., 2018
			•						Suntornnond et al., 2017; Pepelanova et al., 2018; Haring et al., 2019
•									Aydogdu et al., 2019; Jeon et al., 2019
•	•								Khalil and Sun, 2009; Raddatz et al., 2018
		•				•			Wang et al., 2016; Giuseppe et al., 2017
				•	•				Ersumo et al., 2016; Gu et al., 2018
							•		Das et al., 2015; AnilKumar et al., 2019
•		•							Polley et al., 2017
•			•						Liu et al., 2018
•			•	•					Krishnamoorthy et al., 2019
•	•		•	•					Zhang X. et al., 2018
•						•	•		Ding et al., 2018
•	•						•		Chung et al., 2013
	•	•				•			Gao et al., 2018
•	•	•					•		Bandyopadhyay et al., 2018
	•							•	Ding et al., 2017
			•	•					Mouser et al., 2016
					•				Kang et al., 2017
			•				•		García-Lizarribar et al., 2018
								•	Li et al., 2018c

Dots shows concentration of these materials which applies in each reference.

and for this reason it is very important for hydrogel extrusion. So, the more the viscous, the more the inner pressure of hydrogel during the extrusion process and increased cell damage. Pepelanova et al. (2018) proposes shear-thinning hydrogels to get an easy filament deposition during the printing process and a high shape fidelity after printing (low shear stress). However, only 12.1% of analyzed papers details viscosity or perform rheological tests of hydrogels.

He et al. (2016) performs tests with a mixture of alginate/gelatin to established a "300–30,000 cps" as the optimum range of viscosities for this kind of hydrogels. Other tests performed by Campbell et al. (2015) with a mixture of collagen/alginate recommend a viscosity higher than "2,000 cps" to maintain shape fidelity. Raddatz et al. (2018) studies some alginate concentrations and their viscosities which vary from 13.5 mPa·s (0.5% w/v) to 2,156 mPa·s (4% w/v). As said before, these viscosities are obtained with the most used concentration of alginate. Hence, according to these range of concentrations that change viscosity of hydrogel, stiffness can be modified for a proper balance between good shape fidelity (harder hydrogels) and better printability (softer hydrogels). Finally, other authors show results of hydrogel behavior in graphics, but do not provide specific values of viscosity obtained from a rheological study of a non-Newtonian fluid (Jia et al., 2014; Das et al., 2015; Pepelanova et al., 2018; Aydogdu et al., 2019; Jeon et al., 2019).

Extrusion-Based Bioprinting

Bioprinting Parameters

Bioprinting parameters can be defined as those bioprinter settings (firmware inputs) needed to properly produce bioprinted

structures. In this sense, only a specific range of values are adequate for bioprinting and its selection is a key factor to obtain viable bioprinted structures. However, these values are highly dependent on the hydrogel composition, so they should be carefully selected in each case. An important feature of hydrogel is printability that was no analyzed in this review because it is rarely used (He et al., 2016; Gao et al., 2018). It is defined in three levels of meaning according to viscosity (shear thinning property), curation (cross-linking), and biofabrication window (range of bioprinting parameters) (He et al., 2016). Some objective metrics to measure printability and the printability window are *Pr* (He et al., 2016), extrudability, extrusion uniformity, and structural integrity (Gao et al., 2018), but only few papers used them. For this reason, the most relevant bioprinting parameters have been selected to be analyzed in this review: cartridge temperature, bed temperature, printing pressure and printing speed.

Cartridge temperature

In this review, cartridge temperature is defined as the internal temperature of the cartridge/printhead and it is inversely related to hydrogel viscosity. Thus, the higher the temperature, the lower the viscosity, inducing a less shear stress decreasing cell damage. Although we are using this terminology for better understanding, *printing temperature* it is commonly used in many papers to refer the same concept. Only 45% of all the analyzed papers indicate their cartridge temperature. In this sense, up to 65 papers lack this critical parameter in its methodology. We grouped papers in five different ranges: below 20, 20–30, 30–40, above 40°C, and room temperature.

The most usual range of cartridge temperature is 30–40°C with 20 papers that use cell-laden hydrogels. In this sense, this range is focused on cells incubation temperature (37°C) together with those materials that can be used with this temperature, such as alginate, gelatin, agarose, or GelMA (13 papers) (Schuurman et al., 2013; Du et al., 2015; Fan et al., 2016; He et al., 2016; Narayanan et al., 2016; Giuseppe et al., 2017; Hafeez et al., 2018; López-Marcial et al., 2018; Pepelanova et al., 2018; Raddatz et al., 2018; Wu D. et al., 2018; Haring et al., 2019). The remaining papers use 30°C (Suntornnond et al., 2017), 35°C (Aljohani et al., 2018; Noh et al., 2019), 36°C (Blaeser et al., 2013), 38°C (Campos et al., 2015), 39°C (Blaeser et al., 2013), 40°C (Jia et al., 2014), and a range of 35–37°C (Wang et al., 2016).

On the other hand, the range of 20–30°C appears in 12 papers (Bakarich et al., 2014; Das et al., 2015; Irvine et al., 2015; Kosik-Kozioł et al., 2017; Bandyopadhyay et al., 2018; Berg et al., 2018; Cochis et al., 2018; Contessi Negrini et al., 2018; Datta et al., 2018; Gao et al., 2018; Li et al., 2018b,c; Naghieh et al., 2018). Furthermore, temperatures below 20°C are used in eight papers (Izadifar et al., 2016; Ren et al., 2016; Zhang K. et al., 2016; Celikkin et al., 2018; Gu et al., 2018; Law et al., 2018; Li et al., 2018c; Yan et al., 2018). The range above 40°C uses synthetic hydrogels with post-printing cell addition at 93°C for PCL (Stichler et al., 2017) and at 250°C for PNIPAAM polymers (Bakirci et al., 2017). However, Costantini et al. (2016) is the only author that use a *low temperature* without a specific value.

Other authors define cartridge temperature as room temperature. In our opinion, this definition can lead to misunderstandings due to the existence of different regulatory frameworks for this concept (e.g., 20–25°C for the USP-NF or 15–25°C for the European Pharmacopeia). In this review, there are 6 papers that use room temperature for their cartridge temperature (Chung et al., 2013; Kundu et al., 2015; Li et al., 2017; Zheng et al., 2018; AnilKumar et al., 2019; Ji et al., 2019). Hence, this indistinct setting of temperatures makes reproducibility of their experiments difficult, since small variations of this parameter can significantly modify the hydrogel behavior during the extrusion process as commented by Mouser et al. (2016).

Some other studies use more than one temperature or an extra wide range of temperatures that do not fit in our selected ranges. First, Mouser et al. (2016) used from 15 to 37°C in different tests to obtain the yield stress for each concentration or temperature of its GelMA/gellan gum hydrogel. Second, Daly et al. (2016a) uses 37/28/21/21°C for each component of an agarose/GelMA/alginate/PEGMA hydrogel, respectively. Third, Xu X. et al. (2018) uses from 4 to 30°C to variate viscosity of a gelatin/oxidized nanocellulose hydrogel. And finally, Mouser et al. (2017) uses 37° and 80°C for each component of a HAMA/PCL hydrogel.

Bed temperature

Although bed temperature can suppose a thermal shock for hydrogels and cells when high differences between bed and cartridge temperature are present, only 33 papers define this parameter in their studies. This means that most of the authors consider this information non-relevant. The temperature range is wide open from −80°C to more than 70°C. There are also five studies that defined bed temperature as room temperature (Kundu et al., 2015; Giuseppe et al., 2017; Li et al., 2017; Raddatz et al., 2018; AnilKumar et al., 2019). As said before, this indistinct temperature definition must be avoided. Specifically, Raddatz et al. (2018) sets a maximum temperature of 40°C although they use room temperature. In order to categorize this parameter, we grouped papers in five different ranges: below 0, 0–20, 20–30, 30–40, and above 40°C. According to this, there are two temperature ranges widely used: 0–20°C (9 papers) (Jia et al., 2014; Das et al., 2015; He et al., 2016; Köpf et al., 2016; Ren et al., 2016; Wang et al., 2016; Li et al., 2017, 2018c; Gu et al., 2018; Xu X. et al., 2018) and 30–40°C, being 37°C the most used temperature (5 papers) (Duarte Campos et al., 2013; Fan et al., 2016; Lin et al., 2016; Narayanan et al., 2016; Law et al., 2018), while Celikkin et al. (2018) uses 37 and 40°C, and the rest uses one temperature between this range (3 papers) (Bakirci et al., 2017; Mouser et al., 2017; Noh et al., 2019). Other bed temperature ranges are less commonly used: 20–30°C (5 papers) (Billiet et al., 2014; Ding et al., 2017, 2018; Contessi Negrini et al., 2018; Wu D. et al., 2018), below 0°C (2 papers) (Béduer et al., 2018; Choi et al., 2018), and above 40°C (2 papers) (Daly et al., 2016a,b). On the other hand, some extreme values of the whole range are used by Béduer et al. (2018) with carboxymethylcellulose hydrogel (−80°C) and Daly

et al. (2016a) with a mixture of agarose/alginate/GelMA/PEGMA hydrogel (70°C).

In order to understand the importance of heating systems, Ahn et al. (2017) perform some interesting experiments that include not only a heated bed, but even an upper heated system over the nozzle. Specifically, they use a 23°C non-heated bed, a 30°C heated bed, a 32°C upper heating system, and a 36°C heated bed with upper heating system. These results are quite interesting, mainly because they enhance the importance of bed temperature, but additionally they propose a broad heated printing volume that can be controlled using a closed chamber or a specific heating system. They conclude that non-heated bed obtains the worst shape fidelity, but a combination of heated bed with upper heated system improved the shape fidelity of the bioprinted structures and got the best results in its experiments.

Printing pressure

Many authors (55) do not inform about printing pressure used during their experiments or use the indistinct term *low pressure* (Maiullari et al., 2018). From our point of view, this parameter is critical for a proper management of live cells during bioprinting. Additionally, it is important to note that there is no pressure unit defined for bioprinting. Although most studies use Pa, other studies use bar, psi, N/mm^2 (Narayanan et al., 2016) or mTorr (Bakirci et al., 2017) units. In order to compare all the papers, all units were converted to SI (kPa) in this review.

Some authors use several pressures in their studies, so 127 different printing pressures were obtained. **Table 2** shows these printing pressures grouped into ten different ranges: below 60, 60, 60–100, 100, 100–200, 200, 200–300, 300, 300–1,000, and above 1,000 kPa. All pressures vary between $5{\cdot}10^{-4}$ and $4.7{\cdot}10^{5}$ kPa, but the most used range is from $5{\cdot}10^{-4}$ to 400 kPa (103 entries).

Almost all pressures in the range of 400–1,000 kPa are used with alginate (Li et al., 2017; López-Marcial et al., 2018), GelMA (Schuurman et al., 2013; Billiet et al., 2014; Ersumo et al., 2016; Suntornnond et al., 2017), or hyaluronic acid (Ji et al., 2019). However, the highest pressures are used in some specific materials, such as PCL/PLCL (650, 760, and 800 kPa) (Kundu et al., 2015; Izadifar et al., 2016; Zhang K. et al., 2016), or chemically-derived chitosan (600 and 700 kPa) (Li et al., 2019).

Finally, Aljohani et al. (2018) use 0.5 and 1 Pa for a gelatin/alginate/agar hydrogel. This is a very low pressure compared with the rest of papers (>5 kPa). On the other hand, Narayanan et al. (2016) use a cell-laden alginate/PLA hydrogel at 2,000 kPa, while Wei et al. (2019) use 2.2, 2.8, 4.3, and $4.7{\cdot}10^{5}$ kPa to print an alginate hydrogel with post-printing cell addition. It is important to note that those ranges of pressure are far away from commonly used with alginate hydrogels (10–300 kPa). However, printing pressure is no longer a critical parameter of bioprinting using post-printing cell addition. In cell laden bioprinting the pressure ranges are in accordance to cellular viability, where the data obtained corroborate this affirmation. In all papers in which there are values of printing pressure and viability, 75.3% of pressure values have a viability over 80%.

Printing speed

Printing speed (X-Y movement) is important because it is directly related with the total bioprinting time. Additionally, extrusion-based controls the hydrogel flow (filament width) using mainly printing speed and printing pressure. So, printing speed appears in 65 papers with 87 different velocities that vary from 0.2 to 150 mm/s. By taking a closer look, 91% of values are in the range of 1–30 mm/s where 57% of speeds are below 10 mm/s. In fact, the most used speed is 10 mm/s (13 entries) (Kim et al., 2016; Wang et al., 2016; Nguyen et al., 2017; Ahlfeld et al., 2018;

TABLE 2 | Pressure ranges for all papers that studied this setting parameter.

Range	References
<60 kPa	Chung et al., 2013; Irvine et al., 2015; Kundu et al., 2015; Markstedt et al., 2015; He et al., 2016; Izadifar et al., 2016; Lin et al., 2016; Bakirci et al., 2017; Levato et al., 2017; Li et al., 2017, 2018a; Nguyen et al., 2017; Aljohani et al., 2018; Berg et al., 2018; Celikkin et al., 2018; Habib et al., 2018; Naghieh et al., 2018; Pepelanova et al., 2018; Raddatz et al., 2018; Wu Y. et al., 2018; Zhang J. et al., 2018; AnilKumar et al., 2019; Haring et al., 2019; Kiyotake et al., 2019
60 kPa	Bakarich et al., 2014; Daly et al., 2016a; Lin et al., 2016; Zhang K. et al., 2016; Ahn et al., 2017; Gao et al., 2018; Li et al., 2018a,c; Yan et al., 2018
60–100 kPa	Bakarich et al., 2014; Schütz et al., 2017; Gao et al., 2018; Gu et al., 2018; Li et al., 2018b,c; Raddatz et al., 2018; Zhang J. et al., 2018; Haring et al., 2019
100 kPa	Irvine et al., 2015; Kosik-Kozioł et al., 2017; Mouser et al., 2017; Schütz et al., 2017; Li et al., 2018a,c; Tijore et al., 2018b; Gonzalez-Fernandez et al., 2019; Krishnamoorthy et al., 2019; Zhou et al., 2019
100–200 kPa	Khalil and Sun, 2009; Daly et al., 2016a; Kim et al., 2016; Giuseppe et al., 2017; Levato et al., 2017; Ahlfeld et al., 2018; Gu et al., 2018; Hafeez et al., 2018; Li et al., 2018c; Wu Y. et al., 2018; Ji et al., 2019; Kiyotake et al., 2019; Noh et al., 2019
200 kPa	Das et al., 2015; Daly et al., 2016a,b; Wang et al., 2016; Ahlfeld et al., 2018; Chen et al., 2018; Law et al., 2018; Gonzalez-Fernandez et al., 2019; Zhou et al., 2019
200–300 kPa	Das et al., 2015; Ahlfeld et al., 2018; Li et al., 2018c; Schmieg et al., 2018; Yu et al., 2018; Ji et al., 2019
300 kPa	Kim et al., 2016; Wang et al., 2016; Mouser et al., 2017; Stichler et al., 2017; Suntornnond et al., 2017; Yu et al., 2018
300–1,000 kPa	Schuurman et al., 2013; Billiet et al., 2014; Kundu et al., 2015; Ersumo et al., 2016; Izadifar et al., 2016; Zhang K. et al., 2016; Li et al., 2017, 2019; Suntornnond et al., 2017; López-Marcial et al., 2018; Ji et al., 2019
>1,000 kPa	Narayanan et al., 2016; Wei et al., 2019

Tijore et al., 2018b; Wu D. et al., 2018; Yan et al., 2018; Zhang J. et al., 2018; Ji et al., 2019; Kiyotake et al., 2019; Krishnamoorthy et al., 2019; Xin et al., 2019) followed by 5 mm/s (10 entries) (Bakarich et al., 2014; Campbell et al., 2015; Irvine et al., 2015; Markstedt et al., 2015; Narayanan et al., 2016; Giuseppe et al., 2017; Stichler et al., 2017; Habib et al., 2018; Xu X. et al., 2018). There is a printing speed that stands out because of its high value. It is used by Gao et al. (2018) with gelatin/alginate hydrogels at 150 mm/s.

Cross-Linking Methods

Cross-linking is usually a post-printing procedure that consists of the modification of the internal structure of the printed hydrogel to harden it and to achieve the expected mechanical properties of the bioprinted structure. It can be performed in three different ways depending on its reaction trigger: thermal (controlled by temperatures changes), chemical (controlled by the addition of reacting agents), or physical (triggered by physical procedures, usually UV light). In this sense, hydrogel composition determines the cross-linking type to use. It is a critical part in bioprinting process and surprisingly almost all authors define perfectly the materials and their protocols. Only Duarte Campos et al. (2013), Ahn et al. (2017), Contessi Negrini et al. (2018), Li et al. (2018a, 2019), Zhang J. et al. (2018) do not use any type of cross-linking. **Figure 7** shows all cross-linking methods of the three most used materials: alginate, gelatin, and GelMA with its combinations. Additionally, **Table 3** summarizes all analyzed studies with these three materials.

Thermal cross-linking is commonly used in gelatin or agarose hydrogels (16 papers). From those 16 papers, six of them perform cross-linking at 37°C (Ren et al., 2016; McBeth et al., 2017; Law et al., 2018; Tijore et al., 2018a,b; Zheng et al., 2018) and three use room temperature (Köpf et al., 2016; Lin et al., 2016; Berg et al., 2018). The rest use thermal cross-linking without specifying temperature (Fan et al., 2016; Giuseppe et al., 2017; Bandyopadhyay et al., 2018; Chen et al., 2018; Cochis et al., 2018; Xu X. et al., 2018). On the other hand, in alginate/gelatin hydrogels Berg et al. (2018) uses room temperature, He et al. (2016) uses a cool substrate, and Bandyopadhyay et al. (2018) and Giuseppe et al. (2017) use thermal cross-linking but without specific temperature. For gelatin hydrogels Blaeser et al. (2013) and Tijore et al. (2018a) use 37°C for thermal cross-linking and Xu X. et al. (2018) do not give any detail on how the thermal cross-linking performs.

Chemical cross-linking is commonly used to harden alginate, chitosan, or gelatin, but it is used with other materials too (69 papers). In general, solution with Ca^{2+} cations are used to trigger the cross-linking reaction. In this sense, 49 out of 69 papers utilize different concentrations of $CaCl_2$ solution to perform the chemical cross-linking. Concentrations vary from 10 mM to 0.5 M or from 1 to 10% w/v. However, other Ca^{2+} solutes are used to perform chemical cross-linking. Specifically, Gao et al. (2018) uses $CaSO_4$ or Wei et al. (2019), and Kundu et al. (2015) use $NaCl_2$, also Freeman and Kelly (2017) uses $CaCO_3$ and $CaSO_4$. Although exposition time of the cross-linking agent is quite relevant, its definition is infrequent and, in some cases, highly different. So, Ahlfeld et al. (2018) uses 10 min while Raddatz et al. (2018) uses a 30 s mist. In order to clarify this issue for alginate Naghieh et al. (2018) performs an analysis of the cross-linking effect of $CaCl_2$ at 0, 2, 4, and 24 h of exposure time. Chemical cross-linking is mostly done to alginate (52 papers) with $CaCl_2$ solution (46 papers), and detailed concentrations can be seen in **Figure 6**. Other (non-Ca^{2+}) solutions are used in two papers (Hafeez et al., 2018; Aydogdu et al., 2019) which use hydrazine and NaOH, respectively, and other two studies do not provide information (Aljohani et al., 2018; Yoon et al., 2019). Other specific cross-linking agents are genipin (Akkineni et al., 2016; Kim et al., 2016), mTgase (Tijore et al., 2018b) or 1-ethyl-3-(3-dimethylaminopropyl)-carbodiimide hydrochloride (EDC) and N-hydroxysuccinimide (NHS) (Choi et al., 2018), and MAL-PEG-MAL (Yan et al., 2018) for gelatin, or different solute for other materials like thrombin (Zhang K. et al., 2016), mushroom tyrosinase (Das et al., 2015), and oxidative reactions (Shin et al., 2018).

Finally, physical cross-linking is usually performed with the exposure of the bioprinted structures to UV light. In this sense, GelMA is the most used material with this kind of cross-linking, but all materials modified with methacrylated groups can be photo-crosslinked, such as HAMA, AlgMA or PEGMA. Among all papers (41) with this kind of cross-linking, only two of them do not use UV: AnilKumar et al. (2019) that use visible light with Rose Bengal and Riboflavin as photoinitiatorand Das et al. (2015) that use sonication procedures. In general, physical cross-linking needs a photoinitiator that triggers the reaction and some usually agents are Irgacure D-2959 or Lithium phenyl-2,4,6-trimethylbenzoylphosphinate (LAP). The most used UV wavelength is 365 nm (18 papers) followed by 405 nm (3 papers) and 312 nm (1 paper). On the other hand, Mouser et al. (2017) and Bertassoni et al. (2014) use 300–600 and 360–480 nm wavelength ranges instead of specific values, respectively. Also, Celikkin et al. (2018) use physical cross-linking without giving any kind of information. An important caution with physical cross-linking is the UV radiation effects on cells that depends mainly on wavelength and exposure time. In this sense, in 14 papers there is not information of the used wavelength. **Table 3** shows that most of physical cross-linking is made to GelMA (24 papers), three papers perform physical cross-linking to alginate (Ooi et al., 2018; Jeon et al., 2019; Ji et al., 2019) and one paper use it with gelatin (AnilKumar et al., 2019). Finally, UV light power is used in a range from 2 mW to 6 W, while the exposure time varies from 10 s to 30 min.

Post-printing Tests

Cellular Tests

Currently, cellular viability is one of the most common features to assess bioprinted structures that must be used on patients or drug testing. Here, post-printing analysis are focused on cellular and mechanical tests, but several biological measures appear during this review: gene expression (25 papers) that is usually related to cellular differentiation, and cell morphology (51 papers) that controls qualitatively cell shape or clustering.

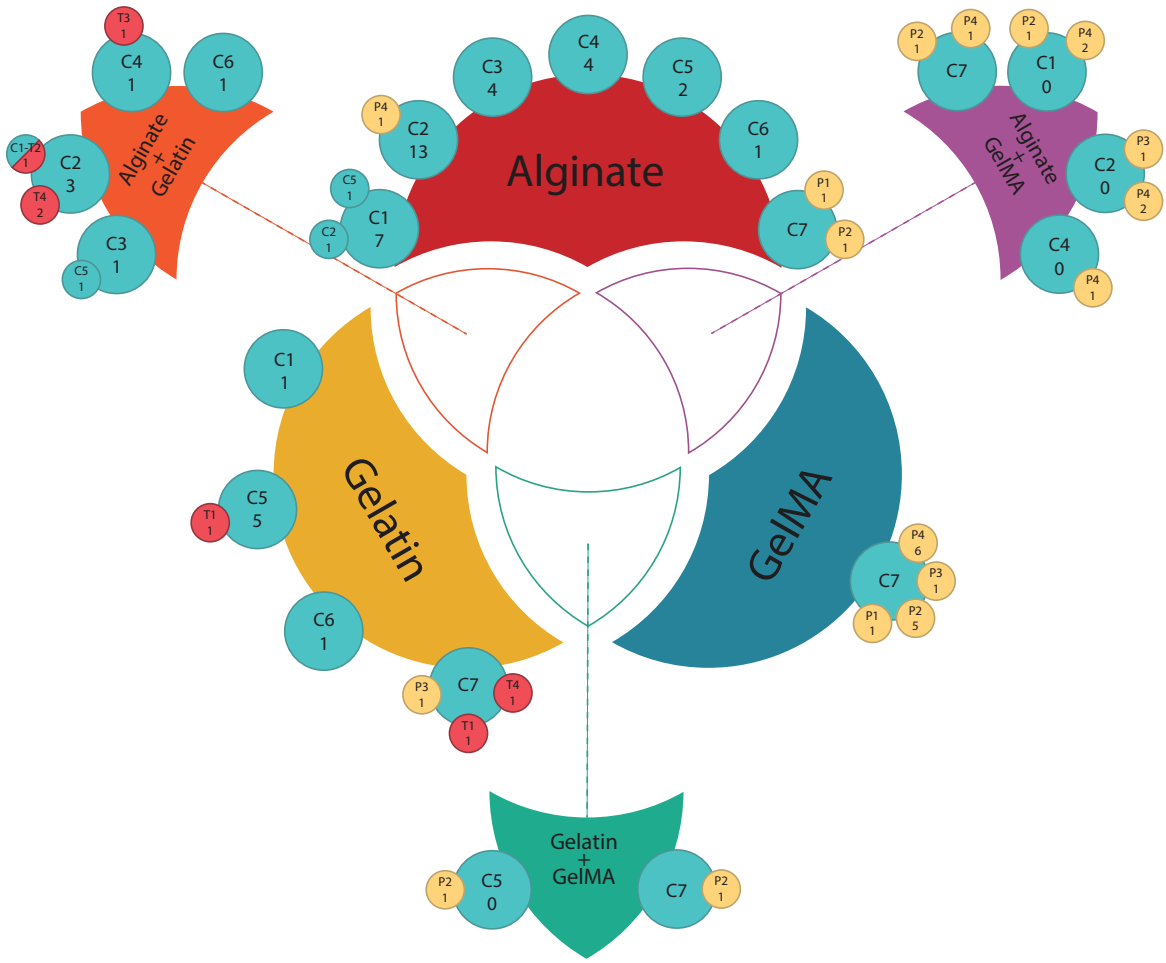

FIGURE 7 | Cross-linking used for the three most common materials and its combinations. Blue, yellow, and red circles represent chemical, physical and thermal cross-linking, respectively. Superposed circles indicate that two cross-linking classifications have been combined. Each circle contains a classification codification (upper code) and the number of papers for the corresponding code combination (lower number). Chemical cross-linking has been chosen as primary classification, therefore papers not using it have been codified under C7 for graphical representation purposes and no papers are allocated to this code alone, e.g., alginate C2/13 – P4/1 (blue and yellow circles superposed) indicates that 13 papers used C2 ([100–500] mM Ca^{2+} solution) to cross-link alginate and another paper used C2 and P4 (UV light—no data of wavelength) to perform the cross-linking.

TABLE 3 | The three most used materials (alginate, gelatin, GelMA, and its combinations in pairs) with its different cross-linking methods.

Material	Chemical	Physical	Thermal	References
Alginate	C1			Campbell et al., 2015; Markstedt et al., 2015; Narayanan et al., 2016; Freeman and Kelly, 2017; Naghieh et al., 2018; Wu Y. et al., 2018
	C1/C2			Khalil and Sun, 2009
	C1/C5			Kundu et al., 2015
	C2			Jia et al., 2014; Izadifar et al., 2016; Apelgren et al., 2017; Kosik-Kozioł et al., 2017; Nguyen et al., 2017; Polley et al., 2017; Schütz et al., 2017; Ahlfeld et al., 2018; Habib et al., 2018; He et al., 2018; Maiullari et al., 2018; Yu et al., 2018; Gonzalez-Fernandez et al., 2019
		P4		Jeon et al., 2019
	C3			Yang et al., 2017; Datta et al., 2018; Gao et al., 2018; Raddatz et al., 2018
	C4			Bakarich et al., 2014; Gao et al., 2015, 2017; Li et al., 2017
	C5			Hafeez et al., 2018; Aydogdu et al., 2019; Wei et al., 2019
	C6			Yoon et al., 2019
	C7	P1		Ji et al., 2019
		P2		Ooi et al., 2018
Gelatin	C1			Yan et al., 2018
	C5			Irvine et al., 2015; Choi et al., 2018
			T1	Tijore et al., 2018b
	C6			Shin et al., 2018
	C7	P3		AnilKumar et al., 2019
			T1	Tijore et al., 2018a
			T4	Xu X. et al., 2018
GelMA	C7	P1		Ersumo et al., 2016
		P2		Schuurman et al., 2013; Mouser et al., 2016; Levato et al., 2017; Celikkin et al., 2018; Zhou et al., 2019
		P3		Bertassoni et al., 2014
		P4		Billiet et al., 2014; Du et al., 2015; Suntornnond et al., 2017; Gu et al., 2018; Li et al., 2018cb; Pepelanova et al., 2018
Alginate Gelatin	C2			Wang et al., 2016; Ding et al., 2017, 2018
			T4	Giuseppe et al., 2017; Bandyopadhyay et al., 2018
	C2/C1		T2	Berg et al., 2018
	C3			Li et al., 2018c
	C3/C5			Akkineni et al., 2016
	C4			Chung et al., 2013
			T3	He et al., 2016
	C6			Aljohani et al., 2018
Alginate GelMA	C1	P2		Daly et al., 2016b
		P4		Daly et al., 2016a; Liu et al., 2018

(Continued)

TABLE 3 | Continued

Material	Chemical	Physical	Thermal	References
	C2	P3		Zhang X. et al., 2018
		P4		Kosik-Kozioł et al., 2019; Krishnamoorthy et al., 2019
	C4	P4		Costantini et al., 2016
	C7	P2		Kang et al., 2017
		P4		García-Lizarribar et al., 2018
Gelatin GelMA	C5	P2		Haring et al., 2019
	C8	P2		McBeth et al., 2017

Codification is at follows: C for Chemical crosslinking: C1: <100 mM Ca^{2+} solution, C2: [100–500] mM Ca^{2+} solution, C3: ≥500 mM Ca^{2+} solution, C4: Not given concentration of Ca^{2+} solution, C5: Other solute solution, C6: No available details for chemical crosslinking, and C7: No chemical crosslinking. P for Physical crosslinking: P1: 405 nm UV light, P2: 365 nm UV light, P3: UV light (special wavelength), P4: UV light (no data of wavelength). T for Thermal Crosslinking: T1: 37 °C, T2: Room temperature, T3: Special temperature, T4: no available details of thermal crosslinking.

On the one hand, the most of gene expression studies used osteogenic- and chondrogenic-related markers such as cartilage formation genes (12 papers): ACAN (aggrecan), COL1, COL2, COL10 (collagen type I, II, X), or SOX-9. On the other hand, 37 papers conclude that there no morphological differences after bioprinting in comparison to a 2D culture and 19 papers clarify that the increasing of the stiffness, due to the increasing of the viscosity and concentration of the material or modifications of crosslinking parameters, tend cells to adopt a round shape losing its functionality (Prasad and Alizadeh, 2019). In this sense, two kinds of tests are commonly performed to determine the live/dead proportion of cells (viability tests) and its metabolic activity (metabolic tests). **Table 4** compiles cellular tests grouped in these two categories, including reagents and techniques.

In total, 19 Live/Dead assay kits to measure the viability of bioprinted structures have been used, but none of these kits mention its composition. So, we could not perform any kind of analysis in this category. On the other hand, calcein AM has been used in 60 papers for staining alive cells and in combination with two complementary compounds: Ethidium homodimer (37 papers) or propidium iodide (23 papers) as an orange-red and red stain for dead cells, respectively (see **Table 4**). Additionally, propidium iodide also appears alone as viability cell marker in 10 papers, combined with fluorescein diacetate in four papers (Blaeser et al., 2013; Campbell et al., 2015; Campos et al., 2015; Jeon et al., 2019), combined with acridine orange (2 papers) (Lin et al., 2016; Kosik-Kozioł et al., 2017), and combined with other unspecified agents (4 papers) (Duarte Campos et al., 2013; Köpf et al., 2016; Giuseppe et al., 2017; Law et al., 2018). Alamar blue is a cellular viability reagent used in eight papers for staining living cells in blue color with metabolic reduction (O'Brien et al., 2000). Another test used is the trypan blue exclusion test (Béduer et al., 2018) that only stain cells with altered cell membrane, marking dead cells. It is measured as the ratio of non-stained to total cells by optical microscopy. Finally, Hoechst 33342 is a fluorescence probe that binds to the nucleus of alive cells (AnilKumar et al., 2019).

According to metabolic tests, authors measure the metabolic activity with CCK-8 (Cell Counting Kit-8) in 3 papers and MTT (3-(4,5-dimethylthiazol-2-yl)-2,5-diphenyltetrazolium bromide) in other 3 papers. CCK-8 is a colorimetric assay where intracellular dehydrogenase activity produces the soluble substrate orange formazan, while MTT is transformed in a purple insoluble salt by living cells. Also, PET (Positron Emission Tomography) measurement was made by Polley et al. (2017) with the addition of ^{18}F-2-Fluor-2-deoxy-D-glucose ([^{18}F]-FDG) tracer to check cell activity in volumetric geometries.

Although several studies present results of specific gene expression, cellular differentiation, or morphology, we have focused our interest in viability results. To do this, five different groups according to periods of viability measurements are established: at 0- (just after printing), 1-, 3-, 7-, and 21-days. However, data heterogeneity does not allow a statistical inference. It is important to note that comparison among studies could be relatively unfair due to many different conditions, such as: variations in bioprinted structures (grid, tubular scaffolds, discs,…), different cell lines survival characteristics (fibroblast vs. HUVECs), different measure periods (e.g., 2, 11, or 28 days), or different assay kits. **Table 5** shows papers (97) that study cellular viability including material, cell type and viability. According to our analysis, the total number of papers for each group is the following: 36 papers for *0-day*, 37 papers for *1-day*, 25 papers for *3-days*, 35 papers for *7-days,* and 24 papers for *21-days*. However, some papers' time points did not fit in our five groups, and they have been grouped in the closet category as follows: 0-day and 1-day groups fit perfectly but in 3-, 7-, and 21-day are counted from 2 to 4, 5 to 11 and 12 to 28 days, respectively. In this sense, 0-, 1-, and 7-days groups are the most used by authors, although only few of them use all groups in their studies (Izadifar et al., 2016; Li et al., 2018c).

As mentioned before, heterogeneity of studies (different materials, cross-linking methods, temperatures, and cell lines, among others) diminishes importance of mean viability (82.70%) obtained at *0-day*. Maybe, a detailed analysis of viability by materials or cell lines could be significant, reducing the

variability. For this reason, the three most used materials (alginate, gelatin, and GelMA) and two of their combinations (alginate with GelMA, and alginate with gelatin) have been selected in **Figure 8** to compare their viabilities. Results show that most of the mean cellular viabilities are up to 80% with a *0-day* mean viability over 83%. This could indicate that cellular viability just after printing, has been partly sorted out. After that, *1-day* viability decreases in most cases, being more accused in the alginate-GelMA combination (58.50% from 83.05%) with the most important exception of gelatin that increases (94.90% from 74.60%). Maybe, this decreasing trend could be due to nutritional or environmental conditions of cells during this first stage. In this sense, during these first hours after the bioprinting process, cells must adapt to a new environment which in some cases, stops their growth while other provoke their death. After this stressing period, *3-days* group usually increases its cell viability, showing an adaptation to the new material in which they are embedded. Moreover, similar trend is found in *7-days* group. Finally, after *21-days* every material behaves in its own way, in GelMA and alginate/gelatin cellular viability continue its increase, while in alginate, gelatin and alginate/GelMA decrease. On the contrary, gelatin startes with a very high viability at *0-* and *1-day*, but after *3-days* decreases, reaching its minimal *21-days* later. It is noticeable that GelMA shows the best cellular viability, despite the fact that it is supposed to have the worst one even though it is synthetic (Abelardo, 2018).

Cell line depends mostly on the kind of tissue that wants to be replicated, but previous experience of authors can be a

TABLE 4 | Cellular tests carried out in the included studies.

Test type	Components		References
Viability tests	Calcein AM Green (live)	Ethidium homodimer (37) Orange-Red (dead)	Bertassoni et al., 2014; Das et al., 2015; Gao et al., 2015; Kundu et al., 2015; Akkineni et al., 2016; Daly et al., 2016a; Ersumo et al., 2016; Hartwell et al., 2016; Izadifar et al., 2016; Kim et al., 2016, 2019; Narayanan et al., 2016; Zhang K. et al., 2016; Ahn et al., 2017; Freeman and Kelly, 2017; Kang et al., 2017; Levato et al., 2017; Schütz et al., 2017; Stichler et al., 2017; Ahlfeld et al., 2018; Aied et al., 2018; Bandyopadhyay et al., 2018; Berg et al., 2018; Hafeez et al., 2018; Maiullari et al., 2018; Ooi et al., 2018; Shin et al., 2018; Wang et al., 2018; Wu Y. et al., 2018; Xu C. et al., 2018; Yan et al., 2018; Gonzalez-Fernandez et al., 2019; Ji et al., 2019; Kiyotake et al., 2019; Krishnamoorthy et al., 2019; Noh et al., 2019; Yoon et al., 2019
		Propidium iodide (23) Red (dead)	Chung et al., 2013; Billiet et al., 2014; Du et al., 2015; He et al., 2016, 2018; Ren et al., 2016; Wang et al., 2016; Bakirci et al., 2017; Li et al., 2017, 2018a,b; Ding et al., 2017, 2018; Gao et al., 2017; Suntornnond et al., 2017; Yang et al., 2017; Chen et al., 2018, 2019; Contessi Negrini et al., 2018; Gu et al., 2018; Pepelanova et al., 2018; Raddatz et al., 2018; Li et al., 2019
	Live/Dead assay kit* (19) Green/red (live/dead)		Censi et al., 2011; Schuurman et al., 2013; Jia et al., 2014; Markstedt et al., 2015; Costantini et al., 2016; Daly et al., 2016b; Fan et al., 2016; Nguyen et al., 2017; Aljohani et al., 2018; Habib et al., 2018; Lee et al., 2018; Li et al., 2018c; Liu et al., 2018; López-Marcial et al., 2018; Wu D. et al., 2018; Zhang X. et al., 2018; Kosik-Kozioł et al., 2019; Xin et al., 2019; Zhou et al., 2019
	Propidium Iodide** (10) Red (dead)		Blaeser et al., 2013; Duarte Campos et al., 2013; Campbell et al., 2015; Campos et al., 2015; Köpf et al., 2016; Lin et al., 2016; Giuseppe et al., 2017; Kosik-Kozioł et al., 2017; Law et al., 2018; Jeon et al., 2019
	Alamar blue (8) Blue (live)		Khalil and Sun, 2009; Irvine et al., 2015; Cochis et al., 2018; García-Lizarribar et al., 2018; Tijore et al., 2018a,b; Zheng et al., 2018; Haring et al., 2019
	Trypan blue (1) Blue (dead)		Béduer et al., 2018
	Hoechst 33342 (1) Blue (live)		AnilKumar et al., 2019
Metabolic tests	CCK8 (3) Orange (cell activity)		Hsiao and Hsu, 2018; Xu X. et al., 2018; Yu et al., 2018
	MTT (3) Purple (cell activity)		Datta et al., 2018; Zhang J. et al., 2018; Aydogdu et al., 2019
	PET activity (1)		Polley et al., 2017

(*) Unknown agents, commercial kits, (**) Different agents: Acridine orange, Fluorescein diacetate or unknown agent.

TABLE 5 | Cell type with its viability grouped according to materials used in five categories (from 0 to 21 days) and expressed in percentage of cells survival.

	Cell type	Cell viability (%)					References	Cell type	Cell viability (%)					References
		0 d	1 d	3 d	7 d	21 d			0 d	1 d	3 d	7 d	21 d	
Alginate	Chondrocytes					79.00	Yang et al., 2017	MSCs		61.00			78.50	Schütz et al., 2017
		90.50					Kundu et al., 2015			85.02				Freeman and Kelly, 2017
		83.30		82.00	80.66	80.30	Kosik-Kozioł et al., 2017		71.50					Gonzalez-Fernandez et al., 2019
		72.00			85.00		Markstedt et al., 2015			88.50	86.00			Ji et al., 2019
		93.00			97.00	93.00	López-Marcial et al., 2018	HUVECs	91.00	93.00				He et al., 2018
	L929	94.00		97.00	95.00		Li et al., 2017		80.00			78.00	90.00	Maiullari et al., 2018
			97.80	95.10	91.40		Gao et al., 2017			97.00	98.00			Campbell et al., 2015
			92.90	84.70	67.10		Gao et al., 2015	ADMSC		37.50	79.00	87.50	68.50	Narayanan et al., 2016
			87.00		86.50		Ooi et al., 2018	ATDC5	85.00	82.50	82.50	82.50	87.50	Izadifar et al., 2016
		96.00	96.00	98.00	97.00		Blaeser et al., 2013	BxPC3		46.50		59.50	82.50	Habib et al., 2018
	3T3	69.00	60.00	54.21			Wu Y. et al., 2018							
		*Khalil and Sun, 2009; Jia et al., 2014; Nguyen et al., 2017; Ahlfeld et al., 2018; Hafeez et al., 2018; Raddatz et al., 2018; Jeon et al., 2019; Yoon et al., 2019												
Gelatin	HUVECs	34.60		57.60			Irvine et al., 2015	NIH3T3	95.90					Shin et al., 2018
	C2C12	93.30				69.60	Li et al., 2018ca	Bladder Ucs		93.80	78.90	81.40		Zhang K. et al., 2016
	hTMSCs		96.00		95.00	90.00	Das et al., 2015							
		*Aied et al., 2018; Tijore et al., 2018a,b; Yan et al., 2018												
GelMA	C2C12	96.00		95.00			Li et al., 2018cb	HepG2		98.61		98.72	98.92	Billiet et al., 2014
			42.00				García-Lizarribar et al., 2018			81.60	92.00	83.30		Bertassoni et al., 2014
		98.30		80.60	89.70		Zhou et al., 2019	BMSCs	91.80			92.10	94.90	Du et al., 2015
	Chondrocytes		91.80		88.50	88.30	Gu et al., 2018			75.00			90.00	Levato et al., 2017
			81.00	77.50			Schuurman et al., 2013	NIH3T3	95.00					Ersumo et al., 2016
		*Suntornnond et al., 2017; Pepelanova et al., 2018; Haring et al., 2019; Noh et al., 2019												

(Continued)

TABLE 5 | Continued

	Cell type	Cell viability (%)					References	Cell type	Cell viability (%)					References
		0 d	1 d	3 d	7 d	21 d			0 d	1 d	3 d	7 d	21 d	
Alginate Gelatin	MSCs	92.30					Giuseppe et al., 2017	Myoblasts	95.00		95.30			Chung et al., 2013
	L929		92.00	81.00	60.00		He et al., 2016	HDMEC		66.20			84.50	Akkineni et al., 2016
	C2C12	80.00	90.00		94.00	98.00	Bandyopadhyay et al., 2018	A549		85.00		76.25		Berg et al., 2018
	ADMSCs		88.13		90.41		Wang et al., 2016	ESCs	92.00	91.50	87.75	85.50	86.25	Li et al., 2018c
							*Ding et al., 2017, 2018; Aljohani et al., 2018							
Alginate GelMA	NIH3T3	90.00	75.00				Krishnamoorthy et al., 2019	BMSCs	88.60			85.00	76.30	Costantini et al., 2016
		89.00					Zhang X. et al., 2018		84.50			80.50	78.00	Kosik-Kozioł et al., 2019
	MSCs	81.25					Daly et al., 2016a							
							*Daly et al., 2016b; Kang et al., 2017; Liu et al., 2018							
Other	MSCs					97.97	Campos et al., 2015	MG63		50.00	80.00	78.00		Chen et al., 2018
		88.00	90.00		90.00	90.00	Xin et al., 2019			95.00	94.00	90.00		Kim et al., 2016
	Chondrocytes		93.00				Ren et al., 2016	C2C12	85.25					Contessi Negrini et al., 2018
			94.00	85.00			Censi et al., 2011	PC12		98.00	94.00			Chen et al., 2019
	HSF	90.00			85.00		Bakirci et al., 2017	NSCs	41.70					Lin et al., 2016
	NIH3T3	85.00					Wang et al., 2018	HUASMCs			90.00	82.00		Köpf et al., 2016
	ATDC5	90.00					Kim et al., 2019	BMSCs		87.00		92.00	91.00	Wu D. et al., 2018
	ADMSCs	82.00					Law et al., 2018	MC3T3		88.00		91.00	88.00	
	HTC116		88.00	83.00	52.00	40.00	Fan et al., 2016	MSCs		99.00			97	Duarte Campos et al., 2013
	BMSCs	100.00			83.00		Kiyotake et al., 2019	MG63		99.00			95.00	
	NSCs	87.00			55.00									
							*Hartwell et al., 2016; Ahn et al., 2017; Stichler et al., 2017; Cochis et al., 2018; Xu C. et al., 2018; Zheng et al., 2018; Li et al., 2019							

All studies are included in the closest period when they used a different timing. References marked with (*) make viability assay but use multiple cell lines or conditions, or not provide any value.

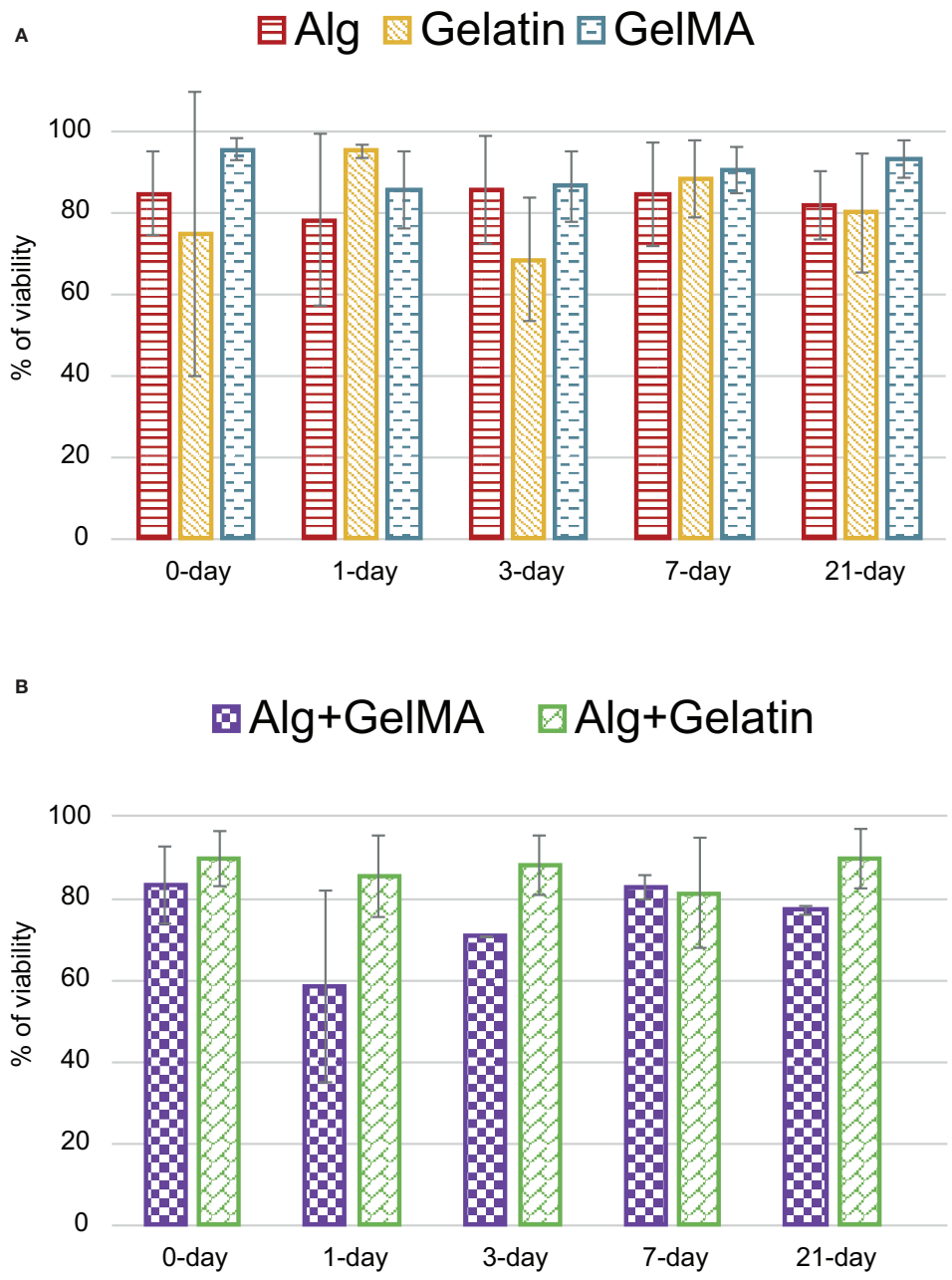

FIGURE 8 | Cell viability for the most important materials: **(A)** alginate, gelatin and GelMA in the five selected periods, **(B)** material combinations for selected periods.

decisive too. In general, multipotent cells (e.g., Mesenchymal Stem Cells) are selected due to their differentiation potential. A total of 46 different cell lines are used in these papers. It is important to note that many papers are only qualifying cell viability using a fuzzy scale, such as good, regular or bad survival and other measures not related to viability, such as cell distribution.

Figure 9 shows that Mesenchymal Stem Cells (MSCs) are the most used cells (16 papers), but only some of these papers provide quantitative cell viability (9) (Duarte Campos et al.,

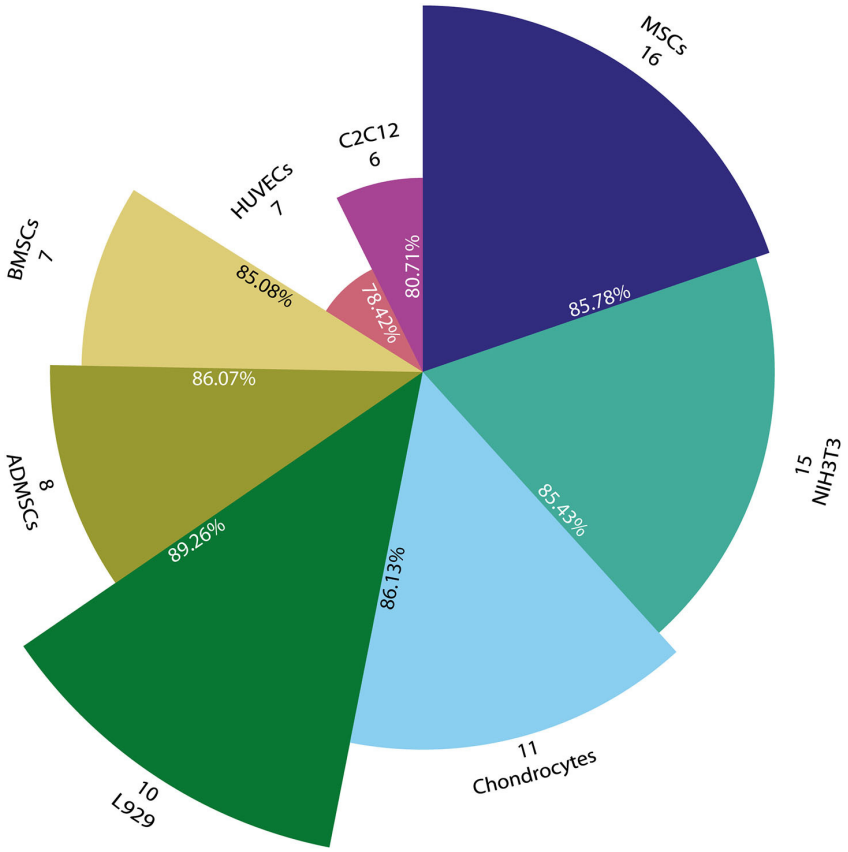

FIGURE 9 | Pie chart with the most representative cell lines used for bioprinting. Angle represents number of papers that use each cell line (#) and radius indicates the mean cell viability of all related papers (%). All circle sections are proportionally scaled with viability in order to facilitate comparison.

2013; Campos et al., 2015; Daly et al., 2016a; Freeman and Kelly, 2017; Giuseppe et al., 2017; Schütz et al., 2017; Gonzalez-Fernandez et al., 2019; Ji et al., 2019; Xin et al., 2019) and the remaining reports provided a qualitative value (6) (Daly et al., 2016b; Stichler et al., 2017; Ahlfeld et al., 2018; Tijore et al., 2018b; Zheng et al., 2018; Jeon et al., 2019) with the only exception of AnilKumar et al. (2019) that does not perform any kind of test. The widely use of MSCs could be due to their ability to be differentiated into bone, cartilage, muscle, marrow, ligament and connective tissue cells (Caplan, 2011).

Additionally, NIH3T3 is used in 15 papers where some analyze percentage of cell viability (7) (Bertassoni et al., 2014; Ersumo et al., 2016; Liu et al., 2018; Shin et al., 2018; Wang et al., 2018; Zhang X. et al., 2018; Krishnamoorthy et al., 2019), others report a qualitative scale of cell viability (5) (Ahn et al., 2017; Cochis et al., 2018; Raddatz et al., 2018; Xu C. et al., 2018; Yoon et al., 2019), and some do not perform any kind of test (3). These cell types are a fibroblast cell line used mostly because of its ease of growth. After that, chondrocytes were used in 11 papers: quantitative analysis (9) (Censi et al., 2011; Markstedt et al., 2015; Ren et al., 2016; Kosik-Kozioł et al., 2017; Yang et al., 2017; Gu et al., 2018; López-Marcial et al., 2018), qualitative analysis (1) (Nguyen et al., 2017), and no test performed (1) (Mouser et al., 2016).

Other studies (10) use L929, a mouse fibroblast cell line: quantitative analysis (7) (Blaeser et al., 2013; Gao et al., 2015, 2017; He et al., 2016; Li et al., 2017; Lee et al., 2018; Ooi et al., 2018), qualitative analysis (2) (Suntornnond et al., 2017; Raddatz et al., 2018), and no test performed (1) (Polley et al., 2017). Adipose-derived mesenchymal stem cells (ADMSCs), which are a cell line used because it is easily obtained from patients (Fernández et al., 2018), appear in 8 papers: quantitative analysis (5) (Campos et al., 2015; Kim et al., 2016; Narayanan et al., 2016; Wang et al., 2016; Law et al., 2018), and qualitative analysis (3) (Jia et al., 2014; Kang et al., 2017; Pepelanova et al., 2018). Bone marrow stromal cells (BMSCs) and Human umbilical vein endothelial cells (HUVECs) are used in 7 different papers: quantitative analysis (6) (Campbell et al., 2015; Irvine et al., 2015; He et al., 2018; Liu et al., 2018; Maiullari et al., 2018; Ji et al., 2019), and qualitative analysis (1) (Suntornnond et al., 2017).

On the other hand, C2C12 cells (a myoblast cell line) are used in 6 papers, all of them analyzed quantitatively (Bandyopadhyay et al., 2018; Contessi Negrini et al., 2018; García-Lizarribar et al., 2018; Li et al., 2018a,b,c; Zhou et al., 2019).

Finally, other cells are used to a lesser extent: MG-63 (5) (Blaeser et al., 2013; Duarte Campos et al., 2013; Kim et al., 2016; McBeth et al., 2017; Chen et al., 2018), MC3T3 (4) (Peak et al., 2018; Wu D. et al., 2018; Yu et al., 2018; Noh et al., 2019), NHDF (3) (Ding et al., 2017, 2018; Choi et al., 2018), 3T3 (3) (Wu Y. et al., 2018; Xu X. et al., 2018; Zheng et al., 2018), ATDC5 (3) (Izadifar et al., 2016; Hafeez et al., 2018; Kim et al., 2019), NSCs (2) (Lin et al., 2016; Kiyotake et al., 2019), Human Fibroblast (2) (Béduer et al., 2018; Zhang J. et al., 2018), PC12 (2) (Chen et al., 2019; Haring et al., 2019), HepG2 (2) (Bertassoni et al., 2014; Billiet et al., 2014), and iPSCs (2) (Nguyen et al., 2017; Maiullari et al., 2018).

Hence, the five most used cell lines are all mesenchymal cell-related. Some studies use more than one kind of cells, e.g., Liu et al. (2018) that use four different cell lines in its study. In this case, they examine cellular activity of these cell types in the GelMA cores of GelMA/alginate core/sheath microfibrous constructs. All these cell types that only appear in a specific paper are excluded from this detailed analysis. Additionally, a cell viability analysis grouped by the most used cell lines is also performed (**Figure 9**). In this sense, the eight most used cell lines are analyzed, but only papers with a quantitative analysis of viability are included.

In summary, all studies show a relatively high viability probably because journals perform quality controls in order to publish papers with acceptable results. In this sense, MSCs obtains a mean viability of 85.78 ± 10.2% while NIH3T3, other mesenchymal cell line, shows a similar cells survival of 85.43 ± 10.3%. In the same way, Chondrocytes (86.13 ± 6.46%), ADMSCs (86.07 ± 11.6%), and BMSCs (85.08 ± 4.95%) obtain similar viabilities. On the other hand, L-929 cells demonstrate a viability of 89.26 ± 7.42%, revealing to be the most resistant cells, in terms of viability, in all the included studies. This result is predictable, taking into consideration that L-929 cells derive from an immortalized cell line (Earle et al., 1943). Finally, HUVECs and C2C12 show less viability than other cell lines with 78.42 ± 19.3 and 80.71 ± 19.6%, respectively. However, this last analysis presents a high standard deviation, probably due to the small sample. A similar analysis could be provided linking materials and type of cells with its viability. But not enough number of combinations of different materials with cell types can assure a cause-effect relation.

Mechanical Tests

This section compiles different tests that obtain mechanical properties of bioprinted structures. In all 66 out of 118 papers perform different mechanical tests, but we have focused our interest into the five most used: (1) compressive stress, (2) Young or elastic modulus, (3) compression modulus, (4) yield stress, and (5) ultimate tensile strength (UTS). To obtain these mechanical properties, tests are done to multiple different materials, where alginate (51% of papers), GelMA (27%), and gelatin (15%) are the most common.

Compressive stress is defined as the stress on materials that leads to a smaller volume (14 papers). Kim et al. (2016) is the only study where graphs are used to show results. We group papers into five different ranges: below 10, 10–40, 40–100, 100–400, and 1,200–4,100 kPa. With the most usual values in the 10–40 kPa subrange (9 papers), values lower than 10 kPa are the second most usual subrange (5 papers), and the rest of data is distributed in 40–100, 100–400 kPa, and 1,200–4,100 subranges (3, 2, and 3 papers, respectively).

Three authors study compressive stress of different materials. On the one hand, Daly et al. (2016a) obtain 4, 16, 20, and 36 kPa for alginate, agarose, PEGMA, and GelMA hydrogels, respectively. On the other hand, Aydogdu et al. (2019) perform their tests in the 1,200–1,400 kPa range. They use different mixtures of alginate, collagen, chitosan, Hlh (Halomonas levan), PLA, and b-TCP to create different hydrogels, obtaining 1,240, 1,290, 1,380, 1,490, 1,540, and 1,590 kPa for each hydrogel. Additionally, Ahlfeld et al. (2018) obtain 16.9, 1,300, and 4,100 kPa for an alginate, methylcellulose, and CMC hydrogel, respectively.

Young modulus is defined as the mechanical property to measure the stiffness of a solid material and it is the most analyzed parameter. Hence, the Young modulus defines the relationship between stress (force per unit area) and strain (proportional deformation) in a material in the linear elasticity regime of a uniaxial deformation. Approximately half of papers (35) study this property and some of them comment the expected result for a specific tissue, e.g., 4 MPa for cartilage tissue (Censi et al., 2011). In this case, six authors show their results in graphs and the quantitative results are within 0–100, 100–400, and above 400 kPa ranges. In general, the whole range varies from 0.15 to $8.3 \cdot 10^5$ kPa, most of the values are in the range 0–100 kPa with 23 papers, followed by 100–400 kPa (10 papers), and above 400 kPa (3 papers). Alginate is the most studied material (16 papers). Several kinds of are present: Wei et al. (2019) analyzes complete mechanical properties of cross-linked wet and dry alginate scaffolds, other authors study cross-linked hydrogels in different times (Khalil and Sun, 2009; Naghieh et al., 2018; Shin et al., 2018), or in different concentrations (Bertassoni et al., 2014; Mouser et al., 2016; Naghieh et al., 2018; Krishnamoorthy et al., 2019). It is important to note the work of Aljohani et al. (2018) that analyzes alginate blended with gelatin and agar, obtaining the highest values of the Young modulus with $5.7 \cdot 10^5$, $6.1 \cdot 10^5$, $6.4 \cdot 10^5$, and $8.3 \cdot 10^5$ kPa for an alginate, gelatin, agar, and alginate/gelatin/agar hydrogel, respectively.

Compression modulus is the ratio of mechanical stress to strain in an elastic material when that material is being compressed, i.e., the compressive force per unit area divided by the change in volume per unit volume. In this case, 17 papers perform 57 tests, where four papers performed this test giving their results only in graphs. The most usual range is 10–100 kPa with 11 papers and 32 different compression values. However, two studies obtain higher values than 1 MPa: Daly et al. (2016b) with 1,402 kPa using an alginate/PCL blend and Ahlfeld et al. (2018) with 36.7, $3.07 \cdot 10^4$, and $5.2 \cdot 10^4$ kPa for an alginate, CPC, and methylcellulose hydrogels, respectively. Additionally, some studies analyze the compression modulus

with different concentrations (Chung et al., 2013; Schuurman et al., 2013; Giuseppe et al., 2017), several cross-linking agents for alginate, PEGDA, and GelMA (Kang et al., 2017), and different cell lines (Levato et al., 2017).

Ultimate tensile strength (UTS) is the maximum stress that a material can withstand while being stretched or pulled before breaking. This property appears in 12 papers and nine of them use alginate in their hydrogel. In this case, when alginate is used (mixed or not with another component) UTS values are within 40–500 kPa range with concentrations of 2–5%w/v.

Finally, yield stress is little studied (3 papers) and most of them provide graphical results. Bandyopadhyay et al. (2018) obtain a yield stress of 3,350 kPa using an alginate/gelatin/collagen hydrogel. Lastly, Li et al. (2018b) study the ultimate shear stress (12 kPa) in a GelMA/Carrageenan hydrogel.

As exposed before, all these properties are highly dependent of pre- and printing process. In this sense, concentration, and crosslinking parameters, are the parameters that affect the most to mechanical stability of bioprinted structure. This is evident when the main modifications in studies relating mechanical properties are made with changes in these parameters. For example, changes in concentration to analyze how it affects the mechanical properties are made in 11 papers, 4 of them young modulus is observed (Bertassoni et al., 2014; Mouser et al., 2016; Naghieh et al., 2018; Krishnamoorthy et al., 2019), in 4 papers UTS (Gao et al., 2015; Yang et al., 2017; Bandyopadhyay et al., 2018; He et al., 2018), and in 3 compressive modulus (Chung et al., 2013; Schuurman et al., 2013; Giuseppe et al., 2017). All of them obtain the same conclusion: mechanical stability rises when the concentration increases. Mechanical properties are also influenced by crosslinking parameters. In this sense Giuseppe et al. (2017) proposed a 15 min time of exposition of Ca^{2+} for alginate/gelatin blend after measuring different time point and analyze it compressive modulus, noting that with higher time of exposition modulus increases. Also, Kang et al. (2017) made modifications in their photoinitiator, its concentration and power of UV irradiated. In the same way as before, the higher the concentration and the irradiation power the higher the stiffness.

CONCLUSIONS

This article is a systematic review of hydrogel implications during bioprinting process, including a descriptive statistical analysis of materials, bioprinting parameters, mechanical tests, and viability assays.

Maybe, the omission of relevant bioprinting parameters is one of the most important drawbacks detected in most of the papers, making the reproducibility of their results difficult. Obviously, many research fields are involved in bioprinting, so it is possible that authors focused their interest on those parameters directly related to its scope, playing down the rest of essential information. For this reason, we propose some suggestions to solve this problem in section "Recommendations and future works."

First, alginate is the most commonly used material followed by gelatin and GelMA. For this reason, the concentration and cross-linking analysis are highly influenced by these three materials. Here, we show that the most used concentrations are 2–4, 5, and 10% w/v for alginate, gelatin, and GelMA, respectively. Likewise, most cross-linking methods for alginate are chemical and based on Ca^{2+} cations, while 37°C is the most common temperature for thermal cross-linking of gelatin, and UV light is the standard physical cross-linking of GelMA.

Secondly, cell-laden hydrogels are the most used. Consequently, cartridge temperature is usually defined in the range of 30–40°C (allowing cell survival) and the printing pressure at 100–200 kPa (reducing cell stress). Obviously, the addition of cells after hydrogel bioprinting minimize the importance of these parameters.

Finally, MSCs are the cell line most used in combination with hydrogels. In general, good viability results are obtained with all cell lines. Regarding mechanical tests, the Young modulus is widely used in bioprinting, although there is no consensus on the most important mechanical property of each bioprinted structure.

RECOMMENDATIONS AND FUTURE WORKS

In our opinion, those missed bioprinting parameters are usually related to a poor reproducibility. Moreover, inappropriate evaluation tests may cause an unfair comparison of results. For this reason, some guidelines and recommendations are detailed below. Additionally, in order to facilitate reading and understanding for future papers, the International Systems of Units (SI) must be used.

Hence, we strongly recommend defining the following parameters in all studies. *Concentration* of materials and protocols to prepare hydrogels should be fully detailed and could be complemented with its viscosity. Although *cartridge temperature* and *printing pressure* are two essential parameters needed to set the bioprinter, *bed temperature* and *printing speed* will increase the reproducibility of the study. A quantitative measure of printability or the hydrogel printability window will facilitate its practical use. Additionally, in the cross-linking step, *concentration* for chemical-based cross-linking, *temperature* for thermal-based cross-linking, *light wavelength*/*power* for physical-based cross-linking must be defined. Furthermore, the *exposition time* must be defined for all three cross-linking types. On the other hand, cellular tests must include the identification of *cell line* and *assay-kit* information with quantifications at different time points (*0, 1, 3, 7, and 21-days*). And finally, those studies whose bioprinted structures have a specific clinical application must perform mechanical tests to mimic the tissue/organ properties (e.g., compressive stress for cartilage tissue).

In summary, due to time and space restrictions, this review could not analyze all the information available in the selected papers. Thus, future works could focus on comparing results of commercial vs. homemade bioprinters (cell viability, mechanical behavior), analyzing other rheological properties (swelling ratio,

surface tension), printability vs. precision, or degradation speed for different hydrogels.

AUTHOR CONTRIBUTIONS

EM performed literature search, screening, data extraction, preparation of graphics, tables, and manuscript. JG-B contributed to screening, data extraction, preparation of graphics, tables, and manuscript. JP contributed to screening, data extraction, and preparation of manuscript. EL, JC, AM-G, MD, JC-A, and DT contributed to screening, data extraction, and revision work to the manuscript. FS-M performed revision work to the manuscript. All authors contributed to the article and approved the submitted version.

FUNDING

This study has been co-funded by Consejería de Economía, Ciencia y Agenda Digital, Junta de Extremadura, through Grants IB16200 (PI: JP) and PD16067 to JG-B. Co-funded by Unión Europea/FEDER and FSE. Supported by competitive grant 'Miguel Servet I' from Instituto de Salud Carlos III to JC (CP17/00021 and CD17/00021 co-financed by FEDER and FSE) and Sara Borrell grant from Instituto de Salud Carlos III to EL (CD19/00048 co-financed by FSE).

REFERENCES

Abelardo, E. (2018). "Synthetic material bioinks," in *3D Bioprinting for Reconstructive Surgery*, eds D. Thomas, Z. Jessop and I. Whitaker (Duxford: Elsevier), 137–144. doi: 10.1016/B978-0-08-101103-4.00009-0

Ahlfeld, T., Doberenz, F., Kilian, D., Vater, C., Korn, P., Lauer, G., et al. (2018). Bioprinting of mineralized constructs utilizing multichannel plotting of a self-setting calcium phosphate cement and a cell-laden bioink. *Biofabrication* 10:045002. doi: 10.1088/1758-5090/aad36d

Ahn, G., Min, K. H., Kim, C., Lee, J. S., Kang, D., Won, J. Y., et al. (2017). Precise stacking of decellularized extracellular matrix based 3D cell-laden constructs by a 3D cell printing system equipped with heating modules. *Sci. Rep.* 7:8624. doi: 10.1038/s41598-017-09201-5

Aied, A., Song, W., Wang, W., Baki, A., and Sigen, A. (2018). 3D Bioprinting of stimuli-responsive polymers synthesised from DE-ATRP into soft tissue replicas. *Bioprinting* 9, 37–43. doi: 10.1016/j.bprint.2018.02.002

Akkineni, A. R., Ahlfeld, T., Lode, A., and Gelinsky, M. (2016). A versatile method for combining different biopolymers in a core/shell fashion by 3D plotting to achieve mechanically robust constructs. *Biofabrication* 8:045001. doi: 10.1088/1758-5090/8/4/045001

Aljohani, W., Ullah, M. W., Li, W., Shi, L., Zhang, X., and Yang, G. (2018). Three-dimensional printing of alginate-gelatin-agar scaffolds using free-form motor assisted microsyringe extrusion system. *J. Polym. Res.* 25:62. doi: 10.1007/s10965-018-1455-0

AnilKumar, S., Allen, S. C., Tasnim, N., Akter, T., Park, S., Kumar, A., et al. (2019). The applicability of furfuryl-gelatin as a novel bioink for tissue engineering applications. *J. Biomed. Mater. Res. Part B Appl. Biomater.* 107, 314–323. doi: 10.1002/jbm.b.34123

Apelgren, P., Amoroso, M., Lindahl, A., Brantsing, C., Rotter, N., Gatenholm, P., et al. (2017). Chondrocytes and stem cells in 3D-bioprinted structures create human cartilage *in vivo*. *PLoS ONE* 12:e0189428. doi: 10.1371/journal.pone.0189428

Ashammakhi, N., Ahadian, S., Xu, C., Montazerian, H., Ko, H., Nasiri, R., et al. (2019). Bioinks and bioprinting technologies to make heterogeneous and biomimetic tissue constructs. *Mater. Today Biol.* 1:100008. doi: 10.1016/j.mtbio.2019.100008

Aydogdu, M. O., Oner, E. T., Ekren, N., Erdemir, G., Kuruca, S. E., Yuca, E., et al. (2019). Comparative characterization of the hydrogel added PLA/β-TCP scaffolds produced by 3D bioprinting. *Bioprinting* 13:e00046. doi: 10.1016/j.bprint.2019.e00046

Bakarich, S. E., Gorkin, R., Panhuis, M., and Spinks, G. M. (2014). Three-dimensional printing fiber reinforced hydrogel composites. *ACS Appl. Mater. Interfaces* 6, 15998–16006. doi: 10.1021/am503878d

Bakirci, E., Toprakhisar, B., Zeybek, M. C., Ince, G. O., and Koc, B. (2017). Cell sheet based bioink for 3D bioprinting applications. *Biofabrication* 9:024105. doi: 10.1088/1758-5090/aa764f

Bandyopadhyay, A., Dewangan, V. K., Vajanthri, K. Y., Poddar, S., and Mahto, S. K. (2018). Easy and affordable method for rapid prototyping of tissue models *in vitro* using three-dimensional bioprinting. *Biocybern. Biomed. Eng.* 38, 158–169. doi: 10.1016/j.bbe.2017.12.001

Béduer, A., Piacentini, N., Aeberli, L., Da Silva, A., Verheyen, C. A., Bonini, F., et al. (2018). Additive manufacturing of hierarchical injectable scaffolds for tissue engineering. *Acta Biomater.* 76, 71–79. doi: 10.1016/j.actbio.2018.05.056

Berg, J., Hiller, T., Kissner, M. S., Qazi, T. H., Duda, G. N., Hocke, A. C., et al. (2018). Optimization of cell-laden bioinks for 3D bioprinting and efficient infection with influenza A virus. *Sci. Rep.* 8:13877. doi: 10.1038/s41598-018-31880-x

Bertassoni, L. E., Cardoso, J. C., Manoharan, V., Cristino, A. L., Bhise, N. S., Araujo, W. A., et al. (2014). Direct-write bioprinting of cell-laden methacrylated gelatin hydrogels. *Biofabrication* 6:24105. doi: 10.1088/1758-5082/6/2/024105

Billiet, T., Gevaert, E., De Schryver, T., Cornelissen, M., and Dubruel, P. (2014). The 3D printing of gelatin methacrylamide cell-laden tissue-engineered constructs with high cell viability. *Biomaterials* 35, 49–62. doi: 10.1016/j.biomaterials.2013.09.078

Blaeser, A., Duarte Campos, D. F., Weber, M., Neuss, S., Theek, B., Fischer, H., et al. (2013). Biofabrication under fluorocarbon: a novel freeform fabrication technique to generate high aspect ratio tissue-engineered constructs. *Bioresour. Open Access* 2, 374–384. doi: 10.1089/biores.2013.0031

Boontheekul, T., Kong, H.-J., and Mooney, D. J. (2005). Controlling alginate gel degradation utilizing partial oxidation and bimodal molecular weight distribution. *Biomaterials* 26, 2455–2465. doi: 10.1016/j.biomaterials.2004.06.044

Campbell, J., McGuinness, I., Wirz, H., Sharon, A., and Sauer-Budge, A. F. (2015). Multimaterial and multiscale three-dimensional bioprinter. *J. Nanotechnol. Eng. Med.* 6:021001. doi: 10.1115/1.4031230

Campos, D. F. D., Blaeser, A., Korsten, A., Neuss, S., Jäkel, J., Vogt, M., et al. (2015). The stiffness and structure of three-dimensional printed hydrogels direct the differentiation of mesenchymal stromal cells toward adipogenic and osteogenic lineages. *Tissue Eng. Part A* 21, 740–756. doi: 10.1089/ten.tea.2014.0231

Caplan, A. I. (2011). "MSCs in Regenerative Medicine," in *Principles of Regenerative Medicine*, eds A. Atala, R. Lanza, J. A. Thomson and R. Nerem (San Diego, CA: Elsevier), 253–262. doi: 10.1016/B978-0-12-381422-7.10014-8

Celikkin, N., Padial, J. S., Costantini, M., Hendrikse, H., Cohn, R., Wilson, C. J., et al. (2018). 3D printing of thermoresponsive polyisocyanide (PIC) hydrogels as bioink and fugitive material for tissue engineering. *Polymers* 10:555. doi: 10.3390/polym10050555

Censi, R., Schuurman, W., Malda, J., Di Dato, G., Burgisser, P. E., Dhert, W. J. A., et al. (2011). A printable photopolymerizable thermosensitive p(HPMAm-lactate)-PEG hydrogel for tissue engineering. *Adv. Funct. Mater.* 21, 1833–1842. doi: 10.1002/adfm.201002428

Chen, Y., Wang, Y., Yang, Q., Liao, Y., Zhu, B., Zhao, G., et al. (2018). A novel thixotropic magnesium phosphate-based bioink with excellent printability for application in 3D printing. *J. Mater. Chem. B* 6, 4502–4513. doi: 10.1039/c8tb01196f

Chen, Z., Zhao, D., Liu, B., Nian, G., Li, X., Yin, J., et al. (2019). 3D printing of multifunctional hydrogels. *Adv. Funct. Mater.* 29:1900971. doi: 10.1002/adfm.201900971

Choi, D. J., Park, S. J., Gu, B. K., Kim, Y. J., Chung, S., and Kim, C. H. (2018). Effect of the pore size in a 3D bioprinted gelatin scaffold on fibroblast proliferation. *J. Ind. Eng. Chem.* 67, 388–395. doi: 10.1016/j.jiec.2018.07.013

Chung, J. H. Y., Naficy, S., Yue, Z., Kapsa, R., Quigley, A., Moulton, S. E., et al. (2013). Bio-ink properties and printability for extrusion printing living cells. *Biomater. Sci.* 1, 763–773. doi: 10.1039/c3bm00012e

Cochis, A., Bonetti, L., Sorrentino, R., Negrini, N. C., Grassi, F., Leigheb, M., et al. (2018). 3D printing of thermo-responsive methylcellulose hydrogels for cell-sheet engineering. *Materials* 11:579. doi: 10.3390/ma11040579

Contessi Negrini, N., Bonetti, L., Contili, L., and Far,è, S. (2018). 3D printing of methylcellulose-based hydrogels. *Bioprinting* 10:e00024. doi: 10.1016/j.bprint.2018.e00024

Costantini, M., Idaszek, J., Szöke, K., Jaroszewicz, J., Dentini, M., Barbetta, A., et al. (2016). 3D bioprinting of BM-MSCs-loaded ECM biomimetic hydrogels for *in vitro* neocartilage formation. *Biofabrication* 8:035002. doi: 10.1088/1758-5090/8/3/035002

Daly, A. C., Critchley, S. E., Rencsok, E. M., and Kelly, D. J. (2016a). A comparison of different bioinks for 3D bioprinting of fibrocartilage and hyaline cartilage. *Biofabrication* 8, 1–10. doi: 10.1088/1758-5090/8/4/045002

Daly, A. C., Cunniffe, G. M., Sathy, B. N., Jeon, O., Alsberg, E., and Kelly, D. J. (2016b). 3D Bioprinting of developmentally inspired templates for whole bone organ engineering. *Adv. Healthc. Mater.* 5, 2353–2362. doi: 10.1002/adhm.201600182

Das, S., Pati, F., Choi, Y.-J., Rijal, G., Shim, J.-H., Kim, S. W., et al. (2015). Bioprintable, cell-laden silk fibroin-gelatin hydrogel supporting multilineage differentiation of stem cells for fabrication of three-dimensional tissue constructs. *Acta Biomater.* 11, 233–246. doi: 10.1016/j.actbio.2014.09.023

Datta, S., Sarkar, R., Vyas, V., Bhutoria, S., Barui, A., Roy Chowdhury, A., et al. (2018). Alginate-honey bioinks with improved cell responses for applications as bioprinted tissue engineered constructs. *J. Mater. Res.* 33, 2029–2039. doi: 10.1557/jmr.2018.202

Ding, H., Tourlomousis, F., and Chang, R. C. (2017). Bioprinting multidimensional constructs: a quantitative approach to understanding printed cell density and redistribution phenomena. *Biomed. Phys. Eng. Express* 3:035016. doi: 10.1088/2057-1976/aa70f0

Ding, H., Tourlomousis, F., and Chang, R. C. (2018). A methodology for quantifying cell density and distribution in multidimensional bioprinted gelatin–alginate constructs. *J. Manuf. Sci. Eng.* 140:051014. doi: 10.1115/1.4037572

Du, M., Chen, B., Meng, Q., Liu, S., Zheng, X., Zhang, C., et al. (2015). 3D bioprinting of BMSC-laden methacrylamide gelatin scaffolds with CBD-BMP2-collagen microfibers. *Biofabrication* 7:044104. doi: 10.1088/1758-5090/7/4/044104

Duarte Campos, D. F., Blaeser, A., Weber, M., Jäkel, J., Neuss, S., Jahnen-Dechent, W., et al. (2013). Three-dimensional printing of stem cell-laden hydrogels submerged in a hydrophobic high-density fluid. *Biofabrication* 5:015003. doi: 10.1088/1758-5082/5/1/015003

Earle, W. R., Schilling, E. L., Stark, T. H., Straus, N. P., Brown, M. F., and Shelton, E. (1943). Production of malignancy *in vitro*. IV. The mouse fibroblast cultures and changes seen in the living cells. *JNCI J. Natl. Cancer Inst.* 4, 165–212. doi: 10.1093/jnci/4.2.165

Ersumo, N., Witherel, C. E., and Spiller, K. L. (2016). Differences in time-dependent mechanical properties between extruded and molded hydrogels. *Biofabrication* 8:035012. doi: 10.1088/1758-5090/8/3/035012

Eswaramoorthy, S. D., Ramakrishna, S., and Rath, S. N. (2019). Recent advances in three-dimensional bioprinting of stem cells. *J. Tissue Eng. Regen. Med.* 13, 908–924. doi: 10.1002/term.2839

Fan, R., Piou, M., Darling, E., Cormier, D., Sun, J., and Wan, J. (2016). Bio-printing cell-laden Matrigel–agarose constructs. *J. Biomater. Appl.* 31, 684–692. doi: 10.1177/0885328216669238

Fernández, O., Izquierdo, G., Fernández, V., Leyva, L., Reyes, V., Guerrero, M., et al. (2018). Adipose-derived mesenchymal stem cells (AdMSC) for the treatment of secondary-progressive multiple sclerosis: a triple blinded, placebo controlled, randomized phase I/II safety and feasibility study. *PLoS ONE* 13:e0195891. doi: 10.1371/journal.pone.0195891

Freeman, F. E., and Kelly, D. J. (2017). Tuning alginate bioink stiffness and composition for controlled growth factor delivery and to spatially direct MSC Fate within bioprinted tissues. *Sci. Rep.* 7, 1–12. doi: 10.1038/s41598-017-17286-1

Gao, Q., He, Y., Fu, J., zhong, Liu, A., and Ma, L. (2015). Coaxial nozzle-assisted 3D bioprinting with built-in microchannels for nutrients delivery. *Biomaterials* 61, 203–215. doi: 10.1016/j.biomaterials.2015.05.031

Gao, Q., Liu, Z., Lin, Z., Qiu, J., Liu, Y., Liu, A., et al. (2017). 3D Bioprinting of vessel-like structures with multilevel fluidic channels. *ACS Biomater. Sci. Eng.* 3, 399–408. doi: 10.1021/acsbiomaterials.6b00643

Gao, T., Gillispie, G. J., Copus, J. S., Kumar, A. P. R., Seol, Y.-J., Atala, A., et al. (2018). Optimization of gelatin-alginate composite bioink printability using rheological parameters: a systematic approach. *Biofabrication* 10:034106. doi: 10.1088/1758-5090/aacdc7

García-Lizarribar, A., Fernández-Garibay, X., Velasco-Mallorqu,í, F., Castaño, A. G., Samitier, J., and Ramon-Azcon, J. (2018). Composite biomaterials as long-lasting scaffolds for 3D bioprinting of highly aligned muscle tissue. *Macromol. Biosci.* 18:e1800167. doi: 10.1002/mabi.201800167

Giuseppe, M. D., Law, N., Webb, B., A., Macrae, R., Liew, L. J., et al. (2017). Mechanical behaviour of alginate-gelatin hydrogels for 3D bioprinting. *J. Mech. Behav. Biomed. Mater.* 79, 150–157. doi: 10.1016/j.jmbbm.2017.12.018

Gonzalez-Fernandez, T., Rathan, S., Hobbs, C., Pitacco, P., Freeman, F. E., Cunniffe, G. M., et al. (2019). Pore-forming bioinks to enable spatio-temporally defined gene delivery in bioprinted tissues. *J. Control. Release* 301, 13–27. doi: 10.1016/j.jconrel.2019.03.006

Gu, Y., Zhang, L., Du, X., Fan, Z., Wang, L., Sun, W., et al. (2018). Reversible physical crosslinking strategy with optimal temperature for 3D bioprinting of human chondrocyte-laden gelatin methacryloyl bioink. *J. Biomater. Appl.* 33, 609–618. doi: 10.1177/0885328218805864

Habib, A., Sathish, V., Mallik, S., and Khoda, B. (2018). 3D printability of alginate-carboxymethyl cellulose hydrogel. *Materials* 11:454. doi: 10.3390/ma11030454

Hafeez, S., Ooi, H., Morgan, F., Mota, C., Dettin, M., van Blitterswijk, C., et al. (2018). Viscoelastic oxidized alginates with reversible imine type crosslinks: self-healing, injectable, and bioprintable hydrogels. *Gels* 4:85. doi: 10.3390/gels4040085

Haring, A. P., Thompson, E. G., Tong, Y., Laheri, S., Cesewski, E., Sontheimer, H., et al. (2019). Process- and bio-inspired hydrogels for 3D bioprinting of soft free-standing neural and glial tissues. *Biofabrication* 11:25009. doi: 10.1088/1758-5090/ab02c9

Hartwell, R., Chan, B., Elliott, K., Alnojeidi, H., and Ghahary, A. (2016). Polyvinyl alcohol-graft-polyethylene glycol hydrogels improve utility and biofunctionality of injectable collagen biomaterials. *Biomed. Mater.* 11:035013. doi: 10.1088/1748-6041/11/3/035013

He, J., Shao, J., Li, X., Huang, Q., and Xu, T. (2018). Bioprinting of coaxial multicellular structures for a 3D co-culture model. *Bioprinting* 11:e00036. doi: 10.1016/j.bprint.2018.e00036

He, Y., Yang, F., Zhao, H., Gao, Q., Xia, B., and Fu, J. (2016). Research on the printability of hydrogels in 3D bioprinting. *Sci. Rep.* 6:29977. doi: 10.1038/srep29977

Hsiao, S. -H., and Hsu, S. -H. (2018). Synthesis and characterization of dual stimuli-sensitive biodegradable polyurethane soft hydrogels for 3D cell-laden bioprinting. *ACS Appl. Mater. Interfaces* 10, 29273–29287. doi: 10.1021/acsami.8b08362

Irvine, S. A., Agrawal, A., Lee, B. H., Chua, H. Y., Low, K. Y., Lau, B. C., et al. (2015). Printing cell-laden gelatin constructs by free-form fabrication and enzymatic protein crosslinking. *Biomed. Microdevices* 17:16. doi: 10.1007/s10544-014-9915-8

Izadifar, Z., Chang, T., Kulyk, W., Chen, X., and Eames, B. F. (2016). Analyzing biological performance of 3D-printed, cell-impregnated hybrid constructs for cartilage tissue engineering. *Tissue Eng. Part C Methods* 22, 173–188. doi: 10.1089/ten.tec.2015.0307

Jeon, O., Lee, Y. B., Hinton, T. J., Feinberg, A. W., and Alsberg, E. (2019). Cryopreserved cell-laden alginate microgel bioink for 3D bioprinting of living tissues. *Mater. Today Chem.* 12, 61–70. doi: 10.1016/j.mtchem.2018.11.009

Ji, S., Almeida, E., and Guvendiren, M. (2019). 3D bioprinting of complex channels within cell-laden hydrogels. *Acta Biomater.* 95, 214–224. doi: 10.1016/j.actbio.2019.02.038

Jia, J., Richards, D. J., Pollard, S., Tan, Y., Rodriguez, J., Visconti, R. P., et al. (2014). Engineering alginate as bioink for bioprinting. *Acta Biomater.* 10, 4323–4331. doi: 10.1016/j.actbio.2014.06.034

Jovic, T. H., Kungwengwe, G., Mills, A. C., and Whitaker, I. S. (2019). Plant-derived biomaterials: a review of 3D bioprinting and biomedical applications. *Front. Mech. Eng.* 5:19. doi: 10.3389/fmech.2019.00019

Kang, L. H., Armstrong, P. A., Lee, L. J., Duan, B., Kang, K. H., and Butcher, J. T. (2017). Optimizing photo-encapsulation viability of heart valve cell types in 3D printable composite hydrogels. *Ann. Biomed. Eng.* 45, 360–377. doi: 10.1007/s10439-016-1619-1

Khalil, S., and Sun, W. (2009). Bioprinting endothelial cells with alginate for 3D tissue constructs. *J. Biomech. Eng.* 131:111002. doi: 10.1115/1.3128729

Kim, S. W., Kim, D. Y., Roh, H. H., Kim, H. S., Lee, J. W., and Lee, K. Y. (2019). Three-dimensional bioprinting of cell-laden constructs using polysaccharide-based self-healing hydrogels. *Biomacromolecules* 20, 1860–1866. doi: 10.1021/acs.biomac.8b01589

Kim, Y. B., Lee, H., and Kim, G. H. (2016). A strategy to achieve highly porous/biocompatible macroscale cell blocks, using a collagen/genipin-bioink and an optimal 3d printing process. *ACS Appl. Mater. Interfaces* 8, 32230–32240. doi: 10.1021/acsami.6b11669

Kiyotake, E. A., Douglas, A. W., Thomas, E. E., and Detamore, M. S. (2019). Development and quantitative characterization of the precursor rheology of hyaluronic acid hydrogels for bioprinting. *Acta Biomater.* 95, 176–187. doi: 10.1016/j.actbio.2019.01.041

Köpf, M., Campos, D. F. D., Blaeser, A., Sen, K. S., and Fischer, H. (2016). A tailored three-dimensionally printable agarose-collagen blend allows encapsulation, spreading, and attachment of human umbilical artery smooth muscle cells. *Biofabrication* 8:025011. doi: 10.1088/1758-5090/8/2/025011

Kosik-Kozioł, A., Costantini, M., Bolek, T., Szöke, K., Barbetta, A., Brinchmann, J., et al. (2017). PLA short sub-micron fiber reinforcement of 3D bioprinted alginate constructs for cartilage regeneration. *Biofabrication* 9:044105. doi: 10.1088/1758-5090/aa90d7

Kosik-Kozioł, A., Costantini, M., Mróz, A., Idaszek, J., Heljak, M., Jaroszewicz, J., et al. (2019). 3D bioprinted hydrogel model incorporating β-tricalcium phosphate for calcified cartilage tissue engineering. *Biofabrication* 11:035016. doi: 10.1088/1758-5090/ab15cb

Krishnamoorthy, S., Zhang, Z., and Xu, C. (2019). Biofabrication of three-dimensional cellular structures based on gelatin methacrylate–alginate interpenetrating network hydrogel. *J. Biomater. Appl.* 33, 1105–1117. doi: 10.1177/0885328218823329

Kundu, J., Shim, J.-H., Jang, J., Kim, S.-W., and Cho, D.-W. (2015). An additive manufacturing-based PCL-alginate-chondrocyte bioprinted scaffold for cartilage tissue engineering. *J. Tissue Eng. Regen. Med.* 9, 1286–1297. doi: 10.1002/term.1682

Kyle, S., Jessop, Z. M., Al-Sabah, A., and Whitaker, I. S. (2017). 'Printability' of candidate biomaterials for extrusion based 3D printing: state-of-the-art. *Adv. Healthc. Mater.* 6:1700264. doi: 10.1002/adhm.201700264

Law, N., Doney, B., Glover, H., Qin, Y., Aman, Z. M., Sercombe, T. B., et al. (2018). Characterisation of hyaluronic acid methylcellulose hydrogels for 3D bioprinting. *J. Mech. Behav. Biomed. Mater.* 77, 389–399. doi: 10.1016/j.jmbbm.2017.09.031

Leberfinger, A. N., Dinda, S., Wu, Y., Koduru, S. V., Ozbolat, V., Ravnic, D. J., et al. (2019). Bioprinting functional tissues. *Acta Biomater.* 95, 32–49. doi: 10.1016/j.actbio.2019.01.009

Lee, J., Lee, S.-H., Kim, B. S., Cho, Y.-S., and Park, Y. (2018). Development and evaluation of hyaluronic acid-based hybrid bio-ink for tissue regeneration. *Tissue Eng. Regen. Med.* 15, 761–769. doi: 10.1007/s13770-018-0144-8

Lee, K. Y., and Mooney, D. J. (2012). Alginate: properties and biomedical applications. *Prog. Polym. Sci.* 37, 106–126. doi: 10.1016/j.progpolymsci.2011.06.003

Levato, R., Webb, W. R., Otto, I. A., Mensinga, A., Zhang, Y., van Rijen, M., et al. (2017). The bio in the ink: cartilage regeneration with bioprintable hydrogels and articular cartilage-derived progenitor cells. *Acta Biomater.* 61, 41–53. doi: 10.1016/j.actbio.2017.08.005

Li, C., Wang, K., Zhou, X., Li, T., Xu, Y., Qiang, L., et al. (2019). Controllable fabrication of hydroxybutyl chitosan/oxidized chondroitin sulfate hydrogels by 3D bioprinting technique for cartilage tissue engineering. *Biomed. Mater.* 14:025006. doi: 10.1088/1748-605X/aaf8ed

Li, H., Tan, Y. J., Leong, K. F., and Li, L. (2017). 3D Bioprinting of highly thixotropic alginate/methylcellulose hydrogel with strong interface bonding. *ACS Appl. Mater. Interfaces* 9, 20086–20097. doi: 10.1021/acsami.7b04216

Li, H., Tan, Y. J., and Li, L. (2018a). A strategy for strong interface bonding by 3D bioprinting of oppositely charged κ-carrageenan and gelatin hydrogels. *Carbohydr. Polym.* 198, 261–269. doi: 10.1016/j.carbpol.2018.06.081

Li, H., Tan, Y. J., Liu, S., and Li, L. (2018b). Three-dimensional bioprinting of oppositely charged hydrogels with super strong interface bonding. *ACS Appl. Mater. Interfaces* 10, 11164–11174. doi: 10.1021/acsami.7b19730

Li, Z., Huang, S., Liu, Y., Yao, B., Hu, T., Shi, H., et al. (2018c). Tuning alginate-gelatin bioink properties by varying solvent and their impact on stem cell behavior. *Sci. Rep.* 8:8020. doi: 10.1038/s41598-018-26407-3

Lin, H., Hsieh, F., Tseng, C., and Hsu, S. (2016). Preparation and characterization of a biodegradable polyurethane hydrogel and the hybrid gel with soy protein for 3D cell-laden bioprinting. *J. Mater. Chem. B* 4, 6694–6705. doi: 10.1039/C6TB01501H

Liu, W., Zhong, Z., Hu, N., Zhou, Y., Maggio, L., Miri, A. K., et al. (2018). Coaxial extrusion bioprinting of 3D microfibrous constructs with cell-favorable gelatin methacryloyl microenvironments. *Biofabrication* 10:024102. doi: 10.1088/1758-5090/aa9d44

López-Marcial, G. R., Zeng, A. Y., Osuna, C., Dennis, J., García, J. M., and O'Connell, G. D. (2018). Agarose-based hydrogels as suitable bioprinting materials for tissue engineering. *ACS Biomater. Sci. Eng.* 4, 3610–3616. doi: 10.1021/acsbiomaterials.8b00903

Ma, J., Wang, Y., and Liu, J. (2018). Bioprinting of 3D tissues/organs combined with microfluidics. *RSC Adv.* 8, 21712–21727. doi: 10.1039/C8RA03022G

Ma, X., Liu, J., Zhu, W., Tang, M., Lawrence, N., Yu, C., et al. (2018). 3D bioprinting of functional tissue models for personalized drug screening and *in vitro* disease modeling. *Adv. Drug Deliv. Rev.* 132, 235–251. doi: 10.1016/j.addr.2018.06.011

Maiullari, F., Costantini, M., Milan, M., Pace, V., Chirivì, M., Maiullari, S., et al. (2018). A multi-cellular 3D bioprinting approach for vascularized heart tissue engineering based on HUVECs and iPSC-derived cardiomyocytes. *Sci. Rep.* 8:13532. doi: 10.1038/s41598-018-31848-x

Markstedt, K., Mantas, A., Tournier, I., Martínez Ávila, H., Hägg, D., and Gatenholm, P. (2015). 3D bioprinting human chondrocytes with nanocellulose-alginate bioink for cartilage tissue engineering applications. *Biomacromolecules* 16, 1489–1496. doi: 10.1021/acs.biomac.5b00188

McBeth, C., Lauer, J., Ottersbach, M., Campbell, J., Sharon, A., and Sauer-Budge, A. F. (2017). 3D bioprinting of GelMA scaffolds triggers mineral deposition by primary human osteoblasts. *Biofabrication* 9:015009. doi: 10.1088/1758-5090/aa53bd

Moldovan, F. (2019). Recent trends in bioprinting. *Procedia Manuf.* 32, 95–101. doi: 10.1016/j.promfg.2019.02.188

Moroni, L., Boland, T., Burdick, J. A., De Maria, C., Derby, B., Forgacs, G., et al. (2018). Biofabrication: a guide to technology and terminology. *Trends Biotechnol.* 36, 384–402. doi: 10.1016/j.tibtech.2017.10.015

Mouser, V. H. M., Abbadessa, A., Levato, R., Hennink, W. E., Vermonden, T., Gawlitta, D., et al. (2017). Development of a thermosensitive HAMA-containing bio-ink for the fabrication of composite cartilage repair constructs. *Biofabrication* 9:015026. doi: 10.1088/1758-5090/aa6265

Mouser, V. H. M., Melchels, F. P. W., Visser, J., Dhert, W. J. A., Gawlitta, D., and Malda, J. (2016). Yield stress determines bioprintability of hydrogels based on gelatin-methacryloyl and gellan gum for cartilage bioprinting. *Biofabrication* 8:035003. doi: 10.1088/1758-5090/8/3/035003

Naghieh, S., Karamooz-Ravari, M. R., Sarker, M. D., Karki, E., and Chen, X. (2018). Influence of crosslinking on the mechanical behavior of 3D printed alginate scaffolds: experimental and numerical approaches. *J. Mech. Behav. Biomed. Mater.* 80, 111–118. doi: 10.1016/j.jmbbm.2018.01.034

Narayanan, L. K., Huebner, P., Fisher, M. B., Spang, J. T., Starly, B., and Shirwaiker, R. A. (2016). 3D-bioprinting of polylactic acid (PLA) nanofiber–alginate hydrogel bioink containing human adipose-derived stem cells. *ACS Biomater. Sci. Eng.* 2, 1732–1742. doi: 10.1021/acsbiomaterials.6b00196

Nguyen, D., Hägg, D. A., Forsman, A., Ekholm, J., Nimkingratana, P., Brantsing, C., et al. (2017). Cartilage tissue engineering by the 3D bioprinting of iPS cells in a nanocellulose/alginate bioink. *Sci. Rep.* 7:658. doi: 10.1038/s41598-017-00690-y

Noh, I., Kim, N., Tran, H. N., Lee, J., and Lee, C. (2019). 3D printable hyaluronic acid-based hydrogel for its potential application as a bioink in tissue engineering. *Biomater. Res.* 23, 114–123. doi: 10.1186/s40824-018-0152-8

O'Brien, J., Wilson, I., Orton, T., and Pognan, F. (2000). Investigation of the Alamar Blue (resazurin) fluorescent dye for the assessment of mammalian cell cytotoxicity. *Eur. J. Biochem.* 267, 5421–5426. doi: 10.1046/j.1432-1327.2000.01606.x

Ooi, H. W., Mota, C., Tessa Ten Cate, A., Calore, A., Moroni, L., and Baker, M. B. (2018). Thiol-ene alginate hydrogels as versatile bioinks for bioprinting. *Biomacromolecules* 19, 3390–3400. doi: 10.1021/acs.biomac.8b00696

Ouellette, R. J., and Rawn, J. D. (2015). "Synthetic polymer," in *Organic Chemistry Study Guide: Key Concepts, Problems, and Solutions*, eds R. J. Ouellette and J. DavidRawn (Amsterdam: Elsevier), 16. doi: 10.1016/b978-0-12-801889-7.00028-5

Ozbolat, I. T., Moncal, K. K., and Gudapati, H. (2017). Evaluation of bioprinter technologies. *Addit. Manuf.* 13, 179–200. doi: 10.1016/j.addma.2016.10.003

Peak, C. W., Stein, J., Gold, K. A., and Gaharwar, A. K. (2018). Nanoengineered Colloidal Inks for 3D Bioprinting. *Langmuir* 34, 917–925. doi: 10.1021/acs.langmuir.7b02540

Pepelanova, I., Kruppa, K., Scheper, T., and Lavrentieva, A. (2018). Gelatin-methacryloyl (GelMA) hydrogels with defined degree of functionalization as a versatile toolkit for 3D cell culture and extrusion bioprinting. *Bioengineering* 5:55. doi: 10.3390/bioengineering5030055

Polley, C., Mau, R., Lieberwirth, C., Stenzel, J., Vollmar, B., and Seitz, H. (2017). Bioprinting of three dimensional tumor models: a preliminary study using a low cost 3D printer. *Curr. Dir. Biomed. Eng.* 3, 135–138. doi: 10.1515/cdbme-2017-0028

Prasad, A., and Alizadeh, E. (2019). Cell Form and function: interpreting and controlling the shape of adherent cells. *Trends Biotechnol.* 37, 347–357. doi: 10.1016/j.tibtech.2018.09.007

Raddatz, L., Lavrentieva, A., Pepelanova, I., Bahnemann, J., Geier, D., Becker, T., et al. (2018). Development and application of an additively manufactured calcium chloride nebulizer for alginate 3D-bioprinting purposes. *J. Funct. Biomater.* 9:63. doi: 10.3390/jfb9040063

Reid, J. A., Palmer, X.-L., Mollica, P. A., Northam, N., Sachs, P. C., and Bruno, R. D. (2019). A 3D bioprinter platform for mechanistic analysis of tumoroids and chimeric mammary organoids. *Sci. Rep.* 9:7466. doi: 10.1038/s41598-019-43922-z

Ren, X., Wang, F., Chen, C., Gong, X., Yin, L., and Yang, L. (2016). Engineering zonal cartilage through bioprinting collagen type II hydrogel constructs with biomimetic chondrocyte density gradient. *BMC Musculoskelet. Disord.* 17:301. doi: 10.1186/s12891-016-1130-8

Schmieg, B., Schimek, A., and Franzreb, M. (2018). Development and performance of a 3D-printable poly(ethylene glycol) diacrylate hydrogel suitable for enzyme entrapment and long-term biocatalytic applications. *Eng. Life Sci.* 18, 659–667. doi: 10.1002/elsc.201800030

Schütz, K., Placht, A.-M., Paul, B., Brüggemeier, S., Gelinsky, M., and Lode, A. (2017). Three-dimensional plotting of a cell-laden alginate/methylcellulose blend: towards biofabrication of tissue engineering constructs with clinically relevant dimensions. *J. Tissue Eng. Regen. Med.* 11, 1574–1587. doi: 10.1002/term.2058

Schuurman, W., Levett, P. A., Pot, M. W., van Weeren, P. R., Dhert, W. J. A., Hutmacher, D. W., et al. (2013). Gelatin-methacrylamide hydrogels as potential biomaterials for fabrication of tissue-engineered cartilage constructs. *Macromol. Biosci.* 13, 551–561. doi: 10.1002/mabi.201200471

Shin, M., Galarraga, J. H., Kwon, M. Y., Lee, H., and Burdick, J. A. (2018). Gallol-derived ECM-mimetic adhesive bioinks exhibiting temporal shear-thinning and stabilization behavior. *Acta Biomater.* 95, 165–175. doi: 10.1016/j.actbio.2018.10.028

Silva, L. P. (2018). "Current trends and challenges in biofabrication using biomaterials and nanomaterials: future perspectives for 3D/4D bioprinting," in *3D and 4D Printing in Biomedical Applications*, ed M. Maniruzzaman (Weinheim: Wiley-VCH Verlag GmbH & Co. KGaA), 373–421. doi: 10.1002/9783527813704.ch15

Sodupe-Ortega, E., Sanz-Garcia, A., Pernia-Espinoza, A., and Escobedo-Lucea, C. (2018). Accurate calibration in multi-material 3d bioprinting for tissue engineering. *Materials.* 11:1402. doi: 10.3390/ma11081402

Stichler, S., Böck, T., Paxton, N. C., Bertlein, S., Levato, R., Schill, V., et al. (2017). Double printing of hyaluronic acid / poly(glycidol) hybrid hydrogels with poly(ε-caprolactone) for MSC chondrogenesis. *Biofabrication* 9:044108. doi: 10.1088/1758-5090/aa8cb7

Suntornnond, R., Tan, E. Y. S., An, J., and Chua, C. K. (2017). A highly printable and biocompatible hydrogel composite for direct printing of soft and perfusable vasculature-like structures. *Sci. Rep.* 7:16902. doi: 10.1038/s41598-017-17198-0

Tijore, A., Behr, J.-M., Irvine, S. A., Baisane, V., and Venkatraman, S. (2018a). Bioprinted gelatin hydrogel platform promotes smooth muscle cell contractile phenotype maintenance. *Biomed. Microdevices* 20:32. doi: 10.1007/s10544-018-0274-8

Tijore, A., Irvine, S. A., Sarig, U., Mhaisalkar, P., Baisane, V., and Venkatraman, S. (2018b). Contact guidance for cardiac tissue engineering using 3D bioprinted gelatin patterned hydrogel. *Biofabrication* 10:025003. doi: 10.1088/1758-5090/aaa15d

Wang, L. L., Highley, C. B., Yeh, Y. C., Galarraga, J. H., Uman, S., and Burdick, J. A. (2018). Three-dimensional extrusion bioprinting of single- and double-network hydrogels containing dynamic covalent crosslinks. *J. Biomed. Mater. Res. Part A* 106, 865–875. doi: 10.1002/jbm.a.36323

Wang, X.-F., Song, Y., Liu, Y.-S., Sun, Y., Wang, Y., Wang, Y., et al. (2016). Osteogenic differentiation of three-dimensional bioprinted constructs consisting of human adipose-derived stem cells *in vitro* and *in vivo*. *PLoS ONE* 11:e0157214. doi: 10.1371/journal.pone.0157214

Wei, X., Luo, Y., and Huang, P. (2019). 3D bioprinting of alginate scaffolds with controlled micropores by leaching of recrystallized salts. *Polym. Bull.* 76, 6077–6088. doi: 10.1007/s00289-019-02690-6

Wu, D., Yu, Y., Tan, J., Huang, L., Luo, B., Lu, L., et al. (2018). 3D bioprinting of gellan gum and poly (ethylene glycol) diacrylate based hydrogels to produce human-scale constructs with high-fidelity. *Mater. Des.* 160, 486–495. doi: 10.1016/j.matdes.2018.09.040

Wu, Y., Lin, Z. Y., Wenger, A. C., Tam, K. C., and Tang, X. (2018). 3D bioprinting of liver-mimetic construct with alginate/cellulose nanocrystal hybrid bioink. *Bioprinting* 9, 1–6. doi: 10.1016/j.bprint.2017.12.001

Xia, C., Chen, P., Mei, S., Ning, L., Lei, C., Wang, J., et al. (2017). Photo-crosslinked HAMA hydrogel with cordycepin encapsulated chitosan microspheres for osteoarthritis treatment. *Oncotarget* 8, 2835–2849. doi: 10.18632/oncotarget.13748

Xin, S., Chimene, D., Garza, J. E., Gaharwar, A. K., and Alge, D. L. (2019). Clickable PEG hydrogel microspheres as building blocks for 3D bioprinting. *Biomater. Sci.* 7, 1179–1187. doi: 10.1039/c8bm01286e

Xu, C., Lee, W., Dai, G., and Hong, Y. (2018). Highly elastic biodegradable single-network hydrogel for cell printing. *ACS Appl. Mater. Interfaces* 10, 9969–9979. doi: 10.1021/acsami.8b01294

Xu, X., Zhou, J., Jiang, Y., Zhang, Q., Shi, H., and Liu, D. (2018). 3D printing process of oxidized nanocellulose and gelatin scaffold. *J. Biomater. Sci. Polym. Ed.* 29, 1498–1513. doi: 10.1080/09205063.2018.1472450

Yan, M., Lewis, P. L., and Shah, R. N. (2018). Tailoring nanostructure and bioactivity of 3D-printable hydrogels with self-assemble peptides amphiphile (PA) for promoting bile duct formation. *Biofabrication* 10:035010. doi: 10.1088/1758-5090/aac902

Yang, X., Lu, Z., Wu, H., Li, W., Zheng, L., and Zhao, J. (2017). Collagen-alginate as bioink for three-dimensional (3D) cell printing based cartilage tissue engineering. *Mater. Sci. Eng. C* 83, 195–201. doi: 10.1016/j.msec.2017.09.002

Yoon, Y., Kim, C. H., Lee, J. E., Yoon, J., Lee, N. K., Kim, T. H., et al. (2019). 3D bioprinted complex constructs reinforced by hybrid multilayers of electrospun nanofiber sheets. *Biofabrication* 11:025015. doi: 10.1088/1758-5090/ab08c2

Yu, F., Han, X., Zhang, K., Dai, B., Shen, S., Gao, X., et al. (2018). Evaluation of a polyvinyl alcohol-alginate based hydrogel for precise 3D bioprinting. *J. Biomed. Mater. Res. Part A* 106, 2944–2954. doi: 10.1002/jbm.a.36483

Zalipsky, S., and Harris, J. M. (1997). "Introduction to Chemistry and Biological Applications of Poly(ethylene glycol)," in *Poly(ethylene glycol) ACS Symposium Series*, eds J. M. Harris and S. Zalipsky (Washington, DC: American Chemical Society), 1. doi: 10.1021/bk-1997-0680.ch001

Zhang, J., Allardyce, B. J., Rajkhowa, R., Zhao, Y., Dilley, R. J., Redmond, S. L., et al. (2018). 3D Printing of silk particle-reinforced chitosan hydrogel structures and their properties. *ACS Biomater. Sci. Eng.* 4, 3036–3046. doi: 10.1021/acsbiomaterials.8b00804

Zhang, K., Fu, Q., Yoo, J., Chen, X., Chandra, P., Mo, X., et al. (2016). 3D bioprinting of urethra with PCL/PLCL blend and dual autologous cells in fibrin hydrogel: An *in vitro* evaluation of biomimetic mechanical

property and cell growth environment. *Acta Biomater.* 50, 154–164. doi: 10.1016/j.actbio.2016.12.008

Zhang, X., Kim, G. J., Kang, M. G., Lee, J. K., Seo, J. W., Do, J. T., et al. (2018). Marine biomaterial-based bioinks for generating 3D printed tissue constructs. *Mar. Drugs* 16:484. doi: 10.3390/md16120484

Zheng, Z., Wu, J., Liu, M., Wang, H., Li, C., Rodriguez, M. J., et al. (2018). 3D bioprinting of self-standing silk-based bioink. *Adv. Healthc. Mater.* 7:1701026. doi: 10.1002/adhm.201701026

Zhou, M., Lee, B. H., Tan, Y. J., and Tan, L. P. (2019). Microbial transglutaminase induced controlled crosslinking of gelatin methacryloyl to tailor rheological properties for 3D printing. *Biofabrication* 11:25011. doi: 10.1088/1758-5090/ab063f

Conflict of Interest: The authors declare that the research was conducted in the absence of any commercial or financial relationships that could be construed as a potential conflict of interest.

7.2 Optimization of computational simulations on bioprinting nozzles: A combination of systematic review and design of experiments

applied sciences

MDPI

Review

Optimization of Computational Simulations on Bioprinting Nozzles: A Combination of Systematic Review and Design of Experiments

Juan Carlos Gómez Blanco[1,*], María López Espino[2], Antonio Macías-García[2], Antonio Díaz-Parralejo[2], Pedro Macías Blanco[3], José Blas Pagador Carrasco[1*], Francisco Miguel Sánchez Margallo[1]

[1] Jesús Usón Minimally Invasive Surgery Centre. Carretera N-521, km41.8 (10071) Cáceres, Spain
[2] University of Extremadura. Avda. Elvas, s/n (06006) Badajoz, Spain
[3] Hospital del Perpetuo Socorro. Servicio de Rayos X. Av. Damián Téllez Lafuente, S/N, (06010) Badajoz, Spain
* Correspondence: jcgomez@ccmijesususon.com

Received: date; Accepted: date; Published: date

Abstract: 3D printing, also known as additive manufacturing, is a process that builds physical objects depositing material layer by layer. One of the main applications of additive manufacturing is bioprinting. This technology is based in the use on living cells and biocompatible materials to create specific three-dimensional structures facilitating the efficient development of living tissues. Bioprinting can be a harmful process to cells because high pressures and shear stress can be found within the hydrogel. In this sense, computational simulations are used to study and improve the bioprinting procedure reducing inner pressure and stress while increasing cell viability. Hence, this work is focused on performing a systematic review on computational simulation of bioprinting nozzles and proposing a design of experiment test to optimize the nozzle design. Results show that the heterogeneous data obtained is hardly comparable but some ranges for nozzle geometry are defined: diameter (0.2–1 mm) and length (8–10 mm; 300–900 μm). Additionally, some recommendations to improve nozzle performance are detected: inner angle (20–30°) and inner coating (EDTA). Likewise, shear stress below 5 kPa is recommended. Finally, a design of experiments is presented such as tool to obtain optimum bioprinting setting for a specific bioink based on data collected from the review.

Keywords: Bioprinting; μ-extrusion; computational simulation; nozzle; Design of Experiments

1. Introduction

3D printing, also known as additive manufacturing, is a fabrication process in which physical objects are created by the superposition of different material layers based on a digital model. The additive manufacturing process begins with a 3D model generated by CAD software (Computer Aided Design). This file is the input needed to generate a G-code file where all 3D printer parameters and movement orders are set up. This technology allows the use of different materials such as polymers, resins, metals or paper, among others, depending on the type of 3D printing procedure used. So, materials and procedures determine the application, although the most common one is prototyping on industrial design, architecture or medicine.

As said before, one of the main applications of additive manufacturing is related with medicine. The application of additive manufacturing to the creation of tissue is called 3D bioprinting. This technology uses cells together with a biocompatible material to create specific three-dimensional

structures that serves as a support and nutrient for these cells. The later incubation of this seeded structure will produce a living tissue.

In bioprinting, materials with well-defined properties are often used as a vehicle for cells. That is, they have specific biological, physical and mechanical properties to facilitate the bioprinting process while minimizing cell damage. The development of adequate biomaterials (bioinks) to get complex geometries while enhance cell survival is considered one of the most important challenges of bioprinting [1].

According to the bioprinting technology, there are three main families: inkjet, laser-assisted, and μ-extrusion bioprinters [2,3]. Each one of these techniques has advantages and limitations such as cellular density in bioink, resolution or fabrication speed that must be considered for each specific application.

Although most of hydrogel studies for bioprinting are usually done by experimental tests, only a few of them use computer simulations. Computational Fluid Dynamics (CFD), as a part of fluid mechanics, uses computational numerical analysis to analyze and solve flow and fluid movement. According to the complexity of the equations to be solved, the dependence of the solution with the problem geometry, the boundary conditions used and the high number of degrees of freedom present in this type of problem, CFD can be a reasonable alternative when it comes to obtain solutions in fluid dynamic problems in many cases. In this sense, CFD is a powerful tool to perform systematic studies of bioinks. The possibility of modifying rheological parameters of bioinks and study their behavior with a computer is an optimum path to maximize the amount of bioinks while minimizing costs. However, due to high number of parameters and multiple possible combinations, performing all simulations would be costly and time consuming. For this reason, a design of experiments (DoE) is proposed as a complementary technique to use collected data in this review to get optimized bioprinting parameter values with an affordable number of experiments.

This work focuses on knowing the state of the art in this technology, through a systematic review on computational simulations in bioprinting nozzles. Specifically, this review studies CFD of μ-extrusion bioprinting technique, making a compilation of useful concepts for the design and improvements of μ-extrusion systems. Additionally, using all data obtained from the review a design of experiments is proposed as an example of possible optimized procedure to perform several computational simulations.

2. Materials and Methods

2.1. Systematic review

A PRISMA guideline systematic review was conducted. The review included all original peer-review articles with the following criteria:

1. The paper is in Spanish or English language.
2. Papers are related to CFD simulations in bioprinting, but specifically in terms of the nozzle or the printhead.
3. Only peer review original articles were accepted.
4. All papers based on laser assisted or stereolithography bioprinting were excluded.

Papers based on inkjet bioprinting were accepted due the existence of a extruder-head despite they are not μ-extrusion bioprinting.

PUBMED, WOS and SCOPUS were the selected search engines with the following search strings:

- "bioprinting AND extrusion AND nozzle".
- "bioprinting AND nozzle AND computational".
- "bioprinting AND nozzle AND fluid".
- "bioprinting AND nozzle AND printhead".

All data were collected and recorded following the conceptual map of Figure 1. In this sense, all possible information will be divided into 2 main blocks. The first one regarding to bioprinting hardware and laboratory conditions and, the second one regarding to all features of computational simulations. Both main blocks are sequentially sub-divided to grant equally distributed information and fair comparison.

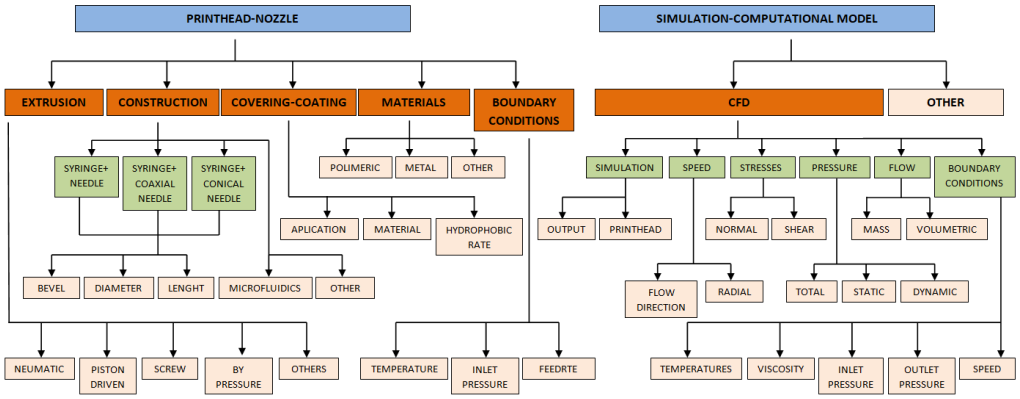

Figure 1. Concept map for data extraction of computational simulation of bioprinting nozzles.

As an example of one possible application of the data of the reviewed information an example of design of experiments is proposed.

2.2. Design of experiments

A design of experiments could be used to select the most favorable conditions to obtain the optimum values of those parameters that can affect the bioprinting process. To this end, different working conditions should be simulated using the bioprinting model. The objective would be to establish the influence of these operating variables on the bioprinting process, as well as the possible interactions between them. After that, results should be analyzed to determine optimum values within the study limits.

A Factorial, Central, Composite, Orthogonal and Rotatable Design of Experiments (FCCOR DoE) is proposed, and some operational variables and response variables should be selected.

The total number of experimental runs (N) for the statistical design will be $N=2^k + 2k + n$, where k is the number of operational variables and n is the number of replications of the central experiment. In the case k was equal to 4, and n was 12 to ensure both, orthogonality and rotatability of the design, the design should consist of a total of 36 experiments. The axial distance must be defined as $\phi=(Nf)/4$ where Nf is the number of factorial experiments, e.g., 2k. Hence, since k=4, ϕ was equal to 2. The values of every parameter that must be used in the experiments are usually codified as (-2, -1, 0, 1, 2) for easy reading of the experimental procedure and they are collected in tables (see Table 1, Table 2 and Table 3 in results).

Once all experiments are done the statistical analysis of the experimental results is usually performed using a specific software, e.g., Statgraphics Centurion XVI™ software. The statistical analysis must include an ANOVA test and a Quadratic Regression Analysis to obtain the response fitting curve. This fitted curve shows the experimental conditions leading to an optimum value of the response variables. Lastly, a graphical analysis of the experimental results is usually done using the Pareto, main effects, interactions and response surface (RS) plots.

In this work is calculated the first part of an example of DoE using the review data obtained. The idea is to provide the reader with an example of how DoE can help in the optimization of the number of tests to be done. In this sense, only the codification of data is performed and shown in results.

3. Results

3.1. Systematic review analysis

A total of 74 papers were obtained using these search strings. After that, repeated ones and those that did not match the inclusion criteria were discarded, obtaining a final number of 18 papers to analyze (Figure 3).

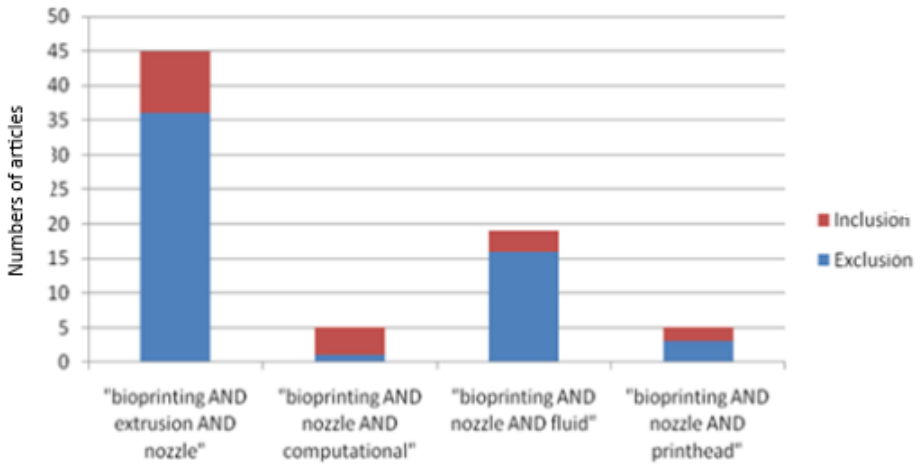

Figure 3. Items included and excluded from the systematic review based on the connectors used.

3.2. Data analysis

Once all papers were analyzed some features can be discussed. Following the block division performed, the first results to discuss are the ones regarding to all features of bioprinting hardware. In this sense, from all selected papers 14 are original works, the other 4 papers are general bioprinting reviews. In those reviews [2,3,5,6] general information of bioprinting is provided including an explanation of technology types, materials used, among other useful information. In general, most of papers use extrusion bioprinting, except for Carmelo de María et al. [7] and Shi et al. [8] that use inkjet bioprinting or Ponce-Torres et al. [9] that use a gas flow to produce fibers.

According to the 14 original papers, there are a huge discrepancy between the geometrical construction of the nozzle. Three main constructions were used: syringe with a coaxial needle [5,10], syringe with a conical tip [8,11,12] and microfluidics nozzles [13,14]. Other authors use different geometries [7,9,15–19]. From all information, the nozzle diameter varies from 0.2 to 1 mm. Specifically, those studies using coaxial needle proposed diameters of 810, 710 and 630 μm [10] or 200-450 μm [5], while those ones using conical tip used 100 μm [8], 500-1000 μm [11] or 440 μm [12]. Additionally, the studies simulating microfluidics used nozzles with several diameters: 840, 610, 400, 250 and 200 μm [13] or 1270, 910 and 470 μm [14]. Regarding the nozzle length, Martanto et al. [11] and Reid et al. [20] agree using 8.9 and 10 mm, while Jia Shi et al. [8] and Ponce-Torres et al. [9] use 300 and 900 μm, respectively. Martanto et al. [11] perform a very complete study of geometrical influence in extrusion simulations and, one of the most important results is the recommendation of an inner nozzle angle from 20 to 30° to reduce shear stress. It is important to note that this large range of variation in geometrical measurements makes it difficult to have a fair comparison of results among different studies (Figure 4).

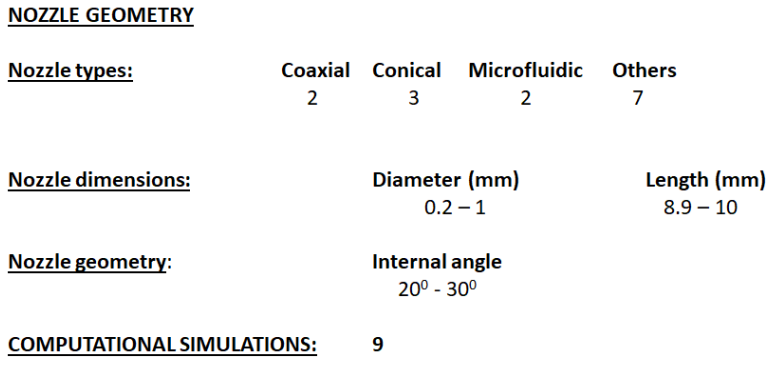

Figure 4. Summarized nozzle geometry data obtained from the 14 original papers.

Other important factor to be considered is the inner coating of the nozzle or the materials used for its construction. This information can be very helpful in computational simulations due to friction between the bioink and the walls of the nozzle, provoking different shear stress and cell damages. Unfortunately, only Parzel et al [16] uses Ethylene Diamine Tetra-acetic Acid (EDTA) as an inner coating and Shi et al [8] and Ponce-Torres [9,19] use glass as a construction material. The rest of the authors do not specify any kind of coating or material to be considered.

On the other hand, the most important physical parameters in the bioprinting process are summarized in Figure 5.

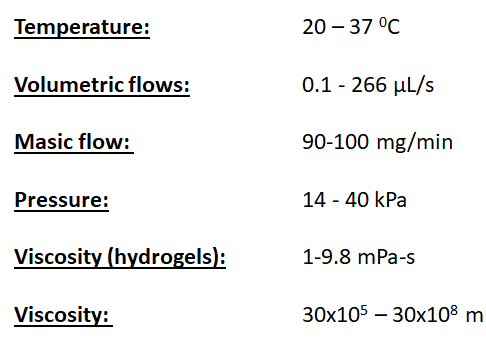

Figure 5. Physical Parameters of the bioprinting.

Laboratory atmospheric parameters can have a high impact on the rheological parameters of the used bioink. Among all analyzed papers, authors present their results at room temperature [3,16,19] or at 37 °C [5,11,15,20].

The second main block is regarding to all features of computational simulations. Regarding to boundary conditions, inlet flow is the most important condition to set due to without it no flow is possible. According to Bernouilli equation the inlet flow can be set using a pressure or a velocity. It can be also set as an amount of material per time which is, at last term, a velocity as it is described by the continuum equation. So, authors used inlet volumetric flows with values varying from 0.1 to 266 µL/s [11,12,14,20] or masic flow of 90-100 mg/min [12]. In the same way, Göhl et al [12] used pressure varying from 14 to 40 kPa as the inlet pressure of the bioink. These inlet values together with geometries and material properties, as viscosity or surface tension, determines the material flow. Unfortunately, not all authors showed the viscosity of their bioinks. For example, authors as Shi et al

[8] and Martanto et al [11] used hydrogels with viscosities varying in the range of 1-9.8 mPa·s. Other authors as Derakshanfar et al [2], Suntornnond et al [18] or Kyle et al [3] use bioinks with higher viscosities on the range $3x10^3$ – $3x10^6$ Pa·s. In this sense, all boundary data obtained from the 9 papers performing computational simulation of their systems is hardly comparable. Different geometries, materials, boundary conditions and/or inlet parameters makes nearly impossible to obtain usable common features apart from a summarization of the results.

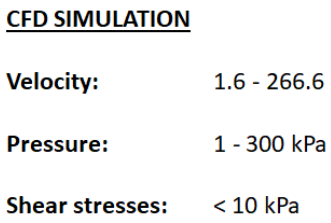

Figure 6. CFD simulation (14 original papers).

The main results of CFD simulations works are summarized in Figure 6. The most usual reported parameters are velocity, pressure, and stress. In this sense, the velocities reported by authors vary from 1.6 to 266.6 mm/s [5,10,12,14,15,17–20] with a single value beyond this range which is 3.04m/s in the work of Shi et al [8]. Pressures varies from 1 to 300 kPa [5,11,15,18–20], but several authors conclude that shear stress must be below 10 kPa [3,8].

3.3. Design of experiments

Although all obtained data from the review is hardly comparable it can be used in DoE as input data to calculate a desired output. In the proposed example the selected input data vary from, 20 to 37 °C for temperature (T), from 266 to 0.1 μL/s for volumetric flow (V), from 0.2 to 1 mm for inner diameter (D) and from $3x10^3$ – $3x10^6$ Pa·s for viscosity (ν).

So, in our example the number of variables was 4, so ϕ was equal to 2 and the coded values of each of the four operating design variables were (-2, -1, 0, 1, 2).

The input values of each variables of the simulations of this example are calculated from maximum, minimum and central values. The calculated step for the codification of data is shown in Table 1 as well as central, maximum and minimum values.

Table 1. Maximum, central, minimum value and step of the variables.

Variables	Minimum	Central	Maximum	Step
Temperature (T)	20	28.50	37	4.25
Volumetric flow (V)	0.1	133.050	266	66.475
Inner diameter (D)	0.20	0.60	1.00	0.2
Viscosity (v)	$3x10^3$	$1.50x10^6$	$3x10^6$	$7.49x10^5$

Using the values in Table 1, the codification of values for each input variable are shown in Table 2.

Table 2. De-codification table for experiments of each input variable.

Variables	-2	-1	0	1	2
Temperature (T)	20	24.25	28.50	32.75	37
Volumetric flow (V)	0.10	66.58	133.05	199.53	266
Inner diameter (D)	0.20	0.40	0.60	0.80	1.00
Viscosity (v)	$3.00x10^3$	$7.52x10^3$	$1.50x10^6$	$2.25x10^6$	$3.00x10^6$

Experiments, in this example all different simulations, must be done using the order shown in Table 3 to prevent bias. Input values for each simulation must be obtained de-coding the values with Table 2. Once all experiments are performed and measured the response variables statistical analysis must be done to obtain determine the optimal conditions that should be used to obtain the best experimental result.

Table 3. Codification table for experiments.

Experiment	T	V	D	ν	Experiment	T	V	D	ν
1	0	2	0	0	**19**	0	0	0	2
2	0	0	0	0	**20**	-1	1	-1	-1
3	1	1	-1	-1	**21**	0	0	-2	0
4	-1	-1	-1	-1	**22**	-1	1	1	1
5	-1	-1	-1	1	**23**	0	0	0	0
6	0	0	0	0	**24**	0	-2	0	0
7	0	0	2	0	**25**	1	-1	-1	-1
8	0	0	0	0	**26**	0	0	0	0
9	1	1	1	-1	**27**	0	0	0	0
10	0	0	0	-2	**28**	1	1	1	1
11	0	0	0	0	**29**	1	-1	-1	1
12	-1	1	1	-1	**30**	0	0	0	0
13	-1	-1	1	1	**31**	0	0	0	0
14	-1	-1	1	-1	**32**	1	-1	1	1
15	0	0	0	0	**33**	0	0	0	0
16	0	0	0	0	**34**	1	-1	1	-1
17	1	1	-1	1	**35**	-2	0	0	0
18	2	0	0	0	**36**	-1	1	-1	1

4. Conclusions

In this review, the main variables involved in a bioprinting nozzle design and its use are identified. Furthermore, common ranges for nozzle diameter (0.2 – 1 mm) and length (standard of 8 – 10 mm and microneedle version of 300 - 900 μm) are exposed. Regarding to CFD, a heterogeneous setting of simulation makes difficult a fair comparison among all studies, but maybe an interesting conclusion is the need to keep shear stress below 5 kPa to maximize cell viability. Likewise, some authors recommend the following features for a better performance of the nozzle: inner angle (20 – 30°) to reduce shear stress or inner coating (EDTA).

Finally, design of experiments method is proposed to optimize bioprinting parameters using data obtained in the previous review. An example of the first steps of this method were calculated but, as future work all simulations and final DoE calculations of this example will be done.

Author contribution: Conceptualization: Juan Carlos Gómez Blanco, Antonio Macías García, Antonio Díaz-Parralejo. and José Blas Pagador Carrasco; Methodology: Juan Carlos Gómez Blanco, Antonio Macías García and José Blas Pagador Carrasco; Formal Analysis: Juan Carlos Gómez Blanco and María López Espino.; Investigation: Juan Carlos Gómez Blanco, Antonio Díaz-Parralejo and José Blas Pagador Carrasco; Resources: José Blas Pagador Carrasco; Writing – Original Draft Preparation: Juan Carlos Gómez Blanco, María López Espino, Antonio Macías García and José Blas Pagador Carrasco; Writing – Review & Editing: Juan Carlos Gómez Blanco, Antonio Macías García, Antonio Díaz-Parralejo, Pedro Macías Blanco, José Blas Pagador Carrasco and Francisco Miguel Sánchez Margallo; Supervision: José Blas Pagador Carrasco and Francisco Miguel Sánchez Margallo; Project Administration: Juan Carlos Gómez Blanco and José Blas Pagador Carrasco; Funding Acquisition: José Blas Pagador Carrasco and Francisco Miguel Sánchez Margallo.

Acknowledgments: This research was financed by project number IB16200, project number 0633_BIOIMPACE_4_A and predoctoral grant number PD16067 to J.C.G.-B. Co-financed by European Union/ERDF, ESF, European Regional Development Fund ERDF under the Interreg V A Spain - Portugal (POCTEP) 2014-2020 program and Consejería de Economía, Ciencia y Agenda Digital de la Junta de Extremadura. The APC was funded by project number 0633_BIOIMPACE_4_A

Conflicts of Interest: The authors declare that they have no conflict of interest.

References

1. F. Pati, J. Gantelius, and H. A. Svahn, "3D bioprinting of tissue/organ models," Angew. Chemie Int. Ed., vol. 55, no. 15, pp. 4650–4665, 2016.
2. S. Derakhshanfar, R. Mbeleck, K. Xu, X. Zhang, W. Zhong, and M. Xing, "3D bioprinting for biomedical devices and tissue engineering: A review of recent trends and advances," Bioact. Mater., vol. 3, no. 2, pp. 144–156, 2018, doi: 10.1016/j.bioactmat.2017.11.008.
3. S. Kyle, Z. M. Jessop, A. Al-Sabah, and I. S. Whitaker, "'Printability'' of Candidate Biomaterials for Extrusion Based 3D Printing: State-of-the-Art,'" Adv. Healthc. Mater., vol. 6, no. 16, 2017, doi: 10.1002/adhm.201700264.
4. O. A. Beltrán, "Revisionessistemáticas de la literatura," Rev. Colomb. Gastroenterol., vol. 20, no. 1, pp. 60–69, 2005.
5. A. Panwar and L. P. Tan, "Current status of bioinks for micro-extrusion-based 3D bioprinting," Molecules, vol. 21, no. 6, 2016, doi: 10.3390/molecules21060685.
6. I. T. Ozbolat and M. Hospodiuk, "Current advances and future perspectives in extrusion-based bioprinting," Biomaterials, vol. 76, pp. 321–343, 2016, doi: 10.1016/j.biomaterials.2015.10.076.
7. C. De Maria et al., "Design and validation of an open-hardware print-head for bioprinting application," Procedia Eng., vol. 110, pp. 98–105, 2015, doi: 10.1016/j.proeng.2015.07.015.
8. J. Shi, B. Wu, S. Li, J. Song, B. Song, and W. F. Lu, "Shear stress analysis and its effects on cell viability and cell proliferation in drop-on-demand bioprinting," Biomed. Phys. Eng. Express, vol. 4, no. 4, 2018, doi: 10.1088/2057-1976/aac946.
9. A. Ponce-Torres, E. Ortega, M. Rubio, A. Rubio, E. J. Vega, and J. M. Montanero, "Gaseous flow focusing for spinning micro and nanofibers," Polymer (Guildf)., vol. 178, p. 121623, 2019.
10. Q. Gao, Y. He, J. zhong Fu, A. Liu, and L. Ma, "Coaxial nozzle-assisted 3D bioprinting with built-in microchannels for nutrients delivery," Biomaterials, vol. 61, pp. 203–215, 2015, doi: 10.1016/j.biomaterials.2015.05.031.
11. W. Martanto, S. M. Baisch, E. A. Costner, M. R. Prausnitz, and M. K. Smith, "Fluid dynamics in conically tapered microneedles," AIChE J., vol. 51, no. 6, pp. 1599–1607, 2005.
12. J. Göhl, K. Markstedt, A. Mark, K. Håkansson, P. Gatenholm, and F. Edelvik, "Simulations of 3D bioprinting: Predicting bioprintability of nanofibrillar inks," Biofabrication, vol. 10, no. 3, 2018, doi: 10.1088/1758-5090/aac872.
13. D. Kang et al., "Pre-set extrusion bioprinting for multiscale heterogeneous tissue structure fabrication," Biofabrication, vol. 10, no. 3, 2018, doi: 10.1088/1758-5090/aac70b.
14. R. Attalla, E. Puersten, N. Jain, and P. R. Selvaganapathy, "3D bioprinting of heterogeneous bi- and tri-layered hollow channels within gel scaffolds using scalable multi-axial microfluidic extrusion nozzle," Biofabrication, vol. 11, no. 1, 2019, doi: 10.1088/1758-5090/aaf7c7.
15. K. H. Kang, L. A. Hockaday, and J. T. Butcher, "Quantitative optimization of solid freeform deposition of aqueous hydrogels," Biofabrication, vol. 5, no. 3, p. 35001, 2013.
16. C. A. Parzel, M. E. Pepper, T. Burg, R. E. Groff, and K. J. L. Burg, "EDTA enhances high-throughput two-dimensional bioprinting by inhibiting salt scaling and cell aggregation at the nozzle surface," J. Tissue Eng. Regen. Med., vol. 3, no. 4, pp. 260–268, 2009.
17. K. Pusch, T. J. Hinton, and A. W. Feinberg, "Large volume syringe pump extruder for desktop 3D printers," HardwareX, vol. 3, no. February, pp. 49–61, 2018, doi: 10.1016/j.ohx.2018.02.001.
18. R. Suntornnond, E. Y. S. Tan, J. An, and C. K. Chua, "A Mathematical Model on the Resolution of Extrusion Bioprinting for the Development of New Bioinks," Materials (Basel)., vol. 9, no. 9, 2016, doi: 10.3390/ma9090756.

19. A. Ponce-Torres, E. J. Vega, A. A. Castrejón-Pita, and J. M. Montanero, "Smooth printing of viscoelastic microfilms with a flow focusing ejector," J. Nonnewton. Fluid Mech., vol. 249, pp. 1–7, 2017, doi: 10.1016/j.jnnfm.2017.09.004.
20. J. A. Reid, P. A. Mollica, G. D. Johnson, R. C. Ogle, R. D. Bruno, and P. C. Sachs, "Accessible bioprinting: Adaptation of a low-cost 3D-printer for precise cell placement and stem cell differentiation," Biofabrication, vol. 8, no. 2, 2016, doi: 10.1088/1758-5090/8/2/025017.

7.3 Bioink temperature influence on shear stress, pressure and velocity using computational simulation

Dr. José Blas Pagador Carrasco, como director de la tesis titulada “Desarrollo de un sistema de bioimpresión para posicionar líneas celulares”, certifico el factor de impacto y la categorizacion de la siguiente publicación, incluida en la tesis doctoral. Del mismo modo, se especifica la aportación del doctorando.

Autores: **J. Carlos Gómez-Blanco**, Enrique Mancha-Sánchez, Alfonso C. Marcos, Manuel Matamoros, Antonio Díaz-Parralejo and J. Blas Pagador

Título: Bioink Temperature Influence on Shear Stress, Pressure and Velocity Using Computational Simulation

Revista: Processes

Otros datos: vol 8, nº: 7, pág. 865, año 2020

DOI: 10.3390/pr8070865

Factor de impacto: 2.753 (Q2 – Engineering, Chemical)

Abstract: Bioinks are usually cell-laden hydrogels widely studied in bioprinting performing experimental tests to tune their rheological properties, thus increasing research time and development costs. Computational Fluids Dynamics (CFD) is a powerful tool that can minimize iterations and costs simulating the material behavior using parametric changes in rheological properties under testing. Additionally, most bioinks have specific functionalities and their properties might widely change with temperature. Therefore, commercial bioinks are an excellent way to standardize bioprinting process, but they are not analyzed in detail. Therefore, the objective of this work is to study how three temperatures of the Cellink Bioink influence shear stress pressure and velocity through computational simulation. A comparison of three conical nozzles (20, 22, and 25G) for each temperature has been performed. The results show that shear stress, pressure, and velocity vary in negligible ranges for all combinations. Although these ranges are small and define a good thermo-responsive bioink, they do not generate a filament on the air and make drops during extrusion. In conclusion, this bioink provides a very stable behavior with low shear stress, but other bioprinting parameters must be set up to get a stable filament width.

Contribución del doctorando: Conceptualization, Formal analysis, Investigation, Methodology, Project administration, Software, Writing—original draft, Writing—review and editing

Contribuciones de los coautores: Conceptualization, J.C.G.-B., A.D.-P. and J.B.P.; Formal analysis, J.C.G.-B.; Investigation, J.C.G.-B., E.M.-S. and J.B.P.; Methodology, J.C.G.-B. and E.M.-S.; Project administration, J.C.G.-B. and J.B.P.; Software, J.C.G.-B., E.M.-S., A.C.M. and M.M.; Supervision, J.B.P.; Writing—original draft, J.C.G.-B.; Writing—review and editing, J.C.G.-B., E.M.-S., A.C., M.M., A.D.-P. and J.B.P. All authors have read and agreed to the published version of the manuscript.

processes

MDPI

Article

Bioink Temperature Influence on Shear Stress, Pressure and Velocity Using Computational Simulation

J. Carlos Gómez-Blanco [1,*], Enrique Mancha-Sánchez [1], Alfonso C. Marcos [2], Manuel Matamoros [2], Antonio Díaz-Parralejo [3] and J. Blas Pagador [1,*]

1 Jesús Usón Minimally Invasive Surgery Centre, 10002 Cáceres, Spain; emancha@ccmijesususon.com
2 Graphic Expression Department, Industrial Engineering School, Universidad de Extremadura, 06006 Badajoz, Spain; acmarcos@unex.es (A.C.M.); manuelmp@unex.es (M.M.)
3 Mechanical, Energy and Materials Engineering Department, Industrial Engineering School, Universidad de Extremadura, 06006 Badajoz, Spain; adp@unex.es
* Correspondence: jcgomez@ccmijesususon.com (J.C.G.-B.); jbpagador@ccmijesususon.com (J.B.P.)

Received: 28 May 2020; Accepted: 16 July 2020; Published: 17 July 2020

Abstract: Bioinks are usually cell-laden hydrogels widely studied in bioprinting performing experimental tests to tune their rheological properties, thus increasing research time and development costs. Computational Fluids Dynamics (CFD) is a powerful tool that can minimize iterations and costs simulating the material behavior using parametric changes in rheological properties under testing. Additionally, most bioinks have specific functionalities and their properties might widely change with temperature. Therefore, commercial bioinks are an excellent way to standardize bioprinting process, but they are not analyzed in detail. Therefore, the objective of this work is to study how three temperatures of the Cellink Bioink influence shear stress pressure and velocity through computational simulation. A comparison of three conical nozzles (20, 22, and 25G) for each temperature has been performed. The results show that shear stress, pressure, and velocity vary in negligible ranges for all combinations. Although these ranges are small and define a good thermo-responsive bioink, they do not generate a filament on the air and make drops during extrusion. In conclusion, this bioink provides a very stable behavior with low shear stress, but other bioprinting parameters must be set up to get a stable filament width.

Keywords: bioprinting; computational simulation; bioprinting material; commercial bioink; temperature; level-set; fluid dynamics

1. Introduction

Additive manufacturing technology is currently contributing with many possibilities to tissue engineering. In this sense, 2D structures created by standard procedures of tissue engineering can evolve into complex 3D structures using bioprinting [1]. Specifically, bioprinting could produce these complex structures by superposing biomaterial layers with several biological compounds that finally can generate artificial tissues and organs [2]. Bioprinting can also minimize rejection risk when patient's cells are used in the creation of autologous tissues and/or organs [1]. Bioprinting is usually divided into four main technologies: micro-extrusion, inkjet, laser-assisted, and stereolithography [3]. However, properties such as versatility, printing speed, and the possibility of using high viscous materials with a high cell density make micro-extrusion the most used bioprinting technique [1,3,4].

Because of their high importance in the bioprinting process, several studies analyzed how different materials affect cellular survival [5,6], printability [7–9], curing or cross-linking [9–12], and shape fidelity [13,14]. The bioinks used in bioprinting are usually cell-laden hydrogels with

very specific rheological properties. One of the most important properties is viscosity, which has a great impact on the bioink behavior of the bioink during bioprinting [15,16]. Most hydrogels are classified as non-Newtonian fluids, so their viscosity changes when a force is applied. Attending to this viscous behavior, non-Newtonian fluids are mainly classified into shear thickening (viscosity rises when shear rate increases) or shear thinning (viscosity decreases when shear rate increases). Some reviews focus their interest on these hydrogel properties and their influence on the bioprinting process [17–19]. Specifically, the material concentration was experimentally tested to analyze the behavior of the hydrogel at different temperatures and to optimize printability [8,9,20]. Usually, the higher the material viscosity, the higher the printability, at least up to a viscosity value in which internal pressures generated can damage cells. Additionally, other works analyze how temperature affects the bioink viscosity [21–24]. All of them conclude that viscosity decreases when temperature is increased in most bioprinting materials, such as GelMA, alginate and, many other thermo-responsive materials. However, each bioink must be studied separately to quantify these rheological changes with temperature. Therefore, the behavior of the bioink flowing inside a nozzle is an important aspect to determine, but difficult to achieve with experimental tests, mainly due to the small size of the nozzles, which are hardly sensorized without any scaling technique. In this sense, experimental tests of bioink behavior are usually focused on bioprinting results, such as printability, shape fidelity, or cell viability, but not so commonly on the parameters of the process that can influence the results, such as shear stress, pressure or velocity, during bioprinting. This approach is far from ideal due to the high number of test iterations and economic costs associated, so computational simulation is proposed as a very helpful tool to perform parametrical series of studies [25,26]. Computational Fluids Dynamics (CFD) are widely used to obtain flow behavior in simple (e.g., pipes) or more complicated (e.g., cranial aneurysms) designs [27]. Specifically, CFD can calculate microfluidics inner parameters, such as velocity, pressure or shear stress, which are experimentally difficult to measure. It is well known that nozzle inner pressures, and more specifically shear stress, have a major impact on cell viability [28]. Therefore, the higher the shear stress is, the lower the cellular viability. Specifically, Blaeser et al. [29] determined that cells affected by low shear stress (<5 kPa) have high cellular viability (up to 96%), while increasing the shear stress (5-10 and >10 kPa) results in lower cellular viability (91% and 76%, respectively). Other authors have performed several computational simulations to study shear stress [30], non-commercial nozzle geometries [31–33], different bioprinting materials [34] or tuned rheological properties of specific materials [26,35]. It is important to note that printability and shape fidelity are bioprinting measures which are highly dependent on the dynamic relationship between nozzle and printing substrate. For this reason, several studies analyze parameters such as the separation between nozzle and printing substrate and the XY-plane speed of the nozzle while printing in detail [9,30,34]. These bioprinting settings will affect the bioink filament width that directly relates not only to shape fidelity, but also to filament width stability. In this sense, we understand stability, such as the property of a bioink, produces a well-known width of filament that could be maintained during the whole bioprinting process. A computational simulation of this dynamic interaction is highly complex, so, in this study, the interaction with the printing substrate is removed and a preliminary analysis of the bioink filament stability on the air is proposed.

Computational simulations are used to study several inner nozzle parameters of the nozzle in two main fields: either referring to the effect of nozzle geometry with fixed bioink properties [31–33,36,37] or to the bioink behavior with fixed geometry [26,30,34,38–40]. However, very few authors also perform simulations and studying cells deformation during the bioprinting procedure [37]. Some authors performed more complex simulations to study droplet formation using a Two-Phase Level Set [40,41] and to analyze the filament deposition and the final bioprinted shape using a surface tension model [26]. Liravi et al. [40] and Smanipour et al. [41] used COMSOL Multiphysics to simulate the generation of droplets with a 27G conical tip and a custom-made micro-encapsulation device, respectively. Both studies focused on obtaining a realistic geometrical droplet compared to an experimental test. Thus, inner nozzle flow parameters (pressure, velocity or shear stress) were not reported, although

these parameters are essential to determine whether cells survive. Despite using the same mathematical model, none of them reported the numerical methods used, so the reproducibility of their research is hindered. Furthermore, three main differences can be noticed between both works. Firstly, they provide different levels of detail for the mesh. Liravi et al. [40] used a very specific mesh generation with a remeshing procedure developed by Wilkes et al. [42] to properly generate droplets. On the contrary, Samanipour et al. [41] did not even mention the mesh they generated for their simulations. Secondly, the characterization of the material is done under different fluid assumptions. Liravi et al. [40] used a Carreau–Yasuda potential model to fit the rheological data of a non-Newtonian material, while Samanipour et al. [41] used a constant value for viscosity for simplicity. The former method is used to fit all data, at the expense of using a complex equation, while a simpler Potential Law cannot fit very low or very high shear rate values. Lastly, regarding materials, Liravi et al. [40] used several concentrations of a polysiloxane-based hydrogel extruded into the air. Samanipour et al. [41] used a GelMA hydrogel extruded into oil. Therefore, all previous simulations analyze the behavior of non-commercial bioinks and, as far as the authors know, no previous computational analysis has been performed for Cellink Bioink. This bioink is made of alginate with nanocellulose fibers and some authors have experimentally demonstrated the adequate bioprinting properties of this type of bioink (good rheological behavior, cellular viability or mechanical response) [43–45]. Among those authors, Müller et al. have also performed additional CFD computational simulations to study pressure and shear stress inside a needle [46].

Hence, the objective of this work is to analyze the Cellink Bioink behavior while bioprinting using computational simulations. Specifically, the pressure, velocity, and shear stress of this bioink are studied using three temperatures (15, 25, and 37 °C) and three conical tips' geometries (20, 22, and 25G) as inlet parameters. Additionally, an analysis of the bioink filament volume is performed to measure its stability undero nine different combinations of temperatures and geometries in simple conditions.

2. Materials and Methods

2.1. Computational Model

Three geometrical models were created and simulated in COMSOL Multiphysics 5.4a (COMSOL Inc., Burlington, MA, USA, 2018) through a 2D axisymmetric model and a Two-Phase Flow level set interface. Commercial 20G, 22G, and 25G conical tip geometries (Figure 1) were selected for simulations. A 22G conical tip is the recommended tip for Cellink Bioink by Cellink in its bioprinting manual [46], while 20 and 25G were selected because they are the bigger and smaller most used sizes after 22G. All conical tips were modelled after experimental measurements using a caliper. The geometrical model and its measurements can be seen in Figure 2. left, where X is 0.30, 0.20, and 0.13 mm for 20, 22, and 25G, respectively. The conical tip was modelled using a trapezium and a rectangle, while the air was composed of a rectangle and a trapezium. Two different domains were considered in the geometrical model. The first domain was related to the nozzle where the hydrogel was placed, and the second domain was the outside of the nozzle and corresponds to the air where the bioprinting material was ejected (Figure 2 right). Models were meshed using COMSOL-optimized mesh generation for fluid dynamics with 2D triangular elements obtaining a total of 6353 elements with sizes ranging from 0.015 to 0.335 mm. The average skewness mesh quality is 0.9121 with a minimum value of 0.5715.

Figure 1. Cellink bioprinting conical tips. From left to right: 20, 22, and 25G. Reproduced with permission from Cellink®.

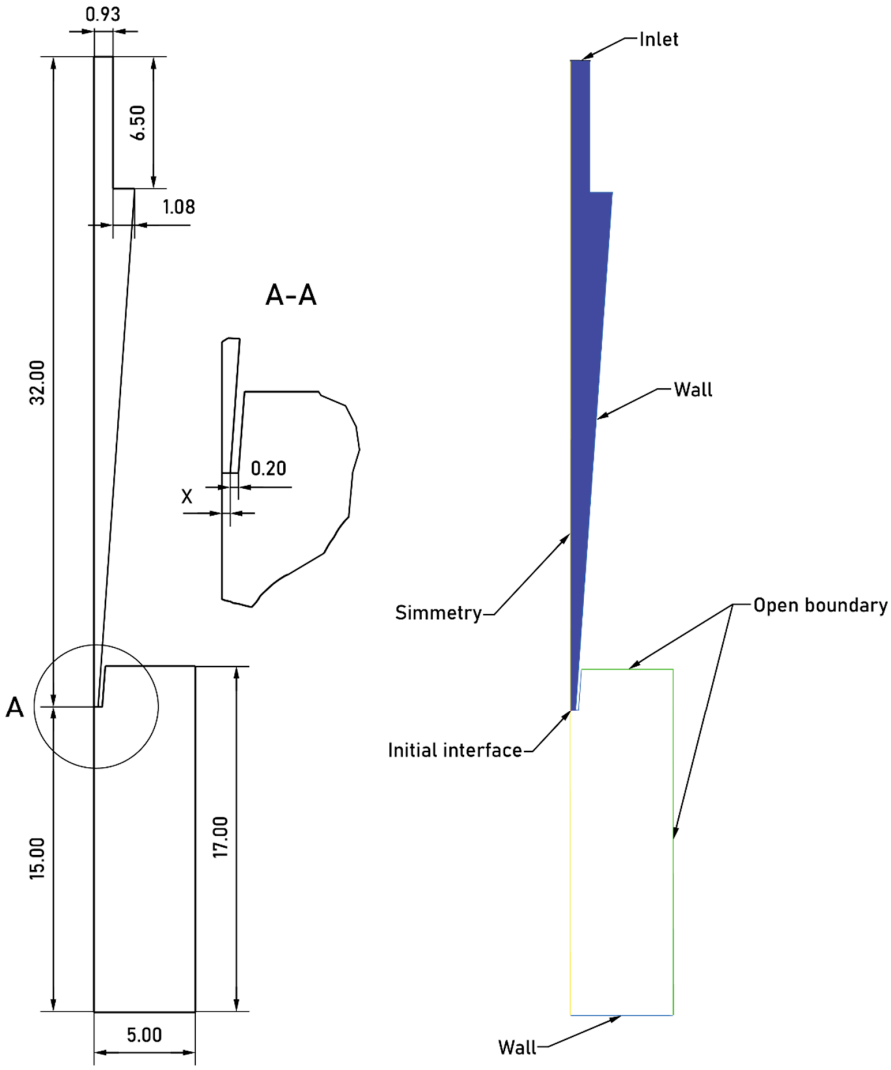

Figure 2. Representation of models' geometry, in millimeters, based on real measures of a commercial conical tip where X = 0.30, 0.20, and 0.13 mm for 20, 22, and 25G, respectively (**right**). Representation of bioink domain (light grey) and air domain (dark grey) with all boundary conditions (**left**).

Level Set method is a Eulerian transport method capable of capturing the interface of two fluids and the changes of the interface because of motion. This method couples the track of the interface with a fluids dynamic of each fluid, expressed by incompressible Navier–Stokes equations

$$\rho\frac{\partial u}{\partial t} + \rho\,(u\cdot\nabla)u = \nabla\cdot\left[-pI + \mu\left(\nabla u + \nabla u^T\right)\right] + F_{st} + \rho g \tag{1}$$

$$\nabla\cdot u = 0 \tag{2}$$

where ρ is the density, u is the speed of the fluid, p denotes the pressure, I is the identity matrix, μ is the fluid viscosity, g is the gravity, and F_{st} is the surface tension force calculated as

$$F_{st} = \nabla\cdot\left[\left(\sigma\left(I - \frac{\nabla\phi}{|\nabla\phi|}\left(\frac{\nabla\phi}{|\nabla\phi|}\right)^T\right)\right)\delta\right] \tag{3}$$

where σ is the surface tension, ϕ is the contour line of the gas–liquid two-phase flow interface, and δ is the Dirac delta function formulized as follows

$$\delta = |\phi(1-\phi)||\nabla\phi| \tag{4}$$

Initially, the flow is assumed to be laminar, but a posterior verification is needed after simulation by calculating the Reynolds number.

The material used for the simulations was the commercially available Cellink Bioink, composed of alginate and nanocellulose fibers, with a density equal to 1000 kg/m^3. Its surface tension was measured and calculated using a KRUSS G20/DSA10 drop shape analyzer, obtaining a value of 55.8 mN/m. Additionally, its viscosity/shear rate at 15, 25, and 37 °C was provided by Cellink and fitted to a simple viscosity Potential Law

$$\mu = m\left(\dot{\gamma}\right)^{n-1} \tag{5}$$

where μ is the dynamic viscosity (Pa·s), m is the fluid consistency index, $\dot{\gamma}$ is the shear rate (s^{-1}), and n is the flow behavior index. The selection of a simpler viscosity law pursues minimizing the computational cost, as long as the shear rate is within the proper values. The fitting parameters and goodness of the fit are listed in Table 1 and in Figure 3.

Table 1. Consistency index (m) and flow behavior index (n) of Cellink Bioink at 15, 25, and 37 °C.

Parameters	15 °C	25 °C	37 °C
m ($Pa{\cdot}s^n$)	92.735	102.53	87.906
n (adimensional)	0.146	0.170	0.208
Goodness of the fit (R^2)	0.9985	0.9925	0.9906

All bioink data were introduced in COMSOL as a user defined material and air data was obtained from COMSOL material library.

In the Level Set method, Cellink Bioink is expressed by ϕ = 0, the air is expressed by ϕ = 1, and the level set interface (transition area between both materials) is expressed by ϕ = 0.5. The level set equation can be seen as the volume percentage of liquid in the gas-liquid two-phase flow [47].

Density and viscosity of the involved material can change in the interface following the level-set functions

$$\rho = \rho_{air} + (\rho_{bioink} - \rho_{air})\phi \tag{6}$$

$$\mu = \mu_{air} + (\mu_{bioink} - \mu_{air})\phi \tag{7}$$

The track of the level set interface is described in the following equation when it moves under the velocity field u

$$\frac{\partial \phi}{\partial t} + u \cdot \nabla \phi = 0 \tag{8}$$

Only the normal component of the velocity is needed because the level-set method considers the interface movement to be normal to itself. Therefore, Equation (8) can be reformulated as follows

$$\frac{\partial \phi}{\partial t} + u_n \left| \nabla \phi \right| = 0 \tag{9}$$

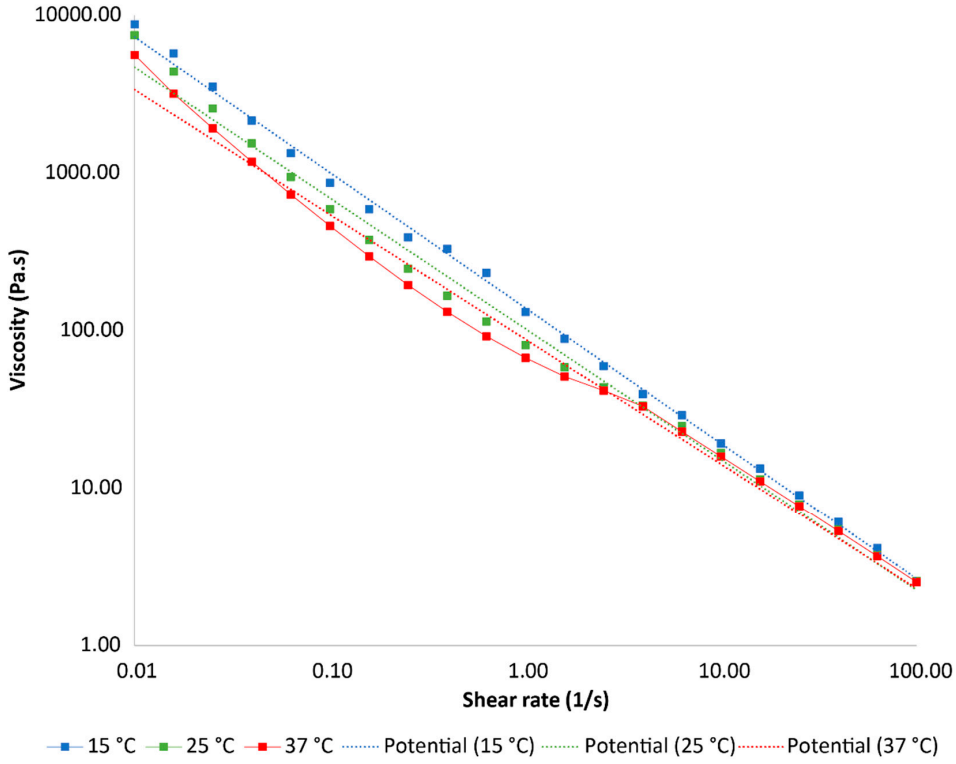

Figure 3. Cellink Bioink rheological data. Reproduced with permission of Cellink®.

The Level Set method needs its function to be a distance function within all simulation to depict the interface. To assure a correct depict of the interface, numerical reinitialization and stabilization terms are added to the level set equation. Therefore, the non-conservative reinitialized level set function can be formulated as

$$\frac{\partial \phi}{\partial t} + u \cdot \nabla \phi = \gamma \nabla \left(\epsilon \nabla \phi + \phi (1 - \phi) \frac{(\nabla \phi)}{\left| \nabla \phi \right|} \right) \tag{10}$$

where ϕ is the contour line of the gas-liquid two-phase flow interface, γ is the reinitialization parameter (approximately the maximum value of the velocity field), and ϵ is the interface thickness parameter (usually half of the mesh size in the region). Here, the bioprinting material corresponds to the domain where $\phi < 0.5$, and air corresponds to the domain where $\phi > 0.5$.

Boundary conditions were set as shown in Figure 2, they were stablished taking into account that all simulations are a 2D axisymmetric simulation and to make possible a realistic shear-thinning non-Newtonian flow. In this sense, the laminar flow inlet was set as a full developed flow, described with

the following equations to assure tangential flow component on the boundary is zero (Equation (11)) and to set the real inlet value (Equation (12))

$$u - (u \cdot n)n = 0 \tag{11}$$

$$[-pI + K] = -p_{in}n \tag{12}$$

where p is the user average pressure (N/m^2), in our simulations 15 kPa, as recommended by Cellink in their bioprinting manuals for Cellink Bioink [46], K is the viscous stress (N/m^2), and p_{in} is the real inlet pressure (N/m^2).

The outlet boundary condition was set as an open boundary condition with no normal stress to allow bioprinting material to fill this domain and air to leave. Additionally, wall boundaries were set with a non-slip condition, which means that the velocity on the walls is zero, and level set interface in the wall is described by

$$n \cdot \left(\epsilon \nabla \phi - \phi(1 - \phi) \frac{\nabla \phi}{|\nabla \phi|} \right) = 0 \tag{13}$$

Because the simulation is an 2D axisymmetric simulation, a symmetry boundary condition was set, as shown in Figure 2. It was modelled as a combination of Neumann and Dirichlet boundary conditions, allowing flow to not penetrate this boundary, and vanishing shear stress for an incompressible flow

$$u \cdot n = 0 \tag{14}$$

$$\left(-pI + \mu \left(\nabla u + (\nabla u)^T \right) \right) n = 0 \tag{15}$$

2.2. Simulation

Nine simulations of 10 s with a 1 ms step were carried out for each geometry and temperature. Each simulation was composed of two study steps: Phase Initialization and Time-Dependent. The Phase Initialization step is in charge of obtaining all initial values of the Level Set method on every mesh element. In this sense, Phase Initialization is solved in COMSOL using the distance to the initial interface, D_{wi} (m), and initializes the level set variable ϕ to ensure a smoothly variation between 0 and 1 (maximum and minimum values) and to minimize numerical instabilities. Then, this initial level set value is translated to the Time-Dependent step using the following expressions for the two different domains

$$\phi_0 = \frac{1}{1 + \frac{e^{D_{wi}}}{\epsilon}} \tag{16}$$

in domains initially filled with bioprinting material, and

$$\phi_0 = \frac{1}{1 + \frac{e^{-D_{wi}}}{\epsilon}} \tag{17}$$

in domains initially filled with air, where ϕ is the domain reference (volumetric fraction), and ϵ is the interface thickness (m).

For the Phase Initialization step, a stationary solver was used to calculate the level set initial values that later were used as t = 0 values by the time-dependent solver of the Time-Dependent step. Both the Phase initialization and the Time-Dependent steps used a Newton non-linear method in a fully coupled solver with a Parallel Direct sparse Solver (PARDISO). The Newton non-linear method is in charge of the successive iterative calculation of all coupled Fluids Dynamics and Level Set formulas described before. This method evaluates all non-linear expressions and the Jacobean on each iteration and assures that the calculation error between successive iterations is below the user tolerance (set at 10^{-6}). If the error is higher than tolerance, the damping factor is automatically changed, and the time

step is reduced. The time step is calculated using a Backward Euler BDF method which is known for its stability and is the most recommended one for fluid transportation in COMSOL.

The PARDISO is a solver based on LU decomposition that tries to improve the sequential and parallel sparse numerical factorization performance. This method can use all computer cores to perform parallel calculations, reducing the simulation time to the detriment of computer expenditure.

3. Results and Discussion

Reynolds numbers were calculated for all simulations obtaining a maximum value of the order of 10^{-4}, which means that the initial assumption of laminar flow is correct. In the same way, the shear rate of all simulations has been checked, ranging from 0.1 to 155 1/s. Therefore, the Cellink Bioink behavior curve can be modelled using the Potential Law.

All simulation errors were measured in the velocity field. The error between successive time steps was below 10^{-6} in the 18th step with a later average error of 10^{-13}. To achieve these low errors, a very small-time step (approximately 10^{-6} s) is calculated by the BDF method, ranging the simulation time between 3 and 10 h.

3.1. Outlet Pressure

Simulated outlet pressure was measured using a line probe at the very end of the nozzle, specifically in the initial gas–liquid interface. Figure 4 shows all pressures for 20, 22, and 25G conical tips at 15, 25, and 37 °C.

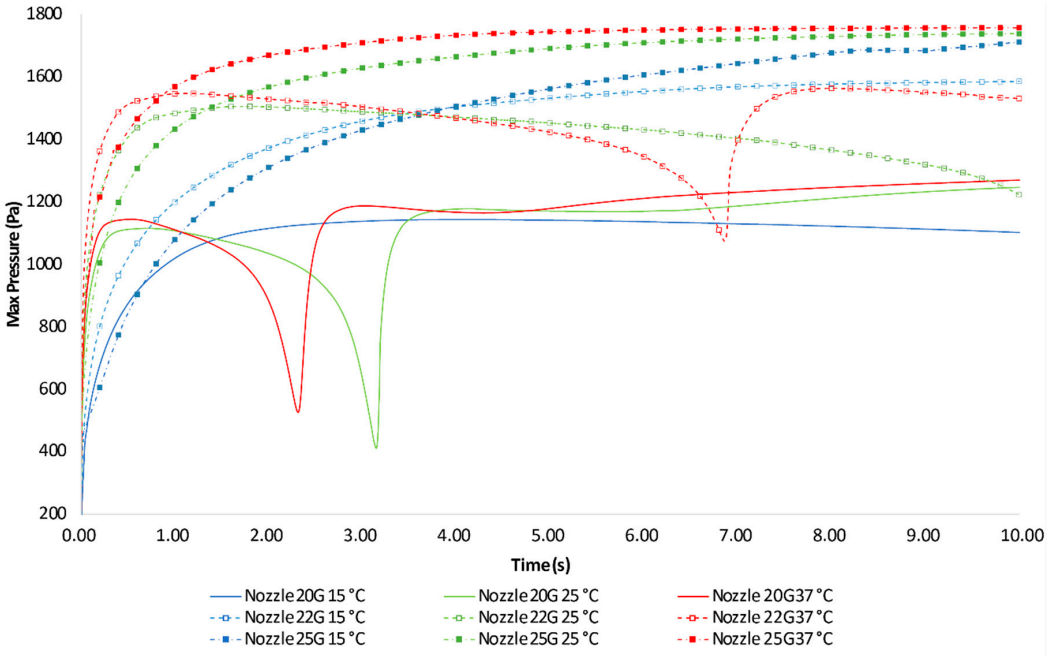

Figure 4. Maximum outlet pressure for 20, 22, and 25G conical tips using Cellink Bioink at 15, 25, and 37 °C.

Three out of nine simulations present a low-pressure peak in their temporal evolution of maximum outlet pressure (25 and 37 °C for 20G and 37 °C for 22G). Additionally, the outlet pressure of 22G conical tip at 25 °C decreases at the end of the simulation, which implies that a low-pressure peak is being formed beyond the 10 s, similarly to the peaks in the other simulations. In this sense, to properly analyze and compare the pressure behavior of all simulations, a set of relevant points are identified. These points are: (1) the maximum value before the low-pressure peak, (2) the minimum pressure

value, (3) the stable pressure value just after the peak, and (4) the pressure value at the end of the simulation. All plots were analyzed to identify these key points when available (for plots without peak, only the value at the end of the simulation is provided) and their pressure values are shown in Table 2.

Table 2. Maximum outlet pressure values (Pa) and time (s).

Geometry	Temp	Before Peak (Time)	Peak (Time)	After Peak (Time)	End Simulation (Time)
20G	15 °C	1143.6 (4.10)	-	-	1102.3 (10.00)
	25 °C	1115.3 (0.67)	409.4 (3.14)	1178.3 (4.10)	1246.9 (10.00)
	37 °C	1144.3 (0.52)	526.8 (2.31)	1187.6 (3.01)	1269.9 (10.00)
22G	15 °C	-	-	-	1585.5 (10.00)
	25 °C	1505.2 (1.72)	-	-	1222.4 (10.00)
	37 °C	1547.2 (1.13)	1074.9 (6.86)	1563.2 (8.01)	1530.9 (10.00)
25G	15 °C	-	-	-	1711.3 (10.00)
	25 °C	-	-	-	1738.2 (10.00)
	37 °C	-	-	-	1757.1 (10.00)

It might be expected Cellink Bioink at 37 °C to have the lowest pressure for each one of the different conical tips. This supposition is based in the viscosity analysis, as a low viscosity fluid is supposed to provoke lower inner pressures when compared to a higher-viscosity fluid for the same conical tip. Specifically, in bioprinting materials, other authors as Bartnikowski et al. [48] have checked that hydrogels' viscosity usually decreases when temperature increases. However, there are some cases, such as Pluronic, that an increment in temperature provokes an increase in viscosity. This specific material contains (poly (ethylene oxide))$_{100}$-(poly (propylene oxide))$_{65}$-(poly (ethylene oxide))$_{100}$. At a low temperature, it is an individual block of copolymers but when temperature increases, its internal structure changes and forms micelles that increase its viscosity [49]. In our case, Cellink Bioink is composed by alginate and nanocellulose fibers. Its behavior was analyzed in several works [26,43,45,50] and they all determine that the normal behavior of this kind of bioink is that the higher the temperature is, the lower the viscosity. Therefore, considering Table 2 and Figure 4, it is clear that this expected behavior is not obtained by all but one of the analyzed conical tips. More specifically, 22G conical tip is the only geometry where outlet pressure is higher at 15 °C than at 25 and 37 °C. This unexpected behavior is caused by the different inlet volumetric flow in all simulations. In this sense, the total extruded volume of Cellink Bioink along the time is shown in Figure 5. Additionally, the total volume values referring to the key points defined before can be seen in Table 3. Therefore, when pressure is selected as simulation inlet parameter, the volumetric flow cannot be further controlled. It depends on the fluid viscosity and the inner geometry where the fluid flows.

Therefore, two main considerations can be extracted from the pressure results. On the one hand, the geometry can change the outlet pressure value. In general, the bigger the outlet diameter is (the smaller the conical tip gauge), the lower the pressure is (Figure 4). On the other hand, the temperature has a slight influence on pressure for the same geometry. Despite different bioink temperatures leading to different pressures, the average differences are around 600 Pa, so they can be considered negligible.

In order to properly compare our pressure results with those from bibliography, we have selected the values not considering excluding the low-pressure peak values. Thus, our maximum pressure values vary between 1143 and 1757 Pa. As far as the authors know, Reid et al. [33] have performed the only study that analyzed this pressure under experimental settings. They found that pressure ranged from 101 to 107 kPa using *"a fluid with similar properties to blood"*, such as the bioink, but further information is not provided. They focused on the geometrical optimization of the inner nozzle geometry using different shapes and lengths and set up the inlet flow at 0.1 mm^3/s. In this regard, the lack of information about the used bioink makes difficult to compare results. However, it seems that their high-pressure values are caused by the very small outlet diameter (60 µm) used.

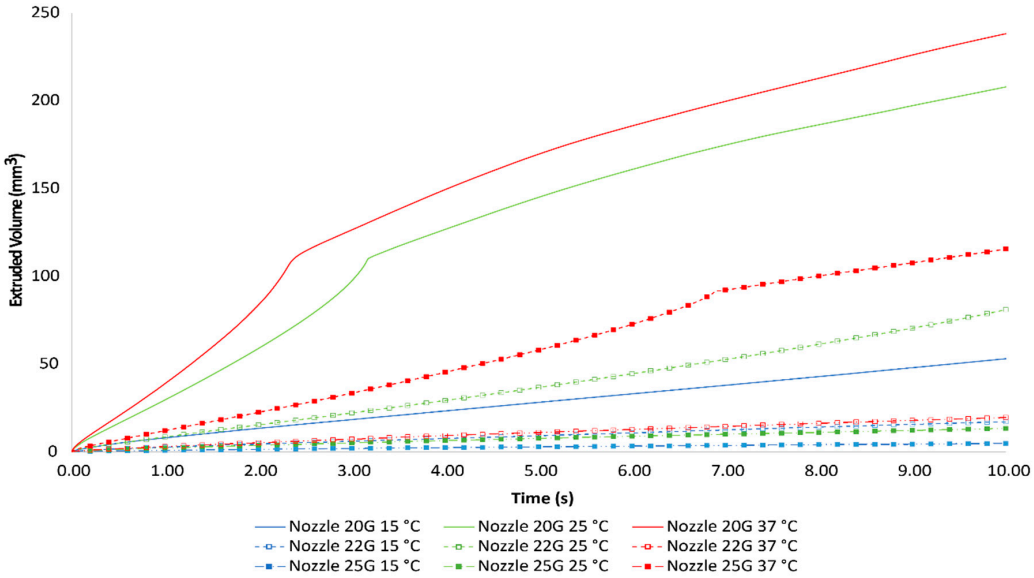

Figure 5. Total extruded volume for 20, 22, and 22G conical tips using Cellink Bioink at 15, 25, and 37 °C.

Table 3. Cellink Bioink extruded volume (mm^3) and time (s).

Geometry	Temp	Before Peak (Time)	Peak (Time)	After Peak (Time)	End Simulation (Time)
20G	15 °C	-	-	-	53.22 (10.00)
	25 °C	-	107.06 (3.14)	-	208.02 (10.00)
	37 °C	-	105.31 (2.31)	-	238.33 (10.00)
22G	15 °C	-	-	-	17.31 (10.00)
	25 °C	-	-	-	81.20 (10.00)
	37 °C	-	90.28 (6.86)	-	115.67 (10.00)
25G	15 °C	-	-	-	5.00 (10.00)
	25 °C	-	-	-	13.51 (10.00)
	37 °C	-	-	-	19.78 (10.00)

Although Lee et al. [51] determined that alginate bioinks are not thermo-responsive and the viscosity variation is not noticeable, our results (Table 3) show that temperature has an important influence on bioprinting procedure. For a specific conical tip, an increase in temperature provokes the bioink viscosity to decrease, therefore generating a higher flow rate. Controlling the amount of extruded material is one of the key points in a successful bioprinting procedure. Most commercial bioprinters are pneumatic-driven and their main limitation is that the bioink flow cannot be precisely controlled [52]. To create any tissue, it is necessary to deposit a determined amount of material in a certain point, so, if temperature influences the bioink flow, other printing parameters, such as XY-speed, must be carefully selected to achieve proper results.

As mentioned before, there are three simulations with low-pressure peaks and a fourth one where a peak is foreseen. Comparing Figures 4 and 5, the low-pressure peaks are produced at the exact time an abrupt change in volumetric flow is observed. Those peaks are produced at different times depending on the geometry and the temperature: 2.31, 3.14 and 6.86 s for 20G at 37 °C, 20G at 25 °C, and 22G at 37 °C, respectively. At those instants, an initial droplet is formed (Figure 6), which would eventually fall, taking into account that the cross-area is reduced in such way that it can be considered that the droplet will fall. This droplet creation also depends on the distance to the printing substrate. In the light of the presented results, it seems that none of the simulated temperature/geometry configurations at 15 kPa will form a stable filament but droplets. Simulation time (t = 10 s) is not enough to even

generate the initial droplet at the lowest temperature (15 °C) or lowest inner diameter (25G). The four images in Figure 6 show the simulations where a droplet is generated and drops (A, B, C) or is about to drop (D). Table 3 shows that the bioink volume to produce a falling droplet varies depending on the geometry. In this sense, the total volume of Cellink Bioink hanging from the conical tip is around 106 mm^2 on average for 20G, and 90 mm^2 for 22G. The formation of droplets depends on factors such as the volumetric flow, the viscosity of the material, the cross-section area and, in particular for hydrogels, the distance between the nozzle tip and the printing substrate. In our simulations, droplets are formed because two main reasons. First, both 20 and 22G have the same wall thickness (0.2 mm, Figure 2), but the total cross area of the conical tip outlet is 0.50 and 0.38 mm^2 for 20 and 22G, respectively. Since the total droplet volume before falling is dependent on the cross-area in contact as well as the surface tension and this is constant, the cross-area limits the maximum volume of the droplet. Secondly, the distance to the printing substrate, defined as "h" by He et al. [9], usually varies from µm to few mm in a standard bioprinting procedure, but we have set a larger h in our simulations to check whether Cellink Bioink is capable of creating a stable filament on the air. Therefore, in Figure 6A,B, it is shown the simulations at the exact time (3.14 and 2.31 s, respectively) when a visible reduction in the cross-area near the conical tip of 20G at 25 °C and 37 °C that will cause the droplet fall. Additionally, in Figure 6D, the falling droplet of 22G at 37 °C in t = 6.86 s is represented, while Figure 6C shows the 22G at 25 °C simulation in t = 10 s, in which the total extruded volume is not enough to generate a falling droplet. According to our results, none of the analyzed combinations can generate a stable filament flow on the air, due to either the generation of droplets or an insufficient extruded volume. Therefore, other printing parameters related to these printability and shape fidelity features, such as h and XY-plane speed, should be correctly selected to create such stable filament flow.

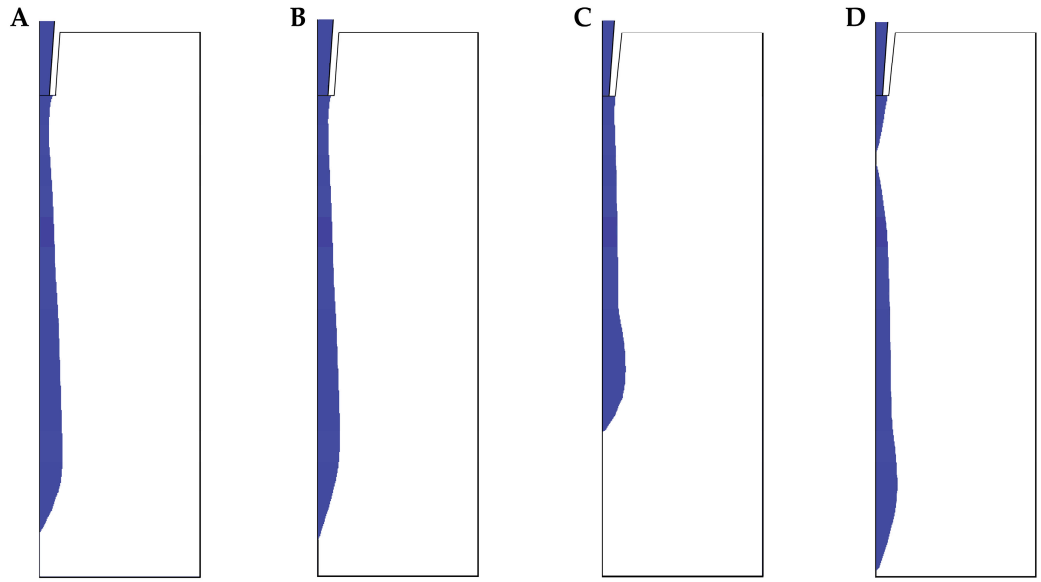

Figure 6. Volume fraction of Cellink Bioink. (**A**) 20G at 25 °C in t = 3.14 s, (**B**) 20G at 37 °C in t = 2.31 s, (**C**) 22G at 25 °C in t = 10.00 s and (**D**) 22G at 37 °C in t = 6.86 s. Blue color represents Cellink Bioink and white color represents the air.

Finally, Figure 4 shows an increase in pressure since 3.01 and 4.10 s in 20G at 37 °C and 20G at 25 °C, respectively, until the end of the simulations. This final increase in pressure is provoked by the material accumulation on the printing substrate. This accumulation reaches de conical tip and causes the rise of pressure to continue to the extruding material. Therefore, to the existing extrusion pressure, the force needed to push away the already extruded material must be added.

3.2. Outlet Velocity

Simulated maximum outlet velocity was measured using the same probe as in pressure, at the very end of the nozzle. Figure 7 shows the maximum velocity for 20, 22, and 25G conical tips for 15, 25, and 37 °C along the time.

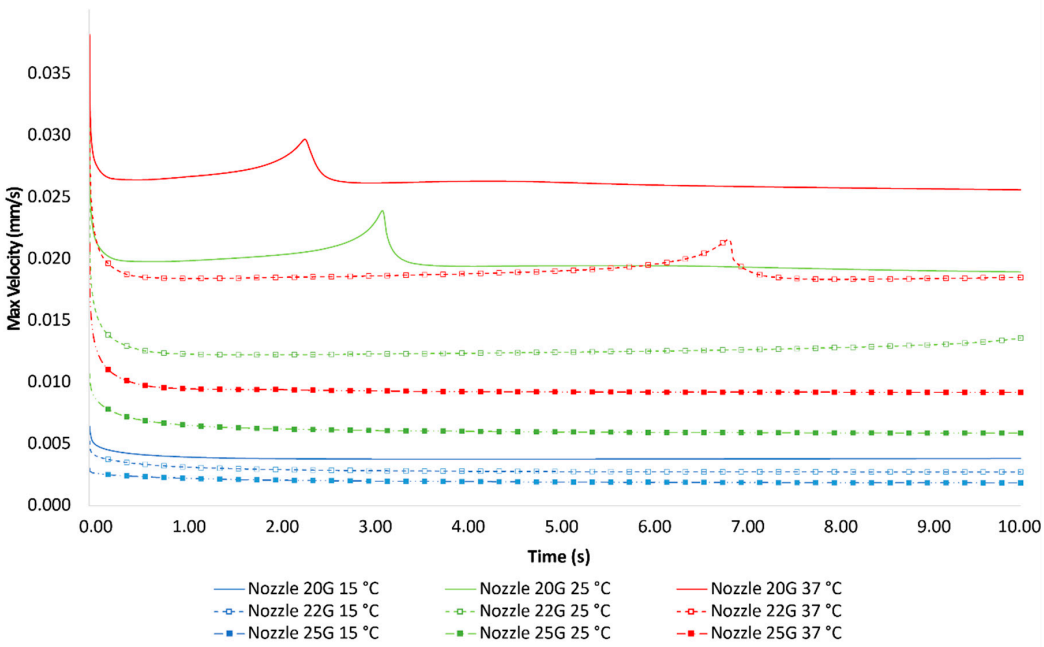

Figure 7. Maximum outlet velocity of 20G, 22G, and 25G conical tips using Cellink Bioink at 15, 25, and 37 °C.

Additionally, Table 4 presents all velocity values in the previously defined key points. It can be observed that there are high-velocity peaks produced at the same time as the low-pressure peaks. The velocity increment is produced by the droplet material pulling the bioink outside the nozzle. When the droplet is completely separated from the nozzle, the velocity peak disappears, and the previous value is restored.

Table 4. Maximum outlet velocities values (cm/s) and time (s).

Geometry	Temp	Before Peak (Time)	Peak (Time)	After Peak (Time)	End Simulation (Time)
20G	15 °C	0.38 (4.10)	-	-	0.38 (10.00)
	25 °C	1.98 (0.67)	2.39 (3.14)	1.94 (4.10)	1.89 (10.00)
	37 °C	2.64 (0.52)	2.97 (2.31)	2.62 (3.01)	2.56 (10.00)
22G	15 °C	-	-	-	0.27 (10.00)
	25 °C	1.22 (1.72)	-	-	1.36 (10.00)
	37 °C	1.84 (1.13)	2.19 (6.86)	1.84 (8.01)	1.85 (10.00)
25G	15 °C	-	-	-	0.19 (10.00)
	25 °C	-	-	-	0.59 (10.00)
	37 °C	-	-	-	0.92 (10.00)

It would be expected that the outlet velocity depends on the outlet geometry for a certain inlet flow, as defined by continuum equation. In this sense, and as explained before, an inlet boundary condition of 15 kPa makes the bioink inlet flow to be dependent on its viscosity and the nozzle

geometry. This dependency results from a variability in the flow for all simulations, as can be seen in Figure 5. Similar to the findings in the pressure, there are two important considerations for velocity. Firstly, for the same geometry, velocity changes with temperature. As explained before, the lower the temperature is, the lower the viscosity and the higher the extruded volume. An increase in volumetric flow leads to an increase in velocity according to continuum equation when cross-area remains constant. Therefore, temperature changes the extrusion velocity. Lastly, the geometry has also an important influence on velocity, and this influence is higher when the conical tip gauge increases. As shown in Figure 7 the influence of temperature on velocity is higher at lower gauges, while at higher gauges the effect of temperature is reduced and the cross-section area reduction plays a major role.

Regarding to other authors velocities, they obtained different results: velocities equal to 5.50 and 7.20 cm/s for a 60 µm diameter conical and needle tip, respectively [33], or 36.70 cm/s for a 28G gauge needle [36]. Again, differences between their results and our simulations might be explained by differences in viscosities, which cannot be assured, as authors do not provide this parameter for their bioink. Nevertheless, our results confirm that differences in cross-area have an important influence on velocities.

3.3. Shear Stress

Simulated shear stress is measured in the whole inner extruder domain using a surface probe. Maximum shear rate values are presented in Figure 8 and Table 5.

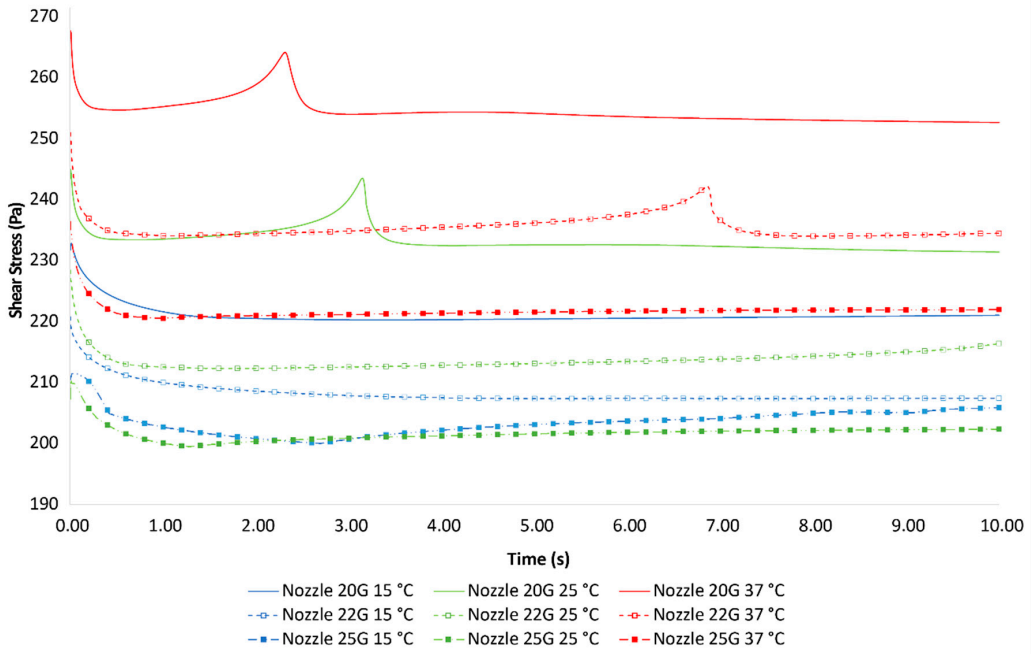

Figure 8. Maximum shear stress of 20, 22, and 25G conical tips using Cellink Bioink at 15, 25, and 37 °C.

Since shear stress depends on shear rate, and shear rate depends on velocity, it might be expected that shear stress behaves similarly to velocity. In any case, the analysis of shear stress must be done carefully for non-Newtonians fluids, as the variations in viscosity with shear rate might change the shear stress behavior. As can be seen in Figure 8, both shear stress and velocity have a similar temporal behavior.

Results show that shear stress varies with temperature and geometry. For a defined geometry, the shear stress decreases when temperature increases, and the temperature influence is reduced when the conical tip gauge increases. Additionally, high-shear stress peaks appear at the same time as

pressure or velocity peaks. Nevertheless, an odd behavior of 25G at 15 °C, and 25G at 25 °C can be found, with an increment of shear rate at the end of the simulation, which might be caused by the high viscosity of the material at those temperatures where the bioink has a low velocity (shear rate).

Table 5. Maximum shear rate values (Pa) and time (s).

Geometry	Temp	Before Peak (Time)	Peak (Time)	After Peak (Time)	End Simulation (Time)
20G	15 °C	220.34 (4.10)	-	-	220.04 (10.00)
	25 °C	233.41 (0.67)	243.48 (3.14)	232.46 (4.10)	231.42 (10.00)
	37 °C	254.71 (0.52)	264.16 (2.31)	254.01 (3.01)	252.66 (10.00)
22G	15 °C	-	-	-	207.41 (10.00)
	25 °C	212.32 (1.72)	-	-	216.41 (10.00)
	37 °C	234.10 (1.13)	242.16 (6.86)	234.01 (8.01)	234.48 (10.00)
25G	15 °C	-	-	-	205.88 (10.00)
	25 °C	-	-	-	202.35 (10.00)
	37 °C	-	-	-	221.96 (10.00)

The measurement of shear stress is done in the whole domain, so the maximum value may not be found in a fixed position. However, Liu et al. [30] observed that maximum shear stress is placed at the very tip of the conical tip nozzle. In this regard, the shear stress distribution in all simulations is very similar to the 22G at 37 °C (Figure 9).

Figure 9. Shear stress distribution (Pa) at 37 °C.

Many authors agree that shear stress is one of the main parameters to analyze and control in order to reduce cell death during the bioprinting process. Similarly to the finding of Yan et al. [28], our results specifically confirm that increasing pressures or increasing outlet diameter provoke wall shear stress to increase. On the contrary, our simulations do not coincide with Liu et al. [30], as we obtain lower shear stress with higher viscosity of the bioink. This different behavior might be caused by the different inlet used in our simulations and their experiments, because Liu et al. used a constant mass flow, while we have used a constant pressure. Müller et al. [45] also studied the shear stress using several nozzles with a very similar bioink, but in the same way as with Liu et al., their results are not directly comparable to ours due to the different geometries and inlet pressures. Hence, previous experimental tests are hardly comparable due to different boundary conditions or scarce definition of bioprinting parameters. On the other hand, shear stress can be found ranging from approximately 200 Pa to 20 kPa. In this sense, our results are quite similar to those obtained by Li et al. [37]. Specifically, those related to an inlet flow of 0.015 mL/s using an alginate hydrogel (0.41 Pa·s).

According to Blaeser et al. [29], shear stresses below 5 kPa do not have a harmful effect on cells (cellular viability over 96%). Although our results show high variability in shear stress values, all of them remain below 5 kPa. Therefore, low damage effect on cells is expected, which allows for high cellular viability.

4. Conclusions

In this work, several simulations have been done to study the impact of temperature and geometry in a commercial bioink: Cellink Bioink, its rheological data and inlet pressures were provided by the company bioprinting protocols. The simulation results demonstrated the suitability of this commercial bioink to be used in micro-extrusion bioprinting techniques, regardless of the temperature or the conical tip used (15, 25, and 37 °C and 20, 22, and 25G). However, it is recommended to use this bioink at 37 °C, not with the aim of having a minimum shear stress, but in order to obtain the higher volumetric flow. A higher volumetric flow leads to higher bioprinting speed, so cells are under pressure for a shorter time. Additionally, shear stress obtained from simulations forecasts a proper cellular viability at all temperatures, according to previous studies for values under 5 kPa.

Despite the suitability of this studied bioink, simulations have been performed with several simplifications, such as not-defined wall friction, the use of a bioink without cells inside, and no interaction between the bioink filament and the printing substrate. Additionally, only conical nozzle geometries have been simulated. As future works, a comparative study of how conical and needle tips geometries should deeply analyze the effect of shear stress under different temperatures of the bioink. Furthermore, other bioprinting settings, such as different height (h) or XY-plane speed, should be also included in future simulations to analyze the bioink filament in dynamic conditions during its deposition on the printing substrate. Finally, experimental tests using this commercial bioink with a 3D bioprinter should be performed to validate simulation results with the actual behavior of bioinks.

Author Contributions: Conceptualization, J.C.G.-B., A.D.-P. and J.B.P.; Formal analysis, J.C.G.-B.; Investigation, J.C.G.-B., E.M.-S. and J.B.P.; Methodology, J.C.G.-B. and E.M.-S.; Project administration, J.C.G.-B. and J.B.P.; Software, J.C.G.-B., E.M.-S., A.C.M. and M.M.; Supervision, J.B.P.; Writing—original draft, J.C.G.-B.; Writing—review and editing, J.C.G.-B., E.M.-S., A.C., M.M., A.D.-P. and J.B.P. All authors have read and agreed to the published version of the manuscript.

Funding: This research was co-financed by Consejería de Economía, Ciencia y Agenda Digital, Junta de Extremadura, project number IB16200 and predoctoral grant number PD16067 to J.C.G.-B. Co-financed by European Union/ERDF and ESF funds.

Conflicts of Interest: The authors declare no conflict of interest.

References

1. Ng, W.L.; Chua, C.K.; Shen, Y.F. Print Me An Organ! Why We Are Not There Yet. *Prog. Polym. Sci.* **2019**, *97*, 101145. [CrossRef]
2. Zhang, Y.S.; Yue, K.; Aleman, J.; Mollazadeh-Moghaddam, K.; Bakht, S.M.; Yang, J.; Jia, W.; Dell'Erba, V.; Assawes, P.; Shin, S.R.; et al. 3D Bioprinting for Tissue and Organ Fabrication. *Ann. Biomed. Eng.* **2016**, *45*, 148–163. [CrossRef] [PubMed]
3. Zhang, B.; Gao, L.; Ma, L.; Luo, Y.; Yang, H.; Cui, Z. 3D Bioprinting: A Novel Avenue for Manufacturing Tissues and Organs. *Engineering* **2019**, *5*, 777–794. [CrossRef]
4. Kyle, S.; Jessop, Z.M.; Al-Sabah, A.; Whitaker, I.S. 'Printability' of Candidate Biomaterials for Extrusion Based 3D Printing: State-of-the-Art. *Adv. Healthc. Mater.* **2017**, *6*. [CrossRef] [PubMed]
5. Rutz, A.L.; Gargus, E.S.; Hyland, K.E.; Lewis, P.L.; Setty, A.; Burghardt, W.R.; Shah, R.N. Employing PEG crosslinkers to optimize cell viability in gel phase bioinks and tailor post printing mechanical properties. *Acta Biomater.* **2019**, *99*, 121–132. [CrossRef]
6. Zhang, J.; Wehrle, E.; Vetsch, J.R.; Paul, G.R.; Rubert, M.; Müller, R. Alginate dependent changes of physical properties in 3D bioprinted cell-laden porous scaffolds affect cell viability and cell morphology. *Biomed. Mater.* **2019**, *14*, 065009. [CrossRef]

7. Chung, J.H.Y.; Naficy, S.; Yue, Z.; Kapsa, R.; Quigley, A.; Moulton, S.E.; Wallace, G.G. Bio-ink properties and printability for extrusion printing living cells. *Biomater. Sci.* **2013**, *1*, 763–773. [CrossRef]
8. Gao, T.; Gillispie, G.J.; Copus, J.S.; Kumar, A.P.R.; Seol, Y.-J.; Atala, A.; Yoo, J.J.; Lee, S.J. Optimization of gelatin-alginate composite bioink printability using rheological parameters: A systematic approach. *Biofabrication* **2018**, *10*. [CrossRef]
9. He, Y.; Yang, F.; Zhao, H.; Gao, Q.; Xia, B.; Fu, J. Research on the printability of hydrogels in 3D bioprinting. *Sci. Rep.* **2016**, *6*, 29977. [CrossRef]
10. Jeon, O.; Lee, Y.B.; Hinton, T.J.; Feinberg, A.W.; Alsberg, E. Cryopreserved cell-laden alginate microgel bioink for 3D bioprinting of living tissues. *Mater. Today Chem.* **2019**, *12*, 61–70. [CrossRef]
11. Pepelanova, I.; Kruppa, K.; Scheper, T.; Lavrentieva, A. Gelatin-methacryloyl (GelMA) hydrogels with defined degree of functionalization as a versatile toolkit for 3D cell culture and extrusion bioprinting. *Bioengineering* **2018**, *5*, 55. [CrossRef] [PubMed]
12. Raddatz, L.; Lavrentieva, A.; Pepelanova, I.; Bahnemann, J.; Geier, D.; Becker, T.; Scheper, T.; Beutel, S. Development and application of an additively manufactured calcium chloride nebulizer for alginate 3D-bioprinting purposes. *J. Funct. Biomater.* **2018**, *9*, 63. [CrossRef]
13. Wu, D.; Yu, Y.; Tan, J.; Huang, L.; Luo, B.; Lu, L.; Zhou, C. 3D bioprinting of gellan gum and poly (ethylene glycol) diacrylate based hydrogels to produce human-scale constructs with high-fidelity. *Mater. Des.* **2018**, *160*, 486–495. [CrossRef]
14. Zheng, Z.; Wu, J.; Liu, M.; Wang, H.; Li, C.; Rodriguez, M.J.; Li, G.; Wang, X.; Kaplan, D.L. 3D Bioprinting of Self-Standing Silk-Based Bioink. *Adv. Healthc. Mater.* **2018**, *7*, 1701026. [CrossRef]
15. Jia, J.; Richards, D.J.; Pollard, S.; Tan, Y.; Rodriguez, J.; Visconti, R.P.; Trusk, T.C.; Yost, M.J.; Yao, H.; Markwald, R.R.; et al. Engineering alginate as bioink for bioprinting. *Acta Biomater.* **2014**, *10*, 4323–4331. [CrossRef]
16. Kiyotake, E.A.; Douglas, A.W.; Thomas, E.E.; Detamore, M.S. Development and quantitative characterization of the precursor rheology of hyaluronic acid hydrogels for bioprinting. *Acta Biomater.* **2019**, *95*, 176–187. [CrossRef]
17. Ashammakhi, N.; Ahadian, S.; Xu, C.; Montazerian, H.; Ko, H.; Nasiri, R.; Barros, N.; Khademhosseini, A. Bioinks and bioprinting technologies to make heterogeneous and biomimetic tissue constructs. *Mater. Today Biol.* **2019**, *1*, 23. [CrossRef]
18. Donderwinkel, I.; van Hest, J.C.M.; Cameron, N.R. Bio-inks for 3D bioprinting: Recent advances and future prospects. *Polym. Chem.* **2017**, *8*, 4451–4471. [CrossRef]
19. Mancha-Sánchez, E.; Gómez-Blanco, J.C.; López-Nieto, E.; García-Casado, J.; Macías, A.; Díaz-Díez, M.A.; Carrasco-Amador, J.P.; Torrejón, D.; Sanchez-Margallo, F.M.; Pagador, J.B. Hydrogels for bioprinting: A systematic review of hydrogels synthesis, bioprinting parameters and bioprinted structures behavior. *Front. Bioeng. Biotechnol.* **2020**, in press. [CrossRef]
20. Ouyang, L.; Yao, R.; Zhao, Y.; Sun, W. Effect of bioink properties on printability and cell viability for 3D bioplotting of embryonic stem cells. *Biofabrication* **2016**, *8*, 1–12. [CrossRef]
21. Kim, W.J.; Kim, G.H. 3D bioprinting of functional cell-laden bioinks and its application for cell-alignment and maturation. *Appl. Mater. Today* **2020**, 19. [CrossRef]
22. Dutta, S.; Cohn, D. Temperature and pH responsive 3D printed scaffolds. *J. Mater. Chem. B* **2017**, *5*, 9514–9521. [CrossRef] [PubMed]
23. Axpe, E.; Oyen, M.L. Applications of alginate-based bioinks in 3D bioprinting. *Int. J. Mol. Sci.* **2016**, *17*, 1976. [CrossRef] [PubMed]
24. Zhou, D.; Chen, J.; Liu, B.; Zhang, X.; Li, X.; Xu, T. Bioinks for jet-based bioprinting. *Bioprinting* **2019**, 16. [CrossRef]
25. Zhang, S.; Vijayavenkataraman, S.; Lu, W.F.; Fuh, J.Y.H. A review on the use of computational methods to characterize, design, and optimize tissue engineering scaffolds, with a potential in 3D printing fabrication. *J. Biomed. Mater. Res. Part B Appl. Biomater.* **2019**, *107*, 1329–1351. [CrossRef]
26. Göhl, J.; Markstedt, K.; Mark, A.; Håkansson, K.; Gatenholm, P.; Edelvik, F. Simulations of 3D bioprinting: Predicting bioprintability of nanofibrillar inks. *Biofabrication* **2018**, *10*. [CrossRef]
27. Li, Y.; Verrelli, D.I.; Yang, W.; Qian, Y.; Chong, W. A pilot validation of CFD model results against PIV observations of haemodynamics in intracranial aneurysms treated with flow-diverting stents. *J. Biomech.* **2020**, *100*, 109590. [CrossRef]

28. Yan, K.C.; Paluch, K.; Nair, K.; Sun, W. Effects of process parameters on cell damage in a 3d cell printing process. In Proceedings of the ASME International Mechanical Engineering Congress and Exposition, Vancouver, BC, Canada, 12–18 November 2010; Volume 2, pp. 75–81.
29. Blaeser, A.; Duarte Campos, D.F.; Puster, U.; Richtering, W.; Stevens, M.M.; Fischer, H. Controlling Shear Stress in 3D Bioprinting is a Key Factor to Balance Printing Resolution and Stem Cell Integrity. *Adv. Healthc. Mater.* **2016**, *5*, 326–333. [CrossRef]
30. Liu, W.; Heinrich, M.A.; Zhou, Y.; Akpek, A.; Hu, N.; Liu, X.; Guan, X.; Zhong, Z.; Jin, X.; Khademhosseini, A.; et al. Extrusion Bioprinting of Shear-Thinning Gelatin Methacryloyl Bioinks. *Adv. Healthc. Mater.* **2017**, *6*, 1–11. [CrossRef]
31. Martanto, W.; Baisch, S.M.; Costner, E.A.; Prausnitz, M.R.; Smith, M.K. Fluid dynamics in conically tapered microneedles. *AIChE J.* **2005**, *51*, 1599–1607. [CrossRef]
32. Magalhães, I.P.; de Oliveira, P.M.; Dernowsek, J.; Las Casas, E.B.; Las Casas, M.S. Investigation of the effect of nozzle design on rheological bioprinting properties using computational fluid dynamics. *Rev. Mater.* **2019**, *24*. [CrossRef]
33. Reid, J.A.; Mollica, P.A.; Johnson, G.D.; Ogle, R.C.; Bruno, R.D.; Sachs, P.C. Accessible bioprinting: Adaptation of a low-cost 3D-printer for precise cell placement and stem cell differentiation. *Biofabrication* **2016**, *8*, 025017. [CrossRef] [PubMed]
34. Leppiniemi, J.; Lahtinen, P.; Paajanen, A.; Mahlberg, R.; Metsä-Kortelainen, S.; Pinomaa, T.; Pajari, H.; Vikholm-Lundin, I.; Pursula, P.; Hytönen, V.P. 3D-Printable Bioactivated Nanocellulose-Alginate Hydrogels. *ACS Appl. Mater. Interfaces* **2017**, *9*, 21959–21970. [CrossRef] [PubMed]
35. Nair, K.; Yan, K.C.; Sun, W. A computational modeling approach for the characterization of mechanical properties of 3D alginate tissue scaffolds. *J. Appl. Biomater. Biomech.* **2008**, *6*, 35–46. [CrossRef]
36. Smith, C.; Oldt, G. Multiaxial Bio-Printer Head. Available online: https://5f6357c8-abe2-426e-bc22-b9f609a0b347.filesusr.com/ugd/e69967_73cde5aebac44f11b0432814832a2110.pdf (accessed on 17 July 2020).
37. Li, M.; Tian, X.; Kozinski, J.A.; Chen, X.; Hwang, D.K. Modeling Mechanical Cell Damage In The Bioprinting Process Employing A Conical Needle. *J. Mech. Med. Biol.* **2015**, *15*, 1–15. [CrossRef]
38. Stewart, B. 3D Bioprinting Hydrogel for Tissue Engineering an Ascending Aortic Scaffold. Master's Thesis, University of Denve, Denver, CO, USA, June 2017.
39. Billiet, T.; Gevaert, E.; De Schryver, T.; Cornelissen, M.; Dubruel, P. The 3D printing of gelatin methacrylamide cell-laden tissue-engineered constructs with high cell viability. *Biomaterials* **2014**, *35*, 49–62. [CrossRef]
40. Liravi, F.; Darleux, R.; Toyserkani, E. Additive manufacturing of 3D structures with non-Newtonian highly viscous fluids: Finite element modeling and experimental validation. *Addit. Manuf.* **2017**, *13*, 113–123. [CrossRef]
41. Samanipour, R.; Wang, Z.; Ahmadi, A.; Kim, K. Experimental and computational study of microfluidic flow-focusing generation of gelatin methacrylate hydrogel droplets. *J. Appl. Polym. Sci.* **2016**, *133*, 24–26. [CrossRef]
42. Gretzinger, S.; Beckert, N.; Gleadall, A.; Lee-Thedieck, C.; Hubbuch, J. 3D bioprinting—Flow cytometry as analytical strategy for 3D cell structures. *Bioprinting* **2018**, *11*, e00023. [CrossRef]
43. Kesti, M.; Fisch, P.; Pensalfini, M.; Mazza, E.; Zenobi-Wong, M. Guidelines for standardization of bioprinting: A systematic study of process parameters and their effect on bioprinted structures. *BioNanoMaterials* **2016**, *17*, 193–204. [CrossRef]
44. Sultan, S.; Siqueira, G.; Zimmermann, T.; Mathew, A.P. 3D printing of nano-cellulosic biomaterials for medical applications. *Curr. Opin. Biomed. Eng.* **2017**, *2*, 29–34. [CrossRef]
45. Müller, M.; Öztürk, E.; Arlov, Ø.; Gatenholm, P.; Zenobi-Wong, M. Alginate Sulfate–Nanocellulose Bioinks for Cartilage Bioprinting Applications. *Ann. Biomed. Eng.* **2017**, *45*, 210–223. [CrossRef]
46. Cellink Bioink Biopritning Protocol. Available online: https://www.cellink.com/wp-content/uploads/2019/03/Bioprinting-Protocol-CELLINK-Bioink_21-Mars-2019.pdf (accessed on 17 July 2020).
47. COMSOL®. *CFD Module User's Guide*; COMSOL Inc.: Stockholm, Sweden, 2016; ISBN 1781273332.
48. Bartnikowski, M.; Wellard, R.M.; Woodruff, M.; Klein, T. Tailoring hydrogel viscoelasticity with physical and chemical crosslinking. *Polymers* **2015**, *7*, 2650–2669. [CrossRef]
49. Jalaal, M.; Cottrell, G.; Balmforth, N.; Stoeber, B. On the rheology of Pluronic F127 aqueous solutions. *J. Rheol. (NY)* **2017**, *61*, 139–146. [CrossRef]

50. Markstedt, K.; Mantas, A.; Tournier, I.; Martínez Ávila, H.; Hägg, D.; Gatenholm, P. 3D bioprinting human chondrocytes with nanocellulose-alginate bioink for cartilage tissue engineering applications. *Biomacromolecules* **2015**, *16*, 1489–1496. [CrossRef] [PubMed]
51. Lee, K.Y.; Mooney, D.J. Alginate: Properties and biomedical applications. *Prog. Polym. Sci.* **2013**, *37*, 106–126. [CrossRef]
52. Pati, F.; Jang, J.; Lee, J.W.; Cho, D.W. Extrusion bioprinting. In *Essentials of 3D Biofabrication and Translation*; Elsevier Inc.: Pohang-si, Korea, 2015; pp. 123–152. ISBN 9780128010150.

7.4 Computational simulation-based comparative analysis of standard 3D printing and conical nozzles for pneumatic and piston-driven bioprinting

Additive Manufacturing

Computational simulation-based comparative analysis of standard FDM 3D printing and conical nozzles for pneumatic and piston-driven bioprinting.

--Manuscript Draft--

Manuscript Number:	
Article Type:	Research Paper
Keywords:	Bioprinting; Computational simulation; Non-Newtonian fluid; FDM 3D printing nozzle; Level-set method
Corresponding Author:	José Blas Pagador, PhD Jesus Uson Minimally Invasive Surgical Centre: Centro de Cirugia de Minima Invasion Jesus Uson SPAIN
First Author:	Juan Carlos Gómez-Blanco
Order of Authors:	Juan Carlos Gómez-Blanco
	José Blas Pagador, PhD
	Victor Galván-Chacón
	Luisa F. Sánchez-Peralta
	Manuel Matamoros
	Alfonso Carlos Marcos, PhD
	Francisco Miguel Sánchez-Margallo, PhD
Abstract:	Bioprinting is currently studied as an application of additive manufacturing with promising results to improve regenerative medicine. Hydrogels, as the most used materials in bioprinting, are experimentally analyzed to assure printability and cell suitability. Beside hydrogel features, inner geometry of the μ-extrusion head can have an equal impact not only on printability but also on cellular viability. In this regard, standard FDM 3D printing nozzles are widely studied to reduce inner pressure and get faster printings using high viscous melted polymers. Computational fluids dynamics is a useful tool capable of simulating and predicting the hydrogel behavior when the extruder inner geometry is modified. Hence, the objective of this work is to comparatively study the performance of a standard FDM 3D printing and conical nozzles in a μ-extrusion bioprinting process through computational simulation. Three bioprinting parameters, namely pressure, velocity, and shear stress, are calculated using the Level-set method, considering a 22G conical tip and a 0.4 mm nozzle. Additionally, two μ-extrusion models, pneumatic and piston-driven, are simulated using dispensing pressure (15kPa) and volumetric flow (10 mm 3 /s) as input, respectively. Results show that the standard nozzle is suitable for bioprinting procedures. Specifically, the inner geometry of this nozzle increases the flow rate, while reducing the dispensing pressure and maintaining similar shear stress compared to the conical tip commonly used in bioprinting.
Suggested Reviewers:	Andreas Blaeser blaeser@idd.tu-darmstadt.de
	Farzad Liravi fliravi@uwaterloo.ca

Computational simulation-based comparative analysis of standard FDM 3D printing and conical nozzles for pneumatic and piston-driven bioprinting.

Gómez-Blanco JC [a], Pagador JB [a*], Galván-Chacón V [a], Sánchez-Peralta, LF [a], Matamoros M [b], Marcos AC [b], Sánchez-Margallo FM [a]

[a] Jesús Usón Minimally Invasive Surgery Centre, 10071 Cáceres, Spain

[b] School of Industrial Engineering, University of Extremadura, 06006 Badajoz, Spain

* Correspondence authors

Abstract

Bioprinting is currently studied as an application of additive manufacturing with promising results to improve regenerative medicine. Hydrogels, as the most used materials in bioprinting, are experimentally analyzed to assure printability and cell suitability. Beside hydrogel features, inner geometry of the μ-extrusion head can have an equal impact not only on printability but also on cellular viability. In this regard, standard FDM 3D printing nozzles are widely studied to reduce inner pressure and get faster printings using high viscous melted polymers. Computational fluids dynamics is a useful tool capable of simulating and predicting the hydrogel behavior when the extruder inner geometry is modified. Hence, the objective of this work is to comparatively study the performance of a standard FDM 3D printing and conical nozzles in a μ-extrusion bioprinting process through computational simulation. Three bioprinting parameters, namely pressure, velocity, and shear stress, are calculated using the Level-set method, considering a 22G conical tip and a 0.4 mm nozzle. Additionally, two μ-extrusion models, pneumatic and piston-driven, are simulated using dispensing pressure (15kPa) and volumetric flow (10 mm^3/s) as input, respectively. Results show that the standard nozzle is suitable for bioprinting procedures. Specifically, the inner geometry of this nozzle increases the flow rate, while reducing the dispensing pressure and maintaining similar shear stress compared to the conical tip commonly used in bioprinting.

Keywords

Bioprinting; Computational simulation; Bioink; 3D printing; Nozzle; Conical tip; Level-set method; Fluid dynamics; Non-Newtonian fluid

1. Introduction

Among all possible additive manufacturing applications, bioprinting is presented as one of the most studied. The combination of novel manufacturing processes with standard tissue engineering protocols is leading to a revolution in the medical field. Bioprinting is formally defined as *"the process of producing tissue or organs similar to natural body parts and containing living cells, using 3-D printing"* [1]. One of the main reasons this technology is widely studied is because it minimizes the rejection risk when patient's cells are used in the process [2]. Researchers are using bioprinting to study the generation of vascular, neural, bone, cardiac, skin or muscle tissues [3,4]. Since each tissue has very specific properties and functionality depending on the role that plays within the body, the procedure in the bioprinting process as well as the main material must be a perfect match with the cell-line of the target tissue. In this sense, μ-extrusion, inkjet, laser-assisted, and stereolithography have been identified as the most common technologies in bioprinting [5], among which μ-extrusion bioprinting is the most used one. Despite its low printing speed, it is

the most versatile technique and allows using high viscous materials with high cell density [2,5,6]. μ-extrusion bioprinting can be done using different approaches, such as pneumatic or piston-driven μ-extrusion. While the former facilitates the bioprinting parameters configuration such as the dispensing pressure, the latter provides a more stable volumetric flow [2,5,6].

Regarding bioprinting materials, there are many studies that analyze the interaction between the material and cell viability [7,8], printability [9–11], crosslinking [12–14] or shape fidelity [15,16]. Hydrogels are the most common material in μ-extrusion bioprinting. Despite they are mainly composed of water, their usual behavior is closer to a shear-thinning non-Newtonian material. In this type of material, the viscosity plays a principal role in how the material flows. In general, the higher the viscosity is, the higher the inner pressure and the shear stress are, which means that higher force is needed to obtain a proper flow. Regarding inner pressure and shear stress, previous studies show that they can provoke cell lysis [17–19], i.e. cells die due to the break of their cellular membrane. As for viscosity, high values are usually required to achieve the best shape fidelity [20]. Viscosity is also sensitive to temperature [21–24] and it is widely studied together with the concentration of components to assure printability [10,11,25]. So, as viscosity affects the nozzle inner flow and cellular viability, it is a key factor to study [26,27]. Therefore, the actual behavior of the bioink flowing inside the nozzle is an important aspect to determine but difficult to achieve with experimental tests. The small nozzle size causes that the nozzle inner geometry has great influence on the material flow. Additionally, the smaller the nozzle, the more difficult is to sensorize it and to experimentally measure the flow without disturbing it or using any scaling technique. There are many studies about bioprinting hydrogels but most of them are experimental and focused on bioprinting results while the study of crucial inner parameters such as pressure or shear stress is often neglected/overlooked [20,28]. For this reason, computational simulations were proposed as a helpful tool to obtain hard to measure, bioprinting inner parameters [29,30]. Previous studies showed that cell viability was highly impacted by the nozzle inner pressure, and even more by the shear stress [17]. In this sense, Blaeser et al. [31] classified the shear stress ranges that affect cellular viability into low shear stress (<5 kPa), that has high cellular viability up to 96%; medium shear stress (5-10 kPa), with a cellular viability of 91%; and high shear stress (>10 kPa), with a cell viability of 76%.

Computational simulation is currently used to study different features of the bioprinting process as shear stress [32], non-commercial nozzle geometries [33–35], bioprinting materials [36] or their tuned rheological properties [30,37]. Regarding the interaction between nozzle geometry and hydrogel flow, two approaches can be followed: either fixing the hydrogel and changing the nozzle geometries [18,34,35,38] or fixing the nozzle geometry and changing the hydrogel properties [30,32,36,39–41]. More complex simulations studied the generation of droplets for inkjet bioprinting [40,42] or the generation of strands for μ-extrusion bioprinting [43]. They all used the Two-Phase Flow Level-set model in COMSOL Multiphysics to simulate the bioprinting process. On the one hand, results from Liravi et al. [40] and Samanipour et al. [42] showed a experimentally tested droplet generation using a 27G conical tip. On the other hand, Gómez-Blanco et al. [43] studied some inner parameters of the μ-extrusion process (shear stress, pressure and velocity), but without experimental validation. Finally, other simulation studies analyzed the flow through a standard 3D printing nozzle and the filament deposition in a fuse deposition modelling process [44,45]. Nevertheless, as far as authors know, there are no previous studies that analyze the performance of standard 3D printing nozzles with bioprinting materials.

Hence, the working hypothesis is that a standard FDM 3D printing nozzle could improve the performance of a conical tip standard bioprinting nozzle. Furthermore, the objective of this work is to analyze the performance of the proposed E3D V6 standard nozzle compared with a 22G conical tip for a μ-extrusion bioprinting process using a commercial bioink (Cellink Bioink, Cellink USA) as hydrogel. Specifically, outlet and inlet (or dispensing) pressure, volumetric flow,

outlet velocity and shear stress are analyzed. To properly study the feasibility of the proposed nozzle, two different inlets parameters are configured to simulate pneumatic and piston-driven μ-extrusion bioprinting.

2. Material and methods

2.1 Computational model and simulation

The methodology used in this work follows the geometrical and computational models, the mathematical solvers and the hydrogel features defined by Gómez-Blanco et al. [43]. Specifically, two 2D axisymmetric geometrical models were created and simulated in COMSOL Multiphysics 5.4a (COMSOL Inc., Burlington, MA, USA, 2018) using a Two-Phase Flow Level-set interface approach. These two geometrical models were a bioprinting 22G conical tip and a 3D-printing E3D V6.4 nozzle, named as Cone and Nozzle, respectively, in the remainder of the paper. The geometries were obtained by experimental measurement for the Cone and from blueprints for the Nozzle [46]. Each simulation considered two domains, the first one referred to the hydrogel inside of the Cone/Nozzle and the second one referred to air. Different inlet parameters were configured to two approaches: a pneumatic process with 15 kPa inlet pressure, as recommended by Cellink [47], and a piston-driven process with 10 mm^3/s volumetric inlet flow.

In this work, Cellink bioink was simulated at 37ºC with the following fitted potential law:

$$\mu = 87.906(\dot{\gamma})^{-0.792}$$

where μ is the dynamic viscosity (Pa·s) and $\dot{\gamma}$ is the shear rate (s^{-1}).

Regarding simulations, a total of four different simulations were performed. A 10 seconds simulation with a 1 ms step was done for each geometrical model and inlet configuration. The simulation study was composed by a Phase initialization and a Time-Dependent steps.

A laminar flow based on the low Reynolds number (Re≅0.4) is assumed in the simulations, according to a previous study [43] where simulations formed a falling drop with a later accumulation of material until it reached the tip.

2.2 Experimental tests

Pneumatic simulations were validated through experimental tests to assure that they were accurate within acceptable error ranges, despite the assumed simplifications. Our validation tests recreated the experimental validation performed by Liravi et al. [40]. The extruded strand was measured and compared with the simulation results, using the total height and the maximum width of this extruded strand. This indirect validation of our simulations is used due to the small outlet diameter of the Cone and Nozzle, that made nearly impossible to measure the pressure or the velocity without disturbing the normal flow and thus, modifying the results. A Sony Alpha 7 ii (ILCE-7m2) camera with a Sony f 2.8/90 OSS macro was used to record the extruded Cellink Bioink strand with a 1920x1080 px resolution and 0.5x magnification. The distance between the camera lens and the nozzle tip was 28 cm (focal distance). The μ-extrusion was performed in Cellink BioX bioprinter with a pre-set of 15 kPa for inlet pressure. Three videos of each experimental test were recorded from which frames were extracted using Open CV and analyzed using ImageJ 1.53e software.

3. Results and discussion

This section only analyzes data until the drop falls, although figures present simulations of 10 seconds. The reason for this partial analysis is that the accumulation of material in the simulations

after the drop falls it is not present in experimental bioprinting due to the X-Y movement of the extruder head that is still not implemented in simulations.

Outlet and inlet pressure

Figure 1 shows the outlet pressure measured at end of the Cone and Nozzle for pneumatic and piston-driven simulations.

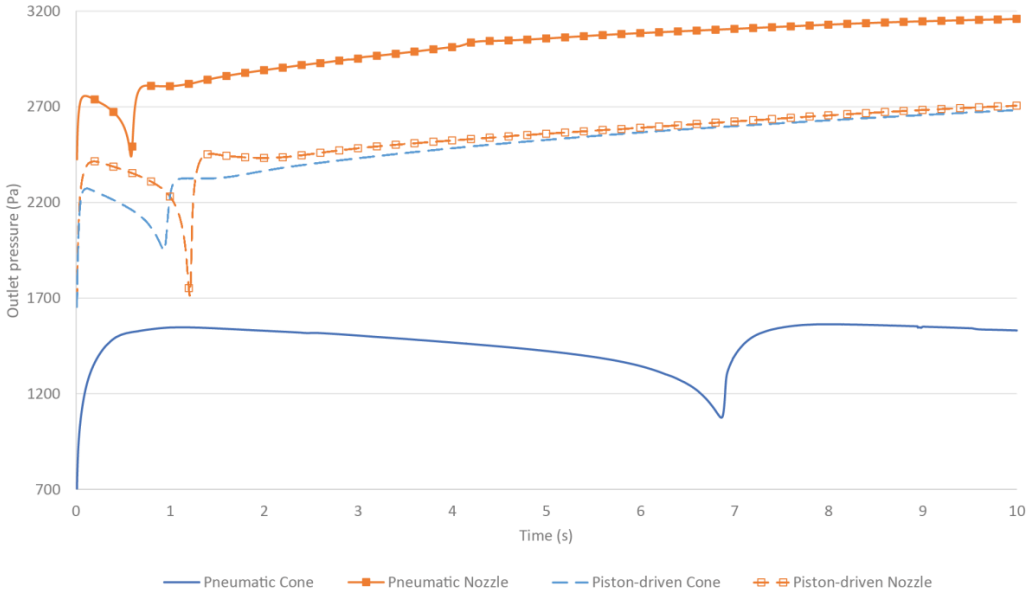

Figure 1. Outlet pressure (Pa) of pneumatic and piston-driven simulations and the two analyzed nozzles.

Analyzing the pressure of pneumatic simulations, using 15 kPa as the simulation inlet, the pressure evolution in both geometries is similar with a low-pressure peak. This low-pressure peak is explained by the formation and falling of a drop, as detected in previous works [43]. Therefore, the maximum outlet pressure before the low-pressure peak reaches 2.75 and 1.54 kPa for the Nozzle and Cone, respectively. Therefore, the outlet pressure of the Nozzle is approximately twice that of the Cone. The peaks are in 0.586 and 6.860 s for Nozzle and Cone, respectively. This difference in times might be caused by the total amount of extruded bioink. In this sense, Figure 2 shows that the flow rate of the Nozzle geometry is higher than in the Cone. Specifically, the drop volume extruded by the Nozzle is 12.70 mm^3 while the one by the Cone is 9.72 mm^3 through the same cross-area. So, the Nozzle geometry extrudes approximately 15 times more bioink that the Cone (21.67 vs 1.42 mm^3/s). This huge difference in the bioink flow rate can be useful to speed up the bioprinting process while maintaining the recommended dispensing pressure for this specific bioink. The use of a Nozzle type µ-extrusion head in pneumatic bioprinting can partially solve the current challenge of low printing speed for bioprinting [2,5,6,19].

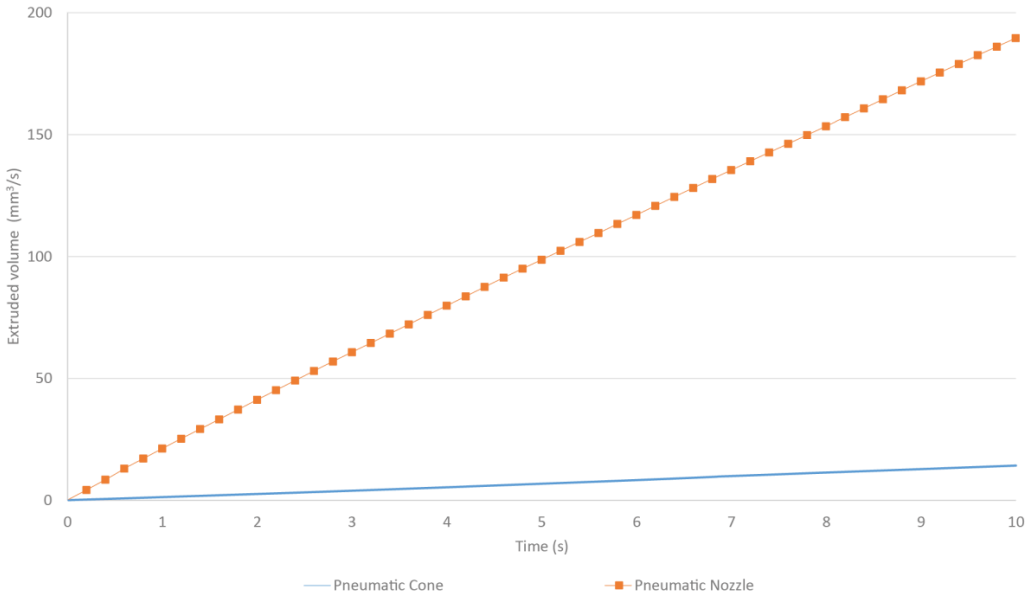

Figure 2. Extruded volume (mm^3/s) of pneumatic simulations. Extruded volume of piston-driven simulations is not shown in the figure because volumetric flow is set as simulation inlet ($10mm^3/s$ so the extruded volume in 10 s is 100 mm^3).

Outlet pressure from piston-driven simulations shows a similar evolution in values and times (Figure 1). Therefore, there were not noticeable differences between the Nozzle and Cone maximum pressure values (2.41 and 2.27 kPa), the time when the drop falls (0.928 and 1.208 s) or the low-pressure peak values (250 Pa lower for the Nozzle).

Comparing all simulations, the Nozzle outlet pressure is higher than the Cone for all cases. However, Figure *1* shows that for piston-driven simulations the outlet pressure is nearly the same. Hence, the input or dispensing pressure plays an important role when obtaining the outlet pressure, but in all cases they vary in a short range with a maximum variation of approximately 2.2 kPa.

Regarding to the inlet or dispensing pressure, pneumatic simulations fixed it at 15 kPa, but piston-driven simulations that fixed the volumetric flow reduce it for the Nozzle (Figure 3).

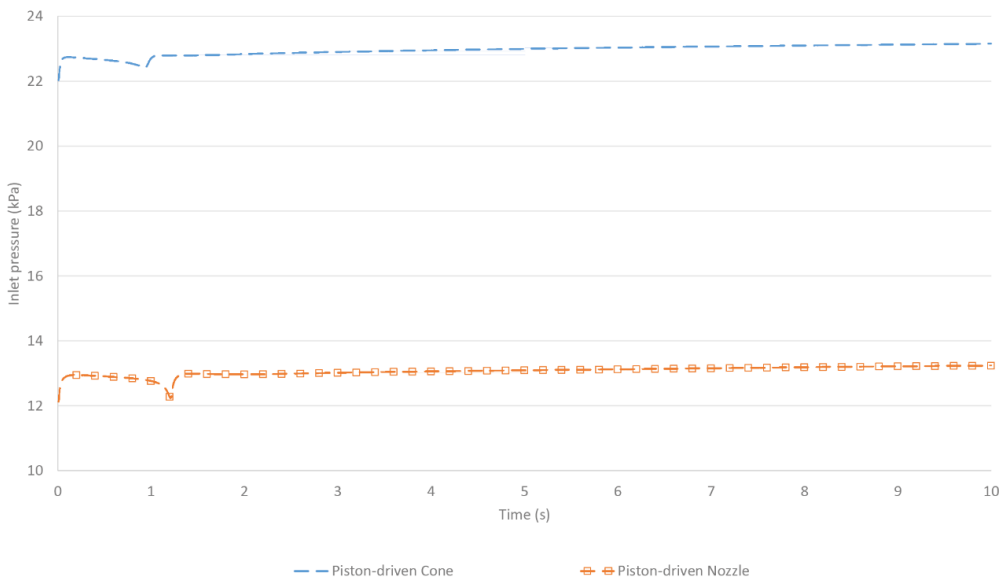

Figure 3. Dispensing pressure (kPa) of piston-driven simulations. Pneumatic dispensing pressure are not shown in the figure because they are set as 15 kPa inlet pressure for simulations.

The maximum inlet pressure values are 22.73 and 12.95 kPa for the piston-driven Cone and Nozzle geometries, respectively. The obtained values are consistent with the pneumatic simulation extruded volume (Figure 2). The Cone needs an inlet pressure over 15 kPa to achieve the expected extruded volume while the Nozzle requires lower pressure to extrude the same volume. In this sense, the Cone inlet pressure is 1.76 times bigger than the Nozzle pressure. According to Boularaoui et al. [19], the lower the dispensing pressure, the better the cellular viability. Therefore, the lower dispensing pressure obtained with the Nozzle should be better for µ-extrusion bioprinting to improve cellular viability.

Our simulation results are also similar to Gómez-Blanco et al. [43], who obtained maximum values in the range of 1.14-1.76 kPa for conical tips using 15 kPa as inlet pressure. Thus, the pressure values are in their range for pneumatic simulations and Cone geometry but not for the rest. Additionally, Reid et al. [35] set the outlet pressure to 1 atm (101 kPa) and obtained maximum inner pressure with an approximate value of 107 kPa. This value can be understood as the inlet pressure, but proper explanation is missing in the manuscript to assure this statement. In this sense, while they obtained 6 kPa of inlet pressure, which seems better than ours results, it is difficult to make a fair comparison between both studies due to three main differences in the methodologies. The first one is the selected extrusion material, they used *"a fluid with similar properties to blood"* as the bioink with no further information, while we properly defined the rheological data of the material. Secondly, the different inlet volumetric flow, as in our simulations we set 10 mm^3/s while they set 0.1 mm^3/s. Finally, the different geometry, since we used a standard 0.4 mm 3D printing nozzle and a 22G (0.4mm) conical tip, whereas they used a custom-made glass "*similar to conical*" tip with an outlet diameter of 60 µm.

Attending to the inner pressure, set as the difference between inlet (or dispensing) and outlet pressure, results are 13.46 and 12.25 kPa for Cone and Nozzle, respectively, in pneumatic simulations; and 20.46 and 10.54 kPa for Cone and Nozzle piston-driven simulations, respectively. Inner pressure must be carefully analyzed, as even though lower inner pressure might be beneficial for cells, if it is a result of very high inlet and outlet pressure, it would still

compromise cellular viability. In this sense, Boularaoui et al. [19] concluded in their work that cellular viability is inversely related to the dispensing pressure and although they forewarn of the influence of this parameter, they do not define a threshold value. So according to our results, inner pressure in pneumatic simulations is very similar, but the total extruded volume makes the Nozzle to have a better performance. Similar conclusion can be obtained from piston-driven simulations pressure, as the Nozzle geometry is capable of extruding the same amount of material that the Cone with 10 kPa less of inner pressure and half the inlet pressure.

Outlet Velocity

As literally concluded by Boularaoui et al. [19]: "*cell damage appears to be affected by exposure time to stress more than the magnitude of the stress itself*". Thus, outlet velocity is another important parameter to be analyzed. In this regard, results of maximum velocity obtained in the bioink domain for all simulations can be found in Figure 4.

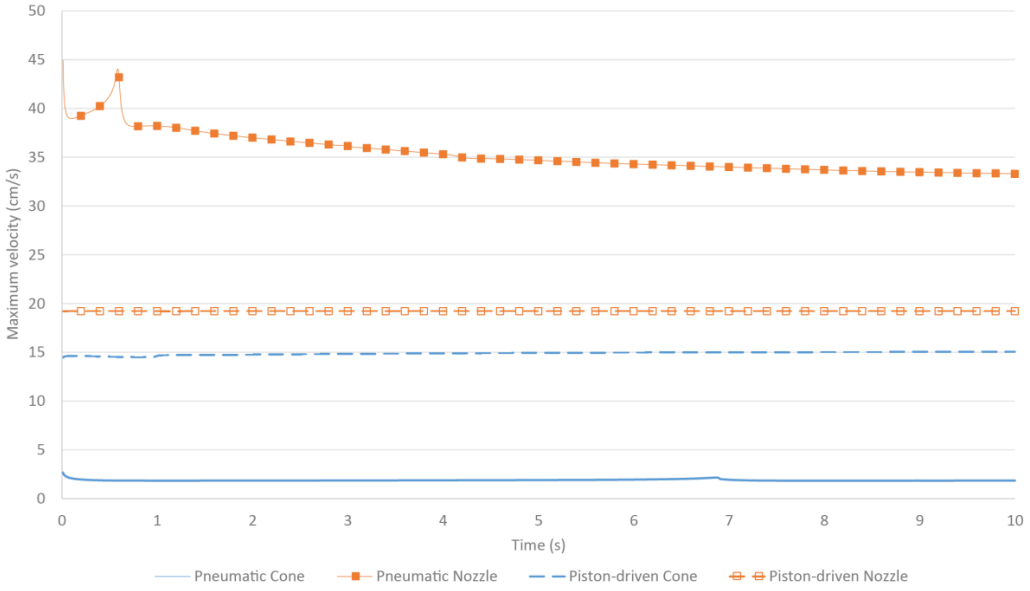

Figure 4. Maximum velocity (cm/s) of pneumatic and piston-driven simulations.

Figure 4 shows that all Nozzle simulations have higher velocities than those for the Cone. In all cases, a high-velocity peak is formed, but only in the simulation for the Nozzle under pneumatic μ-extrusion is easily noticeable. The lowest velocities for each simulation are 1.88 and 38.96 cm/s for Cone and Nozzle pneumatic simulations, and further 14.50 and 19.20 cm/s for Cone and Nozzle piston-driven simulations, respectively. These differences in velocities can be explained by the different extruded volume (flow rate) in pneumatic simulations and the different geometry in piston-driven simulations. Despite velocity values are similar in piston-driven simulations, the Nozzle velocity is 32% higher than the Cone one. Hence, according to Boularoui at al. [19] and looking at our results, it can be concluded that cells are expected to stay less time under stress in the Nozzle geometry, which might eventually reduce cell damage while increasing the viability.

Regarding to other authors, Reid et al. [35] obtained 5.50 and 7.20 cm/s for 60 μm diameter conical and needle tips, respectively, but direct comparison with our results is not fair enough due to methodological differences, as exposed in the previous subsection about pressure. Additionally, Smith et al. [38] obtained, at the end of their 28G (0.184 mm diameter) multiaxial needle, a velocity of 36.70 cm/s. They used a similar material mainly composed of alginate and also fitted to the standard Potential Law, but their alginate bioink seems to be more viscous than ours. Nevertheless, their inlet was composed of three different needle entrances and they set one

velocity for each entrance (0.4, 1.81 and 6.57 cm/s). Therefore, and similarly as what happened with Reid et al., results of Smith are not directly comparable to ours due to these major differences in the inlet.

Shear Stress

Shear stress is the most important parameter to determine the cellular viability of any bioprinting process. Boularaoui et al. [19] and Blaeser et al. [31] performed a thorough study of shear stress in bioprinting and both concluded that the shear stress has a direct negative impact on the cellular viability. Additionally, Blaeser et al. [31] also determined that shear stress lower than 5 kPa might not have an important influence on cellular survival. Figure 5 shows the shear stress obtained for all simulations. We report the worst-case scenario, which corresponds to the highest-stress peak for each simulation. Therefore, our values of shear stress are 455.43 and 242.16 Pa for Nozzle and Cone pneumatic simulations, respectively, and 362.85 and 383.24 Pa for Nozzle and Cone piston-driven simulations, respectively. From results, the Nozzle geometry provokes higher shear stress than the Cone one in all cases. Nevertheless, the maximum difference is approximately 213 Pa and the maximum value of shear stress for all simulations is 455.43 Pa, which are in both cases more than 10 times lower than the threshold proposed by Blaeser et al [31]. Thus, it can be concluded that both geometries generate a shear stress below what is indicated as unappropriated for cells and both can be used in these conditions for bioprinting.

Besides Bleaser et al., other authors also studied the shear stress for bioprinting purposes. Liu et al. [32] obtained low shear stress (30, 180 and 300 Pa) using different concentrations of a bioink with lower viscosity and using needle and conical tips. Despite they use similar geometries, the different material and the much lower inlet volumetric flow (1.67 mm^3/s) make the comparison of results to be not fair. Müller et al. [48] also studied the shear stress using several needle and conical tips (namely 22, 23, 25, 27, and 30G) with a very similar alginate with nanocellulose bioink, obtaining results around 160 Pa. Specifically, the shear stress for the same 22G conical tip geometry is 151.88 Pa. While this result is lower than any of our shear stress, they used a 6 kPa as inlet pressure instead of the 15kPa that we used. Since lower inlet pressure means lower volumetric flow and lower shear stress, the results are not directly comparable to ours by the same reasons as with Liu et al. work.

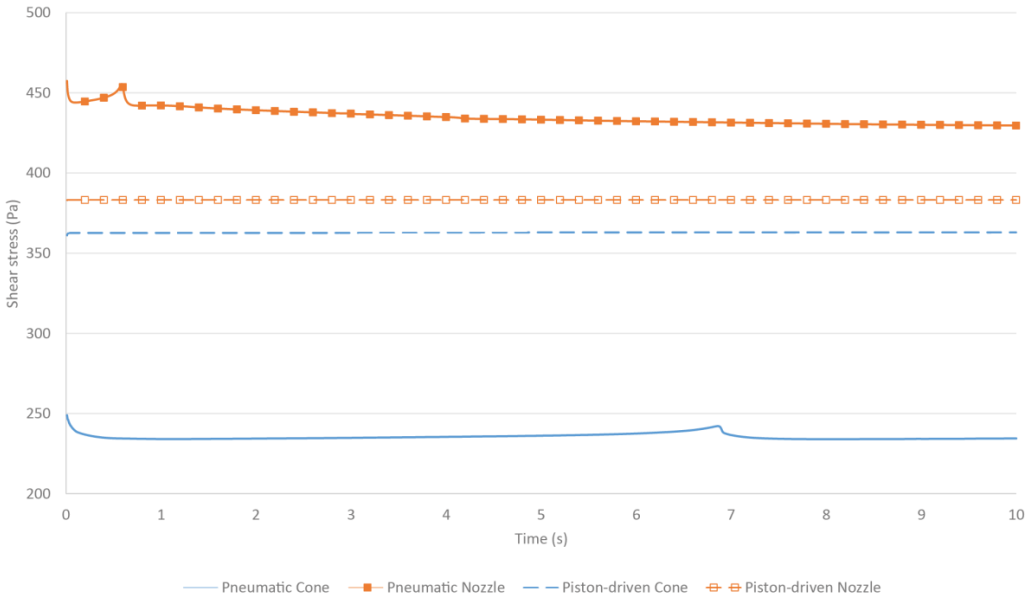

Figure 5. Maximum Shear Stress (Pa) of pneumatic and piston-driven simulations.

Experimental tests

The experimental test was set to analyze the strand during the first drop formation. Since drops are formed at different time for the Cone and Nozzle in the pneumatic μ-extrusion processes, measurement times were established at 25, 50, 75 and 100% of the time needed to generate a drop. Exact times are given in Table *1*.

	Cone (s)	Nozzle (s)
t=25%	1.715	0.145
t=50%	3.430	0.293
t=75%	5.145	0.439
t=100%	6.860	0.586

Table 1. Four measurement times at different percentages of a drop generation for each geometry in the pneumatic simulations.

The measurement results as well as the relative error between measurements can be seen in Table *2*.

	Cone Exp h, w (mm)	Cone Sim h, w (mm)	Cone Err h, w (%)	Nozzle Exp h, w (mm)	Nozzle Sim h, w (mm)	Nozzle Err h, w (%)
t=25%	3.32, 0.67	3.52, 0.60	5.99, 10.53	3.47, 0.87	3.36, 0.72	3.01, 17.26
t=50%	7.59, 0.64	6.53, 0.62	14.00, 3.33	7.29, 0.82	6.35, 0.74	12.80, 9.62
t=75%	13.35, 0.66	10.34, 0.65	22.53, 2.67	11.92, 0.81	9.67, 0.73	18.86, 9.87
t=100%	24.86, 0.70	19.68, 0.68	20.85, 2.29	20.44, 0.79	14.84, 0.72	27.42, 7.32
Average error	-	-	12.85, 4.70	-	-	15.52, 11.02

Table 2. Experimental and simulation average measurements of maximum height (h) and width (w) in millimeters with the relative error (%) of the extruded strand in pneumatic simulations.

All relative errors are similar to the results obtained by Liravi et al. [40]. Additionally, relative errors from Table *2* show a similar evolution along time for the Cone and Nozzle. Specifically, height error increases from 5.99 to 20.85 % and from 3.01 to 27.42 % for Cone and Nozzle, respectively. The width error trend is exactly the opposite one, as error decreases when the time increases. It might be expected that simplifications assumed for the simulations are the main cause of these errors.

Figure 6 shows the frames and simulation images of the previous measurement times for both geometries. In the experimental frames, an initial accumulation of material is produced both in the Cone and Nozzle. This accumulation is provoked by a rolling up of the bioink when it starts to be extruded. This real behavior is not simulated because the current simplified geometry does not include any manufacturing imperfections, such as fabrication failures or surface finish, of the actual nozzle or conical tip. In particular, the frame showing the drop at t=100% for the experimental test of the Nozzle shows an extruded strand that is not perfectly vertical despite the Nozzle was perfectly positioned. This deviation might be caused by a possible fabrication failure of the inner geometry of the Nozzle that can not be easily observed.

Looking at the average errors and the results obtained by Liravi et al. [40], it can be concluded that our simulations recreate the geometry of the extruded strand with an acceptable error. Additionally, Liravi et al. [40] concluded that if the external geometry of the extruded bioink is similar to the experimental tests, assuming the errors, the model can predict the falling drop and the suitable combination of inner parameters. With this in mind, experimental pressure, velocity and shear stress values, which are difficult to measure without modifying the actual flow, might have similar values to those obtained in our simulations.

According to the experimental errors, our results can be considered as an approximation of the real values of a material using a new geometry of the extruder head. Thus, our simulations can guarantee acceptable and similar bioprinting inner parameters values with less computational cost

that more precise and complex simulations. However, the 2D axis-symmetrical approximation might be insufficient to obtain more precise values of these inner parameters. This approximation simplifies the geometry assuming that the material behavior is equal in its revolution. Taking this into account, further modifications in the simulations and the rheological data of the bioink might be necessary to reduce the error as well as a comparative study of the current simulations with a more complex 3D simulation model.

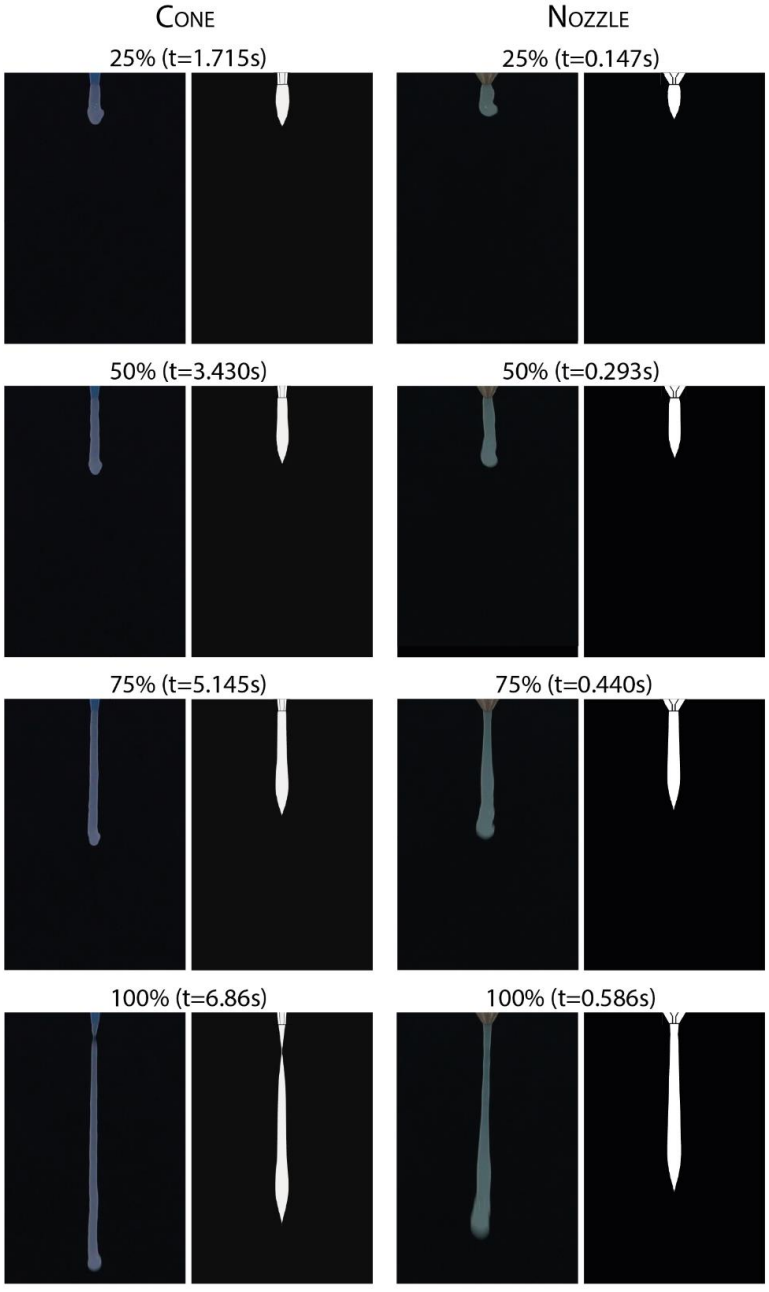

Figure 6. *Comparative images of experimental validation (*left*) and simulations (*right*) for* the *Cone and* the *Nozzle pneumatic simulations.*

4. Conclusions

In this work we prove the feasibility of a standard 0.4 mm FDM 3D printing nozzle for its use in bioprinting applications, providing computational fluid dynamics simulations that were experimentally verified. Specifically, different inlet properties of these simulations were considered to study pneumatic and piston-driven bioprinting and the FDM 3D printing nozzle was compared with a 22G conical tip, commonly used for bioprinting. Additionally, pneumatic simulations were experimentally checked to validate the computational models.

Both simulation and experimental results demonstrate that the FDM 3D printing nozzle can be used for bioprinting with better performance than the 22G conical tip. Shear stress, as the most relevant factor for cellular viability, has similar values independently of using either the 0.4 mm 3D printing nozzle or the 22G conical tip. Additionally, the 3D printing nozzle can halve the needed dispensing pressure while keeping the same volumetric flow; or it can increase the volumetric flow, therefore speeding up the bioprinting process while maintaining the dispensing pressure.

5. Acknowledgements

This research was financed by predoctoral grant number PD16067 and project number 0633_BIOIMPACE_4_A. Co-financed by European Union/ERDF, ESF, European Regional Development Fund ERDF under the Interreg V A Spain - Portugal (POCTEP) 2014-2020 program and Consejería de Economía, Ciencia y Agenda Digital de la Junta de Extremadura.

6. References

[1] Cambridge dictionary, Cambidge dictionary - Bioprinting, (n.d.). https://dictionary.cambridge.org/es/diccionario/ingles/bioprinting (accessed February 19, 2021).

[2] W.L. Ng, C.K. Chua, Y.F. Shen, Print Me An Organ! Why We Are Not There Yet, Prog. Polym. Sci. 97 (2019) 101145. https://doi.org/10.1016/j.progpolymsci.2019.101145.

[3] I.T. Ozbolat, W. Peng, V. Ozbolat, Application areas of 3D bioprinting, Drug Discov. Today. 21 (2016) 1257–1271. https://doi.org/10.1016/j.drudis.2016.04.006.

[4] M.A. Heinrich, W. Liu, A. Jimenez, J. Yang, A. Akpek, X. Liu, Q. Pi, X. Mu, N. Hu, R.M. Schiffelers, J. Prakash, J. Xie, Y.S. Zhang, 3D Bioprinting: from Benches to Translational Applications, Small. 15 (2019) 1–47. https://doi.org/10.1002/smll.201805510.

[5] B. Zhang, L. Gao, L. Ma, Y. Luo, H. Yang, Z. Cui, 3D Bioprinting: A Novel Avenue for Manufacturing Tissues and Organs, Engineering. 5 (2019) 777–794. https://doi.org/10.1016/j.eng.2019.03.009.

[6] S. Kyle, Z.M. Jessop, A. Al-Sabah, I.S. Whitaker, 'Printability'' of Candidate Biomaterials for Extrusion Based 3D Printing: State-of-the-Art,' Adv. Healthc. Mater. 6 (2017). https://doi.org/10.1002/adhm.201700264.

[7] A.L. Rutz, E.S. Gargus, K.E. Hyland, P.L. Lewis, A. Setty, W.R. Burghardt, R.N. Shah, Employing PEG crosslinkers to optimize cell viability in gel phase bioinks and tailor post printing mechanical properties, Acta Biomater. 99 (2019) 121–132. https://doi.org/10.1016/j.actbio.2019.09.007.

[8] J. Zhang, E. Wehrle, J.R. Vetsch, G.R. Paul, M. Rubert, R. Müller, Alginate dependent changes of physical properties in 3D bioprinted cell-laden porous scaffolds affect cell viability and cell morphology, Biomed. Mater. 14 (2019) 065009.

https://doi.org/10.1088/1748-605X/ab3c74.

[9] J.H.Y. Chung, S. Naficy, Z. Yue, R. Kapsa, A. Quigley, S.E. Moulton, G.G. Wallace, Bio-ink properties and printability for extrusion printing living cells, Biomater. Sci. 1 (2013) 763–773. https://doi.org/10.1039/c3bm00012e.

[10] T. Gao, G.J. Gillispie, J.S. Copus, A.P.R. Kumar, Y.-J. Seol, A. Atala, J.J. Yoo, S.J. Lee, Optimization of gelatin-alginate composite bioink printability using rheological parameters: A systematic approach, Biofabrication. 10 (2018). https://doi.org/10.1088/1758-5090/aacdc7.

[11] Y. He, F. Yang, H. Zhao, Q. Gao, B. Xia, J. Fu, Research on the printability of hydrogels in 3D bioprinting., Sci. Rep. 6 (2016) 29977. https://doi.org/10.1038/srep29977.

[12] O. Jeon, Y.B. Lee, T.J. Hinton, A.W. Feinberg, E. Alsberg, Cryopreserved cell-laden alginate microgel bioink for 3D bioprinting of living tissues, Mater. Today Chem. 12 (2019) 61–70. https://doi.org/10.1016/j.mtchem.2018.11.009.

[13] I. Pepelanova, K. Kruppa, T. Scheper, A. Lavrentieva, Gelatin-methacryloyl (GelMA) hydrogels with defined degree of functionalization as a versatile toolkit for 3D cell culture and extrusion bioprinting, Bioengineering. 5 (2018). https://doi.org/10.3390/bioengineering5030055.

[14] L. Raddatz, A. Lavrentieva, I. Pepelanova, J. Bahnemann, D. Geier, T. Becker, T. Scheper, S. Beutel, Development and application of an additively manufactured calcium chloride nebulizer for alginate 3D-bioprinting purposes, J. Funct. Biomater. 9 (2018). https://doi.org/10.3390/jfb9040063.

[15] Z. Zheng, J. Wu, M. Liu, H. Wang, C. Li, M.J. Rodriguez, G. Li, X. Wang, D.L. Kaplan, 3D Bioprinting of Self-Standing Silk-Based Bioink, Adv. Healthc. Mater. 7 (2018) 1701026. https://doi.org/10.1002/adhm.201701026.

[16] D. Wu, Y. Yu, J. Tan, L. Huang, B. Luo, L. Lu, C. Zhou, 3D bioprinting of gellan gum and poly (ethylene glycol) diacrylate based hydrogels to produce human-scale constructs with high-fidelity, Mater. Des. 160 (2018) 486–495. https://doi.org/10.1016/j.matdes.2018.09.040.

[17] K.C. Yan, K. Paluch, K. Nair, W. Sun, Effects of process parameters on cell damage in a 3d cell printing process, in: ASME Int. Mech. Eng. Congr. Expo. Proc., 2010: pp. 75–81. https://doi.org/10.1115/IMECE2009-11528.

[18] M. Li, X. Tian, J.A. Kozinski, X. Chen, D.K. Hwang, MODELING MECHANICAL CELL DAMAGE in the BIOPRINTING PROCESS EMPLOYING A CONICAL NEEDLE, J. Mech. Med. Biol. 15 (2015) 1–15. https://doi.org/10.1142/S0219519415500736.

[19] S. Boularaoui, G. Al Hussein, K.A. Khan, N. Christoforou, C. Stefanini, An overview of extrusion-based bioprinting with a focus on induced shear stress and its effect on cell viability, Bioprinting. 20 (2020) e00093. https://doi.org/10.1016/j.bprint.2020.e00093.

[20] E. Mancha, J. Gómez-Blanco, E. López-Nieto, J. García-Casado, A. Macías, M. Díaz-Díez, J. Carrasco-Amador, D. Torrejón, F. Sanchez-Margallo, J. Pagador, Hydrogels for bioprinting: A systematic review of hydrogels synthesis, bioprinting parameters and bioprinted structures behavior, Front. Bioeng. Biotechnol. In Press (2020). https://doi.org/10.3389/fbioe.2020.00776.

[21] E. Axpe, M.L. Oyen, Applications of alginate-based bioinks in 3D bioprinting, Int. J. Mol. Sci. 17 (2016). https://doi.org/10.3390/ijms17121976.

[22] S. Dutta, D. Cohn, Temperature and pH responsive 3D printed scaffolds, J. Mater. Chem.

B. 5 (2017) 9514–9521. https://doi.org/10.1039/c7tb02368e.

[23] W.J. Kim, G.H. Kim, 3D bioprinting of functional cell-laden bioinks and its application for cell-alignment and maturation, Appl. Mater. Today. 19 (2020). https://doi.org/10.1016/j.apmt.2020.100588.

[24] D. Zhou, J. Chen, B. Liu, X. Zhang, X. Li, T. Xu, Bioinks for jet-based bioprinting, Bioprinting. 16 (2019). https://doi.org/10.1016/j.bprint.2019.e00060.

[25] L. Ouyang, R. Yao, Y. Zhao, W. Sun, Effect of bioink properties on printability and cell viability for 3D bioplotting of embryonic stem cells, Biofabrication. 8 (2016) 1–12. https://doi.org/10.1088/1758-5090/8/3/035020.

[26] E.A. Kiyotake, A.W. Douglas, E.E. Thomas, S.L. Nimmo, M.S. Detamore, Development and quantitative characterization of the precursor rheology of hyaluronic acid hydrogels for bioprinting, Acta Biomater. 95 (2019) 176–187. https://doi.org/10.1016/j.actbio.2019.01.041.

[27] J. Jia, D.J. Richards, S. Pollard, Y. Tan, J. Rodriguez, R.P. Visconti, T.C. Trusk, M.J. Yost, H. Yao, R.R. Markwald, Y. Mei, Engineering alginate as bioink for bioprinting, Acta Biomater. 10 (2014) 4323–4331. https://doi.org/10.1016/j.actbio.2014.06.034.

[28] N. Ashammakhi, S. Ahadian, C. Xu, H. Montazerian, H. Ko, R. Nasiri, N. Barros, A. Khademhosseini, Bioinks and bioprinting technologies to make heterogeneous and biomimetic tissue constructs, Mater. Today Bio. 1 (2019) 23. https://doi.org/10.1016/j.mtbio.2019.100008.

[29] S. Zhang, S. Vijayavenkataraman, W.F. Lu, J.Y.H. Fuh, A review on the use of computational methods to characterize, design, and optimize tissue engineering scaffolds, with a potential in 3D printing fabrication, J. Biomed. Mater. Res. - Part B Appl. Biomater. 107 (2019) 1329–1351. https://doi.org/10.1002/jbm.b.34226.

[30] J. Göhl, K. Markstedt, A. Mark, K. Håkansson, P. Gatenholm, F. Edelvik, Simulations of 3D bioprinting: Predicting bioprintability of nanofibrillar inks, Biofabrication. 10 (2018). https://doi.org/10.1088/1758-5090/aac872.

[31] A. Blaeser, D.F. Duarte Campos, U. Puster, W. Richtering, M.M. Stevens, H. Fischer, Controlling Shear Stress in 3D Bioprinting is a Key Factor to Balance Printing Resolution and Stem Cell Integrity, Adv. Healthc. Mater. 5 (2016) 326–333. https://doi.org/10.1002/adhm.201500677.

[32] W. Liu, M.A. Heinrich, Y. Zhou, A. Akpek, N. Hu, X. Liu, X. Guan, Z. Zhong, X. Jin, A. Khademhosseini, Y.S. Zhang, Extrusion Bioprinting of Shear-Thinning Gelatin Methacryloyl Bioinks, Adv. Healthc. Mater. 6 (2017) 1–11. https://doi.org/10.1002/adhm.201601451.

[33] I.P. Magalhães, P.M. de Oliveira, J. Dernowsek, E.B. Las Casas, M.S. Las Casas, Investigation of the effect of nozzle design on rheological bioprinting properties using computational fluid dynamics, Rev. Mater. 24 (2019). https://doi.org/10.1590/s1517-707620190003.0714.

[34] W. Martanto, S.M. Baisch, E.A. Costner, M.R. Prausnitz, M.K. Smith, Fluid dynamics in conically tapered microneedles, AIChE J. 51 (2005) 1599–1607. https://doi.org/10.1002/aic.10424.

[35] J.A. Reid, P.A. Mollica, G.D. Johnson, R.C. Ogle, R.D. Bruno, P.C. Sachs, Accessible bioprinting: adaptation of a low-cost 3D-printer for precise cell placement and stem cell differentiation., Biofabrication. 8 (2016) 025017. https://doi.org/10.1088/1758-5090/8/2/025017.

[36] J. Leppiniemi, P. Lahtinen, A. Paajanen, R. Mahlberg, S. Metsä-Kortelainen, T. Pinomaa, H. Pajari, I. Vikholm-Lundin, P. Pursula, V.P. Hytönen, 3D-Printable Bioactivated Nanocellulose-Alginate Hydrogels, ACS Appl. Mater. Interfaces. 9 (2017) 21959–21970. https://doi.org/10.1021/acsami.7b02756.

[37] K. Nair, K.C. Yan, W. Sun, A computational modeling approach for the characterization of mechanical properties of 3D alginate tissue scaffolds, J. Appl. Biomater. Biomech. 6 (2008) 35–46. https://doi.org/10.1177/228080000800600106.

[38] C. Smith, G. Oldt, Multiaxial Bio-Printer Head, 2018. https://5f6357c8-abe2-426e-bc22-b9f609a0b347.filesusr.com/ugd/e69967_73cde5aebac44f11b0432814832a2110.pdf (accessed July 17, 2020).

[39] B. Stewart, 3D Bioprinting Hydrogel for Tissue Engineering an Ascending Aortic Scaffold, University of Denve, Denver, CO, USA, 2017.

[40] F. Liravi, R. Darleux, E. Toyserkani, Additive manufacturing of 3D structures with non-Newtonian highly viscous fluids: Finite element modeling and experimental validation, Addit. Manuf. 13 (2017) 113–123. https://doi.org/10.1016/j.addma.2016.10.008.

[41] T. Billiet, E. Gevaert, T. De Schryver, M. Cornelissen, P. Dubruel, The 3D printing of gelatin methacrylamide cell-laden tissue-engineered constructs with high cell viability, Biomaterials. 35 (2014) 49–62. https://doi.org/10.1016/j.biomaterials.2013.09.078.

[42] R. Samanipour, Z. Wang, A. Ahmadi, K. Kim, Experimental and computational study of microfluidic flow-focusing generation of gelatin methacrylate hydrogel droplets, J. Appl. Polym. Sci. 133 (2016) 24–26. https://doi.org/10.1002/app.43701.

[43] J.C. Gómez-Blanco, E. Mancha-Sánchez, A.C. Marcos, M. Matamoros, A. Díaz-Parralejo, J.B. Pagador, Bioink temperature influence on shear stress, pressure and velocity using computational simulation, Processes. 8 (2020). https://doi.org/10.3390/PR8070865.

[44] A. Verma, P. Vishnoi, V. Sukhotskiy, E.P. Furlani, Numerical simulation of extrusion additive manufacturing: Fused deposition modeling, in: TechConnect Briefs 2018 - Adv. Mater., 2018: pp. 118–121.

[45] M.P. Serdeczny, R. Comminal, D.B. Pedersen, J. Spangenberg, Experimental validation of a numerical model for the strand shape in material extrusion additive manufacturing, Addit. Manuf. 24 (2018) 145–153. https://doi.org/10.1016/j.addma.2018.09.022.

[46] E3D-ONLINE, E3D V6 Series Blueprint, (2016). https://e3d-online.dozuki.com/Document/oALPlTAN3DpmeLYq/V6-NOZZLE-ALL.pdf (accessed March 20, 2021).

[47] J.B., Cellink Bioink Biopritning Protocol, (2019). https://www.cellink.com/wp-content/uploads/2019/03/Bioprinting-Protocol-CELLINK-Bioink_21-Mars-2019.pdf.

[48] M. Müller, E. Öztürk, Ø. Arlov, P. Gatenholm, M. Zenobi-Wong, Alginate Sulfate–Nanocellulose Bioinks for Cartilage Bioprinting Applications, Ann. Biomed. Eng. 45 (2017) 210–223. https://doi.org/10.1007/s10439-016-1704-5.

7.5 Temperature and humidity PID controller for a bioprinter atmospheric enclosure system

Dr. José Blas Pagador Carrasco, como director de la tesis titulada “Desarrollo de un sistema de bioimpresión para posicionar líneas celulares”, certifico el factor de impacto y la categorizacion de la siguiente publicación, incluida en la tesis doctoral. Del mismo modo, se especifica la aportación del doctorando.

Autores: Manuel Matamoros, **J. Carlos Gómez-Blanco**, Álvaro J. Sánchez, Enrique Mancha, Alfonso C. Marcos, J. Pablo Carrasco-Amador and J. Blas Pagador

Título: Temperature and Humidity PID Controller for a Bioprinter Atmospheric Enclosure System

Revista: Micromachines

Otros datos: vol 11, nº: 11, pág. 999, año 2020

DOI: 10.3390/mi11110999

Factor de impacto: 2.524 (Q2 – Instruments & Instrumentation; Q3 – Nanoscience & Nanotechnology)

Abstract: Bioprinting is a complex process, highly dependent on bioink properties (materials and cells) and environmental conditions (mainly temperature, humidity and CO2 concentration) during the bioprinting process. To guarantee proper cellular viability and an accurate geometry, it is mandatory to control all these factors. Despite internal factors, such as printing pressures, temperatures or speeds, being well-controlled in actual bioprinters, there is a lack in the controlling of external parameters, such as room temperature or humidity. In this sense, the objective of this work is to control the temperature and humidity of a new, atmospheric enclosure system for bioprinting. The control has been carried out with a decoupled proportional integral derivative (PID) controller that was designed, simulated and experimentally tested in order to ensure the proper operation of all its components. Finally, the PID controller can stabilize the atmospheric enclosure system temperature in 311 s and the humidity in 65 s, with an average error of 1.89% and 1.30%, respectively. In this sense, the proposed atmospheric enclosure system can reach and maintain the proper temperature and humidity values during post-printing and provide a pre-incubation environment that promotes stability, integrity and cell viability of the 3D bioprinted structures.

Contribución del doctorando: Conceptualization, methodology, validation, formal analysis, investigation, writing—original draft preparation, writing—review and editing, visualization, project administration

Contribuciones de los coautores: Conceptualization, M.M., J.C.G.-B., Á.J.S., E.M. and J.B.P.; methodology, M.M., J.C.G.-B. and J.B.P.; software, Á.J.S.; validation, M.M., J.C.G.-B., Á.J.S., E.M., A.C.M., J.P.C.-A. and J.B.P.; formal analysis, M.M. and J.C.G.-B.; investigation, M.M., J.C.G.-B., Á.J.S., E.M., A.C.M., J.P.C.-A. and J.B.P.; writing—original draft preparation, M.M., J.C.G.-B. and J.B.P.; writing—review and editing, Á.J.S., E.M., A.C.M., J.P.C.-A. and J.B.P.; visualization, M.M., J.C.G.-B. and J.B.P.; supervision, J.B.P.; project administration, J.C.G.-B. and J.B.P.; funding acquisition, J.B.P. All authors have read and agreed to the published version of the manuscript.

micromachines

MDPI

Article

Temperature and Humidity PID Controller for a Bioprinter Atmospheric Enclosure System

Manuel Matamoros [1,*], J. Carlos Gómez-Blanco [2,*], Álvaro J. Sánchez [1], Enrique Mancha [2], Alfonso C. Marcos [1], J. Pablo Carrasco-Amador [1] and J. Blas Pagador [2]

1 Department of Graphic Expression, School of Industrial Engineering, University of Extremadura, 06006 Badajoz, Spain; ajs@unex.es (Á.J.S.); acmarcos@unex.es (A.C.M.); jpcarrasco@unex.es (J.P.C.-A.)
2 Jesús Usón Minimally Invasive Surgery Centre, 10002 Cáceres, Spain; emancha@ccmijesususon.com (E.M.); jbpagador@ccmijesususon.com (J.B.P.)
* Correspondence: manuelmp@unex.es (M.M.); jcgomez@ccmijesususon.com (J.C.G.-B.)

Received: 13 October 2020; Accepted: 9 November 2020; Published: 12 November 2020

Abstract: Bioprinting is a complex process, highly dependent on bioink properties (materials and cells) and environmental conditions (mainly temperature, humidity and CO_2 concentration) during the bioprinting process. To guarantee proper cellular viability and an accurate geometry, it is mandatory to control all these factors. Despite internal factors, such as printing pressures, temperatures or speeds, being well-controlled in actual bioprinters, there is a lack in the controlling of external parameters, such as room temperature or humidity. In this sense, the objective of this work is to control the temperature and humidity of a new, atmospheric enclosure system for bioprinting. The control has been carried out with a decoupled proportional integral derivative (PID) controller that was designed, simulated and experimentally tested in order to ensure the proper operation of all its components. Finally, the PID controller can stabilize the atmospheric enclosure system temperature in 311 s and the humidity in 65 s, with an average error of 1.89% and 1.30%, respectively. In this sense, the proposed atmospheric enclosure system can reach and maintain the proper temperature and humidity values during post-printing and provide a pre-incubation environment that promotes stability, integrity and cell viability of the 3D bioprinted structures.

Keywords: bioprinting; Proportional Integral Derivative control (PID); atmospheric enclosure; temperature; humidity

1. Introduction

Bioprinting is a booming technology that could revolutionize regenerative medicine [1]. It has a specific application in medicine of traditional additive manufacturing technology that superposes layers of material to build a biological structure. Although there are several bioprinting techniques, all of them present some common challenges to be solved, such as cell death during and after bioprinting, a long bioprinting time or insufficient micro-vascularization, among others [2]. Bioinks are commonly cell-laden hydrogels due to their good biocompatibility, so they present highly hydrated 3D networks, such as extracellular matrix, that promote oxygen and nutrient interchange [3].

It is important to know that hydrogels are very sensitive to external changes (e.g., temperature or humidity) because of their high-water content (80–90% *w*/*v*). For this reason, several processes can be associated to uncontrolled bioprinting conditions. Some of them are related to the stability and integrity of 3D bioprinting structures [4] and other ones are focused on the survival of cells during and after the bioprinting process [5]. In the first block, drying hydrogels will increase the concentration of macromolecules and will promote their crowding [3]. Furthermore, the rheological properties of hydrogels are affected by temperature, among other parameters [6]. These two problems are usually

controlled during the printing process inside of the bioink cartridge, but unfortunately, the post-printing stage can suffer similar atmospheric-related problems that are currently uncontrolled inside of the current bioprinter enclosure. Hence, the proposed atmospheric enclosure system for bioprinters expects to fill this gap, increasing post-printing stability and, consequently, allowing a higher resolution of the 3D bioprinted structures [7]. In the second block, cell viability can be affected during both the printing and post-printing processes. In the same way, good cell conditions during the bioprinting process are controlled by bioink cartridges, which are out of the scope of this work [8]. However, the control of the atmospheric enclosure inside of bioprinters to assure proper conditions in the post-printing stage, promoting high cell viability, is the other main interest of this work [9].

As far as the authors know, no previous studies have focused on designing, developing and testing an atmospheric enclosure system for bioprinting that could control these critical parameters to assure the integrity and stability of the 3D structure together with the viability of its cells during the post-printing stage. Instead of generating an atmospheric enclosure system, other authors propose to control these atmospheric parameters by reducing bioprinting time, bioprinting into a water-based bath or reducing air flow [3]. Commercial bioprinters, such as Cellink BioX® (Cellink; Boston, MA, USA), Poietis® (Poietis; 33600 Pessac, France) or 3D-Discovery BioFactory® (REGENHU; 1690 Villaz-Saint-Pierre, Switzerland), control the air flow to minimize biological contamination using High Efficiency Particle Arresting (HEPA) filters [10–12]. However, none of them currently solve these issues and the 3D bioprinting process is still relatively slow [7], so large 3D structures can greatly benefit from our proposed post-printing control of atmospheric conditions, which could turn bioprinters into a temporal bioincubator while the bioprinting process is ongoing [7,13].

Proportional integral derivative (PID) controllers are commonly used in atmospheric enclosures of other fields, e.g., neonatal [14–16] or egg/bird [17,18] incubators. Each different application requires complex or simple adaptations of their mathematical models, according to the factors involved in each of these environments. On the one hand, large enclosures, such as greenhouses [19,20], animal buildings [21] or large spaces [22], must consider many factors: air convection, wall heat loses, inner heat, humidity generation or solar radiation. On the other hand, small enclosures, such as neonatal [14,16,23] or egg/bird [15,24] incubators, can considerer negligible some of these previous factors, but they present a high cross-coupling effect among their variables [25]. For this reason, some studies have focused their interest only on temperature [15,16,23] or just merge two variables, such as temperature and humidity [14,24,26]. Temperature and humidity are highly related variables, so their simultaneous control is complex and requires a fine tuning of the PID parameters [27]. Additionally, both temperature and humidity are significantly influenced by CO_2, which increases the complexity of PID controllers due to the cross-coupling effects among these three variables [28,29]. It has been observed that the structural stability of Type I collagen cannot be ensured after the bioprinting process without a controlled 37 °C environment [7]. With this in mind, the CO_2 variable was left out of the scope of this work for two main reasons. Firstly, it is not expected that cells produce significant CO_2 emissions during post-printing, so its concentration should remain stable in the global system. Additionally, the cross-coupling interaction of CO_2 with temperature and humidity will make difficult the optimization of the PID parameters and, consequently, will decrease the robustness and stability of the final PID controller. Hence, we focus our interest on developing a stable and robust PID controller of the two main variables involved in the post-printing stage of bioprinting—temperature and humidity.

Therefore, the main objective of this work is the design, development and validation of a temperature and humidity PID controller for an atmospheric enclosure system with bioprinting purpose. This atmospheric enclosure system could control the post-printing stage independently of the bioprinting technique used. For this purpose, theoretical, simulated and experimental studies have been performed to assure a proper functioning of the proposed system.

2. Materials and Methods

2.1. Atmospheric Enclosure System Design

The designed atmospheric enclosure system is a sub-divided parallelepipedal with different areas: a bioprinting sub-chamber, a climatic conditions generation sub-chamber and an electronic/mechanic components sub-chamber. All designing was done using Autodesk Inventor®, and different area dimensions are shown in Table 1.

Table 1. Atmospheric enclosure dimensions.

Areas of the Atmospheric Enclosure	Size (mm)
Atmospheric enclosure full size	600 × 410 × 420
Bioprinting sub-chamber (z1)	380 × 242 × 340
Climatic conditions generation sub-chamber (z2)	380 × 242 × 75
Electronic and mechanical components sub-chamber (z3)	390 × 250 × 410

Figure 1 shows the atmospheric enclosure system prototype with its atmospheric enclosure made of methacrylate. Different methacrylate widths were used in each one of the areas to control heat insulation and minimize conduction heat losses. Figure 2 shows the different sub-chambers that make up the atmospheric enclosure system.

(**a**) (**b**)

Figure 1. Atmospheric enclosure top (**a**) and lateral (**b**) view.

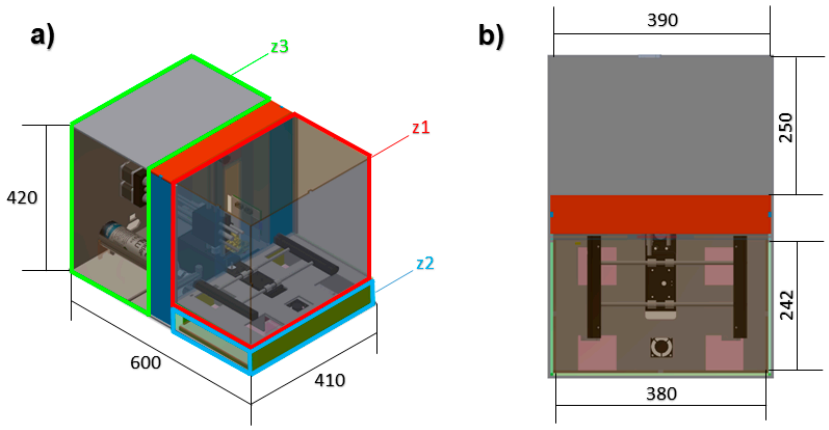

Figure 2. Atmospheric enclosure system tridimensional design: (**a**) perspective and (**b**) top view, where the bioprinting sub-chamber (z1), the climatic conditions generation sub-chamber (z2) and the electronic and mechanical components sub-chamber (z3) are located.

Bioprinter control is divided into three different processes: bioprinter mechanical control, atmospheric enclosure control and data visualization. All three processes were individually controlled by Arduino® (Arduino s.r.l.; 20900 Monza, Italy) UNO boards, all connected to a Raspberry® (Rapsberry Pi Foundation; Cambridge CB2 1NF, UK) Pi 3, and the whole system was controlled by a personalized Python® version 3.9 (Python Software Foundation; Wilmington, DE, USA) script. This script provides the user full live control over the bioprinter atmospheric enclosure parameters while temperature, humidity and CO_2 data are shown.

The control of proper atmospheric conditions inside the enclosure needs generation and sensorization of each one of the inner parameters. In this sense, temperature is generated with two 200-W electrical finned resistances, humidity is produced with cold vaporization of water in a tank using a piezoelectrical transducer and, finally, CO_2 is injected from an external AquaMedic® (AB Aqua Medic GmbH; Bissendorf, Germany) CO_2 pressurized bottle when a Blau® (Barcelona Marine Farm S.L.; Barcelona, Spain) (3VA, 14mA, IP 85) electro valve is opened. Likewise, the type and location of every one of the sensors used is shown in Table 2. Generation electronics is switched ON/OFF by a TONGLING (Xiamen Hongfa Electroacoustic Co; 361021 Xiamen, China) JQC-3FF-S-Z relay moduli.

Table 2. Atmospheric enclosure sensors.

Sensors	Designation	Position
2× Temperature sensor	PT 100 PRO	Top left and bottom right
2× Humidity sensor	DHT22	Top left and bottom right
2× CO_2 sensor	MG811	Top left and bottom right

The main area of the atmospheric enclosure system is the climatic conditions generation sub-chamber. All generation apparatuses were placed in this area to produce the appropriate atmospheric conditions. This sub-chamber is a separated area of the enclosure connected by 4 air inlets/outlets, 2 inlets with axial fans and 2 outlets, as shown in Figure 3. The working principle of this area is to force the air to enter into the generation sub-chamber where its temperature, humidity and CO_2 are modified and then exit to the enclosure atmosphere again. This process is continuously repeated, creating an air conditioning flow until the atmospheric parameters' target values are reached.

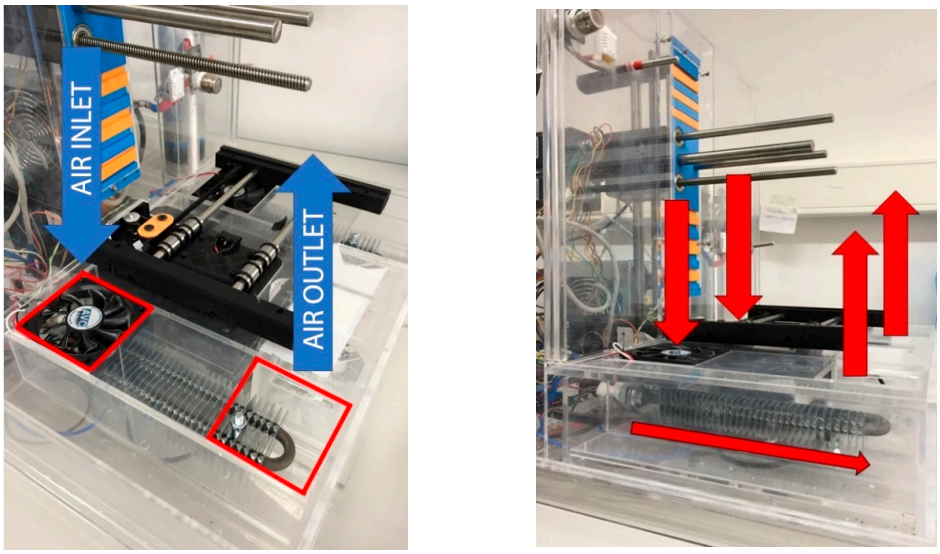

Figure 3. Air inlets/outlets schema.

To ensure a sterile environment at the beginning of the bioprinting process, the bioprinter sub-chamber is sterilized by action of four UV LED panels (420 nm and 440 mW) incorporated in the bioprinter sub-chamber. After this process, air is introduced into the system from outside, passed through a HEPA filter and generates positive pressure to prevent the entry of contaminating external agents.

Although the proposed atmospheric enclosure system has a CO_2 pressurized bottle and two CO_2 sensors for future purposes, they have not been used in this study.

2.2. Mathematical Modelling

The purpose of this work is to control the inner temperature and humidity of an atmospheric enclosure system. In this sense, the inner heat balance and water mass balance equations are the general non-lineal differential equations used in temperature and humidity control processes [21,22]. In this work, terms with a negligible interaction in the total balance were not considered. Therefore, our heat and water mass balance equations [20] were given by:

$$C_v V \frac{dT_h}{dt} = Q_{in} - Q_{out} = \left(G_a \rho C_p T_c + Q_n\right) - \left(G_a \rho C_p T_h + \frac{T_h - T_o}{R}\right) \quad (1)$$

$$\rho V \frac{d(d_n)}{dt} = G_a \rho d_c + D_n - G_a \rho d_n \quad (2)$$

where C_v is the volumetric air heat capacity (J/kg·°C); V is the inner air volume (m^3); T_h is the inner temperature (°C); G_a is the air mass flow that a fan extracts from the chamber to the generation sub-chamber (m^3/s); ρ is the air density (1.25 Kg/m^3); C_p is the air-specific heat (1006 J/kg·°C); T_c is the generation sub-chamber air temperature (°C); Q_n is the heat dissipation capacity (J/s); T_0 is the external temperature (°C); R is the enclosure thermal resistance (°C·s/J); d_n is the inner humidity (g/kg); d_c is the external humidity(g/kg); D_n is the enclosure humidity gain (g/s).

Transfer functions for the PID controller were obtained applying the Laplace transform to Equations (1) and (2). Defining X as $\frac{1}{G_a \rho C_p + \frac{1}{R}}$ these functions are:

$$G_1(s) = \frac{T_h(s)}{T_c(s)} = \frac{K}{1 + Ts} = \frac{G_a \rho C_p X}{1 + (C_v V X)s} \quad (3)$$

$$G_2(s) = \frac{d_n(s)}{d_c(s)} = \frac{1}{1 + T_1 s} = \frac{1}{1 + \frac{V}{G_a}s} \quad (4)$$

where $G_1(s)$ and $G_2(s)$ are temperature and humidity terms, respectively.

2.3. Experimental Evaluation

A comparative between theoretical and experimental behaviors (theoretical and experimental transfer functions) of the atmospheric enclosure was proposed. For this purpose, the different experimental behaviors of each parameter (inner temperature and humidity) were tested and determined. To obtain data for the experimental transfer function, single input, single output (SISO) and multiple inputs, multiple outputs (MIMO) tests were performed as follows:

1. SISO test to study inner temperature when heater (electric resistance) was switched on.
2. SISO test to study inner humidity when humidifier (cold mist humidifier) was switched on.
3. MIMO test to study coupling of inner temperature and humidity [24,29].

Initial inputs and target values for all tests are shown in Table 3. Atmospheric values have been chosen based on criteria consulted in the literature [30].

Table 3. Initial inputs and target values used in tests.

Variable	Input Value	Target Value
Temperature	25 °C	37 °C
Humidity	50%	90%

Experimental transfer functions were obtained from test data using the Matlab® R2018b System Identification Toolbox™. This tool is commonly used to obtain mathematical models of dynamic systems from experimental input and output data. As such, Matlab® R2018b Simulink™ was used to simulate and compare both theoretical and experimental transfer functions.

2.4. PID Controller

Variations in temperature and humidity can change bioprinting materials' properties and affect the cellular viability, stability and integrity of 3D bioprinted structures. To minimize variations, a PID controller was added to the atmospheric enclosure system. PID controller algorithms are widely used in feedback control systems and are mathematically expressed as [31]:

$$u(t) = \mathrm{K}\left(\mathrm{e(t)} + \frac{1}{\mathrm{T_i}}\int_0^t e(\tau)d\tau + T_d\frac{de(t)}{dt}\right) \quad (5)$$

A good PID control system can provide the atmospheric enclosure with the necessary stability in the shortest time. In this sense, the Ziegler–Nichols closed-loop method was used in Matlab® R2018b (MathWorks; Natick, Massachusetts, United States) to tune all PID parameters using process input/output signals. All these calculations were done through a simulation block diagram implemented in Matlab® R2018b Simulink™, which follows the standard structure shown in Figure 4.

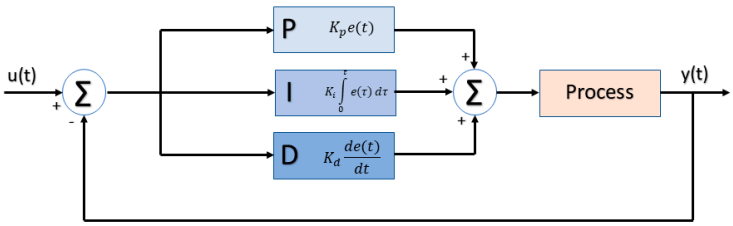

Figure 4. Atmospheric enclosure block diagram with a proportional integral derivative (PID) controller.

2.5. Procedure

The workflow was performed as Yinping et al. [28] in their work. First, mathematical model behavior equations were solved, obtaining all constants needed to calculate the theoretical system transfer functions. Second, temperature and humidity transfer functions were calculated and evaluated with experimental transfer functions obtained from MIMO and SISO tests. Several behavior approaches of the system were obtained using the least-square method in the Matlab® R2018b System Identification Toolbox™. All possible types in this toolbox were used: one pole (P1), two poles (P2), three poles (P3), one pole and one zero (P1Z), two poles and one zero (P2Z), three poles and one zero (P3Z), two poles sub-damped (P2U), three poles sub-damped (P3U), two poles and one zero sub-damped (P2ZU), three poles and one under-damped zero (P3ZU), one pole and one integrator (P1I), two poles and one integrator (P2I), three poles and one integrator (P3I), one pole and one delay (P1D) and two poles and one delay (P2D) transfer functions.

Next, both transfer functions' (theoretical and experimental) block diagrams were designed and evaluated. Finally, theoretical and experimental transfer functions were analyzed, obtaining the first Kp (proportional controller), Ki (integral controller) and Kd (derivative controller) values using

the Ziegler–Nichols method. Then, this first PID tuning was tested and manually re-tuned to limit overshoots produced by the Ziegler–Nichols method.

To validate the atmospheric enclosure system, several tests were performed using the former calculated Kp, Ki and Kd values. Finally, to check the quality of calculated PID, an experimental error (6) was calculated.

$$\varepsilon_r = \frac{|V_{real} - V_{model}|}{V_{real}} \cdot 100 \tag{6}$$

3. Results

The following temperature (7) and humidity (8) theoretical transfer functions were obtained once inherent constants of the system were replaced in Equations (3) and (4).

$$G_1(s) = \frac{T_h(s)}{T_c(s)} = \frac{0.839}{1 + 0.263\ s} \tag{7}$$

$$G_2(s) = \frac{d_n(s)}{d_c(s)} = \frac{1}{1 + 0.557\ s} \tag{8}$$

3.1. SISO Test to Study Inner Temperature When Heater (Electric Resistance) Was Switched on

The experimental transfer function for temperature was obtained from a SISO test with laboratory environmental conditions set to 22 °C and 50% relative humidity. In the tests, actuators (electric heat resistance) were powered on or off when the inner temperature registered by sensors was below or above the target temperature (37 ± 1 °C). Data acquisition from sensors takes 700 s (test time) to assure a complete study with enough data.

The experimental transfer function, Equation (9), is calculated from the selected fitting plot for electric heater switching, the one pole and one delay (P1D) plot (Figure 5a). The accuracy rate calculated with Matlab® R2018b for this transfer function was 99.49%.

$$G_{t,exp}(s) = \frac{Kp}{1 + \mathrm{Tp1 \cdot s}} = \frac{2.55 \cdot e^{-42\ s}}{1 + 576.74\ s} \tag{9}$$

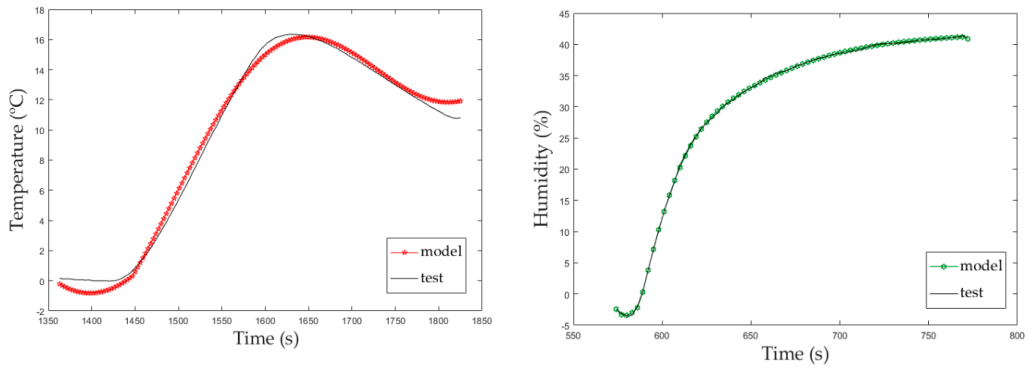

(**a**) (**b**)

Figure 5. (**a**) Single input, single output (SISO) temperature study; (**b**) SISO humidity study.

3.2. SISO Test to Study Inner Humidity When Humidifier (Cold Mist Humidifier) Was Switched on

Using previously described methodology for SISO tests, the plot that best fit the humidity behavior (Figure 5b) was one pole and one delay (P1D). Equation (10) is the experimental transfer function for

humidity calculated from P1D plot. The accuracy rate calculated with Matlab® R2018b for this transfer function was 99.03%.

$$G_{h,exp}(s) = \frac{Kp \cdot e^{-Td \cdot s}}{1 + \mathrm{Tp1} \cdot \mathrm{s}} = \frac{1.05 \cdot e^{-10.26\ s}}{1 + 48.83\ s} \quad (10)$$

A slightly variation between the experimental and theoretical transfer functions (Equations (7) and (9) vs. Equations (8) and (10)) can be observed; an exponential function is multiplied to the proportional constant. Albright et al. [25] explain in their work that temperature and humidity sensors usually need this exponential function to control what they called dead time (Td), meaning a significative delay in the sensor measurement.

Figure 5 shows a comparison between the experimental data (test) and the Matlab® R2018b model from these data that extract the transfer function with a specific accuracy (model). These graphs represent the first approach of the solution that will be used as input of Section 3.3 and, after that, as initial values of the MIMO test to build a decoupled feedback of the atmospheric enclosure system.

3.3. Comparative between Theoretical and Experimental Transfer Functions

An open-loop block diagram (Figure 6) to compare theoretical and experimental SISO transfer functions before adding the PID controller was designed in Matlab® R2018b Simulink™. Additionally, two delay blocks have been added to this diagram to simulate the delay of sensors while reading in experimental functions. Table 3 shows all values used in inlet steps. As can be seen in Figure 7, without the addition of a controller, both temperature and humidity surpass the target values and stabilize at a higher value, taking 2500 and 250 s, respectively.

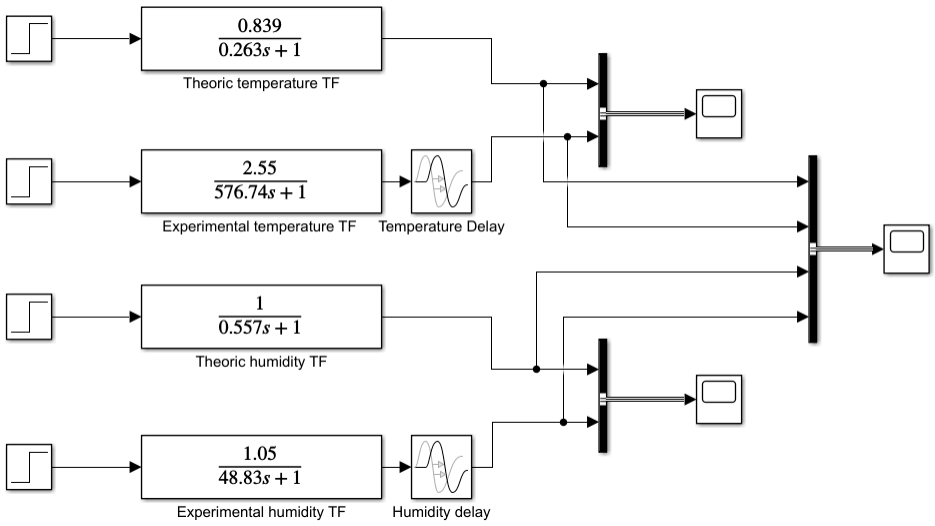

Figure 6. Comparative transfer functions implemented using a Simulink block diagram.

3.4. MIMO Test to Study Coupling of Inner Temperature and Humidity

The dependency between temperature and humidity means that control could be a hard task when they are actuating at the same time. Wang et al. [24] exposed a higher influence of temperature on relative humidity and vice versa. They also observed a decrease by about 2–3% of relative humidity when temperature increases by 1 °C. Figure 8 shows this influence of temperature on humidity in our atmospheric enclosure system before the PID controller was set. It can be seen, without the PID controller, that both temperature and humidity fluctuate in a wide range.

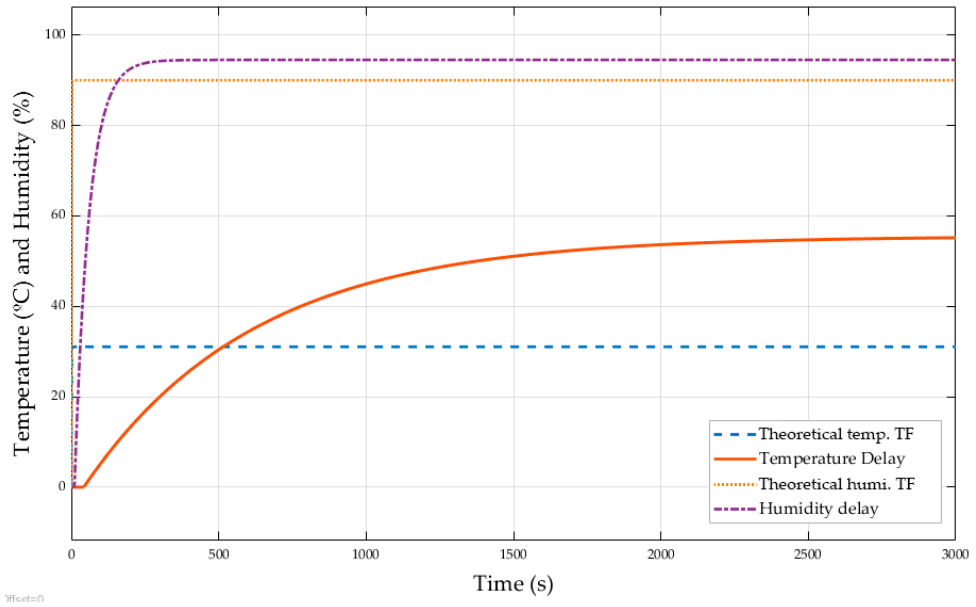

Figure 7. Theoretical and experimental transfer functions simulation without a PID controller.

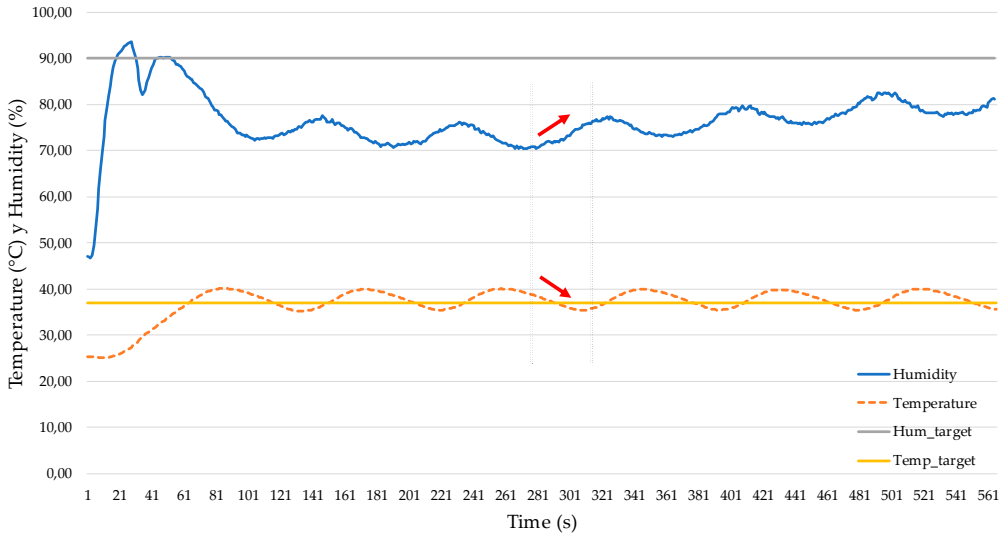

Figure 8. Humidity behavior against temperature without a PID controller.

Analyzing Figure 8 plots, the system responses to some characteristic parameters of the atmospheric enclosure system are exposed in Table 4.

Table 4. Atmospheric enclosure system responses to some characteristic parameters.

Value (s)	Temperature	Humidity
Delay time	16.00 s	6.00 s
Rise time	40.00 s	11.00 s
Peak time	85.00 s	26.00 s
Percent overshoot	8.35%	3.88%
Settling time	155.00 s	106.00 s

Using the before-mentioned methodology, a MIMO test was performed on the atmospheric enclosure system to obtain the inherent values of the system. Laboratory environmental conditions were set to 22 °C and 50% relative humidity and the target values were the same as those used in the previous MIMO tests. Analyzing all obtained plots, P1D with delay models were the ones that best fit the temperature and humidity behaviors (Figure 9). The associated transfer functions are described in Equations (11) and (12), with a 95.01% and 99.42% accuracy rate, respectively.

$$G_{t+h,exp}(s) = \frac{Kp}{1 + \mathrm{Tp1{\cdot}s}} = \frac{2.55{\cdot}e^{-57.89\ s}}{1 + 576.74\ s} \tag{11}$$

$$G_{h+t,exp}(s) = \frac{Kp{\cdot}e^{-Td{\cdot}s}}{1 + \mathrm{Tp1{\cdot}s}} = \frac{1.05{\cdot}e^{-13.62\ s}}{1 + 48.83\ s} \tag{12}$$

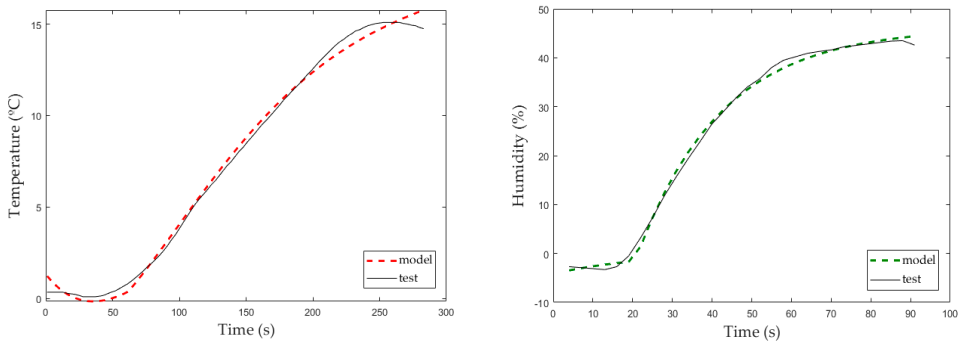

(**a**) (**b**)

Figure 9. (**a**) SISO temperature study, (**b**) SISO humidity study.

Figure 9 shows a comparison between the experimental data (test) and the Matlab® R2018b model from these data that extract the transfer function with a specific accuracy (model). These graphs represent a former approach to the final solutions that will integrate other elements, such as the response time of the sensor, which will be exposed in Section 3.4.

3.5. Obtaining PID Values and Modeling System in Matlab/Simulink™

Previous results of our theoretical transfer functions cannot be considered good enough to describe our system. Interrelations between variables, non-linearity, high hysteresis or real-time variations are some reasons why temperature and humidity are complex systems to control. In this sense, performing temperature and humidity tests without any kind of control system variables will provoke high fluctuation and poor stabilization of the system. Therefore, to design a good PID controller, natural fluctuations of variables were considered in the new system modelling.

Using the Matlab® R2018b Pidtool toolbox, PID controller values of transfer functions (11) and (12) were obtained. This tool provides two different PID behavior adjustments: response velocity and long-time stabilization. PID values (Table 5) were obtained by setting a fast and robust response to the controlled system.

Table 5. PID values obtained.

Value	Temperature (°C)	Humidity (%)
Proportional (Kp)	150.00	25.00
Integral (Ki)	1.00	2.00
Derivative (Kd)	6000.00	100.00

The block diagram shown in Figure 10 uses the fitted PID values in Table 5 and compares the modelled and the real system behaviors in Matlab®/Simulink™.

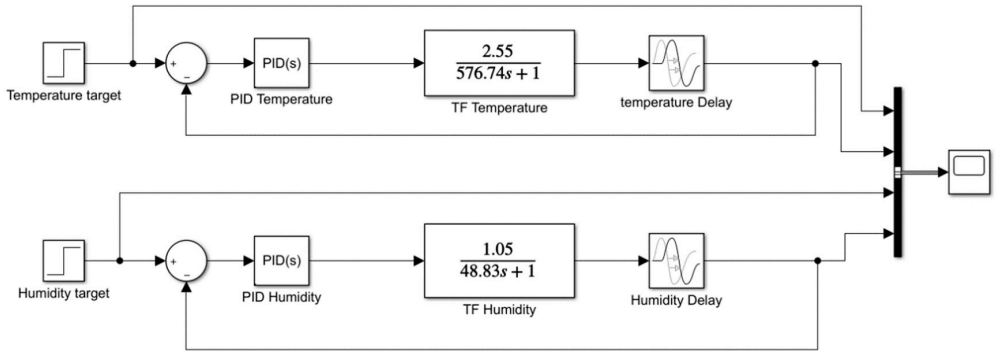

Figure 10. System block diagram with temperature and humidity.

Results from the experimental test using a decoupled PID controller of temperature and humidity can be seen in Figure 11.

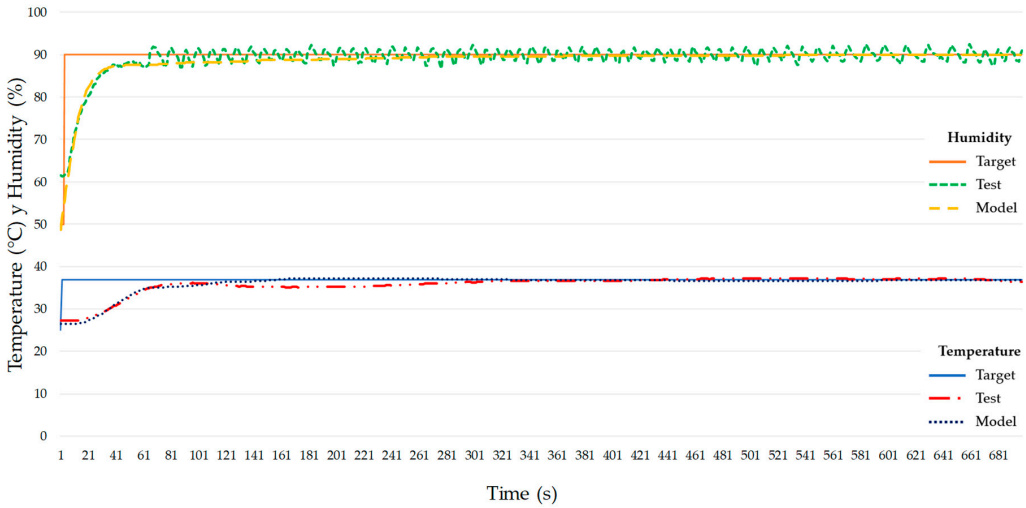

Figure 11. Theoretical and experimental simulated system using a decoupled approach for the PID controller.

The temperature behaviors for the theoretical and the real system are very close. Figure 12 shows a maximum error for temperature of 6.01% at 185 s and the system has an average error of 1.89% once stabilized. Regarding humidity, there is a maximum error of 4.59% at 68 s, then the humidity value oscillates around the target value with an average error of 1.30% (Figure 13). The stabilization times for the theoretical models were 161 s for temperature and 281 s for humidity. Despite temperature stabilizing faster than humidity for the theoretical models, the stabilization times achieved with the proposed PID values (test values) were 311 s for temperature and 65 s for humidity. Maybe this is due to a higher error (6.01%) of the temperature model as opposed to a 1.89% error of the humidity model. Matlab® R2018b calculates the theoretical transfer function for the temperature with a 95.01% accuracy that can justify these differences between the theoretical and experimental values.

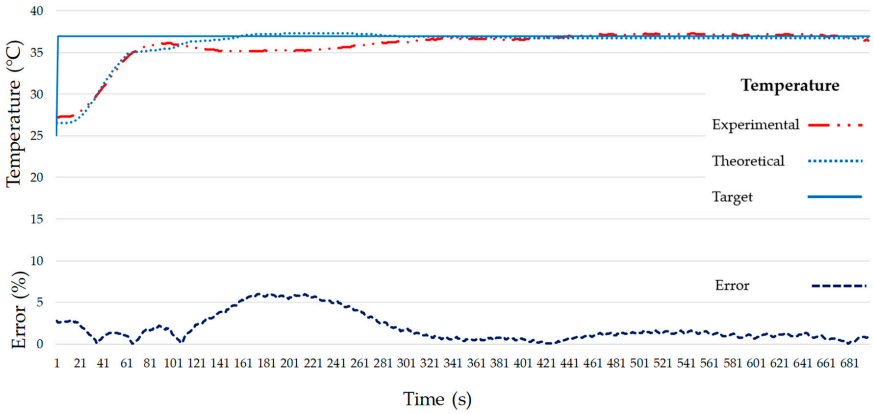

Figure 12. Target, model and experimental temperature (**top**) and experimental temperature error (**bottom**) of the final atmospheric enclosure system.

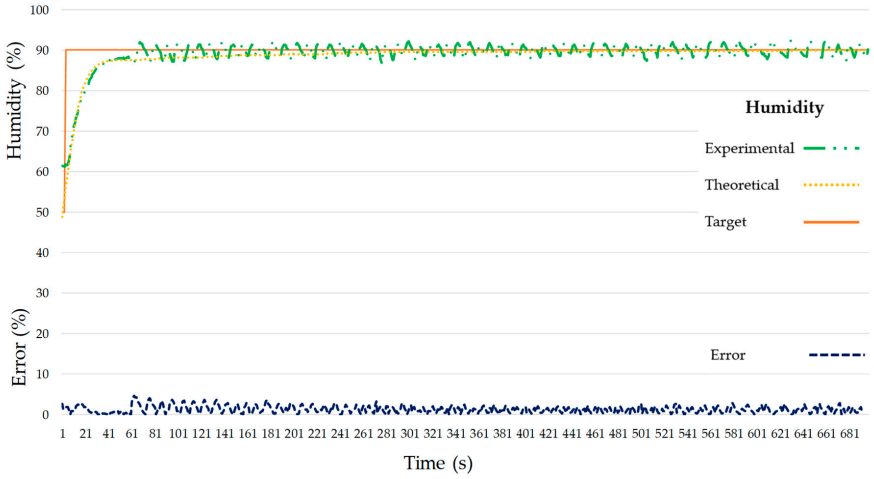

Figure 13. Target, model and experimental humidity with experimental humidity error.

4. Discussion

The objective of this work is to determine the optimum PID controller values of an atmospheric enclosure system for bioprinting. Specifically, we propose to control temperature and humidity to improve the integrity, stability and cell viability of 3D bioprinted structures. In order to design and develop our atmospheric enclosure, three components of the system were analyzed and compared with previous studies: the mathematical model, the transfer functions and the block diagram, but it was also analyzed whether to use coupled or uncoupled variables.

The similarity between the proposed atmospheric enclosure system and greenhouses or animal buildings suggests that the mathematical model used by Daskalov et al. [20] and Albright et al. [25] (heat and humidity balances) can be used in our system after some important adaptations. In this sense, the presence of animals in the study of Daskalov et al. [20] requires some factors in the mathematical model, such as sensitivity to heat or water steam produced by animals and the heat lost due to mechanical ventilation. All of these factors must be eliminated for our bioprinting environment. In addition, Albright et al. included terms of solar radiation heat, ventilation volumetric flow and plant evapotranspiration, which have no purpose in our mathematical model. Lastly, our transfer function calculations from differential equations were based on Yinping et al.'s [28] work, using a similar structure for transfer functions relating to the behavior of temperature and humidity.

According to the bibliography, there is no agreement about the best way to control temperature and humidity. So, some authors propose coupled controllers [28,32,33] while others propose decoupled controllers [24,25,34]. In this sense, knowing that an increase of 1 °C can decrease humidity by about 2–4 % [24], we performed SISO and MIMO tests to study each parameter independently and simultaneously, respectively. Considering our design and the MIMO test results (Figure 8), we finally decided to design a decoupled temperature and humidity controller that produces better results with simple PID calculations as well as increasing stability and robustness of the goal system [24].

Once the type of controller was chosen, the next step was the composition of block diagram, whose main element will be the system's plant transfer function for temperature and humidity. Previous studies proposed different types of transfer function to control temperature and humidity: some of them without delay [14,32] and others considering delay [24,34,35], which is a parameter totally dependent on the technical specifications (response time) of the electronic components [21]. Those authors that proposed no delay transfer functions try to simplify the system interactions, but their models are supposed to be less real [17,25,34]. On the other hand, the delay is commonly considered when complex transfer functions with high oscillatory responses and difficulties in stabilizing disturbances are present [25]. Hence, our system provides a better response using delay, specifically P1D type, similar to other previous studies [24,34,35].

Regarding the block diagram, three different blocks have been used: control, plant and delay. Although this diagram is quite common [25], in the same way as transfer function, delay inclusion or exclusion will modify the performance of the PID controller. So, some studies excluded the delay for temperature [17,22,28] while others considered it in their schemes for temperature and humidity [32,36]. In our case, an adapted version of Yiping et al. [28] that considers delays has been used, but other complex approaches with predictive algorithms should be considered for future improvements [36].

Finally, the global performance of our atmospheric enclosure system is pretty good. In this sense, low stabilization time and errors were obtained in the experimental tests. Other authors presented a temperature stabilization time of 2760 s for a 4 °C increment [14], 600 s for a 10 °C increment [34] or 246 s for a 5 °C increment [33]. Nevertheless, our enclosure system can stabilize a 12 °C temperature increment in 311 s. Regarding humidity, previous stabilization times were 420 s for a 10% increment [33] or 300 s for a 5% increment [34]. However, our system can stabilize a 40% humidity increment in only 65 s. It is important to note that different settings, such as heat devices, humidifiers or enclosure volume, can unfairly bias this comparison. For this reason, a specific comparative study should be performed when other atmospheric enclosure systems will be available for bioprinting. Meanwhile, we have exposed some differences among our work and the previously exposed studies for better understanding of our previous comparisons. In some cases, no technical specifications of sensors/devices are available; in this case, we cannot go into detail about the reasons of differences [34]. Other studies with a larger volume of controllers and heaters/sensors are differentially dimensioned [33]. Maybe the most similar enclosure was an incubator with comparable electronics, but unfortunately, the authors did not control humidity in the analysis [15].

5. Conclusions

In this work, a PID controller for temperature and humidity control of an atmospheric enclosure system for bioprinting was designed, developed and tested. Theoretical and experimental transfer functions for temperature and humidity were calculated and verified. The results show that the proposed atmospheric enclosure system is capable of stabilizing temperature and humidity in 311 s and maintaining target values with an average error of 1.89% and 1.29% for temperature and humidity, respectively. Hence, the proposed atmospheric enclosure system for bioprinting could improve post-printing environmental conditions to increase the integrity, stability and cell viability of 3D bioprinted structures.

As commented, to guarantee a proper atmospheric enclosure system for bioprinting, a CO_2 control is needed in addition to temperature and humidity. In this sense, the next step of this study will be

analyzing the system's behavior after the inclusion of carbon dioxide as well as the interrelation with temperature and humidity. Additionally, bioprinters usually have a heat/cool cartridge in the extruder to control the bioink temperature. So, the addition of this heat/cool source inside the atmospheric enclosure to simulate bioprinter performance while extruding will be another future development.

Author Contributions: Conceptualization, M.M., J.C.G.-B., Á.J.S., E.M. and J.B.P.; methodology, M.M., J.C.G.-B. and J.B.P.; software, Á.J.S.; validation, M.M., J.C.G.-B., Á.J.S., E.M., A.C.M., J.P.C.-A. and J.B.P.; formal analysis, M.M. and J.C.G.-B.; investigation, M.M., J.C.G.-B., Á.J.S., E.M., A.C.M., J.P.C.-A. and J.B.P.; writing—original draft preparation, M.M., J.C.G.-B. and J.B.P.; writing—review and editing, Á.J.S., E.M., A.C.M., J.P.C.-A. and J.B.P.; visualization, M.M., J.C.G.-B. and J.B.P.; supervision, J.B.P.; project administration, J.C.G.-B. and J.B.P.; funding acquisition, J.B.P. All authors have read and agreed to the published version of the manuscript.

Funding: This research was co-funded by the Consejería de Economía, Ciencia y Agenda Digital, Junta de Extremadura and the INTERREG V-A Spain—Portugal Program (POCTEP) 2014-2020, with project reference IB16200, predoctoral grant reference PD16067 and project reference 0663_BIOIMPACE_4_E. The project was co-financed by the European Union/ERDF, ESF and INTERREG programme.

Conflicts of Interest: The authors declare no conflict of interest.

References

1. Mao, A.S.; Mooney, D.J. Regenerative medicine: Current therapies and future directions. *Proc. Natl. Acad. Sci. USA* **2015**, *112*, 14452–14459. [CrossRef] [PubMed]
2. Eswaramoorthy, S.D.; Ramakrishna, S.; Rath, S.N. Recent advances in three-dimensional bioprinting of stem cells. *J. Tissue Eng. Regen. Med.* **2019**, *13*, 908–924. [CrossRef] [PubMed]
3. Jiang, T.; Munguia-Lopez, J.G.; Flores-Torres, S.; Kort-Mascort, J.; Kinsella, J.M. Extrusion bioprinting of soft materials: An emerging technique for biological model fabrication. *Appl. Phys. Rev.* **2019**, *6*, 011310. [CrossRef]
4. Kang, H.W.; Lee, S.J.; Ko, I.K.; Kengla, C.; Yoo, J.J.; Atala, A. A 3D bioprinting system to produce human-scale tissue constructs with structural integrity. *Nat. Biotechnol.* **2016**, *34*, 312–319. [CrossRef]
5. Boularaoui, S.; Al Hussein, G.; Khan, K.A.; Christoforou, N.; Stefanini, C. An overview of extrusion-based bioprinting with a focus on induced shear stress and its effect on cell viability. *Bioprinting* **2020**, *20*, e00093. [CrossRef]
6. Gómez-Blanco, J.C.; Mancha-Sánchez, E.; Marcos, A.C.; Matamoros, M.; Díaz-Parralejo, A.; Pagador, J.B. Bioink Temperature Influence on Shear Stress, Pressure and Velocity Using Computational Simulation. *Processes* **2020**, *8*, 865. [CrossRef]
7. Unagolla, J.M.; Jayasuriya, A.C. Hydrogel-based 3D bioprinting: A comprehensive review on cell-laden hydrogels, bioink formulations, and future perspectives. *Appl. Mater. Today* **2020**, *18*, 100479. [CrossRef]
8. Hölzl, K.; Lin, S.; Tytgat, L.; Van Vilerberghe, S.; Gu, L.; Ovsianikov, A. Bioink properties before, during and after 3D bioprinting. *Biofabrication* **2016**, *8*, 1–19. [CrossRef]
9. Walker, J.M. *3D Bioprinting*; Methods in Molecular Biology Series Editor; Humana: New York, NY, USA, 2020; ISBN 978-1-0716-0519-6.
10. CELLINK BIO X-CELLINK. Available online: https://www.cellink.com/product/cellink-bio-x/ (accessed on 30 October 2020).
11. RegenHU Biofactory. Available online: https://www.regenhu.com/3d-bioprinters#biofactory (accessed on 30 October 2020).
12. Poietis.—4D Bioprinting Next Generation. Available online: https://poietis.com/bioprinters/ (accessed on 3 November 2020).
13. Crook, J.M. *3D Bioprinting Principles and Protocols*; Springer: Berlin, Germany, 2020.
14. Pinto, J.A.D.; Cordova, E.A.; Lévano, C.B.C. Design and Implementation of a Digital PID Temperature Controller for Neonatal Incubator ESVIN. *J. Mech. Eng. Autom.* **2015**, *5*, 167–172.
15. Feki, E.; Zermani, M.A.; Mami, A. GPC Temperature Control of a Simulation Model Infant-Incubator and Practice with Arduino Board. *Int. J. Adv. Comput. Sci. Appl.* **2017**, *8*, 46–59. [CrossRef]
16. Rahman, Z.S.A.; Hussain, F.S.A. Smart Incubator Based on PID Controller. *Int. Res. J. Eng. Technol.* **2017**, *4*, 2501–2509.

17. Okpagu, P.E.; Nwosu, A.W. Development and Temperature Control of Smart Egg. *Eur. J. Eng. Technol.* **2016**, *4*, 13–21.
18. Riahi, J.; Vergura, S.; Mezghani, D.; Mami, A. Intelligent Control of the Microclimate of an Agricultural Greenhouse Powered by a Supporting PV System. *Appl. Sci.* **2020**, *10*, 1350. [CrossRef]
19. Ben Ali, R.; Aridhi, E.; Abbes, M.; Mami, A. Fuzzy logic controller of temperature and humidity inside an agricultural greenhouse. In Proceedings of the 7th International Renewable Energy Congress (IREC), Hammamet, Tunisia, 22–24 March 2016; pp. 1–6.
20. Daskalov, P.I.; Arvanitis, K.G.; Pasgianos, G.D.; Sigrimis, N.A. Non-linear adaptive temperature and humidity control in animal buildings. *Biosyst. Eng.* **2006**, *93*, 1–24. [CrossRef]
21. Buonomano, A.; Montanaro, U.; Palombo, A.; Santini, S. Temperature and humidity adaptive control in multi-enclosed thermal zones under unexpected external disturbances. *Energy Build.* **2017**, *135*, 263–285. [CrossRef]
22. Kapen, P.T.; Mohamadou, Y.; Momo, F.; Jauspin, D.K.; Anero, G. An energy efficient neonatal incubator: Mathematical modeling and prototyping. *Health Technol. (Berlin)* **2019**, *9*, 57–63. [CrossRef]
23. Oliveira, G.H.C.; Amorim, M.F.; Pacholok, C. A real-time predictive scheme for controlling hygrothermal conditions of neonate incubators. *IFAC Proc. Vol.* **2016**, *38*, 387–392. [CrossRef]
24. Wang, L.; Zhu, Z. Research on Temperature and Humidity Decoupling Control of Constant Temperature and Humidity Test Chamber. *IOP Conf. Ser. Mater. Sci. Eng.* **2020**, *711*, 012104. [CrossRef]
25. Albright, L.; Arvanitis, K.; Drysdale, A. Environmental control for plants on Earth and in space. *IEEE Control. Syst.* **2001**, *21*, 28–47. [CrossRef]
26. De Jesus Rubio, J.; Salazar, M.; Lugo, R.; Pacheco, J.; Gomez, A.D. Modeling of the relative humidity and control of the temperature for a bird incubator. *Adv. Intell. Soft Comput.* **2009**, *61 AISC*, 369–377.
27. Poudel, M.; Dunn, B. *Greenhouse Carbon Dioxide Supplementation*; HLA-6723; Oklahoma State University: Stillwater, OK, USA, 2017.
28. Yinping, M.; Lu, Z. Expert controller in multi-variable System of Temperature and Humidity. *Int. J. Eng. Appl. Sci.* **2017**, *9*, 51–59. [CrossRef]
29. Abdelaziz, Y.A. Low Cost Humidity/Temperature Calibration System. *J. Sci. Eng. Res.* **2017**, *4*, 305–311.
30. Ragazzini, G.; Mescola, A.; Corsi, L.; Alessandrini, A.; Ragazzini, G.; Mescola, A.; Corsi, L.; Alessandrini, A. Fabrication of a low-cost on-stage cell incubator with full automation. *J. Biol. Educ.* **2018**, *9266*, 1–9. [CrossRef]
31. Astrom, K.J.; Hagglund, T. *Control PID Avanzado*, 1st ed.; PEARSON EDUCACIÓN, S.A.: Madrid, Spain, 2009; ISBN 978-84-8322-511-0.
32. Morales, J.G. Diseño e Implementación de un Control de Temperatura y Humedad Para un Prototipo de Incubadora Artificial de Pollos. Repositorio de Pontificia Universidad JAVERIANA. 2017. Available online: http://vitela.javerianacali.edu.co/handle/11522/8610 (accessed on 17 June 2020).
33. Widhiada, W.; Antara, I.N.G.; Budiarsa, I.N.; Karohika, I.M.G. The Robust PID Control System of Temperature Stability and Humidity on Infant Incubator Based on Arduino at Mega 2560. *IOP Conf. Ser. Earth Environ. Sci.* **2019**, *248*, 012046. [CrossRef]
34. De, J.; Barçante, G.M.; Cavalcante, M.U.; Da, O.; Torrico, B.C. PI multivariable control applied to temperature and humidity neonate incubators. In Proceedings of the 9th IEEE/IAS International Conference on Industry Applications—INDUSCON 2010, Sao Paulo, Brazil, 8–10 November 2010; pp. 1–6.
35. Jovic, T.H.; Kungwengwe, G.; Mills, A.C.; Whitaker, I.S. Plant-Derived Biomaterials: A Review of 3D Bioprinting and Biomedical Applications. *Front. Mech. Eng.* **2019**, *5*, 1–18. [CrossRef]
36. Cavalcante, M.U.; Torrico, B.C.; Da Mota Almeida, O.; De Souza Braga, A.P.; Da Costa Filho, F.L.M. Filtered model-based predictive control applied to the temperature and humidity control of a neonatal incubator. In Proceedings of the 9th IEEE/IAS International Conference on Industry Applications—INDUSCON 2010, Sao Paulo, Brazil, 8–10 November 2010; pp. 1–6.

7.6 Improving cell viability and velocity in μ-extrusion bioprinting with a novel pre-incubator bioprinter and a standard FDM 3D printing nozzle

materials

MDPI

Article

Improving cell viability and velocity in μ-extrusion bioprinting with a novel pre-incubator bioprinter and a standard FDM 3D printing nozzle

JC Gómez-Blanco [1,*], V Galván-Chacón [1], D Patrocinio [1], M Matamoros [2], A Ojeda [2], AC Marcos [2], M Duarte [1], F Marinaro [1], JB Pagador [1,*] and FM Sánchez-Margallo [1]

[1] Jesús Usón Minimally Invasive Surgery Centre, 10071 Cáceres, Spain; {jcgomez, vpgalvan, dpatrocinio, fmarinaro, jbpagador, msanchez} @ccmijesususon.com
[2] School of Industrial Engineering, University of Extremadura, 06006 Badajoz, Spain; {manuelmp, acmarcos} @unex.es
* Correspondence: {jcgomez, jbpagador} @ccmijesususon.com.com

Abstract:

Bioprinting is a highly topical emerging technology, widely studied by the scientific community for the possibility it offers to create transplantable artificial tissues, with minimal risk to the patient. Although the biomaterials and cells to be used are being carefully studied, there is still a long way to go before a bioprinter can easily and quickly produce printings without harmful effects on the cells. In this sense, we have developed a new μ-extrusion bioprinter formed by an Atom Proton 3D printer, an atmospheric enclosure and a new extrusion-head capable to increment usual printing velocity. Hence, this work has two main objectives. First, to experimentally study the accuracy and precision. Secondly, to study the influence of flow rates on cellular viability using this novel μ-extrusion bioprinter in combination with a standard FDM 3D printing nozzle. Our results show an X, Y and Z axis movement accuracy under 17 μm with a precision around 12 μm while the extruder values are under 5 and 7 μm, respectively. Additionally, the cell viability obtained from different volumetric flow tests varies from 70 to 90 %. So, the proposed bioprinter and nozzle can control the atmospheric conditions and increase the volumetric flow speeding up the bioprinting process without compromising the cell viability.

Keywords: Bioprinting; Pre-incubator; Atmospheric enclosure; 3D printing; Nozzle; Conical tip; Fluid flow; Cell viability

Citation: Lastname, F.; Lastname, F.; Lastname, F. Title. *Materials* **2021**, *14*, x. https://doi.org/10.3390/xxxxx

Academic Editor: Firstname Lastname

Received: date
Accepted: date
Published: date

Publisher's Note: MDPI stays neutral with regard to jurisdictional claims in published maps and institutional affiliations.

1. Introduction

Bioprinting is nowadays an emerging technology widely used in regenerative medicine and tissue engineering. It can be defined as a technology capable of an accurate deposition of cells and biochemical components layer by layer to create defined structures using materials, bioactive molecules and cells [1,2]. The creation of artificial tissues and organs using patient cells can reduce the rejection risk [3]. Among all possible tissues to recreate, researches are focused in bioprinting vascular, neural, bone, cardiac, skin or muscle tissues [4,5]. To obtain a fully functional tissue all properties and functionalities of the desired tissue must be considered and adapted to the material and cell-line for the bioprinting procedure. In this sense, not only the bioink must be appropriate for the process but also the bioprinting procedure itself. The most common technologies in bioprinting are μ-extrusion, inkjet, laser-assisted, and stereolithography [6]. Independently of the bioprinting procedure the ideal bioprinter was described by Dababneh and Ozbolat [7] and they concluded that this bioprinter must have 10 main characteristics:

- High degree-of-freedom in motion.
- High resolution and accuracy.
- The ability to dispense various bioink solutions simultaneously.
- Ease of use.
- Compact size.
- Ease of sterilization.
- Full-automation capability.
- Affordability.
- Versatility.

Current bioprinters can fulfill some of the ideal bioprinter characteristics but they are highly influenced by the technology they used. Each bioprinting procedure has their own advantages such as the possibility of using high viscous bioinks with high cell density or accurately deposit a small number of cells in a fast process in μ-extrusion or inkjet bioprinting, respectively [6]. Despite μ-extrusion bioprinting being a slow procedure, it is the most used because it is highly versatile and brings the possibility of using a wide range of bioink viscosities and cells densities [3,6,8].

Regarding to μ-extrusion bioprinters there are a wide variety of commercial bioprinters in the market. Among the most affordable ones (less than 20,000 $), compact size and high resolution and accuracy are usually common features within a resolution range between 50 and 200 μm [9]. More expensive bioprinters or laboratory non-commercial bioprinters have better resolution, accuracy and printing speed. Independently of the affordability of the bioprinter, some of them have enclosure systems capable of controlling the air flow through High Efficiency Particle Arresting (HEPA) filters, such as Cellink BioX® (Cellink; Boston, MA, USA), Poietis® (Poietis; 33600 Pessac, France) or 3D-Discovery BioFactory® (REGENHU; 1690 Villaz-Saint-Pierre, Switzerland) [10–12]. As far as authors know, only Matamoros et al. [13] have developed and tested an atmospheric enclosure (pre-incubator) capable of controlling the air flow as well as the inner temperature and humidity. Their system can be considered as a pre-incubator, preventing bioink to dry and cells to have better environment to increase their viability. Regarding to the possibility of dispensing various bioinks simultaneously, many bioprinters have multiple print-heads and a few have also rapid interchangeable print-heads as the Cellink BioX® (Cellink; Boston, MA, USA) [10]. Furthermore, most of μ-extrusion bioprinters use a pneumatic approach to perform the extrusion of the material. This approach makes the bioprinter much easier to be used but it neglects the control of volumetric flow, which might reduce the shape fidelity of the printed tissue [3,6,8].

Current research on μ-extrusion bioprinting mechanics is focused in two pathways, minimizing the costs and obtaining the best shape fidelity by using piston driven extrusion. In this sense, authors have been developing and adapting new piston-driven extrusion-head to a conventional 3D printer [14–19] or developing new bioprinters [20,21]. New adapted extrusion-heads are usually based on a design proposed by Wijnen et al. [22]. This design is open-source, easily adaptable to any 3D printer and mainly composed by a NEMA motor, a worm screw, a syringe holder and a syringe pusher. Nevertheless, the larger the size and weight of this extrusion-head, the lower the precision and accuracy of the system [22]. Kahl et al. [18] modified the initial design by changing the location of the motor and reducing possible extruder-head movements by inertia. Regarding to the creation of new bioprinters, Campbell et al [20] used the same extruder head proposed by Wijnen et al. [22] but using external reservoirs connected to a new extruder-head through heated/cooled tubes. The bioprinter designed by McElheny et al. [21] used the same open

source extruder but changing the NEMA motor by a noncaptive stepper motor. Additionally, authors as Ravi et al. [23] or Yenilmez et al. [24] developed and tested new bioprinting systems combining inkjet, FDM and μ-extrusion; and inkjet, μ-extrusion and UV light, respectively.

Not only bioprinters and extrusion heads are in the focus on μ-extrusion bioprinting improvement but also the nozzles. The internal geometry of the nozzle modifies inner bioprinting parameters such as pressure, velocity or shear stress which might have an important impact on the features of the bioprinted structures [25]. In this sense, computational simulation is commonly used to study inner bioprinting parameters [19,26–31] mainly due to the difficulty to perform experimental measurements without disturbing the flow of bioinks. Specifically, Reid et al. [19], Gómez-Blanco et al. [26] or Martanto et al. [30] demonstrate that different conical tips gauges have a noticeable influence in the volumetric flow and the shear stress using numerical methods or computational simulations. Additionally, in a recent work Gómez-Blanco et al. [32] demonstrate that using a 3D printer standard nozzle can increase the velocity of the process when compared with a conical tip with reduced impact on pressure and shear stress that should keep similar levels of cellular viability.

Hence, the objective of this work is to experimentally study the movement accuracy of the bioprinter axis as well as the influence of volumetric flow on cellular viability using a novel μ-extrusion bioprinter and a standard FDM 3D printing nozzle.

2. Materials and Methods

2.1 Bioprinter design

The bioprinter used in this work was an adaptation of an Atom Proton 3D printer. This 3D printer was selected because two main reasons, 1) it is a low-cost open-source 3D printer and 2) it has a different X axis construction. The differences between this Atom Proton and the Prusa type 3D printer (Figure 1) made the Atom Proton the best choice to adapt a new extruder design and install it inside an atmospheric chamber. The design, components, construction and PID controller of the atmospheric enclosure were detailed in a previous work [13].

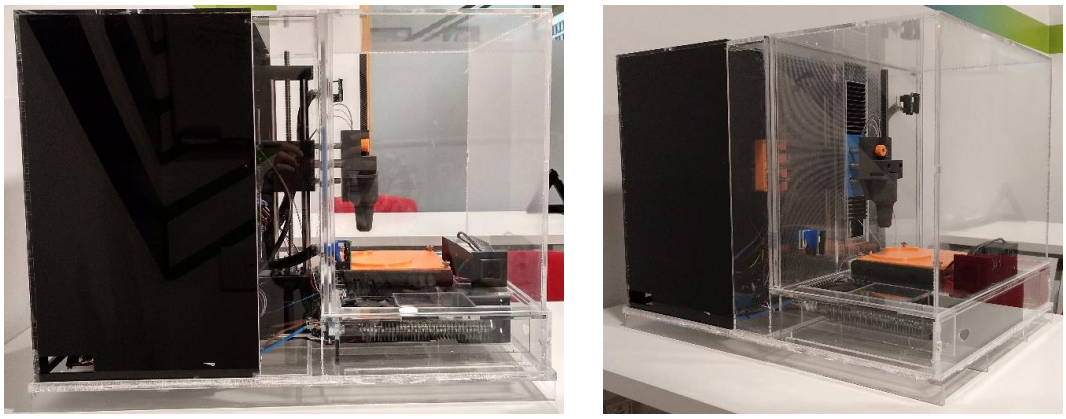

(**a**) (**b**)

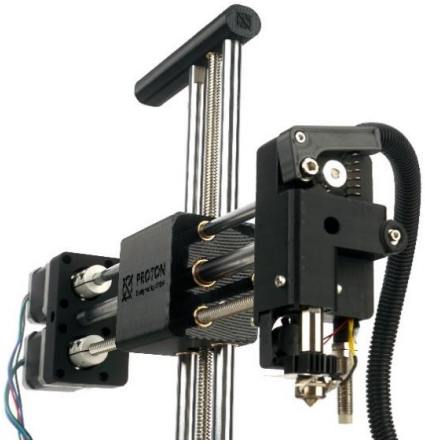

(c)

Figure 1. Bioprinter with atmospheric enclosure system. (a) lateral view, (b) perspective view and (c) Atom Proton 3D printer extruder head.

The new extruder head takes advantage of the location of the extruder motor and its power transmission. Figure 2 shows the two main parts of the new extruder design, the pusher block (white and grey parts) and the syringe holder (black parts). The piston-driven pusher block is formed by a rack and pinion system where the pinion is moved by the extruder motor causing the rack to move linearly up and down extruding the bioink. The syringe holder was a rapid interchangeable tool with non-contacts electronic pins to connect the 5 mL syringe heat block (100 kΩ thermistor and two flexible resistors) to the Atom Proton electronics. The bioink is placed in a 5mL syringe with a specially designed plug to achieve uniform push.

The firmware of the bioprinter was adapted from the original Atom Proton Marlin modifying the range of the axis, maximum and minimum operating temperatures, and the axis steps per unit. Additionally, the bioprinter and the atmospheric enclosure was controlled by a Raspberry Pi 3 Model B through a custom-made interface similar to Repetier Host software.

2.2 Accuracy measurements

Axis (X, Y and Z) and extruder linear movement accuracy was measured using a dial test indicator (Draper Expert Nº 46609) with a 10 μm resolution. The tests were done in three measurement points for the X, Y and Z axis and in one measurement point for the extruder rack. The points were placed at zero (home), maximum axis length and at the middle of the axis. As the extruder did not have maximum and minimum position, one aleatory position of the rack was selected as the measurement point. The test consisted in positioning each axis at the selected point, moved the axis 10 mm and return to the initial position. The positioning error of each movement was repeated and measured 10 times for each selected point. The movement accuracy was calculated as the average value of all measurements for each axis. In a similar manner, the precision of the movement was calculated as the standard deviation of the previous accuracy. Additionally, the mean square error of the X-Y plane is calculated using the average value of each measurement point for X and Y axes obtaining a 3x3 matrix.

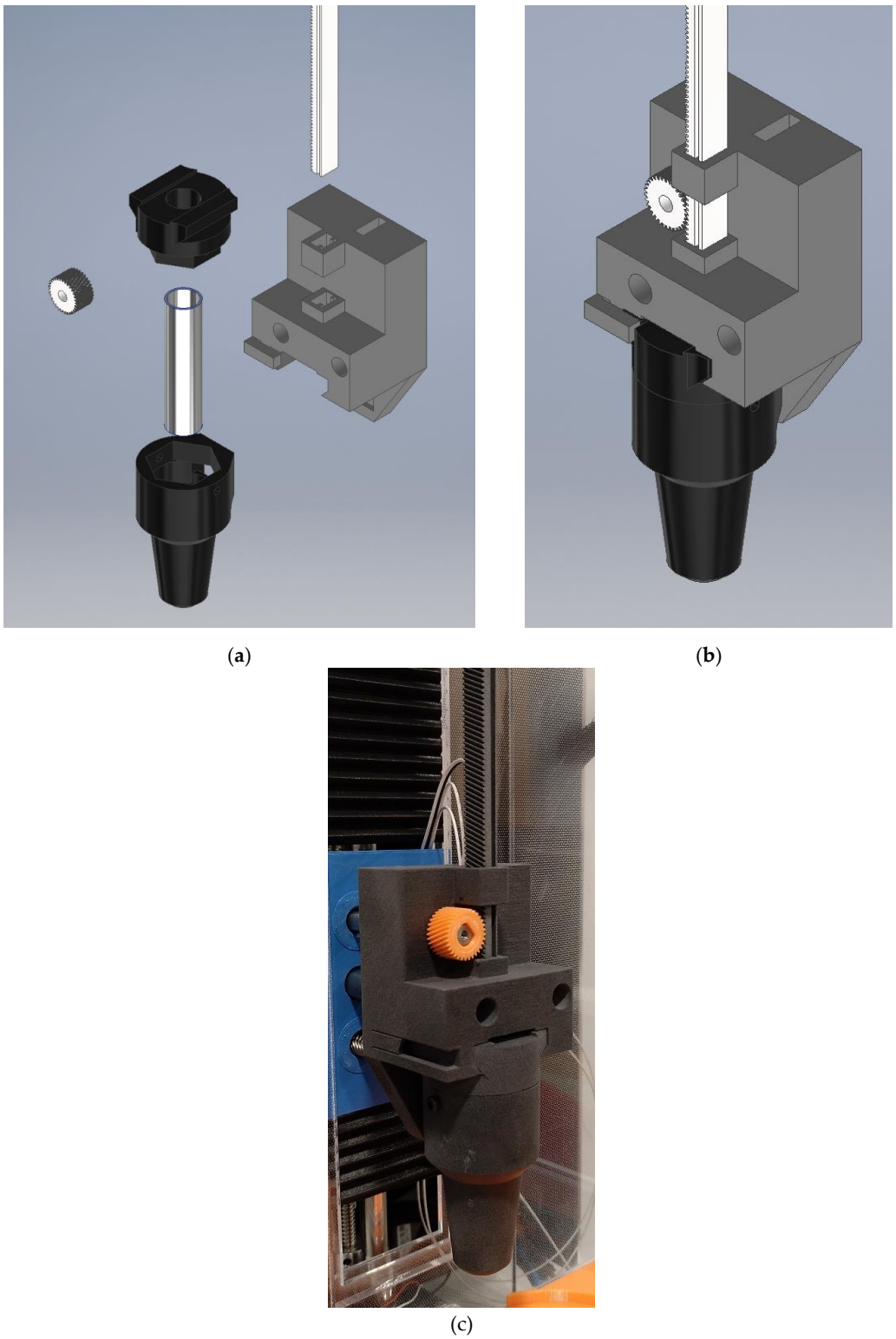

(**a**) (**b**)

(c)

Figure 2. Designed extruder-head with rapid interchangeable syringe system. (a) exploit view of the system's components, (b) full assemble system and (c) image of the prototype of the extrusion-head system.

2.3 Cell culture and bioink preparation

Human mesenchymal endometrial cells were isolated from menstrual blood of a human donor after informed consent following a protocol described elsewhere [33] and were seeded at a density of 5000 cells/cm^2 in T175 flasks incubated at 37 °C, 5 % CO_2 and 95 % humidity and expanded in DMEM cell culture medium supplemented with 10 % FBS (Gibco), 100 U/mL penicilin, 100 µg/mL streptomicin and 10µg/mL cyprofloxacin. After approximately an 80% confluence was reached, the cells were trypsinized and resuspended in 1 mL of cell culture medium prior to mixing with the hydrogel.

The biomaterial used in the bioprinting tests was Cellink Bioink (Cellink, USA). The final bioink mixture was done using a Cellink Mixer with a volumetric ratio of 5:1 and a final cell concentration of 7.5x10^5 cells/mL.

2.4 Bioprinting

To study how different flow rate and nozzle affect cellular viability 4 different tests were performed. For each test, a specific G-code was programmed and the atmospheric enclosure was set to 37ºC and 50% of relative humidity. Each test consisted in the printing of a 40x40 mm scaffold in a Petri dish using a specific nozzle and flow rate. Table 1 resumes the nozzle and flow rate used on each test as well as the printing velocity associated with the flow rate.

Table 1. Nozzle, flow rate and associated printing velocity of the different test performed.

Test	Nozzle	Flow rate (mm^3/s)	Printing velocity (mm/s)
T1	22G conical tip	10	8.55
T2	E3D v6 standard nozzle	10	8.55
T3	E3D v6 standard nozzle	15	12.83
T4	E3D v6 standard nozzle	20	17.11

For the analysis, each printed scaffold was divided into 16 different parts using a scalpel. From all parts, eight were aleatory selected and placed in a 24 well plate to culture and measure cell viability.

2.5 Cell viability evaluation assay

Samples from each test were cultured and tested for cell viability at 0, 1, 3 and 7 days after the bioprinting procedure. Cellular viability of each sample was analyzed using Invitrogen Live/Dead kit (Invitrogen™ R37601, Thermo Fisher Scientific, USA), staining live cells in green (488 nm) and dead cells in red (570 nm).

The cell viability images were obtained using a fluorescence microscope (Nikon TE2000-S) and cell viability was quantified using open-source ImageJ 1.52p software (National Institutes of Health, Bethesda, USA) by converting images to 8-bit grayscales images, adjusting the histogram to get brighter images and reducing the background noise using the subtracting background process.

Cell viability results were processed using Graphpad Prism v. 9.1.0 (Graphpad Software, USA) using a two-way ANOVA with Tukey´s multiple comparison test, with 95% confidence interval (significance threshold p=0.05).

3. Results and discussion

3.1. Accuracy

¡Error! No se encuentra el origen de la referencia. shows the absolute errors obtained from accuracy test for X, Y and Z axis and Extruder.

Table 2. Absolute errors in μm of the X, Y, Z axis and the extruder rack. Initial or Home (H), Middle (M) and Total (T) length measurements points.

Sample	X error (μm)			Y error (μm)			Z error (μm)			Extruder error (μm)
	H	M	T	H	M	T	H	M	T	
1	30	40	20	10	30	20	10	20	10	20
2	0	0	0	10	40	10	10	30	10	0
3	20	10	20	20	40	30	10	40	10	0
4	0	10	0	20	30	10	10	20	20	0
5	20	10	10	0	0	20	0	10	20	0
6	20	20	20	0	0	10	0	0	0	0
7	20	10	20	20	0	10	0	10	10	10
8	0	20	0	20	10	20	0	0	0	10
9	0	10	20	20	0	30	0	10	0	10
10	0	20	0	20	10	30	0	0	0	0

The average absolute errors or the movement accuracy and precision obtained are 11.67±10.85, 16.33±11.89 and 8.67±10.08 μm for X, Y and Z axis, respectively. Additionally, the movement accuracy and precision of the extruder rack is 5.00±7.07 μm. Therefore, the adapted Atom Proton bioprinter has a X, Y and Z movement accuracy under 17 μm with a movement precision around 12 μm. The bioprinter also has a new extruder system capable of extruding bioinks with a linear rack movement accuracy of 5 μm and a precision around 7 μm. Additionally, the mean square error for the X-Y plane can be seen in Figure 3. This error indicates the possible movement deviation of the extruder head in the X-Y plane. The distribution of the error can be divided into two zones, a plateau zone (from middle to total length of the Y axis) and a ramp from the lowest error values (home in Y axis) to the middle line of the X-Y plane. Despite, the plateau zone has higher error values, the difference between the maximum and minimum error is 0.98 μm so it can be considered a stable area for printing with an average error in the X-Y plane of 24.13 μm. Additionally, the total error variation in the plane is 3.98 μm. All X-Y plane errors can be considered negligible in many bioprinting applications because the width of the extruded line is usually higher of 200 μm (27G conical tip or needle). All these errors might be due to the different axes' movements compared with the standard Prusa type printers. While the Atom Proton axes' movements are looser guided because it only has one z motor, the Prusa has two, so the extruder head might quiver more in our setup.

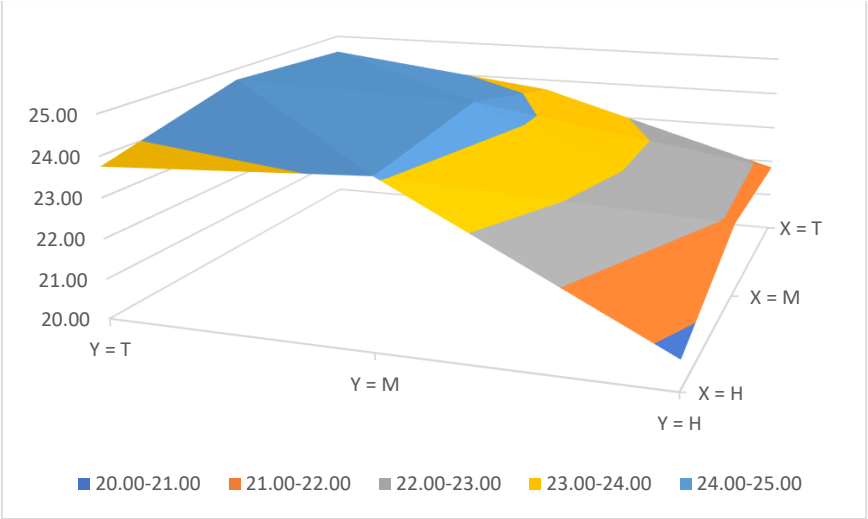

Figure 3. Mean square error of the X-Y plane in μm.

Comparing our movement precision with other bioprinters, we have obtained similar movement precision than other authors. Specifically, Kahl et al [18], Reid et al [19] and Hesuani et al. [34] obtained a X-Y movement precision of 12 μm, 13 μm, and 10 μm, respectively while Z movement precision obtained by Kahl et al [18] is 4 μm. Regarding to commercial bioprinters, Ozbolat et al. [9] resumed this information of several bioprinters and obtained position precision varying between 5 and 150 μm of BioBot 1 (BioBots, USA) and Regemat 3D V (Regemat 3D, Spain), respectively.

3.2. Cell viability

Figure 4 shows the results of cell viability for all tests grouped by timepoints. Results show that the proposed use of a standard 3D printing nozzle is as good as the commonly used conical tip, as no significant differences between printing conditions can be found within the same timepoint (Figure 4). Furthermore, cell viability of the conical tip (T1) and the faster nozzle (T4) are similar independently of the measured days. Specifically, T1 and T4 cell viability values are 71.22 and 69.22 %, 85.05 and 87.93 %, 76.47 and 82.88 %, and 86.20 and 80.34 % for D0, D1, D3 and D7, respectively. Additionally, if all tests are considered the maximum and minimum values of cell viability are 69.22 and 80.15% for D0, 73.62 and 87.93 % for D1, 76.47 and 82.88% for D3, and 80.34 and 86.20 % for D7.

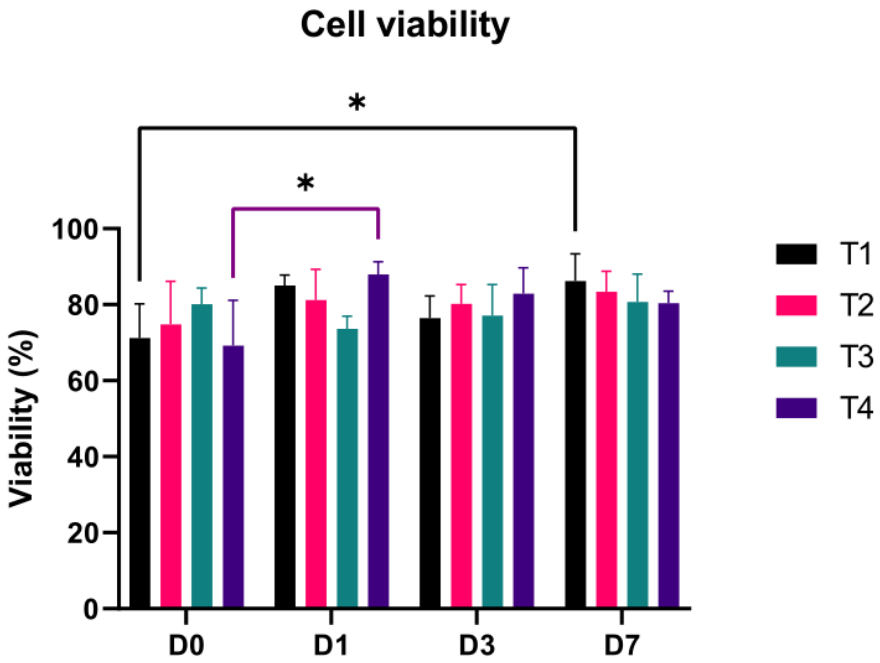

Figure 4. Cell viability of test grouped by timepoins. * represents significative difference ($p<0.05$)

Looking at the evolution of cell viability over time, an increasing tendency of the minimum value can be seen. In this study, there are not significant differences for T2 and T3, independently of the day, but significant differences between D0 and D4, and D0 and D1 can be seen for T1 and T4, respectively (Figure 5). On the one hand, the differences of T1 can be explained as the cell proliferation when the scaffolds samples are cultured. Cell viability of T1 tends to increase with culture time. On the other hand, the different cell viability of T4 from day 0 to day 1 can be explained as both an acclimatization process to the encapsulation and an increase in cell proliferation due to the continuation of the cell cycle. Before trypsinization, cells can be at any of the cell cycle phases, and after encapsulation in the hydrogel they resume the cell cycle before becoming dormant, thus causing an increase in proliferation. Another possible explanation could be the healing process of those cells that might be injured during the bioprinting (Figure 5). The healing or recovery process of cells in bioprinting procedures have been studied by authors as Ozbolat et al. [4] or Ning et al. [35]. In their works, Ozbolat obtained a cell viability increment from 43.92 to 76.06 % in two days culture caused by cell healing as well as cell proliferation, while Ning obtained a cell recovery of approximately 2.5% in 6 hours after printing.

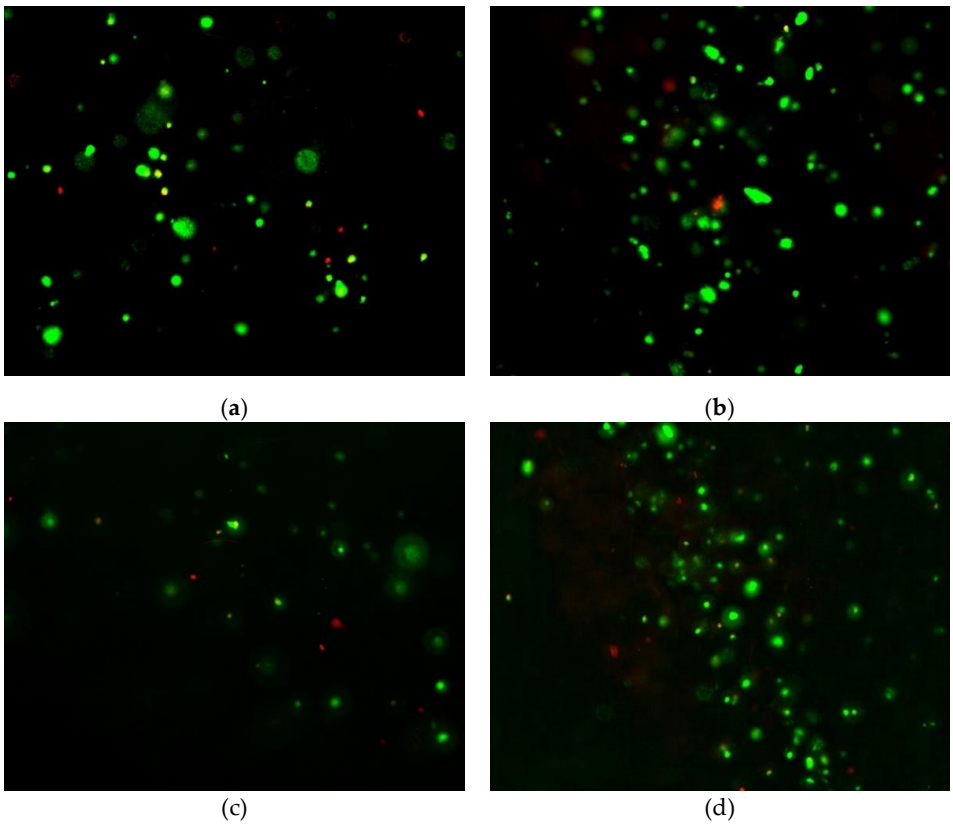

Figure 5. Cell viability images from samples with significance differences. (a) Cell viability of T1 measured at day 0, (b) cell viability of T1 measured at day 7, (c) cell viability of T4 measured at day 0 and (d) cell viability of T4 measured at day 1.

Additionally, the range of values for each day tend to reduce as result of cell healing and proliferation [4,35] when samples are cultured for several days.

Therefore, according to our results, the use of the proposed FDM standard 3D printing nozzle does not produce a noticeable harmful effect to cells when printing twice faster than with the conical tip (Figure 6).

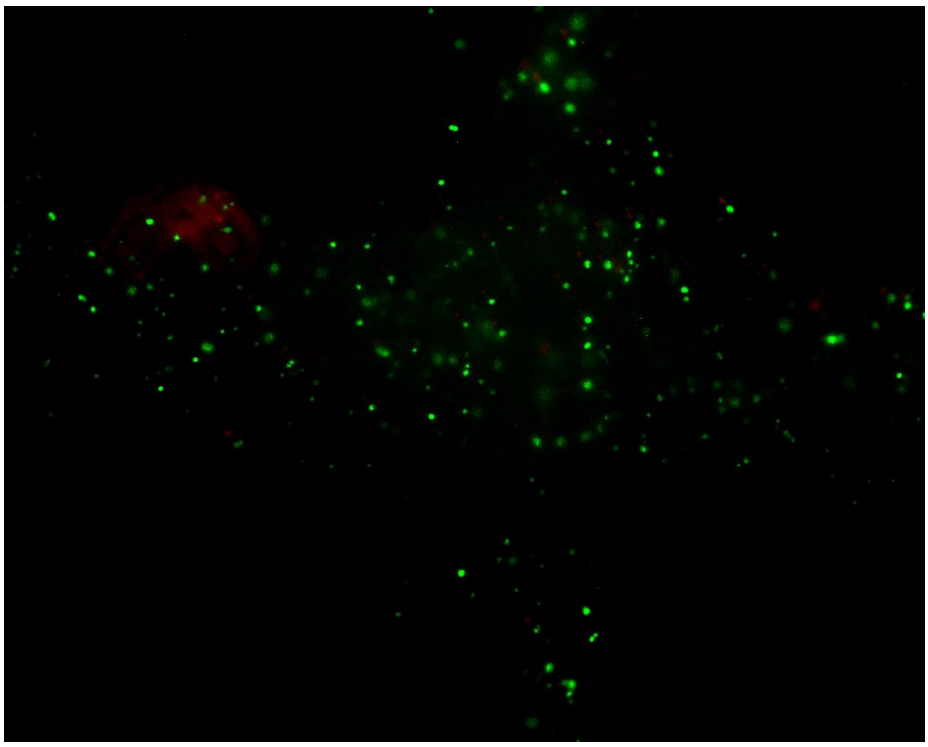

Figure 6. Live (green) and dead (red) cells of T4 at day 7

Cell viability results obtained are similar to those of other authors testing new bioprinters or adapted print-heads. Specifically, Campbell et al. [20] calculate the relative cell viability of their samples with respect to their hand bioprint measured 24 h after the procedure. They do not provide any value of cell viability to compare with our results but in the graph they presented the cell viability tend to decrease. Bessler et al. [16] studied mESC and HEK293 cells using a FRESH printing method and they obtained cell viability varying from 60 to 95 %. Specifically, they measured viability just after the printing procedure and obtained 85±13 % and 81±9 % for mESC and HEK293 cells, respectively. Kahl et al. [18] studied HEK 293 cell viability but they presented their results as the average relative fluorescence intensity (RFU) instead the cellular viability itself. They concluded that as their RFU increase with culture time the cell proliferation and viability of the cultured sample increase. Ozbolat et al. [4] obtained cell viabilities of bioprinted filaments and spheroids using Cartilage progenitor cells (CPCs). In their work, they reported a cell viability at day 1 and 7 that increases from 43.92 to 87.23 % and 60.15 to 92.87 % for filaments and spheroids, respectively. They also explained the increment in cellular viability as the results of cell healing and proliferation while culture. Roehm et al. [36] studied how different flow rate and print velocity through a nozzle affect cellular viability measured 5 days after the printing procedure. They obtained similar results to ours with cell viabilities approximately ranged between 60 to 80% and none of the flow rates or velocities they checked had a significant influence on cellular viability. Sanz-García et al. [37] obtained higher cell viability values than ours (approximately 90 %). They used hASCs cells in a 10 % Gelatin-2 %Alginate bioink and a new pneumatic extrusion-head with a peltier cooling/heating system and a 25G conical tip.

5. Conclusions

In this work, a new bioprinter has been designed and tested. Results show that the new bioprinter has a movement accuracy under 17 μm with a movement precision of

approximately 12 μm for the X, Y and Z axes while the rack, located in the piston-driven print-head pusher block, is capable to extrude material with an accuracy under 5 μm and a precision around 7 μm. Additionally, as the proposed use of a standard FDM 3D printing nozzle brings theoretical higher volumetric flow, the tests performed in this work show that by using this nozzle it is possible to obtain faster printings without compromising cell viability. Specifically, cell viability increments from 70% just after printing to 90% at day 7, as result of cell healing and proliferation. Therefore, the proposed bioprinter with its new extrusion-head and a standard FDM 3D printing nozzle allow to control the atmospheric temperature and humidity performing faster printings while maintain high cell viability.

In future works, a more comprehensive study to obtain the maximum velocity and flow rate of the FDM 3D printing standard nozzle without compromising cell viability must be done.

Author Contributions: Conceptualization, Juan C. Gómez Blanco, Manuel Matamoros, Alfonso C. Marcos and J. Blas Pagador; Formal analysis, Juan C. Gómez Blanco, Victor Galván-Chacón, David Patrocinio and J. Blas Pagador; Funding acquisition, J. Blas Pagador and Francisco M. Sánchez-Margallo; Investigation, Juan C. Gómez Blanco, Victor Galván-Chacón, David Patrocinio, Manuel Matamoros, Álvaro J. Sánchez, Alfonso C. Marcos, María Duarte, Federica Marinaro, J. Blas Pagador and Francisco M. Sánchez-Margallo; Methodology, Juan C. Gómez Blanco, Victor Galván-Chacón, David Patrocinio, Alfonso C. Marcos, Federica Marinaro and J. Blas Pagador; Project administration, Juan C. Gómez Blanco and J. Blas Pagador; Software, Juan C. Gómez Blanco, Manuel Matamoros, Álvaro J. Sánchez and Alfonso C. Marcos; Supervision, J. Blas Pagador and Francisco M. Sánchez-Margallo; Validation, Juan C. Gómez Blanco; Writing – original draft, Juan C. Gómez Blanco, Victor Galván-Chacón and J. Blas Pagador; Writing – review & editing, Juan C. Gómez Blanco, Victor Galván-Chacón and J. Blas Pagador..

Funding: This research was funded by predoctoral grant number PD16067 and project number 0633_BIOIMPACE_4_A. Co-financed by European Union/ERDF, ESF, European Regional Development Fund ERDF under the Interreg V A Spain - Portugal (POCTEP) 2014-2020 program and Consejería de Economía, Ciencia y Agenda Digital de la Junta de Extremadura. The APC was funded by project number 0633_BIOIMPACE_4_A.

Acknowledgments: Authors wants to thank Stem Cell Therapy Unit of Jesús Usón Minimally Invasive Surgery Centre, specifically PhD Javier García, for their advice and fruitful discussions about cells proliferation and Live/Dead dye protocols.

Conflicts of Interest: The authors declare no conflict of interest.

References

1. Eswaramoorthy, S.D.; Ramakrishna, S.; Rath, S.N. Recent advances in three-dimensional bioprinting of stem cells. *J. Tissue Eng. Regen. Med.* **2019**, term.2839, doi:10.1002/term.2839.
2. Moroni, L.; Boland, T.; Burdick, J.A.; De Maria, C.; Derby, B.; Forgacs, G.; Groll, J.; Li, Q.; Malda, J.; Mironov, V.A.; et al. Biofabrication: A Guide to Technology and Terminology. *Trends Biotechnol.* **2018**, *36*, 384–402, doi:10.1016/j.tibtech.2017.10.015.
3. Ng, W.L.; Chua, C.K.; Shen, Y.F. Print Me An Organ! Why We Are Not There Yet. *Prog. Polym. Sci.* **2019**, *97*, 101145, doi:10.1016/j.progpolymsci.2019.101145.
4. Ozbolat, I.T.; Chen, H.; Yu, Y. Development of 'Multi-arm Bioprinter' for hybrid biofabrication of tissue engineering constructs. *Robot. Comput. Integr. Manuf.* **2014**, *30*, 295–304, doi:10.1016/j.rcim.2013.10.005.
5. Heinrich, M.A.; Liu, W.; Jimenez, A.; Yang, J.; Akpek, A.; Liu, X.; Pi, Q.; Mu, X.; Hu, N.; Schiffelers, R.M.; et al. 3D Bioprinting: from Benches to Translational Applications. *Small* **2019**, *15*, 1–47, doi:10.1002/smll.201805510.
6. Zhang, B.; Gao, L.; Ma, L.; Luo, Y.; Yang, H.; Cui, Z. 3D Bioprinting: A Novel Avenue for Manufacturing Tissues and Organs. *Engineering* **2019**, *5*, 777–794, doi:10.1016/j.eng.2019.03.009.

7. Dababneh, A.B.; Ozbolat, I.T. Bioprinting Technology: A Current State-of-the-Art Review. *J. Manuf. Sci. Eng.* **2014**, *136*, 061016, doi:10.1115/1.4028512.
8. Kyle, S.; Jessop, Z.M.; Al-Sabah, A.; Whitaker, I.S. 'Printability'' of Candidate Biomaterials for Extrusion Based 3D Printing: State-of-the-Art.' *Adv. Healthc. Mater.* **2017**, *6*, doi:10.1002/adhm.201700264.
9. Ozbolat, I.T.; Moncal, K.K.; Gudapati, H. Evaluation of bioprinter technologies. *Addit. Manuf.* **2017**, *13*, 179–200, doi:10.1016/j.addma.2016.10.003.
10. CELLINK BIO X - CELLINK Available online: https://www.cellink.com/product/cellink-bio-x/ (accessed on Apr 12, 2021).
11. Poietis Poietis - 4D Bioprinting Next Generation Available online: https://poietis.com/bioprinters/ (accessed on Apr 12, 2021).
12. RegenHU Biofactory Available online: https://www.regenhu.com/3d-bioprinters#biofactory (accessed on Apr 12, 2021).
13. Matamoros, M.; Gómez-Blanco, J.C.; Sánchez, Á.J.; Mancha, E.; Marcos, A.C.; Carrasco-Amador, J.P.; Pagador, J.B. Temperature and Humidity PID Controller for a Bioprinter Atmospheric Enclosure System. *Micromachines* **2020**, *11*, 999, doi:10.3390/mi11110999.
14. Aydın, L.; Küçük, S.; Kenar, H. Design and Construction of a Novel Micro-Extrusion System for Bio-printing Applications. *Int. J. Appl. Math. Electron. Comput.* **2016**, *4*, 52–52, doi:10.18100/ijamec.264681.
15. Goldstein, T.; Smith, L.P.; Krush, A.; Mercadante, K.; Lagalante, D.; Epstein, C.; Schwartz, J.A.; Zeltsman, D.; Grande, D. anthony Feasibility of 3-D Bioprinting With a Modified Desktop 3D Desktop Printer. *Tissue Eng. Part C Methods* **2016**, ten.TEC.2016.0286, doi:10.1089/ten.TEC.2016.0286.
16. Bessler, N.; Ogiermann, D.; Buchholz, M.B.; Santel, A.; Heidenreich, J.; Ahmmed, R.; Zaehres, H.; Brand-Saberi, B. Nydus One Syringe Extruder (NOSE): A Prusa i3 3D printer conversion for bioprinting applications utilizing the FRESH-method. *HardwareX* **2019**, *6*, e00069, doi:10.1016/j.ohx.2019.e00069.
17. Ioannidis, K.; Danalatos, R.I.; Champeris Tsaniras, S.; Kaplani, K.; Lokka, G.; Kanellou, A.; Papachristou, D.J.; Bokias, G.; Lygerou, Z.; Taraviras, S. A Custom Ultra-Low-Cost 3D Bioprinter Supports Cell Growth and Differentiation. *Front. Bioeng. Biotechnol.* **2020**, *8*, 1–13, doi:10.3389/fbioe.2020.580889.
18. Kahl, M.; Gertig, M.; Hoyer, P.; Friedrich, O.; Gilbert, D.F. Ultra-low-cost 3D bioprinting: Modification and application of an off-the-shelf desktop 3D-printer for biofabrication. *Front. Bioeng. Biotechnol.* **2019**, *7*, doi:10.3389/fbioe.2019.00184.
19. Reid, J.A.; Mollica, P.A.; Johnson, G.D.; Ogle, R.C.; Bruno, R.D.; Sachs, P.C. Accessible bioprinting: adaptation of a low-cost 3D-printer for precise cell placement and stem cell differentiation. *Biofabrication* **2016**, *8*, 025017, doi:10.1088/1758-5090/8/2/025017.
20. Campbell, J.; McGuinness, I.; Wirz, H.; Sharon, A.; Sauer-Budge, A.F. Multimaterial and Multiscale Three-Dimensional Bioprinter. *J. Nanotechnol. Eng. Med.* **2015**, *6*, 021001, doi:10.1115/1.4031230.
21. McElheny, C.; Hayes, D.; Devireddy, R. Design and Fabrication of a low-cost three-dimensional bioprinter. *J. Med. Devices, Trans. ASME* **2017**, *11*, 1–9, doi:10.1115/1.4037259.
22. Wijnen, B.; Hunt, E.J.; Anzalone, G.C.; Pearce, J.M. Open-source syringe pump library. *PLoS One* **2014**, *9*, 1–8, doi:10.1371/journal.pone.0107216.
23. Ravi, P.; Shiakolas, P.S.; Oberg, J.C.; Faizee, S.; Batra, A. On the Development of a Modular 3D Bioprinter for Research in Biomedical Device Fabrication. In Proceedings of the ASME 2015 International Mechanical Engineering Congress and Exposition; 2017; pp. 1–9.
24. Yenilmez, B.; Temirel, M.; Knowlton, S.; Lepowsky, E.; Tasoglu, S. Development and characterization of a low-cost 3D bioprinter. *Bioprinting* **2019**, *13*, e00044, doi:10.1016/j.bprint.2019.e00044.
25. Boularaoui, S.; Al Hussein, G.; Khan, K.A.; Christoforou, N.; Stefanini, C. An overview of extrusion-based bioprinting with a focus on induced shear stress and its effect on cell viability. *Bioprinting* **2020**, *20*, e00093, doi:10.1016/j.bprint.2020.e00093.
26. Gómez-Blanco, J.C.; Mancha-Sánchez, E.; Marcos, A.C.; Matamoros, M.; Díaz-Parralejo, A.; Pagador, J.B. Bioink temperature

influence on shear stress, pressure and velocity using computational simulation. *Processes* **2020**, *8*, doi:10.3390/PR8070865.

27. Li, M.; Tian, X.; Kozinski, J.A.; Chen, X.; Hwang, D.K. Modeling Mechanical Cell Damage in the Bioprinting Process Employing a Conical Needle. *J. Mech. Med. Biol.* **2015**, *15*, 1550073, doi:10.1142/S0219519415500736.
28. Liu, W.; Heinrich, M.A.; Zhou, Y.; Akpek, A.; Hu, N.; Liu, X.; Guan, X.; Zhong, Z.; Jin, X.; Khademhosseini, A.; et al. Extrusion Bioprinting of Shear-Thinning Gelatin Methacryloyl Bioinks. *Adv. Healthc. Mater.* **2017**, *6*, 1–11, doi:10.1002/adhm.201601451.
29. Magalhães, I.P.; de Oliveira, P.M.; Dernowsek, J.; Casas, E.B. Las; Casas, M.S. Las Investigation of the effect of nozzle design on rheological bioprinting properties using computational fluid dynamics. *Rev. Mater.* **2019**, *24*, doi:10.1590/s1517-707620190003.0714.
30. Martanto, W.; Baisch, S.M.; Costner, E.A.; Prausnitz, M.R.; Smith, M.K. Fluid dynamics in conically tapered microneedles. *AIChE J.* **2005**, *51*, 1599–1607, doi:10.1002/aic.10424.
31. Smith, C.; Oldt, G. *Multiaxial Bio-Printer Head*; Mechanical Engineering Rowan University; Personal counication; Available online: https://5f6357c8-abe2-426e-bc22-b9f609a0b347.filesusr.com/ugd/e69967_73cde5aebac44f11b0432814832a2110.pdf (accesed on 20/04/2018);
32. Gómez-Blanco, J.; Pagador, J.; Galván-Chacon, V.; Sánchez-Peralta, L.; Matamoros, M.; Marcos, A.; Sánchez-Margallo, F. Computational simulation-based comparative analysis of standard FDM 3D printing and conical nozzles for pneumatic and piston-driven bioprinting. *Addit. Manuf.* **2021** under review.
33. Marinaro, F.; Macías-García, B.; Sánchez-Margallo, F.M.; Blázquez, R.; Álvarez, V.; Matilla, E.; Hernández, N.; Gómez-Serrano, M.; Jorge, I.; Vázquez, J.; et al. Extracellular vesicles derived from endometrial human mesenchymal stem cells enhance embryo yield and quality in an aged murine model†. *Biol. Reprod.* **2019**, *100*, 1180–1192, doi:10.1093/biolre/ioy263.
34. Hesuani, Y.D.; Pereira, F.D.A.S.; Parfenov, V.; Koudan, E.; Mitryashkin, A.; Replyanski, N.; Kasyanov, V.; Knyazeva, A.; Bulanova, E.; Mironov, V. Design and Implementation of Novel Multifunctional 3D Bioprinter. *3d Print. Addit. Manuf.* **2016**, *3*, 65–68, doi:10.1089/3dp.2015.0040.
35. Ning, L.; Betancourt, N.; Schreyer, D.J.; Chen, X. Characterization of Cell Damage and Proliferative Ability during and after Bioprinting. *ACS Biomater. Sci. Eng.* **2018**, *4*, 3906–3918, doi:10.1021/acsbiomaterials.8b00714.
36. Roehm, K.D.; Madihally, S. V. Bioprinted chitosan-gelatin thermosensitive hydrogels using an inexpensive 3D printer. *Biofabrication* **2017**, *10*, 015002.
37. Sanz-Garcia, A.; Sodupe-Ortega, E.; Pernía-Espinoza, A.; Shimizu, T.; Escobedo-Lucea, C. A versatile open-source printhead for low-cost 3d microextrusion-based bioprinting. *Polymers (Basel).* **2020**, *12*, 1–18, doi:10.3390/polym12102346.